

Photometric and spectroscopic analysis of extragalactic early-type eclipsing binaries

Den Naturwissenschaftlichen Fakultäten der
Friedrich-Alexander-Universität Erlangen-Nürnberg
zur
Erlangung des Doktorgrades

vorgelegt von
Stefan Neßlinger
aus Treuchtlingen

Als Dissertation genehmigt
von den Naturwissenschaftlichen Fakultäten
der Universität Erlangen-Nürnberg

Tag der mündlichen Prüfung: 24. 08. 2007

Vorsitzender
der Promotionskommission: Prof. Dr. Eberhard Bänsch

Erstberichterstatter: Prof. Dr. Horst Drechsel

Zweitberichterstatter: Prof. Dr. Stefan Dreizler

Contents

Zusammenfassung	1
Abstract	3
1 Introduction	5
1.1 Binary stars and their relevance to astrophysics	5
1.2 Classification of binary stars	6
1.3 Determination of binary star masses	8
1.4 Distance determination with eclipsing binaries	9
1.5 The Roche model	11
2 Methods of analysis	15
2.1 Photometric analysis	16
2.1.1 MORO design	16
2.1.2 Modified Roche model	18
2.1.3 Parameter optimization	18
2.1.4 Mathematical recipes	18
2.2 Spectroscopic analysis	20
2.2.1 Disentangling spectra	20
2.2.2 FITSB2 design	20
2.2.3 Orbit mode	22
2.2.4 Error estimates	22
3 Photometric analysis of LMC binaries	23
3.1 Motivation	23
3.2 Previous work	24
3.3 Available Data	24
3.3.1 EROS	25
3.3.2 OGLE	25
3.3.3 MACHO	27
3.4 Data selection criteria	28
3.4.1 Orbital period	28
3.4.2 Effective temperature	28
3.4.3 Light curve quality	29
3.5 Data preparation	29
3.5.1 Light curve processing	29

3.5.2	Temperature extraction	31
3.6	Light curve analysis	34
3.6.1	General concept	34
3.6.2	Light curve grid	35
3.6.3	Parameter adjustment	36
3.6.4	Error assessment	37
3.7	Results for individual objects	38
3.7.1	Overcontact systems	41
3.7.2	Semi-detached systems	55
3.7.3	Detached systems	69
3.7.4	Special cases	113
4	Combined spectroscopic and photometric analysis of SMC binaries	131
4.1	Motivation	131
4.2	Previous work	132
4.3	Available data	133
4.4	Data selection	133
4.5	Data preparation	134
4.5.1	Spectroscopic data	134
4.5.2	Photometric data	135
4.6	Combined spectroscopic and photometric analysis	135
4.6.1	Parameter adjustment	136
4.6.2	Absolute parameter determination	138
4.7	Results for individual objects	139
4.7.1	OGLE 9 175323	141
4.7.2	OGLE 11 30116	146
4.7.3	OGLE 7 243913	151
4.7.4	OGLE 5 38089	156
4.7.5	OGLE 6 215965	161
4.8	Comparison with evolutionary tracks	166
4.9	Distance to the LMC	168
5	Conclusions and outlook	169
5.1	Results of the photometric analysis	170
5.2	Results of the spectroscopic analysis	172
5.3	Outlook	173
	Bibliography	175
	Acknowledgements	179
	Lebenslauf	181
	Curriculum Vitae	183

Zusammenfassung

Bedeckungsveränderliche Doppelsterne zählen zu den bedeutendsten Informationsquellen für die Zustandsgrößen von Sternen. Der weitaus größte Teil unseres Wissens über stellare Parameter wie Massen und Radien basiert auf Untersuchungen von Doppelsternen – eine besondere Bedeutung kommt dabei den Bedeckungsveränderlichen zu. Durch technische Grenzen war die Erforschung von Doppelsternen lange Zeit auf unsere eigene Galaxie beschränkt. Inzwischen sind die Ergebnisse großer Himmelsdurchmusterungen verfügbar, mit denen mehrere zehn Millionen extragalaktischer Sterne kontinuierlich überwacht wurden. Daraus ergeben sich einzigartige Möglichkeiten, unser Wissen über Sterne in Millionen von Lichtjahren entfernten Galaxien signifikant zu erweitern.

Zu den seltensten und daher am dürftigsten untersuchten Objekten gehören OB-Sterne frühen Spektraltyps, insbesondere in Umgebungen geringer Metallizität. Aufbauend auf Tausenden von Lichtkurven dieser bedeutenden Objekte in der Kleinen (SMC) und Großen Magellanschen Wolke (LMC), unseren unmittelbaren Nachbargalaxien, ist es nun durch Kombination mit spektroskopischen Daten möglich, ihre absoluten stellaren Zustandsgrößen wie Massen, Radien und Leuchtkräfte direkt zu bestimmen. Quasi als Nebeneffekt kann ihre Entfernung unabhängig von anderen Methoden gemessen werden, wodurch sie als Schlüsselemente für die Kalibration der nach wie vor umstrittenen „kosmischen Entfernungsleiter“ gelten.

Auf diesen Überlegungen baut die vorliegende Arbeit auf. Das Ziel war die Entwicklung eines effektiven Konzeptes für eine simultane photometrische und spektroskopische Analyse, womit es möglich sein sollte, ein höchst konsistentes, homogenes und präzises Set von absoluten Parametern für eine große Zahl von Bedeckungsveränderlichen in den Magellanschen Wolken zu bestimmen.

25 Bedeckungsveränderliche frühen Spektraltyps (OB-Systeme) aus der LMC wurden mit einem für heiße, enge Doppelsterne konzipierten numerischen Lichtkurvensynthese- und Analyseprogramm (MORO) untersucht. Anhand von Vorarbeiten wurde bereits gezeigt, dass die Ergebnisse einer rein photometrischen Analyse hinsichtlich des Massenverhältnisses entartet sind. Eindeutige Lösungen sind nur mit Hilfe einer unabhängigen spektroskopischen Festlegung des Massenverhältnisses möglich. Ähnlich verhält es sich mit den effektiven Oberflächentemperaturen und Leuchtkräften der beiden Komponenten, die aus der Lichtkurve nicht absolut, sondern nur in ihrem Verhältnis abgeleitet werden können. Auch die Radien ergeben sich ohne spektroskopische Radialgeschwindigkeitsmessungen nicht absolut, sondern nur relativ zum Komponentenabstand.

Für das gewählte Sample von OB-Systemen wurde eine Eingrenzung des vieldimensionalen Lösungsraums dadurch erreicht, dass das Massenverhältnis q über seinen gesamten Bereich systematisch variiert wurde und in Abhängigkeit von q die besten Lösungen und damit mögliche Wertebereiche für alle anderen Parameter bestimmt wurden. Dieses

Verfahren ermöglichte einerseits eine Untersuchung von Parameterkorrelationen auf statistischer Basis – unterschiedlich für die verschiedenen Systemkonfigurationen von getrennten, halbgetrennten und Kontaktsystemen – und erlaubt bei späterer Verfügbarkeit von Radialgeschwindigkeitsmessungen auch eine einfache Festlegung der absoluten Parameter der einzelnen Systeme.

Wegen der überragenden Bedeutung der Absolutparameter- und Entfernungsbestimmung enthält diese Arbeit einen zweiten Teil, der sich mit der verfeinerten Analyse einiger als Fallstudie anzusehender Doppelsterne aus der SMC beschäftigt. Die fünf vorgestellten Sterne in diesem Teil der Arbeit zeigen deutlich das große Potential der verwendeten Vorgehensweise. Die ermittelten Resultate sind in sich konsistenter und mit wesentlich geringeren Fehlern behaftet als sie mit bisherigen Methoden bestimmbar wären.

Die Arbeit ist in fünf Kapitel gegliedert, die sich wie folgt aufteilen:

- Kapitel 1 enthält eine kurze Einführung in die Doppelsternanalyse mit besonderem Schwerpunkt auf der Bedeutung von Bedeckungsveränderlichen allgemein.
- Kapitel 2 stellt detailliert die bei der photometrischen und spektroskopischen Analyse verwendeten Methoden und Techniken vor.
- Kapitel 3 beschreibt die verfügbaren photometrischen Daten und erläutert ihre Klassifizierung, Auswahl, Reduktion und Vorbereitung für die Analyse. Die Ergebnisse der Einzelanalysen von LMC-Doppelsternen werden detailliert wiedergegeben und die während der Untersuchung aufgetretenen Besonderheiten diskutiert.
- Kapitel 4 enthält die simultane photometrische und spektroskopische Analyse von fünf Bedeckungsveränderlichen aus der SMC. Jedes Objekt wird separat besprochen und die Ergebnisse diskutiert.
- Kapitel 5 fasst alle Ergebnisse zusammen und vergleicht sie mit anderen aktuellen Forschungsergebnissen. Ein Ausblick auf die künftige Entwicklung des Gebietes schließt die Arbeit ab.

Abstract

Eclipsing binaries are among the most important sources of information about the fundamental properties of stars. Most of our knowledge of stellar parameters like masses and radii is based on the analysis of binary stars – with a special wealth of insights coming from eclipsing binaries. For a long time, technical limitations restricted binary star research to our own galaxy. In the meantime the results of huge dark matter survey programs have become available which have constantly monitored literally tens of millions of extra-galactic stars. This is a unique opportunity for researchers to greatly expand our knowledge of stars to members of other galaxies millions of light-years away.

Among the rarest and therefore most scarcely analyzed objects are early-type OB-stars, especially in low-metallicity environments. With the availability of thousands of high-quality light curves of such objects located in the Small (SMC) and Large Magellanic Clouds (LMC), our next neighbor galaxies, researchers can now gain additional spectroscopic observations for these stars, and directly determine absolute stellar parameters like masses, radii and luminosities for these objects. This also allows us to accurately measure their distance independently from other methods, making them important corner stones in the still ongoing debate about the calibration of the “cosmic distance ladder”.

These promising prospects were the main motivation for this work. The aim was the development and proof of feasibility of an effective concept for a combined photometric and spectroscopic analysis, capable to derive a highly consistent, homogeneous and precise set of absolute parameters for a large number of eclipsing binaries in the Magellanic Clouds.

25 early-type eclipsing binaries (OB systems) from the LMC were analyzed with a numeric light curve synthesis and analysis program (MORO) devised for hot, close binaries. In preparatory work it has already been shown that the results of a purely photometric analysis are degenerate with respect to the mass ratio q . Unambiguous solutions are not possible without fixing the mass ratio at an independently derived spectroscopic value. Similarly, absolute values of effective surface temperatures and luminosities of both binary components cannot be derived from the light curves, only their respective ratios are accessible. Also the radii can only be derived relative to the orbital separation without spectroscopic measurements of radial velocities.

For the selected sample the multi-dimensional parameter space was confined by systematic variation of the mass ratio q over all relevant values and determination of best solution regimes and parameter ranges dependent on q . This approach allowed for an investigation of parameter correlations on a statistical basis – for detached, semi-detached and contact systems. Based on this confinement of parameter space and the quantitative knowledge of the relevant parameter correlations an easy determination of absolute pa-

parameters of the photometrically analyzed systems will be possible once complementary spectroscopic data will become available.

Due to the high importance of absolute parameter and distance determinations and to prove the feasibility of the proposed approach, a second part of this work is devoted to a careful case study of a sample of early-type SMC binaries, for which both photometric and spectroscopic data are available. The five stars analyzed with this method impressively illustrate the power of this kind of investigation. The derived results provide much better consistency and accuracy than would have been possible to achieve with previous methods.

This work is divided into the following five parts:

- Chapter 1 gives a short introduction to binary star research with an emphasis on the significance of eclipsing binaries in general.
- Chapter 2 discusses in detail the methods and techniques used in the photometric as well as spectroscopic analysis.
- Chapter 3 gives an overview of all available photometric data, its classification, selection, reduction and preparation for analysis. Detailed results for each analyzed LMC binary are presented and various issues and problems encountered during analysis are discussed.
- Chapter 4 is concerned with the complete photometric and spectroscopic analysis of five SMC binaries. For each star a thorough interpretation of the results is given.
- Chapter 5 contains a summary of all results and compares them with the findings of related contemporary research. An outlook to future developments in the field concludes the work.

1 Introduction

1.1 Binary stars and their relevance to astrophysics

One of the most important disciplines of stellar astronomy is concerned with the analysis of binary stars. This class of stars is of utmost importance as a major part of our knowledge of absolute physical stellar parameters has been derived from binaries. Since even with today's 10-meter-class telescopes virtually no star in the sky can actually be spatially resolved, we need indirect measurements to determine stellar radii. These mainly come from observing stellar occultations where one component eclipses its companion. The exact shape of the resulting light curve allows conclusions about the relative radii of the involved stars.

A similar problem arises for the determination of stellar masses. To derive these, we need to observe the gravitational interactions between one star and its companion. For example, the mass of our sun has been accurately established from precise observations of the planetary orbits. Due to the enormous distances of other stars we must rely on something else than planets in order to determine their masses: stellar companions. Relative masses of two components can be established by carefully observing their relative motion, usually via spectroscopic methods.

In order to determine absolute masses and radii one must use simultaneous photometric and spectroscopic observations to overcome their respective intrinsic limitations regarding the information they convey. Deriving absolute stellar parameters is of outstanding importance to calibrate, test and enhance theories of stellar formation, structure and evolution. Much of our understanding of the universe depends on stellar astronomy, which has a strong impact also on other fields like galaxy formation and evolution. Thus it is indispensable that stellar astronomical observations are continuously being supported as technology advances and do not lose further weight in favor of pure extragalactic and cosmological research.

Since binary stars with known absolute parameters can serve as excellent distance indicators via their luminosities, especially binaries in our neighbor galaxies should be observed, because they form the first step in the cosmic distance scale. Such a new, binary-based method of distance determination is very desirable, since it not only complements, but considerably surpasses the classical methods. According to Paczyński (1997), distance determination via binary stars can easily reach an accuracy of $\sim 1\%$, much in excess of other methods.

One of the advantages of the binary method stems from the sheer number of extragalactic spectroscopic and eclipsing binaries which are observable with today's technology. According to Halbwachs (1986), about 75% of all stars are members of binary or multi-

ple systems. This huge number of stars opens up the possibility of distance determinations to nearby galaxies with unprecedented accuracy via statistical methods. Apart from these considerations, the mere fact that binary stars form the majority of visible matter in the universe, should be reason enough to warrant their continuing in-depth analysis.

This work focuses on the analysis of close, early-type stars in the Magellanic Clouds. Especially for OB stars there is urgent need for more and better parameters, since these most massive and most luminous stars are very rare, especially in the solar neighborhood. Their enormous luminosity, on the other hand, makes them observable with reasonable effort even over extragalactic distance scales, thereby combining several advantages:

- Availability of extended data archives of photometric observations with good signal-to-noise ratios
- An excellent opportunity to supply theoretical astronomers with new data for the type of stars with the scarcest base of known parameters
- The opportunity to determine extragalactic distances independently of other methods with high accuracy.

1.2 Classification of binary stars

Binary stars can be classified according to various different criteria. One basic classification scheme involves the equipment which is necessary to establish the binary nature of a system. It subdivides the binary population into visual and spectroscopic binaries.

Visual binaries are binary stars which can actually be resolved as two individual stars, even if a large telescope and interferometric techniques may be necessary. Depending on its distance, this type of binary system is usually well-separated, therefore involving large orbits and very long orbital periods of at least several months, years or decades. These long time scales make it impossible to gather information from a full orbit in a reasonable amount of time. On the other hand, the orbit can be directly determined from astrometric measurements and is accessible on an absolute scale, if the distance is also known. Visual binaries are gravitationally bound to each other and must not be confused with optical binaries, two completely independent stars which just happen to lie near the same line of sight.

The vast majority of binary stars are classified as spectroscopic binaries. It is not possible to resolve the individual components with any existing technology. They always appear as just one dot in the sky to the observer. The binary nature of these objects is only revealed by spectroscopic observations. Caused by the orbital motion, the spectral lines of both components exhibit periodic anti-phased shifts in wavelength due to the Doppler effect. As one component approaches the Earth, its lines are shifted towards the blue end of the spectrum, while the other component shows a redshift of its spectral lines. Spectroscopic binaries are further subclassified into single-lined and double-lined binaries, depending on the visibility of one or both components in the common spectrum. If

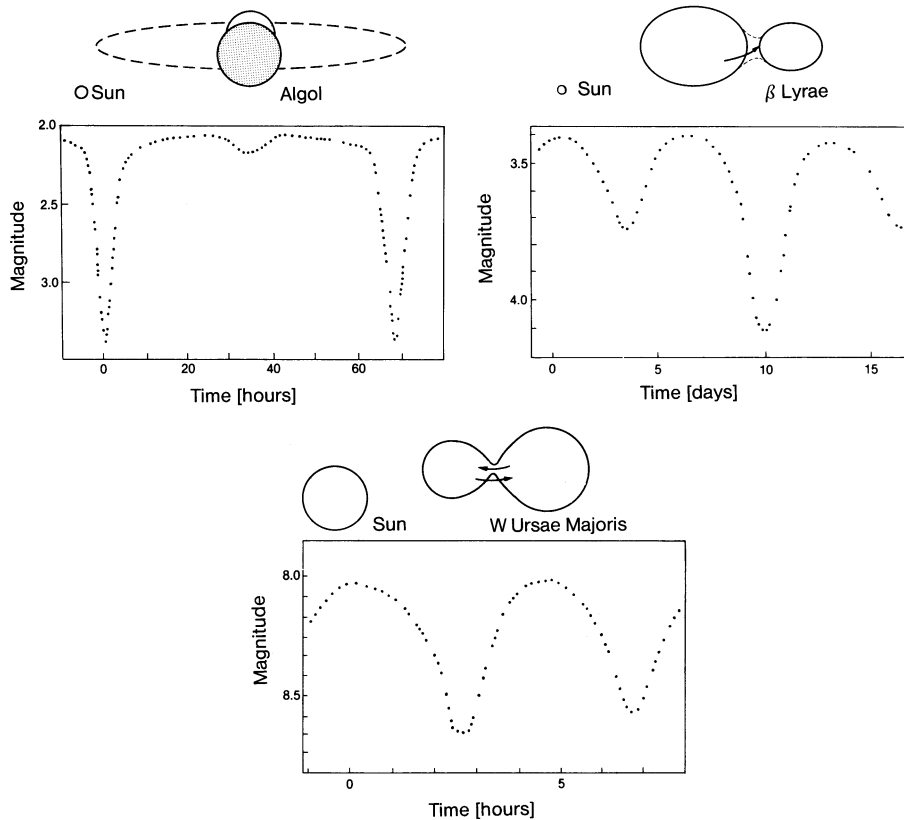


Figure 1.1: The prototypes of the three eclipsing binary types shown together with their light curves. Note that light curve shape is a direct indicator of relative component separation (after Karttunen et al. 1994).

one component is considerably less luminous than the other, it may be difficult or impossible to detect it in the spectrum. Nevertheless, the binary nature of the object can also be established by observing the periodic shifts of the spectral lines corresponding to the more luminous component.

A special subgroup of spectroscopic binaries is formed by the eclipsing binaries. In terms of astrophysical information which can be gained from them, eclipsing binaries are the most important representatives of binary stars. This work is concerned exclusively with the analysis of eclipsing binaries. They are normal spectroscopic binaries with the distinctiveness of a fortunate orientation of their orbital plane with respect to our line of sight. Due to this fact, both components periodically eclipse their respective companion as they orbit around each other. We can observe these eclipses photometrically as periodic light changes of the binary star. From a time series of photometric measurements one can construct a light curve which exhibits a characteristic shape sensitive to certain physical and geometrical parameters of the binary and its orbit.

A subclassification of eclipsing binaries has long been established in the literature, for which essentially three well-analyzed objects with distinctive light curve shapes are selected as prototypes of their classes. According to this scheme, most eclipsing binaries can be classified as of Algol, β Lyrae or W Ursae Majoris type (see Fig. 1.1). Their light

curves mainly differ with respect to shape and relative depths of the minima as well as the strength of out-of-eclipse variability.

1.3 Determination of binary star masses

One of the most important benefits which comes with the analysis of binary stars is the possibility to directly and accurately determine their masses from observations of their orbits. In the following considerations, a circular orbit of the stars will be assumed. For those close binaries which are discussed in this work, it is a reasonable assumption that their orbits have been sufficiently circularized due to tidal interactions. Nevertheless, the determination of stellar masses is completely analogous in the case of eccentric orbits, only the equations given here would contain the additional eccentricity parameter e .

The starting point for mass determination is Kepler's Third Law, which connects orbital separation a (semimajor axis of the relative orbit) and orbital period P with the component masses M_1 and M_2 :

$$\frac{P^2}{a^3} = \frac{4\pi^2}{G(M_1 + M_2)}, \quad (1.1)$$

with $a = a_1 + a_2$ denoting the sum of the semimajor axes of the absolute orbits around the center of mass. This fundamental equation can be rewritten to give the total mass of the binary system:

$$M_1 + M_2 = \frac{4\pi^2 a^3}{GP^2}. \quad (1.2)$$

For the circular orbits found in most close binaries the orbital velocity v_n is given by

$$v_n = \frac{2\pi a_n}{P}. \quad (1.3)$$

with n denoting the respective binary component. As most binary orbits are inclined at some angle i relative to the line of sight, we can only measure the projection $k_n = v_n \sin i$. If we add up the orbital velocities of both components, we find

$$v_1 + v_2 = \frac{k_1 + k_2}{\sin i} = \frac{2\pi a}{P}. \quad (1.4)$$

Combined with Eq. (1.2) this gives the total mass of the two components:

$$M_1 + M_2 = \frac{P}{2\pi G} \frac{(k_1 + k_2)^3}{\sin^3 i}. \quad (1.5)$$

With the definition of the center of mass,

$$\frac{M_1}{M_2} = \frac{a_2}{a_1} = \frac{k_2}{k_1}, \quad (1.6)$$

we can substitute M_1 in Eq. (1.5), ending up with

$$M_2 = \frac{P}{2\pi G} \frac{k_1 (k_1 + k_2)^2}{\sin^3 i}. \quad (1.7)$$

For M_1 the procedure is completely analogous. Of course, the inclination i is still unknown. Therefore, assuming $i = 90^\circ$, we can only give lower limits for the masses. The inclination has to be determined by other means. Usually, this parameter can be readily and unambiguously determined from the light curves of an eclipsing binary. With i from the light curves, P from spectroscopy (or from the light curves as well) and k_n from spectroscopy, the absolute masses of both stars can be determined without making any further assumptions about the system.

As it is evident from Eq. (1.7), one needs to know the projected orbital velocities of both binary components in order to determine their individual masses. In the case of single-lined spectroscopic binaries this is not possible, since only the more luminous of the components is seen in the spectrum. In that case it is still possible to gain some information about the masses, though. With $a = a_1 + a_2$ in combination with Eq. (1.6) we get

$$a_1 = \frac{aM_2}{M_1 + M_2}. \quad (1.8)$$

Substituting this into Eq. (1.3) yields

$$a = \frac{P}{2\pi} \frac{k_1 (M_1 + M_2)}{M_2 \sin i}. \quad (1.9)$$

This can again be substituted into Kepler's Third Law (Eq. 1.1) to give the so-called mass function:

$$f(M) = \frac{k_1^3 P}{2\pi G} = \frac{M_2^3 \sin^3 i}{(M_1 + M_2)^2}. \quad (1.10)$$

If additional knowledge is available to constrain the mass of one of the stars, the mass function can be easily solved for the mass of the companion, always assuming the inclination i is known. Otherwise again only minimum masses can be derived.

1.4 Distance determination with eclipsing binaries

Since the method of stellar parallaxes works only on short distances up to a few tens of light years, for a long time the only way to determine distances on longer – and especially extragalactic – scales has been the well-known period-luminosity relation of Cepheid variables. With the possibility to acquire good photometric and spectroscopic data even from extragalactic eclipsing binaries, there is now another, independent method available for distance determination on larger scales, with the potential of even higher accuracy.

From the eclipse light curve the fractional radii r_n of the two components can be determined either by computer-based light curve analysis, or, in the favorable case of total

eclipses, by directly measuring the ratio of eclipse duration and orbital period. The absolute stellar radii R_n scale with the separation a of the components:

$$r_n = \frac{R_n}{a}. \quad (1.11)$$

a is readily determined from the orbital period, the component masses and Kepler's Third Law. Well-detached binaries are best suited for determining stellar radii since they usually do not suffer from ellipsoidal deformations often encountered in very close binaries. These deformations make it difficult to accurately define the stellar radius. Also the minima do not begin and end abruptly, rather the light curve "fades" in and out gradually, thereby hampering the measurement of accurate eclipse durations.

Unfortunately, one still needs some additional physical knowledge about the binary stars, as their surface brightnesses F_n need to be derived. If good spectroscopic measurements are available, temperature and therefore surface brightness determination are relatively straightforward, though. The luminosities of both components can be written in the Stefan-Boltzmann approximation as

$$L_n = 4\pi R_n^2 F_n. \quad (1.12)$$

As the total amount of energy, which leaves each star per unit time is the same which passes through the surface of an arbitrarily sized sphere centered on the origin of the radiation (and particularly a sphere with a radius equal to the distance d_n between star and observer), we can write

$$4\pi R_n^2 F_n = 4\pi d_n^2 F_{n,\text{obs}}, \quad (1.13)$$

with $F_{n,\text{obs}}$ denoting the amount of energy per time and unit area the observer receives from the respective star. Solving Eq. (1.13) for d_n gives

$$d_n = R_n \sqrt{\frac{F_n}{F_{n,\text{obs}}}} = \sqrt{\frac{L_n}{4\pi F_{n,\text{obs}}}}. \quad (1.14)$$

As $d_1 = d_2 = d$ is an excellent approximation for all practical purposes, we can choose either star to determine the distance. $F_{n,\text{obs}}$ has to be taken from the light curve. Again, total stellar eclipses are of great value, as one can measure the amount of energy arriving from each star separately during minimum times. Otherwise the relative fractions of light have to be determined from computerized light curve analysis.

According to Paczyński (1997), extragalactic distances can be determined to a precision of 1% with this method. This publication also features a more in-depth discussion of distance determination with eclipsing binaries, along with a review of possible errors which have to be taken into account.

1.5 The Roche model

In order to derive eclipsing binary parameters from their light curves, one needs a suitable theoretical model for the structure of the underlying binary system, from which synthetic light curves can be derived and compared with the observations. When analyzing close binaries, it is very important that a physical model is applied, which can adequately reproduce the complicated geometrical shapes of the stars, since tidal distortion of the components (due to the presence of a close companion) has great influence on the actual shape of the light curves. The nature of this influence can be understood easily: during and close to eclipses, we see the stars almost undistorted; during quadrature phases (viewing the “sides” of the stars) the components present larger, elongated projected surfaces to the observer. Therefore additional light is observed in quadrature phases compared to undistorted components. The impact this has on the light curves can be seen in Fig. 1.1: the stronger the stars are tidally distorted, the more out-of-eclipse variation can be seen in the light curves.

It is therefore necessary to model these effects when comparing synthetic light curves with the observations. One of the most widespread models for the binary structure used in contemporary light curve analysis is based on the work of the French mathematician Edouard Albert Roche. Its basic concept dates back to the mid-19th century, when it was originally published by Roche (1849). The Roche model is based on the well-known restricted three-body problem. Therefore several assumptions about the stars are made in order to treat them with the Roche model:

- With respect to the gravitational forces exerted on the companion, both components are considered as point masses.
- Both components orbit their common center of mass, the orbits are circular.
- The rotational axes of both stars are perpendicular to their orbital plane.
- Both components are tidally locked to their orbits (synchronous rotation).

These limitations mean that only gravitational and centrifugal forces are taken into account. Tidal forces due to unsynchronized rotation of the stars as well as radiation pressure are specifically not included. Of course, in modern light curve analysis programs these restrictions have been overcome (see Section 2.1), but for the sake of simplicity, only the original Roche model will be described here.

In the Roche treatment, a binary system is usually modelled in an orthogonal, co-rotating (with the orbit of the components) coordinate system with the origin at the center of mass. The x-axis corresponds to the radius vector of relative orbital motion, and thus the line connecting the centers of mass of both components. The z-axis is orthogonal to the orbital plane (see Fig. 1.2). For a more convenient treatment, the origin can be placed at the center of mass of the component of interest. For example, if the origin is placed at the mass center of the more massive component, the systemic center of mass is found on the x-axis at

$$\frac{M_2 a}{M_1 + M_2}.$$

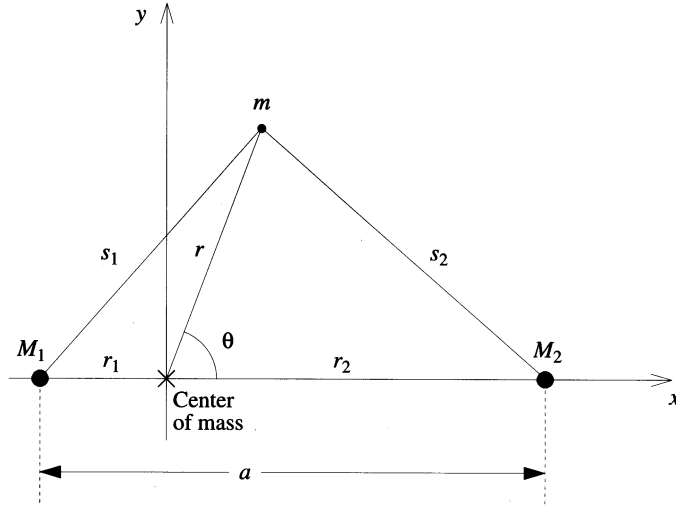


Figure 1.2: Co-rotating coordinate system of the Roche model. M_1 and M_2 denote point masses corresponding to the binary components, separated by the relative semi-major axis a . The total force exerted on a test mass m with coordinates as given in the figure is evaluated. (after Carroll & Ostlie 1996).

The total effective potential taking into account gravitational and centrifugal forces at an arbitrary point $P(x, y, z)$ can therefore be written as

$$-\Psi = G\frac{M_1}{r_1} + G\frac{M_2}{r_2} + \frac{\omega^2}{2} \left\{ \left(x - \frac{M_2 a}{M_1 + M_2} \right)^2 + y^2 \right\} \quad (1.15)$$

with

$$r_1 = \sqrt{x^2 + y^2 + z^2}, \quad r_2 = \sqrt{(a - x)^2 + y^2 + z^2}$$

and the gravitational constant G , the relative semi-major axis a and the angular velocity ω of orbital movement. According to Kepler's third law this can be written as

$$\omega^2 = \frac{G(M_1 + M_2)}{a^3}. \quad (1.16)$$

Thus Eq. (1.15) can be rewritten as the so-called Roche potential:

$$\Omega := -\frac{1}{GM_1}\Psi = \frac{1}{r_1} + \frac{q}{r_2} + \frac{q+1}{2}(x^2 + y^2) - qx + \frac{q^2}{2(1+q)}, \quad (1.17)$$

where a is the unit of length in this equation and q denotes the mass ratio M_2/M_1 with $M_1 \geq M_2$. The last term in Eq. (1.17) is independent of position, it is usually discarded. The advantage of Eq. (1.17) is that at every given coordinate the potential only depends on a single parameter, the mass ratio q .

The surfaces of the components are formed by equipotential surfaces on which matter can flow without energy exchange. In order to facilitate the calculation of these equipotential surfaces, one usually switches to spherical coordinates r, θ, φ . Again, the origin is

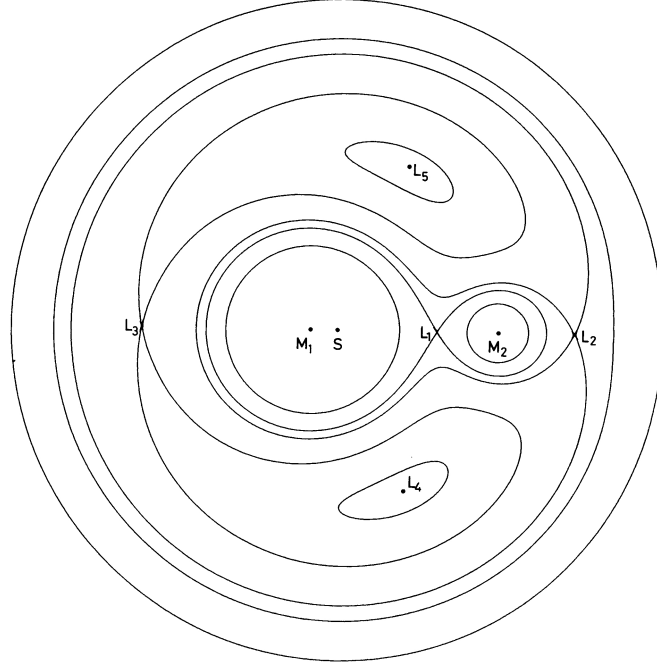


Figure 1.3: Two-dimensional cross-section through selected Roche equipotential surfaces for a binary system with $M_2/M_1 = 0.17$ (after Karttunen et al. 1994); also denoted are the five Lagrangian and libration points $L_{1...5}$ respectively, as well as the center of mass S .

placed at the center of the component of interest. In these coordinates, the Roche potential for the primary (more massive) component can be written as

$$\Omega_1 = \frac{1}{r_1} + q \left(\frac{1}{\sqrt{1 - 2\lambda r_1 + r_1^2}} - \lambda r_1 \right) + r_1^2 \frac{q+1}{2} (1 - \nu^2). \quad (1.18)$$

For the secondary (less massive) component one gets

$$\Omega_2 = \frac{1}{r_2} + q \left(\frac{1}{\sqrt{1 - 2\lambda r_2 + r_2^2}} - \lambda r_2 \right) + r_2^2 \frac{q+1}{2} (1 - \nu^2) + \frac{1-q}{2}, \quad (1.19)$$

with

$$r_n = \sqrt{x_n^2 + y_n^2 + z_n^2}, \quad \lambda = \sin \theta \cos \varphi, \quad \nu = \cos \theta.$$

The Roche equipotential surfaces correspond to points of identical potential energy Ω (see Fig. 1.3). Their actual shapes are determined by the combination of the mass ratio q with a numerical value for the potential. Large values of Ω correspond to equipotential surfaces close to the origin, which assume circular shape for $\Omega \rightarrow \infty$. If smaller values are chosen for Ω , the component surfaces depart from circular shape, until they finally touch the inner Lagrangian point L_1 . This is a point of unstable equilibrium located between both centers

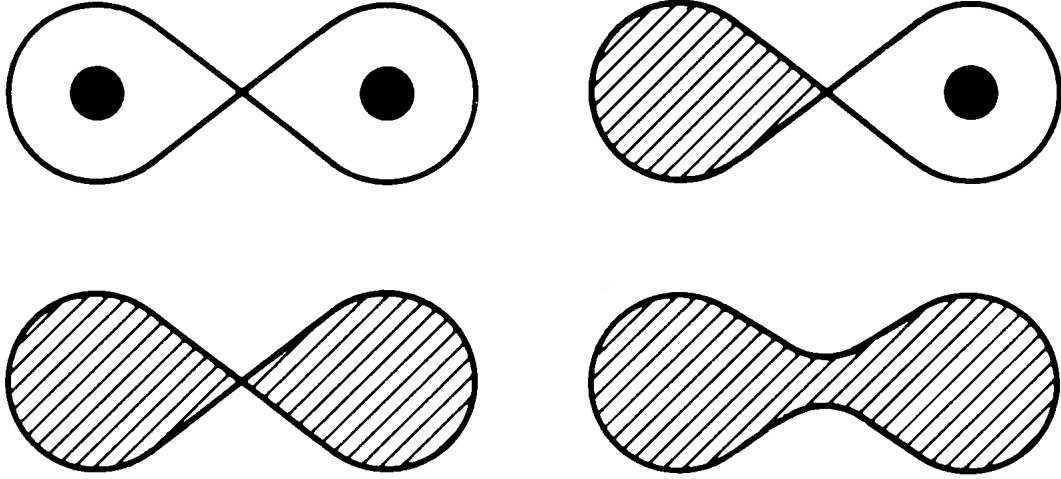


Figure 1.4: The four possible configurations of binary systems: detached (top left), semi-detached (top right), contact (bottom left) and overcontact configurations (bottom right); after Karttunen et al. (1994).

of mass. If one of the components completely fills this so-called inner critical Roche lobe, it can lose matter towards its companion if it expands any further (this phenomenon is generally known as Roche lobe overflow). If the surface potentials of both stars are chosen smaller than the potential of the inner Lagrangian point, a common envelope of both stars results. For a physically meaningful result it is necessary to choose the same potential for both stars in this case.

The limit for a reasonable binary star configuration is formed by the equipotential surface including the outer Lagrangian point L_2 , another point of unstable equilibrium. Any further expansion of the stars would result in an immediate loss of mass which would be ejected from the system via L_2 . Still another point of unstable equilibrium, L_3 , can be found on the side of the more massive companion. For the treatment of binary stars, it is of theoretical interest only. Furthermore, there are two libration points L_4 and L_5 which are points of stable equilibrium. In our solar system the sun and Jupiter have common libration points which are occupied by a group of asteroids known as the “Trojans”.

According to Kopal (1959) one can classify the possible binary star configurations as detached, semi-detached and contact systems, see Fig. 1.4. The last class has been extended to include the so-called overcontact systems. A quantitative discrimination between these system configurations is possible by comparing the surface potentials Ω_1 and Ω_2 with the equipotential surface containing the inner Lagrangian point $\Omega(L_1)$:

1. Detached system: $\Omega_1, \Omega_2 > \Omega(L_1)$
2. Semi-detached system: $\Omega_1 = \Omega(L_1), \Omega_2 > \Omega(L_1)$ or $\Omega_1 > \Omega(L_1), \Omega_2 = \Omega(L_1)$
3. Contact system: $\Omega_1 = \Omega_2 = \Omega(L_1)$
4. Overcontact system: $\Omega(L_1) > \Omega_1 = \Omega_2 \geq \Omega(L_2)$

2 Methods of analysis

In order to derive absolute parameters of binary stars, it is essential to effectively combine as much information as possible from photometric and spectroscopic observations. As can be seen from the discussion in Sections 1.3 and 1.4, there are certain parameters which cannot be derived from either single type of observation. For instance the orbital inclination i of the system is not accessible through spectroscopic data. Nevertheless, it is required to determine the true orbital velocities of the components, since only the projected radial velocity amplitudes manifest themselves in the spectra. The only way to derive the orbital inclination is by careful analysis of photometric light curves.

On the other hand, the light curves usually suffer from a pronounced degeneracy with respect to the mass ratio q of the components. As has been shown by Neßlinger (2004), even very good photometric data can usually be fitted by synthetic light curves derived for wide ranges of q (i. e. $0.3 \lesssim q \leq 1.0$). Since correlations exist between q and other important parameters like orbital inclination i and the values of the surface potentials Ω_1 and Ω_2 (which in turn influence relative stellar radii and luminosities), it is very important to pinpoint the mass ratio first before attempting a precise light curve solution. Here the spectroscopic observations come into play again, as q can be readily measured from a time series of double-lined spectra without any further knowledge about the system.

Information about many of the other parameters like temperature ratio, relative luminosities and even the radii of the stars is contained to a varying degree in photometric and spectroscopic data alike, offering a certain amount of redundancy. At the same time, the methods of analysis are largely independent due to entirely different models which are used to fit photometric and spectroscopic data. This offers an excellent opportunity to cross-check the independently derived values. If these match within the expected errors, good confidence can be gained about their validity, while systematic errors or other problems can be more easily identified if there are serious deviations of the results.

It is this interrelation between photometric and spectroscopic observations which makes the determination of absolute binary parameters interesting yet challenging, since it is often difficult to collect sufficient data of adequate quality. Especially the high demands associated with gaining spectroscopic data of faint stars (fainter than about 14 mag) considerably hampered the progress of this work. Nevertheless, the method is successfully applied in this work to a number of case studies of stars in the Small Magellanic Cloud. The following sections give an overview of the software packages involved in the analysis of both types of data, while detailed information about the procedures applied is discussed in Sections 3.6 and 4.6.

2.1 Photometric analysis

Due to the wealth and complexity of the information contained in eclipsing binary light curves, the analysis of such data is most frequently made with the help of synthetic model light curves. As has been discussed in Section 1.5, good light curve modelling is highly dependent on a realistic physical model. The Roche model is an excellent approximation. It forms the basis of most light curve synthesis programs in use today.

2.1.1 MORO design

The software used for this work is called “MORO” (for MODified ROche model). It has been developed at the Dr. Remeis Observatory in Bamberg and includes, as its name implies, several modifications to the original Roche model. The modified Roche model, which forms the basis of MORO, contains 17 individual parameters, five of which are wavelength-dependent. Therefore in a typical situation where light curves are available in two passbands, the corresponding synthetic light curves are calculated from a total of 22 parameters. The light contribution of each component is calculated via breaking down the surface into small segments, and adding up the light received from each segment which is visible to the observer at the orbital phase considered. Of course, possible eclipses by the companion and the angle at which every segment normal is inclined to the line of sight are taken into account appropriately. An important limitation of the program is its restriction to circular orbits. A detailed description of the program and its geometrical and physical background is given in Drechsel et al. (1995), while in-depth information about its effective use and several tips from practical experience can be found in Lorenz (1988). Some examples of the effects certain parameter changes have on a given light curve are shown in Figs. 2.1 to 2.3, while Table 2.1 provides a list of all parameters comprising the binary star model of MORO.

i	Orbital inclination
g_1, g_2	Gravity darkening coefficients
$T_{\text{eff},1}, T_{\text{eff},2}$	Effective temperatures
A_1, A_2	Albedos
Ω_1, Ω_2	Surface potentials
q	Mass ratio
δ_1, δ_2	Radiation pressure coefficients
$L_1(\lambda), L_2(\lambda)$	Luminosities
$x_1(\lambda), x_2(\lambda)$	Limb darkening coefficients
$l_3(\lambda)$	Third light

Table 2.1: List of all light curve parameters adjustable by MORO. For a detailed description of their usage in this work refer to Section 3.6.3. Some examples of their influence on light curve shapes are shown in Figs. 2.1 to 2.3.

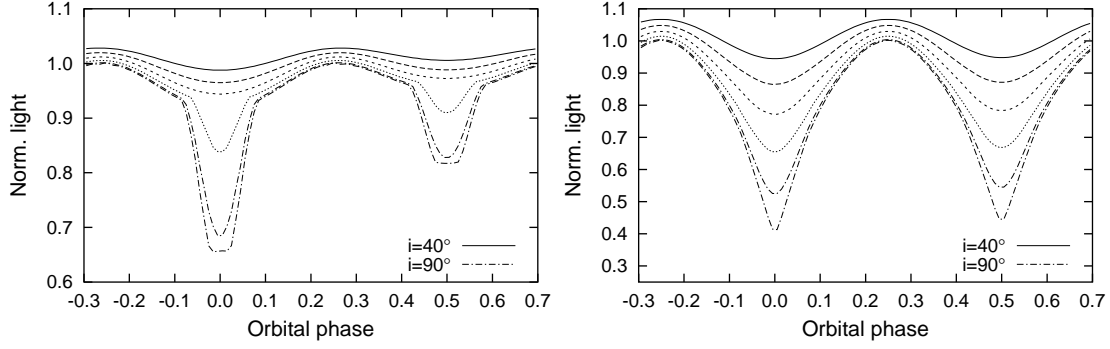


Figure 2.1: Synthetic light curves for different values of orbital inclination i in the detached (left) and overcontact case (right). Inclination range is from 40° to 90° , incremented linearly in between.

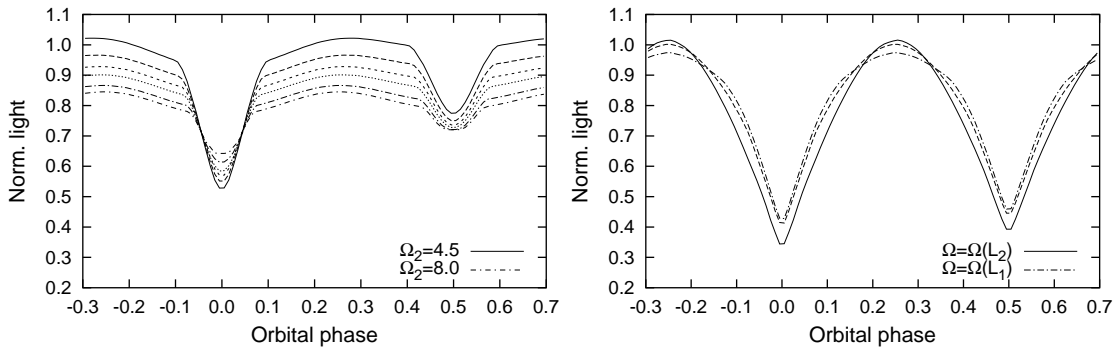


Figure 2.2: The effects of surface potential Ω_2 variation on the light curve of a detached system (left) and variation of both surface potentials Ω_1 and Ω_2 for an overcontact configuration (right). For the detached system, q and Ω_1 were held constant. Therefore increasing Ω_2 is identical to a decreasing ratio of the radii R_2/R_1 . $\Omega(L_1)$ and $\Omega(L_2)$ denote the potentials of the inner and outer Lagrangian points.

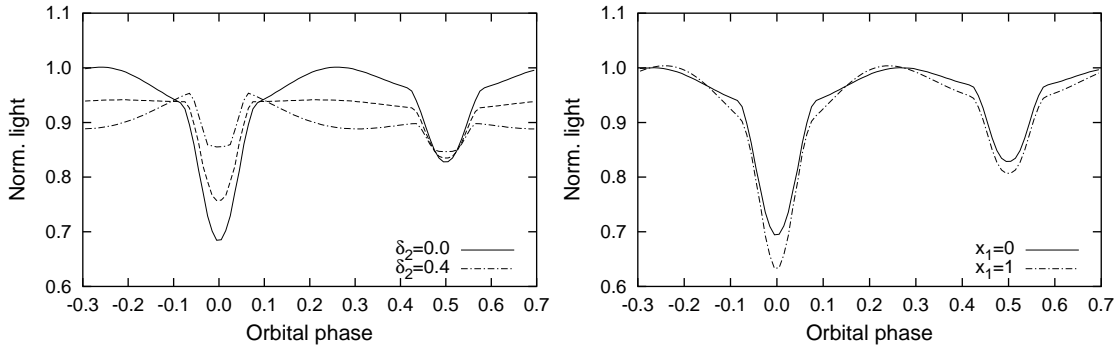


Figure 2.3: Influence of (unrealistically strong) radiation pressure of the secondary component (left) and of extreme values of the primary limb darkening coefficients (right) on the light curves of a detached system.

2.1.2 Modified Roche model

The main modification of the original Roche model in MORO concerns the implementation of radiation pressure effects. Especially in hot, close binary stars, it can be necessary to take the associated surface deformations into account. While radiation pressure and gravity act in approximately opposite directions in the radiating component and can be accounted for by a reduced gravitational potential

$$(1 - \delta) \frac{GM}{r},$$

things are much more complicated for the irradiated surface of its companion.

The actual shape of the surface of the irradiated component must be considered by including radiation pressure parameters in a numerically determined modified Roche potential. At the same time these parameters are dependent on the location on the irradiated surface. Therefore the radiation pressure-induced shape change can only be calculated iteratively via the Newton-Raphson algorithm. For details about the radiation pressure implementation see Haas (1993) and Drechsel et al. (1995). Correct treatment of radiation pressure effects also for overcontact binaries has been implemented by Bauer (2004).

2.1.3 Parameter optimization

The derivation of parameters from binary light curves with MORO follows the classical χ^2 minimization procedure: for a given set of photometric data, the user supplies a set of initial parameter values, which the software uses to calculate the corresponding synthetic light curve. The residuals with respect to the observational data are determined and a χ^2 value is calculated which takes into account the errors of the individual data points, if supplied. According to a predefined “recipe” a new light curve is then calculated from slightly different parameters, again checked against the observations and a new χ^2 calculated. This procedure is repeated until a set abort criterium is reached which is defined by the rate of χ^2 minimization in each step. The final synthetic light curve is considered the best solution of the observational data.

2.1.4 Mathematical recipes

The “recipe” for changing the parameters of the synthetic light curves in subsequent iteration steps depends on the mathematical model used. One of the most widespread techniques is the so-called Wilson-Devinney scheme (WD), which dates back more than 35 years (Wilson & Devinney 1971). The procedure involves the method of differential corrections. It is a fast-converging non-linear least squares procedure, which unfortunately suffers from some severe drawbacks, most notably numerical instability due to inadequate start parameters or simultaneous adjustment of too many (and possibly correlated) parameters.

Therefore MORO is built around a different “recipe” which is called the “simplex algorithm” (Kallrath & Linnell 1987). This method is not sensitive to the number of simul-

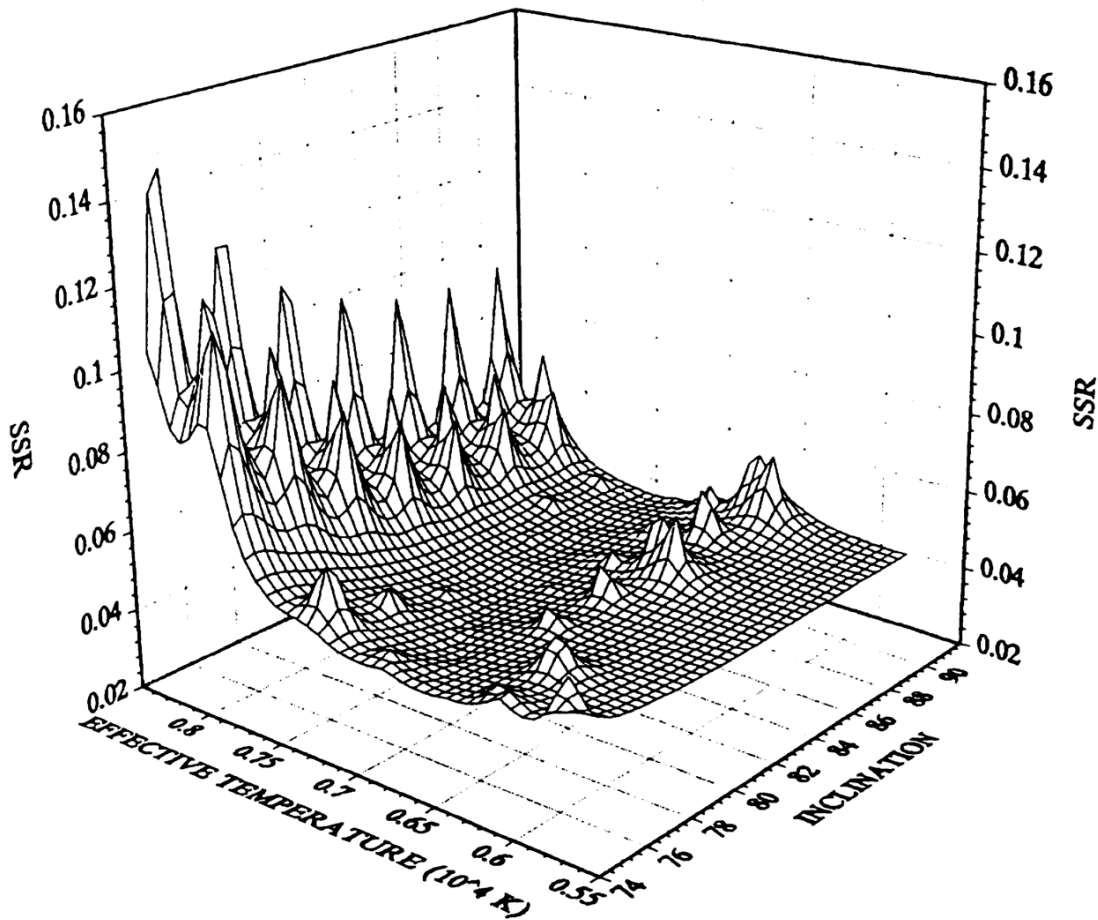


Figure 2.4: Two-dimensional parameter space showing inclination vs. effective temperature of the secondary component. The z-axis shows the residuals of the synthetic light curve with respect to the observations for any given combination of inclination and effective temperature. (illustration reproduced from Kallrath & Milone 1999).

taneously adjusted parameters and generally exhibits extremely high numerical stability. One of the main advantages is that the simplex algorithm cannot diverge, since every step of the iteration must yield an equal or better result than the preceding one. This is accomplished in the following way: from the user-supplied set of start parameters the “simplex” is constructed which is essentially a polygon including $m + 1$ vertices in the m -dimensional parameter space, centered on the start parameter set. Each vertex represents a distinctive set of model parameters. After each iteration, synthetic light curves calculated from parameters corresponding to all vertices are compared with the observational data. The vertex yielding the worst fit is discarded in favor of a new vertex which is calculated according to a pre-defined scheme. This ensures that no iteration can produce a worse fit than the preceding one. For an in-depth discussion of the method see Kallrath & Linnell (1987), and Lorenz (1988) for one of the first applications in light curve analysis.

One can easily visualize the simplex procedure in a two-dimensional parameter space (see Fig. 2.4): in this case, the simplex is a triangle which moves around in parameter space, at each step discarding one point in favor of a new one. In the course of parameter adjustment, the triangle shrinks until it contracts towards a single point. After the abort criterium is reached, the center of this (diminutive) triangle is output as the best solution.

2.2 Spectroscopic analysis

As has been pointed out, no absolute stellar parameters can be derived from photometric data alone. It is necessary to incorporate spectroscopic observations in the analysis. From double-lined binary spectra essential data like the radial velocities as well as effective temperatures and surface gravities can be gained. One needs a time series of spectroscopic observations with (near) full phase coverage in order to construct a radial velocity curve from the varying Doppler shifts of the spectral lines. For determination of the physical parameters, on the other hand, single spectra of the individual components with the highest signal-to-noise ratio possible are necessary. However, these cannot be easily recorded for close (and therefore short-period) binaries, as excessive integration times result in considerable “phase smearing” of the spectra and therefore a significant reduction of their resolution.

2.2.1 Disentangling spectra

Generally the favored method for extracting component spectra from a combined binary spectrum is a procedure known as “disentangling”. It is based on the assumption that the total spectrum is a linear combination of the component spectra at any given orbital phase. The individual spectra can be extracted by essentially comparing the line profiles of both stars at different orbital phases. The methods most widely used for spectral disentangling are the singular value decomposition scheme as described by Simon & Sturm (1994) and a procedure which involves the Fourier transform of the spectra, which is discussed by Hadrava (1995, 1997).

The disentangling procedure readily yields the radial velocities of the individual spectra as well as a spectrum for each component at every orbital phase available. These individual spectra can then be shifted to the rest frame velocity and afterwards combined to form a single spectrum with much better S/N ratio, alleviating the disadvantages of the relatively short integration times necessitated by short orbital periods. From these combined spectra effective temperatures and surface gravities can be derived by appropriate means.

2.2.2 FITSB2 design

The software package “FITSB2” used in this work employs a different technique, which is equivalent to the disentangling procedure with respect to the information which can be extracted from the observations. It is able to manage the complete analyzing process from

JDO	Julian date of zero phase
P	Orbital period
γ	Systemic radial velocity
k_1, k_2	Orbital velocities $\times \sin i$
$v_{\text{rot},1}, v_{\text{rot},2}$	Rotational velocities $\times \sin i$
$T_{\text{eff},1}, T_{\text{eff},2}$	Effective temperatures
$\log g_1, \log g_2$	Surface gravities

Table 2.2: List of all binary star parameters adjustable by FITSB2. For a detailed description of their usage in this work refer to Section 4.6.1.

the reduced spectra to the extraction of all relevant parameters. Furthermore, it is still being actively developed and new features are added in regular intervals. The software has been originally designed to analyze more than 1000 double-lined spectra observed for the ESO Supernova Progenitor Survey at the Very Large Telescope with the UVES spectrograph (Napiwotzki et al. 2003, 2004). It performs a simultaneous χ^2 -based fit of the complete set of spectra of a given system, employing the simplex parameter optimization algorithm, which is also used by MORO (see Sections 2.1.3 and 2.1.4). The composite spectra observed at different orbital phases are a superposition of the spectra of both components, Doppler-shifted against each other according to their anti-phased radial velocities. FITSB2 searches for the best representation of the whole set of composite spectra by optimizing the radial velocity shifts of the superimposed component spectra (yielding the radial velocity curves of both components in an SB2 system), while at the same time an optimum representation of both component spectra themselves by best-fitting model atmospheres is determined (corresponding to a spectrum analysis with determination of atmospheric parameters for both stars). If phase zero point and orbital period of the analyzed object are known, additional restrictions can be applied to the radial velocities, thereby facilitating the solution process (see Section 2.2.3).

Adequate grids of theoretical spectra must be provided to the fitting algorithm. In this case of early-type OB stars actually two different grids of synthetic spectra were used: state-of-the-art NLTE model atmospheres by Lanz & Hubeny (2003, 2007) and by Nieva & Przybilla (2007) for the appropriate ranges in T_{eff} , $\log g$ and metallicity. For a given set of parameters, the actual synthetic spectra are linearly interpolated from the nearest points of the grid. The resulting spectra are then convolved with Gaussian functions to simulate “smearing” effects due to rotational broadening of the lines and limited resolution of the spectrograph. After completion of the fitting procedure, a subsequent application of the bootstrap algorithm also permitted a reliable and realistic estimation of the parameter errors (see Section 2.2.4). Further details about FITSB2 and its original application can be found in Napiwotzki et al. (2001, 2003).

2.2.3 Orbit mode

In a highly complex context like fitting a binary star spectrum with a sophisticated model grid, any reduction of complexity facilitates a swift solution enormously. FITSB2 includes a very important tool to greatly reduce the degrees of freedom of the fitting problem. If orbital periods and zero points can be inferred externally, important constraints can be placed on the radial velocities for each spectrum. Since then the only free parameters of orbital motion are the velocity amplitudes of both components, but not the individual radial velocities of each spectrum anymore, one degree of freedom is eliminated for each spectrum. This of course requires that all observations are supplied together with Julian Date of exposure start, integration time and the coordinates of the object for calculating phase and heliocentric correction.

Especially for this work this so-called “orbit mode” of FITSB2 was very helpful, since orbital periods and zero points were determined with great precision from high-quality light curves with time bases up to several years. Aside from the obvious advantage regarding the required computing time, the parameters usually converge much faster and more reliably if the number of adjusted parameters is held as low as possible.

2.2.4 Error estimates

After the simplex iterations are complete, errors of all adjusted parameters can be estimated. This is done by means of the “bootstrap algorithm” which essentially works the following way: for each spectrum supplied a data point is randomly selected from the n measurements contained in the spectrum. The procedure is repeated n times in total. Because selected points will not be removed from the original data pool, the same measurement can be selected multiple times. Others will not be selected at all. The information density of the original observation is thus reduced in a random fashion. This procedure is repeated m times yielding m new spectra for each original one. The original iterative fit procedure is then repeated with the “crippled” spectra. The errors of the individual parameters are found by taking the respective σ values of the new set of solutions. The larger m is chosen, the more reliable the error estimates will be. The bootstrap algorithm is one of the best error estimation procedures, yet due to the large number of required repetitions, it is also very time-consuming and takes significantly longer than acquiring the original solution. The procedure is described in more detail in Section 3.6.4.

3 Photometric analysis of LMC binaries

3.1 Motivation

An important aim of this work was the derivation of absolute parameters of early-type close LMC binaries through the combined analysis of photometric data from the MACHO archives and new spectroscopic observations to be conducted during this work. Telescope time at the 3.9 m Anglo-Australian Telescope (AAT) was actually granted by the time allocation committee, but could not be used as the 2dF fiber spectrograph was decommissioned early in favor of its successor AAOMEGA. Another option to secure spectroscopic time was offered through a collaboration with a group at Göttingen University. Guaranteed observing time of this institute at the new 11 m Southern African Large Telescope (SALT) was promised to be used for a joint proposal to obtain spectra for the LMC program stars. Unfortunately, diverse technical problems, mainly associated with a poor main focus of the instrument, have prevented these observations to be conducted up to the present time.

Therefore, as an alternative archival spectroscopic data of SMC eclipsing binaries was used in combination with photometric light curves from the OGLE archive. These analyses are presented in Chapter 4.

On the other hand, since so much excellent photometric data from the LMC was available, it was decided that a purely photometric analysis of these light curves should be performed, in spite of the associated drawbacks like the indeterminateness of the mass ratio q (see Chapter 2). These problems were alleviated as much as possible by using an analysis approach to be described in detail in Section 3.6. By predefining a wide range of mass ratios for each binary and conducting independent analyses with q fixed at a variety of values a great deal could be learned about the stars themselves and especially the nature of correlations of the binary parameters. Once spectroscopic observations of these stars will become available in the future, it will be easy to determine the mass ratios and pin down the associated photometric solution, immediately yielding the absolute parameters of the analyzed binary. As will be shown in Section 3.7, the trends of the derived parameters with changing mass ratio are sufficiently predictable that they can be interpolated from the results presented in this chapter for virtually any mass ratio which future spectroscopic analysis will provide. Therefore, the work described in this chapter is an ideal basis for future researchers attempting to derive absolute parameters of LMC binaries.

3.2 Previous work

Several attempts have been made in the past few years to derive the properties of extragalactic eclipsing binaries on a purely photometric basis. Two case studies of photometric analyses of SMC eclipsing binaries were conducted by Wytthe & Wilson (2001, 2002). These authors selected subsamples of detached and semi-detached binaries from the OGLE catalogue and analyzed their light curves with an automated version of the Wilson-Devinney software. Since they generally assumed a mass ratio of $q = 1$ for detached systems, the derived relative radii of the components cannot be reliable. In the case of semi-detached systems, they tried to derive photometric mass ratios, which is also problematic, since the degeneracy of the solutions with regard to q is only broken in the presence of total eclipses.

The same argument applies to the study by Graczyk (2003), who investigated a sample of 19 eclipsing binaries in the SMC, again taken from the OGLE database. In this study, photometric mass ratios were derived even for detached binaries, which is very unlikely to give reliable results, as shown by Terrell & Wilson (2005).

Michalska & Pigulski (2005) analyzed the light curves of 98 LMC binaries, many of them with eccentric orbits. OGLE data was combined with measurements from the MACHO and EROS surveys. In this case, the mass ratio was simply set to $q = 1$, resulting in good parameter determinateness, but possibly very large errors for systems deviating from this assumption. Due to this reason, only the sum of relative radii was given by the authors.

Neßlinger (2004) and Michalska & Pigulski (2004) showed that photometric solutions of identical quality can be found for a wide range of mass ratios in most cases of eclipsing binaries. Therefore, it should not be attempted to derive the mass ratio from photometric data alone. This limitation is appropriately considered in this work by independent derivation of solutions for various fixed mass ratios.

3.3 Available Data

During the last decade, an enormous amount of photometric data of millions of galactic as well as extragalactic stars became available as a byproduct of several large-scale surveys searching for dark matter candidates called MACHOs (**MA**ssive **C**ompact **H**alo **O**bjects). Their existence was proposed to explain the mysterious rotation curves of spiral galaxies including our Milky Way, which require the presence of large amounts of dark matter. The MACHO objects are thought to be dark, compact objects like brown dwarfs, white dwarfs, neutron stars or black holes. The surveys were intended to find the proposed MACHOs by detecting so-called “microlensing” events which arise when massive objects are seen in conjunction with background stars. Gravitational lensing then results in a characteristic short-term increase in brightness of the distant star, and is thus revealing the invisible non-luminous foreground object. The shape of the resulting light curve does not depend on wavelength, making these events discernible from other phenomena of variability. The duration of the brightness increase allows to derive the mass of the foreground object.

In order to ascertain a sufficient detection probability of microlensing objects, a high density of background objects is necessary so that a large number of stars can be monitored simultaneously. On the other hand, a continuous monitoring over several years is needed in order to reliably detect “slow” events caused by very massive objects like Black Holes. All in all microlensing surveys are very complex and sophisticated programs extending over long time bases. Preferred sky regions include both Magellanic Clouds and the Galactic center due to their high star density. More information on the microlensing technique and theoretical estimates of the number of expected events as well as the associated brightness changes can be found in Paczyński (1986).

By conducting photometric monitoring of millions of stars, one was able to find numerous previously unknown variables of different kinds. The database of known eclipsing binaries, cepheids and other variable stars quickly increased while the surveys were being conducted. This database was also used as source of photometric data in this work. The following sections describe the most important microlensing programs and their individual advantages and limitations regarding their eclipsing binary data. Reasons for the selection of the program stars will be explained in Section 3.4.

3.3.1 EROS

The program EROS (**E**xperience pour la **R**echerche d'**O**bjets **S**ombres) was conceived as the first large survey to search the Halo of our Milky Way for dark matter in form of MACHOs. It was started at ESO’s La Silla observatory in 1990. In the beginning a 40-cm-telescope with a CCD camera was used to search for microlensing events on short timescales, while the 1 m ESO Schmidt telescope complemented the survey by means of photographic plates. Eight million stars in the Large Magellanic Cloud (LMC) were monitored. Only two possible candidates for microlensing events were detected during that time, one of which was identified as a variable star later (Ansari et al. 1995). A second phase of the program called EROS 2 was initiated when the 40 cm telescope was replaced by a larger, fully automated instrument. More information about EROS and references to all relevant publications can be found in the world wide web under <http://eros.in2p3.fr/>.

Grison et al. (1995) published a catalogue of 79 eclipsing binaries in the LMC identified during the original EROS survey, containing photometric measurements in *B* and *R* bands. These objects are 15 to 18 mag bright, have relatively short orbital periods and are mainly hot, luminous stars of early spectral type. Although no EROS light curves were analysed in this work, the calibration relations between the EROS instrumental system and the standard Johnson index $B_J - V_J$ given by Grison et al. (1995) proved to be a major corner stone for establishing a temperature scale for the purely photometric work (see Subsections 3.3.3 and 3.5.2).

3.3.2 OGLE

OGLE (**O**ptical **G**ravitational **L**ensing **E**xperiment) began as a cooperation between the University of Warsaw and the Washington Carnegie Institution in 1992. The only in-

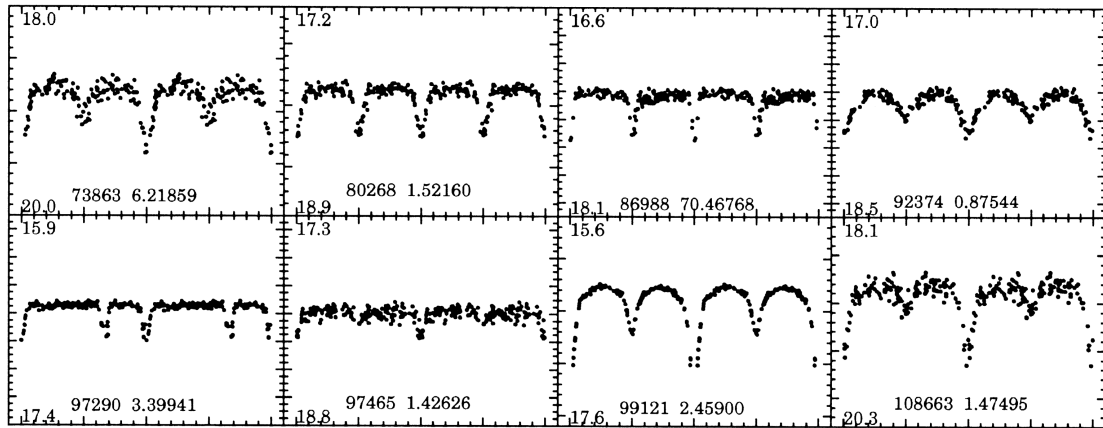


Figure 3.1: Typical I band light curves from the OGLE project (reproduced from Udalski et al. 1998).

strument available was a 1 m telescope at Las Campanas Observatory in Chile. The early observations were limited to the galactic center (Udalski et al. 1992). As soon as 1993 a possible first microlensing event was detected by OGLE (Udalski et al. 1993). The second and much expanded phase of OGLE started in January 1997. A dedicated 1.3 m telescope had been commissioned at Las Campanas Observatory. OGLE-II has detected several hundred possible microlensing events (Udalski et al. 1997, 2000). The galactic disk as well as both Magellanic Clouds were observed. The discovery of several thousand new eclipsing binaries was published in separate catalogues for SMC (Udalski et al. 1998) and LMC (Wyrzykowski et al. 2003). Since June 2001 OGLE's third phase (OGLE-III) has been implemented. One specific aim of this program is the detection of transits by compact objects. Konacki et al. (2003) were the first to discover an extrasolar planet in OGLE-III data with the transit method. Altogether OGLE regularly monitored 170 million stars in the galactic center and 33 million stars in the Magellanic Clouds. Detailed information regarding the OGLE projects and a list of associated publications can be found under <http://sirius.astrouw.edu.pl/~ogle/>. Data access is facilitated via a web-based query interface with which it is possible to find each individual object quickly. The system is described in Szymanski (2005) and can be accessed under <http://ogledb.astrouw.edu.pl/~ogle/photdb/>.

Many publications concerning the analysis of SMC or LMC binary stars have drawn their photometric data from the OGLE surveys since the large number of detected binaries makes a selection of suitable objects quite easy. There is a severe drawback, though: for most objects, good phase coverage (with approximately 150 measurements) is only available in the I band. In the B and V bands phase coverage is usually poor, effectively reducing the achievable definiteness of light curve solutions appreciably. Also, the majority of objects are very faint with magnitudes ranging from 17 to 20 mag, resulting in significant scatter of the observations. Typical examples of OGLE light curves from Udalski et al. (1998) are depicted in Fig. 3.1. Disregarding these disadvantages, some OGLE data had to be used for the combined photometric and spectroscopic analysis in this work,

since spectroscopic data was available only for certain SMC binaries selected from the OGLE archive.

3.3.3 MACHO

The most recently initiated of the three large microlensing surveys is known as the MACHO project (MASSIVE Compact Halo Objects). It was started in June 1992 as a US-Australian cooperation. Its observations were carried out with a 1.3 m telescope at Mt. Stromlo Observatory in combination with eight CCD detectors comprising 2048×2048 pixels each. 45 microlensing events were detected towards the Galactic center (Alcock et al. 1997b, 1998), while the observations of the Magellanic Clouds yielded only sporadic results (Axelrod et al. 1994). Further information and a list of publications can be found under <http://www.macho.anu.edu.au/>.

Aside from the microlensing events, several hundred eclipsing binaries were detected amongst the tens of millions of constantly monitored stars. The final catalogue was published by Alcock et al. (1997a). The big advantage of the MACHO data compared with the other two surveys discussed here certainly is the unique combination of excellent phase coverage in two filters (*V* and *R* bands) with usually 500 to 1500 data points each, the large number of available systems and the relatively low scatter of the observations (see Fig. 3.2). Due to these factors, the MACHO binary archive of LMC stars was selected as the primary source of photometric data for this work.

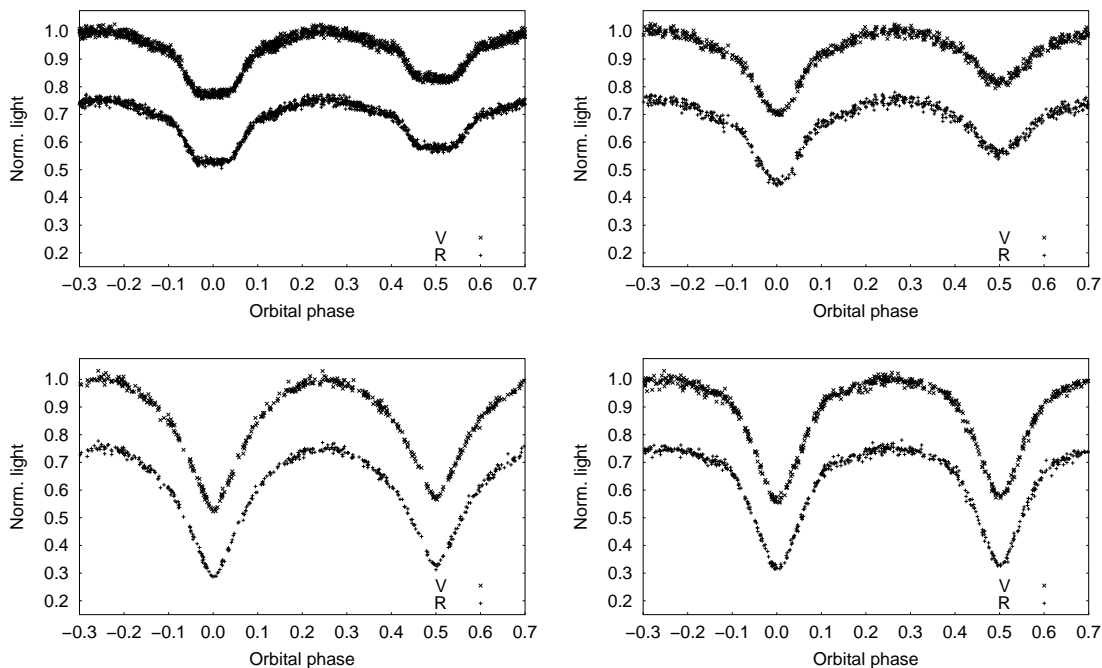


Figure 3.2: Typical *V* and *R* band light curves from the MACHO project.

3.4 Data selection criteria

Since one important goal was to analyze the photometry of close LMC binaries with the highest possible precision, it was necessary to restrict the total number of systems covered. Therefore the first step was to define suitable preselection criteria for the 611 data sets listed in Alcock et al. (1997a). Restricting the selection in accordance with a number of parameters was easy with the “VizieR” service of “Centre de Données astronomiques de Strasbourg” which is found at <http://vizier.u-strasbg.fr/viz-bin/VizieR>.

The aim of this work was the analysis of early-type, close systems. Therefore only short-period binaries with relatively high effective temperature came into consideration. Moreover, only binaries with circular orbits could be considered since the light-curve analysis software used for carrying out fits of the photometric data is not suited for modelling eccentric orbits (see Section 2.1.1). In close binary systems, where the separation of the components is of the same order of magnitude as the sizes of the stars, this condition is usually satisfied, since tidal forces tend to circularize the orbits in relatively short time frames.

3.4.1 Orbital period

The orbital periods of the stars listed in Alcock et al. (1997a) are given with reasonable accuracy. To ensure a dense phase coverage of the light curves without cutting the number of available systems too much, the selection criterion for the orbital period was set to

$$P \leq 2 \text{ days.}$$

Binary star components with such short periods will usually show significant effects of interaction. First of all, clear deviations from spherical surface geometry will be present because of tidal interaction and radiation pressure effects. However, a sophisticated and thorough light curve analysis can shed light on these subtle effects of gravitational interaction between the components. For the actual analysis of the data, the orbital periods of all systems were recalculated to ensure the best precision possible and reduce the scatter of the phase-folded data (see Section 3.5.1).

3.4.2 Effective temperature

Alcock et al. (1997a) do not give the effective surface temperatures of the stars because for most systems no spectroscopic data is available. As mentioned earlier, determining approximate effective temperatures was a necessary criterion for identifying the early-type systems relevant for this work. The only way to do this was by means of the color index $V - R$, which was available for all systems (and has been derived again later for actual analysis). Since there is only a poor correlation between $V - R$ and effective temperature of hot stars, some difficulties were encountered when deriving the relevant calibration. For a detailed description of the procedures employed and the uncertainties associated

with the method, see Section 3.5.2. For a first, rough selection of suitable systems the appropriate selection criterion was set to

$$V - R \leq 0.$$

This choice ensured the exclusion of later spectral types not relevant for this work.

3.4.3 Light curve quality

Since a sufficient confinement of the relevant data sets could not be achieved via orbital period and color index constraints alone, a reasonable method had to be found for sorting the remaining 239 data sets. In order to maximize quality and definiteness of parameter determination, it seemed desirable to use only data sets with highest signal-to-noise ratios. Therefore, the data sets were sorted by magnitude from brightest to faintest (from $V = 13.54$ down to $V = 18.20$). The 25 brightest stars of this list were selected which ensured that only high-quality data were analyzed.

3.5 Data preparation

In order to successfully analyze the photometric data offered by the MACHO archive, several steps had to be taken to process the raw data into a suitable input format for the MORO light curve analysis software.

3.5.1 Light curve processing

Raw data preparation

The original data can be freely downloaded in ASCII format from the website <http://wwwmacho.anu.edu.au/>. The celestial coordinates of the object are input into a search engine, and the objects closest to the given position are shown. It is easy to select the correct object and download the appropriate file containing the measurement data. The header consists of a MACHO star identifier, coordinates of the star, the number of observations and information regarding calibration of the data. In the main part of the file the actual measurements are given in lines containing modified Julian Date of the observation together with observation number, instrumental R and B magnitudes and their respective individual errors. From this raw data file all relevant data points and errors were extracted together with important information for calibration and heliocentric correction.

Processing the raw data

The instrumental magnitudes were then converted to Kron-Cousins V and R magnitudes. This is important for extracting approximate effective temperatures via an appropriate color-temperature relation. For the light curve analysis itself no standard system calibration is necessary since all measurements are converted to fluxes and normalized to 1

for usage with MORO. The calibration relations are given by Alcock et al. (1999) along with in-depth information about their derivation by the MACHO collaboration. Some program routines for the calibration were kindly provided to the author by Becker (2005). The calibrated data from the different filters were stored in two separate files for further processing.

Orbital period search

In a next step, exact orbital periods were determined. For this purpose a period finding algorithm proposed by Stellingwerf (1978) was applied. It folds the data of both filters with different periods in a user-specified range, creates a number of phase bins (depending on the number of measurements usually between 30 and 50 bins), computes the variance of each bin with regard to its median value and adds them up to the sum of variances. This way, with some user interaction, a minimum of bin variance was sought and the associated period is used as the orbital period of the star. The numbers derived were usually quite close to those given by Alcock et al. (1997a), who had only applied an automated period search. Nevertheless in some cases the orbital periods were definitely improved with strong impact on the light curves. The measurements were then heliocentrically corrected and folded with the best period found.

Photometric minimum search

Since the synthetic light curves of MORO are constructed symmetrically with respect to phase point 0, coinciding with the primary light curve minimum, it is essential that this point is correctly identified in the observations. This was done after phase folding the data by fitting both primary and secondary minima with a parabolic curve and determining the positions of their minima. In an iterative process the zero phase position was derived as precisely as possible. At the same time, slight eccentricities can be detected by noting any deviation of the secondary minimum from phase 0.5. Since close binaries with strong tidal interactions are analyzed in this work, only zero eccentricities were found among the selected objects.

Outlier removal

An important step in the reduction process is the “cleaning” of undesired artifacts like outliers wide outside the normal scatter of the measurements. Since some of the MACHO light curves contain a large number of these obviously faulty data points, a manual removal would have been tedious. Therefore, this task was performed by an automatic algorithm which constructs an appropriate number of phase bins (dependent on the total number of measurements), calculates the median magnitude of each bin and rejects all data points beyond predefined limits below and above the local light curve level. These limits have to be appropriately specified by the user to take into account the scatter of each individual light curve. It is important to avoid rejecting valid data points, so care must be

used when setting these limits to remove the outliers only. The remaining points are converted to fluxes and normalized to 1.0 at phase 0.25, corresponding to the maximum of the light curve.

Preparing MORO input

Since even after outlier removal typical MACHO light curves contain roughly between 500 and 1500 data points in each filter, MORO would require an unacceptable amount of CPU time if all of these points were used as input. Therefore – and in order to smooth out the light curves – usually 100 phase bins for each filter were used to form normal points as input for MORO. This resulted in a significant reduction of the light curve scatter while at the same time retaining good phase resolution of important light curve features like the shapes of both minima. The errors of the individual measurements were propagated through the entire preparation sequence for the weighting of the input data.

MORO needs the input in a specific format, whereas the data had been processed in a different three-column format up to this point in the reduction. The binned data points were then converted to the required format, the data from both filters were written in one file together with the initial stellar parameters determined in a procedure described in Section 3.6.2. From there, the data can either be analyzed interactively, or subjected to the semi-automatic procedure devised for this work which is discussed in Section 3.6.3.

3.5.2 Temperature extraction

Since the MACHO archive contains measurements in two different filters which can be converted to a standard (Kron-Cousins) photometric system (Alcock et al. 1999), a $V - R$ color index can be derived from which an estimate of the combined effective temperature of the binary can be made. Nevertheless, there are some problems associated with this procedure which results in large uncertainties for temperatures derived in this way. First, there is a weak dependency of $V - R$ vs. temperature in the range relevant for hot OB-type stars (see Fig. 3.3). Therefore, no reliable color-temperature relations exist for Kron-Cousins $V - R$ colors and hot stars, since calibrations in this temperature regime are usually done by use of the more suitable Johnson $U - B$ color index, which of course was not an option here since such data did not exist. Therefore, a method had to be devised to extract temperature information from the color information contained in the MACHO data.

Converting colors

Since no reliable color-temperature relation for Kron-Cousins filters and the relevant parameter range exists in the literature, such a relation had to be established first. For this purpose, 16 binary stars contained in both the MACHO and EROS archives were used, as the EROS collaboration provides a transformation of their instrumental colors to standard Johnson $B - V$ colors in Grison et al. (1995). First all measurements used were appropriately dereddened with the help of an LMC foreground reddening map (see Fig. 3.4)

provided by Schwering & Israel (1991). The colors of each of the selected EROS stars were then derived by performing linear fits to the instrumental $B_E - R_E$ light curves and converting the result to the standard $B - V$ system. A similar procedure was used with the $(V - R)_C$ color observations of the associated MACHO stars. MACHO $(V - R)_C$ colors were then plotted against $(B - V)_J$ colors, establishing a well-defined linear relationship (see Fig. 3.5), yielding a transformation equation between both color systems:

$$(B - V)_J = \frac{(V - R)_C - 0.029}{0.579}. \quad (3.1)$$

Temperature calibration

With the derived color-color relation, the $(V - R)_C$ color of each MACHO binary subjected to the calibration procedure described in 3.5.1 and dereddened according to Schwering & Israel (1991), can be converted to standard $B - V$ color. For the final temperature calibration a relationship between $B - V$ color and effective temperature was needed. As an approximation Planck's law was used to calculate fluxes for various stellar temperatures, folded by Johnson B and V filter curves. A detailed investigation with synthetic spectra based on a state-of-the-art NLTE stellar atmosphere model (Nieva & Przybilla 2007) showed that application of Planck's law was adequate to acquire the desired accuracy – the corrections tended to be very small. The resulting $B - V$ vs. temperature relation was fitted to empirical data from Cox (2000), thereby establishing the desired calibration. For this purpose, a program was written by the author which takes $(B - V)_J$ as input and automatically calculates the associated effective temperature. Comparisons made to recently published new empirical color-temperature calibrations by Worthey & Lee (2006) showed good agreement. The largest differences observed amounted to roughly 3000 K. Considering the relatively crude method of deriving temperatures from color indices, these discrepancies can be considered minor.

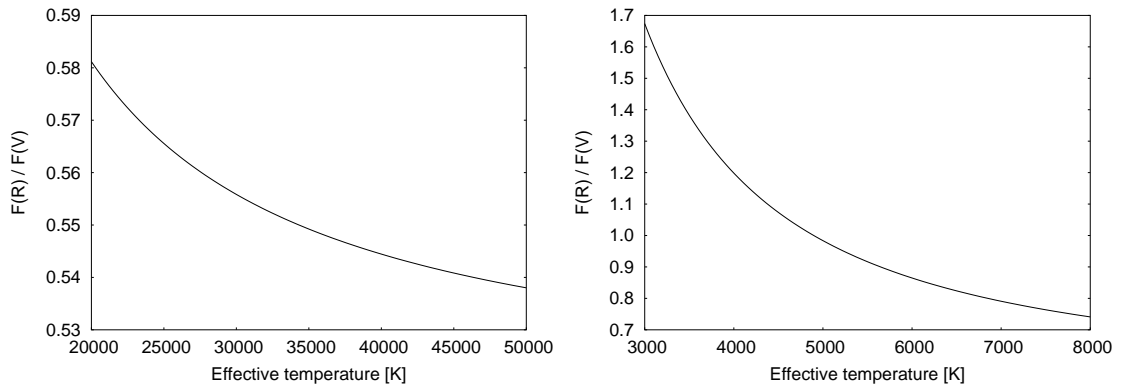


Figure 3.3: Flux ratio at the effective wavelengths of MACHO V and R filters for different stellar surface temperatures, according to Planck's Law. Note the low sensibility of the flux ratio for hot stars (left panel) compared with that for cooler stars (right panel). The flux ratio at two different wavelengths is related to the color index measured with the corresponding filters. This explains the difficulty of obtaining reliable temperature estimates for hot stars from $V - R$ colors.

Deriving component temperatures

Since in the calibration presented above both binary components contribute to the total flux, only a representative temperature T_0 of the binary can be derived. Since this work is concerned with hot OB-type stars only, the Rayleigh-Jeans approximation can be used. The luminosities of both stars are then linear functions of their respective temperatures. An average temperature of the binary can therefore be expressed over the component temperatures weighted by the associated luminosities:

$$T_0 = \frac{L_1 T_1 + L_2 T_2}{L_1 + L_2} = T_1 \frac{1 + \frac{L_2 T_2}{L_1 T_1}}{1 + \frac{L_2}{L_1}}. \quad (3.2)$$

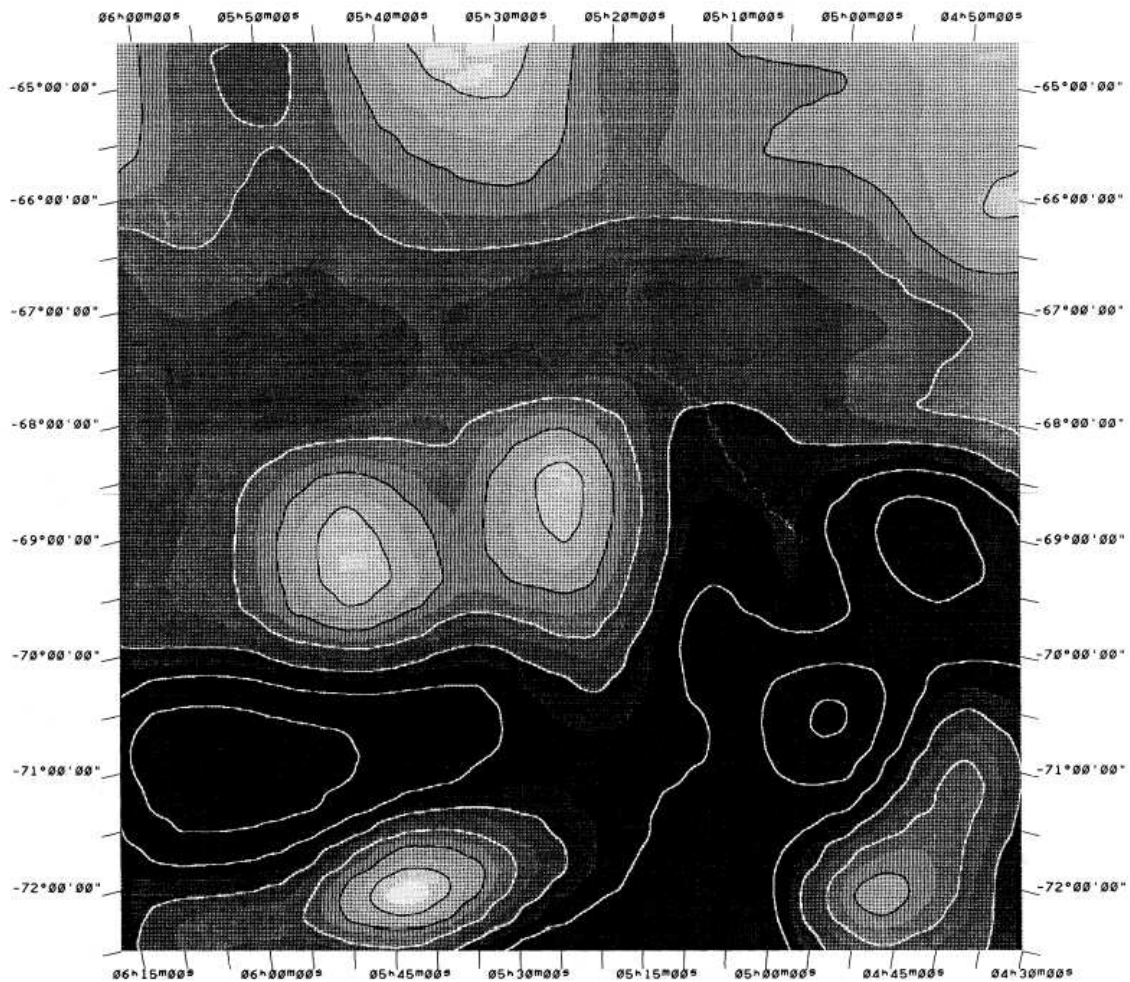


Figure 3.4: LMC foreground reddening map reproduced from Schwering & Israel (1991).

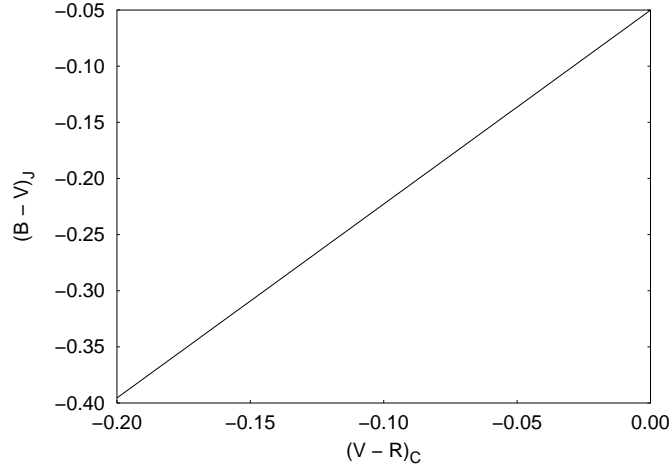


Figure 3.5: Empirically derived conversion between $(V - R)_C$ and $(B - V)_J$.

This can be rewritten as

$$T_1 = T_0 \frac{1 + \frac{L_2}{L_1}}{1 + \frac{L_2 T_2}{L_1 T_1}}. \quad (3.3)$$

Thus, if the luminosity ratio and the temperature ratio of both components can be established, the individual effective temperatures of both stars can be derived. Both ratios are a result of the initial light curve fitting process which is described in Section 3.6.3.

3.6 Light curve analysis

3.6.1 General concept

Due to the large number of adjustable parameters, the intricate correlations between several parameters and the degeneracy of certain solutions, light curve analysis without the aid of spectroscopically determined data is a difficult task. In order to facilitate the problem, a concept was developed to extract the greatest possible amount of information from the light curves in a reliable and reproducible way. Usually a trial-and-error procedure is applied to find a reasonable start parameter set from which to begin the parameter adjustment. Given the large number of program stars this appeared to be an unpracticable task, which would have been a too time-consuming and unsystematic process. Therefore it was decided to proceed in an automated way by use of an extended light curve “library”, completely covering the relevant physical parameter space. The development of such a light curve grid is described in Section 3.6.2. Owing to the degeneracy of the solutions with respect to the mass ratio, a large number of initial parameter sets was used as iteration starting points, and multiple consecutive MORO runs were carried out to get as close to the “best” solution as possible. The procedure is described in detail in Section 3.6.3. A disadvantage of the simplex solution scheme as presented in Section 2.1.4 is the impossibility to calculate realistic errors for the derived parameter sets. Since error margins are of

utmost importance for judging the significance of a solution, another way had to be found to estimate errors. A practicable method is the so-called “bootstrap algorithm” which is discussed in Section 3.6.4.

3.6.2 Light curve grid

One of the main problems of light curve analysis is the selection of appropriate initial parameters from which to start the parameter adjustment. Ideally, the parameters should be close to the final solution for whatever mathematical recipe is used during the adjustment process to eliminate numerical instabilities and avoid irrelevant portions of the parameter space. Naturally, hitting the vicinity of the final solution by pure guessing (even backed up by experience or additional information from external sources) is not too likely even under favorable circumstances. There are also cases where more than one region of similarly good solutions exist in parameter space. Even if one of these was initially guessed correctly, other ones may completely be disregarded due to the bias introduced by the first try guess.

In order to alleviate these possible complications, another, much more reproducible procedure has been devised for this work. For two possible binary star configurations – detached and overcontact (semi-detached and contact being border cases) – synthetic light curve grids have been calculated, densely covering the complete relevant parameter space. For this purpose, an iterative procedure was devised, which used MORO to compute a synthetic light curve for every possible combination of parameters inside the portion of the parameter space, which was deemed relevant for the analysis of all binary stars investigated in this work. The delimiting parameters were the mass ratio q and the orbital inclination i . q was varied in the range of $0.3 \leq q \leq 1.0$ for detached configurations and $0.1 \leq q \leq 1.0$ for overcontact configurations, in both cases by increments of 0.05. i varied in the range of $60^\circ \leq i \leq 90^\circ$ in the detached case and $30^\circ \leq i \leq 90^\circ$ in the overcontact case, with an increment of 1° . For each possible combination of q and i defined by these limits, the parameter space was densely covered by multiple combinations of relative temperature T_2/T_1 and relative radii R_1/a and R_2/a , the latter ones by variation of the surface potentials Ω_1 and Ω_2 within their respective limits dictated by detached and overcontact configurations. T_2/T_1 was covered between $0.1 \leq T_2/T_1 \leq 1.0$ in 30 steps.

Parameter space coverage for the relative radii was not achieved by fixed increments, rather the density of computed points was calculated adaptively: regions where small parameter changes have large impact on the light curve shape, were covered more densely than less sensitive parameter regions. For example, the light curve shape is strongly sensitive to surface potential variations in close-to-contact configurations due to the vanishing potential gradient in the vicinity of the inner Lagrangian point. This has been adequately accounted for by increased parameter space coverage towards the contact and semi-contact configurations.

The resulting light curves were then normalized and organized into single files containing certain parameter ranges, in order to make them selectively accessible to a systematic search of best matches with a measured light curve. Altogether, the detached grid contains slightly more than 9×10^6 points, while the over-contact grid comprises approximately

9×10^5 points, the difference of factor 10 owing to the stronger confinement of the parameter space for overcontact binaries as well as the constraint of both surface potentials being identical.

The procedure for finding start parameter sets was as follows: the V light curve prepared as described in Section 3.5.1 was compared to each of the light curves contained in the appropriate grid. When in doubt, both detached and over-contact grids were used. From the weighted residuals of all available points a χ^2 value was calculated and stored. The best-fitting 100 of all grid points were retained, usually containing parameter sets over a wide range of mass ratios, owing to the mass ratio degeneracy of light curve solutions.

3.6.3 Parameter adjustment

The 100 light curves found in the grid search procedure were then examined for multiple solution regimes, for example clustering around different orbital inclination values or temperature ratios. Usually, only one or two such regimes were found. For each of those, the best-fitting light curve parameters for each individual mass ratio value was extracted. Typically, parameter sets extending over several tenths of q values were found. Each of these sets was used as a starting point for the subsequent fitting procedure. From the start parameters, two consecutive MORO runs were initiated, the second one using the output of the first one as new starting point, thereby decreasing the chance of getting trapped in a local minimum of parameter space. The light curves of both passbands were analyzed simultaneously. Since MORO can only produce monochromatic synthetic light curves (as opposed to passband light curves), the monochromatic wavelengths were set to the respective central wavelengths of the calibrated data: R at 6438 \AA and V at 5454 \AA . The adjusted parameters comprise:

- Orbital inclination i
- Effective temperature of the secondary component T_2
- Surface potentials Ω_1 and Ω_2
- Luminosity of the primary component L_1

Of course, several more parameters are considered by MORO which can have a profound influence on the light curve shapes, as has been shown in Section 2.1.1. These parameters are either calculated by MORO according to physical constraints or set to pre-defined values:

- Mass ratio q is fixed at the individual values found during the light curve grid search to avoid the severe correlation effects with other parameters like i and $\Omega_{1,2}$. Thereby, the whole range of valid mass ratios was independently analyzed for each individual system. As has been discussed at the beginning of Chapter 2, q cannot usually be unambiguously derived from photometric data alone.

- The effective temperature of the primary component T_1 was derived as discussed in Section 3.5.2 and fixed at this value. After the first run of MORO, new temperature and luminosity ratios resulted, yielding an improved value of T_1 and T_2 which were used as starting points for the second MORO run.
- The luminosity of the secondary component L_2 is derived from the temperature ratio T_2/T_1 and the secondary radius (given by mass ratio q and Ω_2).
- “Third light” l_3 is used to simulate a third (constant-flux) component which is either part of the system or located on the line of sight in front of or behind the eclipsing binary. Since this parameter is heavily correlated with the primary and secondary luminosities, and the presence of such a disturbance should not be inferred without good reason, this parameter was generally set to $l_3 = 0$. For most stars this assumption should be correct.
- Limb darkening coefficients x_1 and x_2 have a small, but characteristic influence on the light curve shapes. For this work, the tables published by van Hamme (1993) containing the values for a linear limb darkening law were used along with an interpolation program which calculates limb darkening coefficients for specific effective temperature, $\log g$ and metallicity in predefined passbands. Approximate $\log g$ values were taken from Harmanec (1988) and Repolust et al. (2004) according to the derived temperature and associated spectral type, while metallicity $[M/H]$ was set to the generally accepted value of -0.3 for LMC stars, since no individual information was available. After the first MORO run, x_1 and x_2 were reset for the second run according to the new temperatures.
- Gravity darkening coefficients were set to $g_1 = g_2 = 1.0$ according to Lucy (1976). This assumption is realistic since all analyzed stars are of early spectral type and should therefore have radiative envelopes. Various tests showed that the influence of these parameters on light curve shapes is only marginal.
- Albedos A_1 and A_2 can have a significant effect on the light curves of hot stars due to an increased reflection effect. As shown by Ruciński (1969), $A_1 = A_2 = 1.0$ can mostly be assumed for early-type stars.
- Radiation pressure parameters δ_1 and δ_2 control the effectiveness of mutual irradiation. Details are described in Section 2.1.2. Aside from extremely hot stars, the effects are usually quite small and were therefore not considered in this analysis ($\delta_1 = \delta_2 = 0$) to save CPU time. Light curves of much better quality would be needed for these parameters to have appreciable impact.

3.6.4 Error assessment

In any serious scientific work, every quoted result must come with an associated error margin to permit a proper judgement of the quality of the result. This is one of the main

problems with most light curve analysis programs, since the mathematical parameter optimization algorithms do not allow for a propagation of errors. Some parameter adjustment schemes like the method of differential corrections (see Section 2.1.4) do support the output of standard errors after each iteration step, but these errors are mostly unrealistically small.

In order to overcome these deficiencies, a procedure based on the so-called bootstrap algorithm was devised and implemented for this work. It was used after the actual fitting routines were finished. Due to its nature, CPU usage is rather extensive, amounting to more than 70% of the entire light curve analysis procedure. Details of the procedure can be found in Efron (1979) and Efron & Tibshirani (1993). A general outline of the method can be described as follows: after the fitting is done, the observational data is subjected to a procedure which effectively reduces the information content of the data. If the light curve in question consists of n data points, the following procedure is repeated n times: a data point is drawn from the whole set and stored in a new file. It is not removed from the original data; rather, the same point can be drawn multiple times. Thus the new “information reduced” light curve contains anywhere between 1 and n data points. The whole procedure is conducted a large number of times. Afterwards, the resulting light curves are subjected to exactly the same fitting scheme as the original data set was. Each analysis will yield a slightly different solution parameter set. From these, mean values along with associated standard errors are computed. The mean value of each parameter is adopted as its final value, while the bootstrap-derived errors can serve as realistic estimates for the quality of the parameter determination.

The number of times the bootstrap procedure is being repeated for each system has to be a compromise between the desired significance and accuracy on one side and the available limited computing time on the other side. From the preceding description, it is clear that required CPU time scales linearly with the number of bootstrap runs. During the course of this work experience showed that 500 bootstrap repetitions resulted in a reasonable accuracy of the error estimates while keeping computing time at an acceptable level.

3.7 Results for individual objects

After the details of the entire light curve analysis procedure have been described in the preceding sections, the results derived for individual objects will be discussed next. For each analyzed binary, the original, non-binned light curves will be shown together with examples of the solution light curves and the associated parameters including their error margins. Due to lack of space not all data can be presented here; as results are available for several values of the mass ratio for each star, only those for the most likely mass ratios (determined from temperature ratio and luminosity ratio considerations) are shown. Since no derivation of absolute parameters and therefore no distance determination is possible by these purely photometric analyses (as discussed in Section 1.1), no absolute parameter scale can be given except for orbital inclination and effective temperatures, as long as no spectroscopic data are provided.

The error of the secondary temperature is the bootstrap error computed with T_1 fixed and does not reflect the uncertainty with which the primary temperature has been originally derived. It is given in the text for each individual star. Owing to the lack of an absolute scale, the radii of the stars are given relative to the orbital separation a . Since many of the binaries analyzed in this work suffer from strong tidal distortion, it is not clear how “the” radius of such a component can be characterized. Multiple radii are defined along the different axes (see Fig. 3.6). Therefore a “volume radius” is given which corresponds to a sphere with the actual volume of the star. This is one of the most common radius definitions used in close-binary research. The luminosities are only given for the V band and scaled to total system luminosity in V .

The consistency of the results and the associated errors will be discussed, with particular emphasis on the weakly determined absolute temperature scale as well as the mass ratio degeneracy problem and the dependencies of other parameters on mass ratio variation. Some conclusions about the absolute parameters of the systems will be attempted with the help of standard mass-radius relations. For each mass ratio, an “optimum” orbital separation will be determined for which the component masses derived from Kepler’s Third Law (see 1.2) and the associated radii taken from mass-radius relations published by Harmanec (1988) and Repolust et al. (2004) are in best agreement with the relative radii determined from the photometric analysis. These masses and radii, along with associated spectral types and effective temperatures will be presented as possible (rough) estimates for the absolute parameters of the binary in question. It must be emphasized,

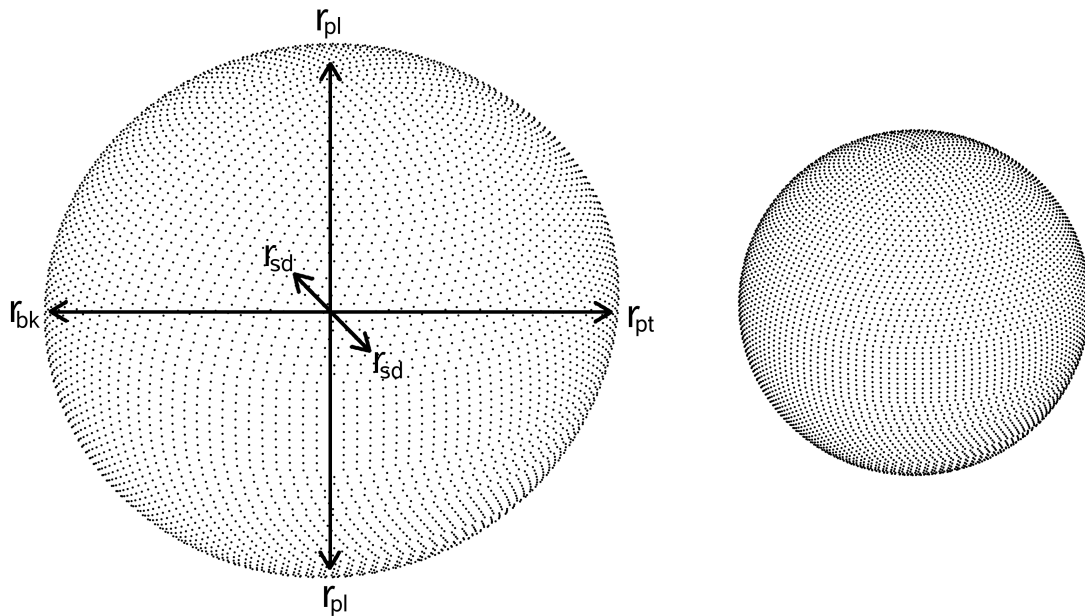


Figure 3.6: Definition of the various radii of a tidally distorted binary component.

though, that these estimates are only valid for stars on the main sequence. Evolved stars or the intricacies of close-binary interactions are not included in the considerations. Where these approximations obviously do not apply, the discrepancies will be discussed. Checks will also be made via the luminosity ascribed to the assumed absolute parameters and the actual apparent brightness observed. For each object a box is given containing some of its properties in concise form, including apparent brightness, orbital period, standard deviation of the measurements from the fit and the derived configuration of the system. The standard deviation σ is defined as

$$\sigma = \sqrt{\frac{n}{n-m} \cdot \frac{\sum_{i=1}^n w_i d_i^2}{\sum_{i=1}^n w_i}},$$

with n denoting the number of measurements, m the number of adjusted parameters, w_i the weights of the individual measurements and d_i the residuals of the measurements. Note that this quantity is a combined measure for the scatter of the measurements and the quality of the fit. For clarity, all stars are labeled with the index numbers of the online catalogue published by Alcock et al. (1997a). Additionally, their “official” identifiers containing their celestial coordinates are given to support an easy access of their entries in the MACHO light curve data base under <http://www.macho.anu.edu.au/>.

3.7.1 Overcontact systems

MACHO 513 (05:34:41.3–69:31:39)

m_V [mag]	P [d]	σ	Conf.
13.7	1.4047420	0.010	OC
– overcontact system			
– possible O’Connell effect			

MACHO 513 is a typical example of an overcontact binary system. The light curve clearly exhibits a continuous magnitude variation throughout all orbital phases, exact ingress or egress points of the eclipses cannot be defined. The quality of the light curves is very good due to the relative brightness of the system reaching $m_V = 13.7$ during quadrature phases. An orbital period of 1.4047420 days was derived and used for phase-folding the light curves. During the ingress to both eclipses one finds a small amount of asymmetry in the light curves which is more pronounced in the V band. Such asymmetries cannot be modelled by MORO in its current version, resulting in clustering of the residuals above the mean curve at the associated orbital phases. This phenomenon is frequently encountered in interacting early-type systems with β Lyr-type light curves and known as the O’Connell effect. The first maximum is somewhat brighter than the second one, which is usually explained in terms of a non-uniform surface brightness distribution, with the primary being slightly brighter at its leading hemisphere. The reason for this is often quoted to be some local heating caused by the interaction of the stellar atmosphere with circumstellar material through which the star is propagating in its orbit. Following the procedures described in Section 3.5.2, a primary effective temperature of 28000 K was derived. The temperatures of both components are quite similar, as is evident from the nearly equal depths of both eclipse minima (see Fig. 3.7). If one assumes both components to be near-main sequence stars and further assumes $q \approx 1$ (justified by $T_2/T_1 \approx 1$),

q	i [deg]	$T_{\text{eff},2}$ [K]	$L_1/(L_1 + L_2)$	$L_2/(L_1 + L_2)$	R_1/a	R_2/a
0.20	74.42 ± 0.45	26316 ± 205	0.818 ± 0.013	0.182 ± 0.013	0.5445 ± 0.0009	0.2751 ± 0.0014
0.25	71.06 ± 0.31	26835 ± 216	0.783 ± 0.016	0.217 ± 0.016	0.5282 ± 0.0015	0.2940 ± 0.0020
0.30	70.00 ± 0.29	26782 ± 229	0.757 ± 0.019	0.243 ± 0.019	0.5103 ± 0.0015	0.3052 ± 0.0019
0.35	69.03 ± 0.27	26828 ± 200	0.731 ± 0.017	0.269 ± 0.017	0.4963 ± 0.0016	0.3165 ± 0.0019
0.40	68.33 ± 0.21	26937 ± 197	0.706 ± 0.016	0.294 ± 0.016	0.4859 ± 0.0009	0.3285 ± 0.0011
0.45	67.59 ± 0.24	27133 ± 211	0.682 ± 0.018	0.318 ± 0.018	0.4754 ± 0.0012	0.3377 ± 0.0013
0.50	67.31 ± 0.26	27234 ± 195	0.661 ± 0.018	0.339 ± 0.018	0.4649 ± 0.0015	0.3450 ± 0.0016
0.55	67.34 ± 0.19	26618 ± 176	0.650 ± 0.017	0.350 ± 0.017	0.4510 ± 0.0004	0.3470 ± 0.0005
0.60	66.92 ± 0.17	26856 ± 184	0.629 ± 0.018	0.371 ± 0.018	0.4436 ± 0.0004	0.3547 ± 0.0005
0.65	66.62 ± 0.21	27021 ± 192	0.610 ± 0.019	0.390 ± 0.019	0.4367 ± 0.0007	0.3619 ± 0.0007
0.70	66.51 ± 0.24	27222 ± 174	0.592 ± 0.018	0.408 ± 0.018	0.4296 ± 0.0006	0.3675 ± 0.0006
0.75	66.67 ± 0.18	26933 ± 170	0.581 ± 0.019	0.419 ± 0.019	0.4200 ± 0.0006	0.3696 ± 0.0006
0.80	66.56 ± 0.18	26756 ± 155	0.569 ± 0.018	0.431 ± 0.018	0.4146 ± 0.0003	0.3753 ± 0.0003
0.85	66.40 ± 0.14	26620 ± 192	0.558 ± 0.022	0.442 ± 0.022	0.4095 ± 0.0000	0.3809 ± 0.0000
0.90	66.28 ± 0.13	26782 ± 151	0.543 ± 0.018	0.457 ± 0.018	0.4048 ± 0.0002	0.3863 ± 0.0003
0.95	66.30 ± 0.26	26913 ± 222	0.529 ± 0.027	0.471 ± 0.027	0.4003 ± 0.0008	0.3913 ± 0.0008
1.00	66.33 ± 0.18	27145 ± 244	0.515 ± 0.030	0.485 ± 0.030	0.3957 ± 0.0004	0.3957 ± 0.0004

Table 3.1: Parameters of MACHO 513 (05:34:41.3–69:31:39) derived from the photometric analysis shown together with 1σ bootstrap errors.

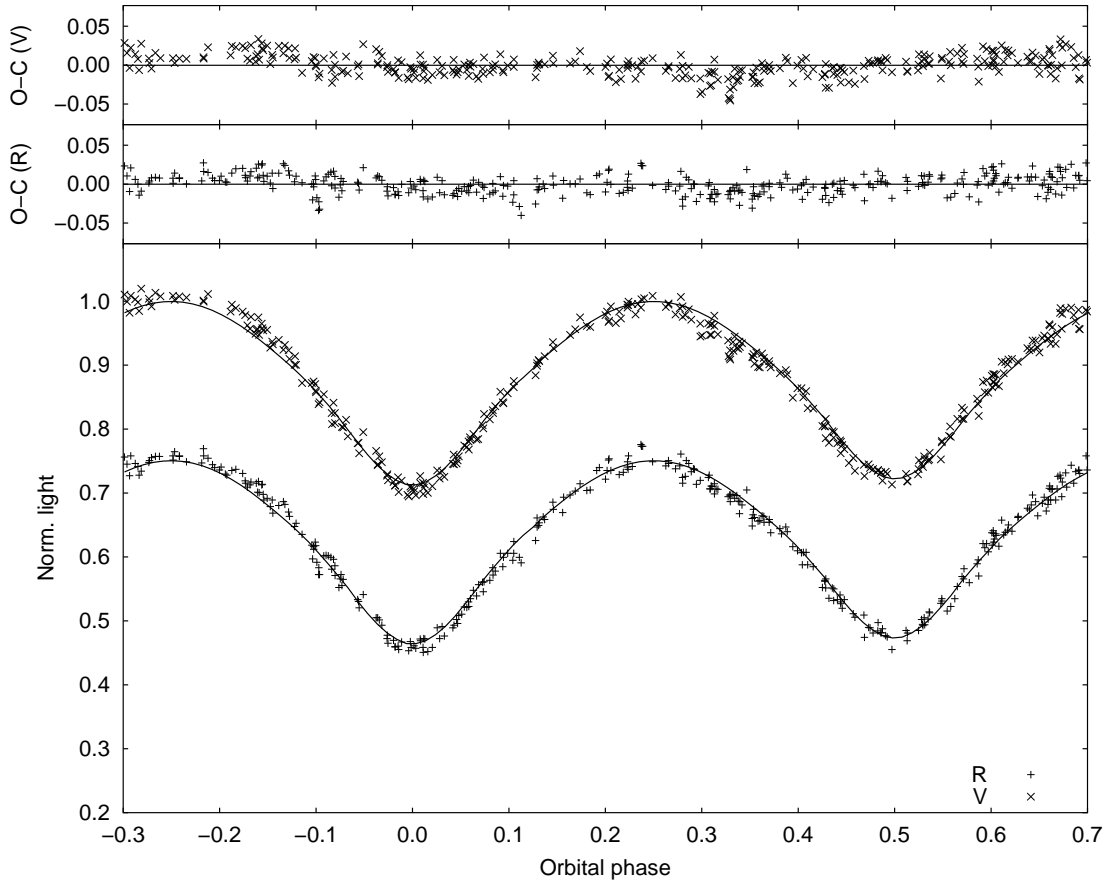


Figure 3.7: V and R light curves of MACHO 513 (05:34:41.3–69:31:39) shown together with best fits for mass ratio $q = 1.0$. For clarity, error bars of the individual data points are omitted and the R light curve is shifted down 0.25 light units.

from an effective temperature of about 28000 K (spectral type B0) one can derive component masses of about $14M_{\odot}$. From Eq. 1.2 $a \approx 16R_{\odot}$ can be computed, leading to component radii of about $6R_{\odot}$. Assuming an accepted mean value of the LMC distance modulus of 18.5 and distributing the apparent magnitude of $m_V = 13.7$ evenly among both components, one derives absolute magnitudes of $M_V \approx -4.0$ for each star which again is in very good agreement with a spectral type of B0 on the main sequence.

The specifics of the solution-finding process and the mutual correlations and interactions of the light curve parameters can be illustrated nicely with MACHO 513. As is often the case for semi-contact or overcontact systems, good solutions were only found in one specific region of the parameter space, notwithstanding the usual indefiniteness with respect to the mass ratio q . The derived parameters are shown in Table 3.1. This example clearly demonstrates how the change in mass ratio is counteracted by appropriate variations of the other parameters. The orbital inclination stays nearly constant for $0.65 \leq q \leq 1.00$, indicating the good reliability with which this parameter can be derived from photometry. Only for smaller and less realistic mass ratios, the inclination shows a

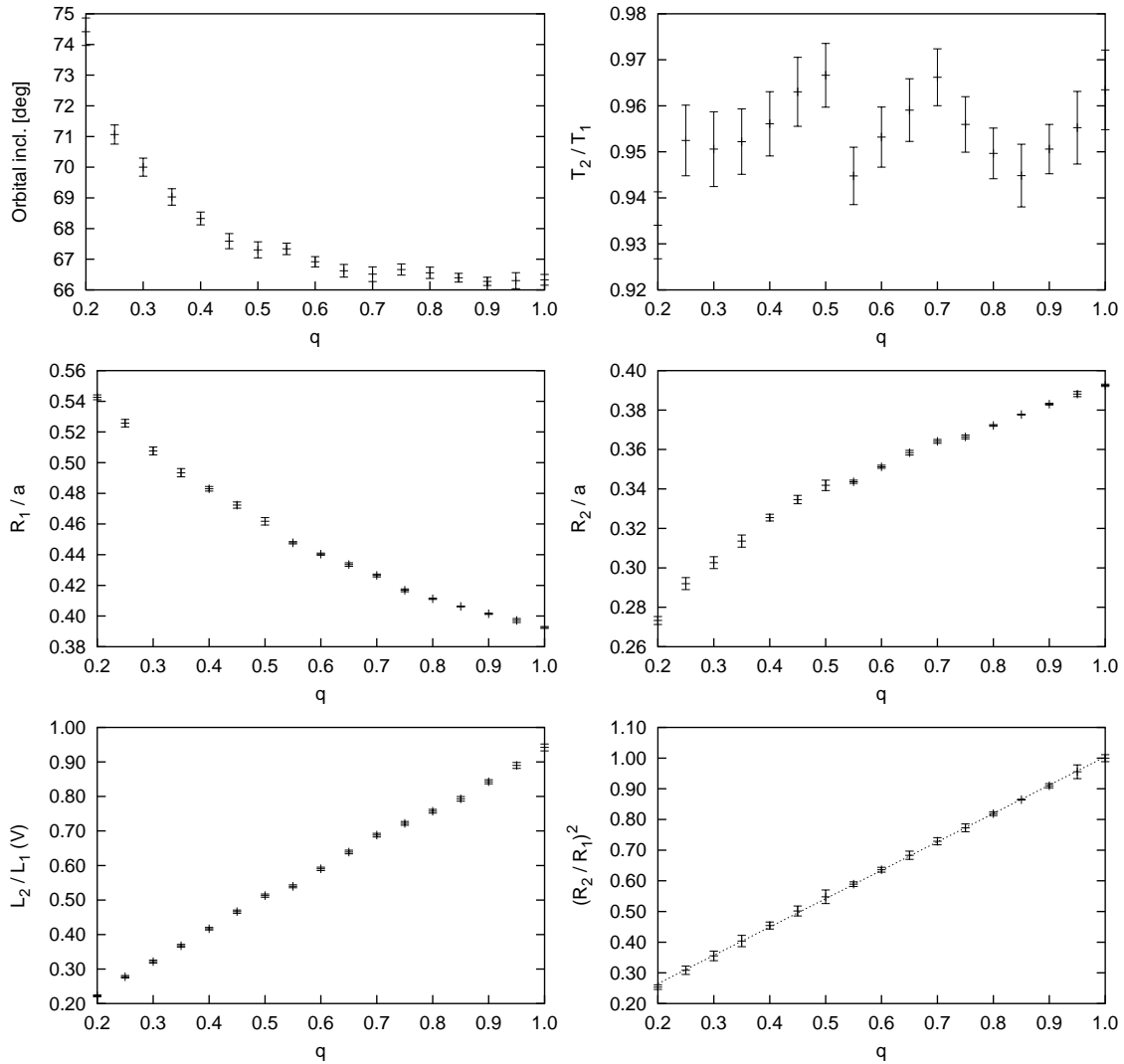


Figure 3.8: Final parameters of MACHO 513 (05:34:41.3–69:31:39) for different values of mass ratio q plotted together with their 1σ bootstrap errors. A linear fit is shown in the bottom right diagram to demonstrate the linear relationship between R_2^2/R_1^2 and q for overcontact binaries.

marked increase (see Fig. 3.8). The effective temperature of the secondary component remains practically constant through the entire q range. Since the relative depths of eclipse minima (regardless of i) are a direct measure for the ratio T_2/T_1 , this parameter cannot change to accommodate other parameter variations.

On the other hand, the relative stellar radii do change in a certain way (see Fig. 3.8). These changes can be explained easily: in an overcontact system the surface potentials of both stars must necessarily have the same value. Therefore, for $q = 1$ (where the center of mass is exactly halfway between both components), the radii of both components are identical. If the value of q is decreased, the center of mass shifts towards the primary component. As the surface potentials are still identical, the ratio of radii changes. Since any decrease of R_2/R_1 causes less pronounced light curve minima (as can be seen in

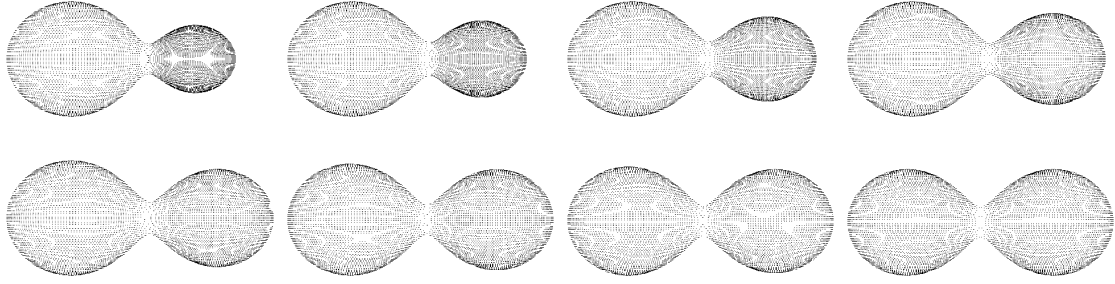


Figure 3.9: 3D plots of MACHO 513 (05:34:41.3–69:31:39) for mass ratio 0.3 (upper left) to 1.0 (lower right) with 0.1 increments. Note how changing ratio of the radii reflects the condition of equal surface potentials in this overcontact configuration.

Fig. 2.2), it has to be counteracted by increasing orbital inclination i which deepens the minima again. Since $T_2/T_1 = \text{const}$ follows directly from the relative depths of eclipses, the luminosity ratio can be given as

$$\frac{L_2}{L_1} \propto \frac{R_2^2}{R_1^2} \cdot \frac{T_2^4}{T_1^4} \propto \frac{R_2^2}{R_1^2}.$$

From the light curve fits in Fig. 3.8 we see that L_2/L_1 also scales linearly with q . Therefore for overcontact systems we can conclude that

$$q \propto \frac{R_2^2}{R_1^2}$$

which can be clearly seen in the bottom right plot of Fig. 3.8. Also note the very small errors of the radii, indicative of the accuracy with which these can be derived from light curves with strong ellipsoidal variation, even if no total eclipses are present.

MACHO 027 (04:57:30.5–68:49:51)

m_V [mag]	P [d]	σ	Conf.
15.4	0.7873555	0.005	OC
– overcontact system			
– large temperature discrepancy			

Very much like MACHO 513 (see Section 3.7.1, MACHO 027 is a typical example for a binary star in a pronounced overcontact configuration. Again, the quality of the light curves is excellent, the system reaches a brightness of $m_V = 15.4$. With 0.7873555 days its orbital period is half as long as that of MACHO 593, while the light curves and configurations of both stars are remarkably similar (see Figs. 3.10 and 3.12 and compare with 3.7 and 3.9). The light curves in both passbands are very well defined and exhibit the classical continuous brightness variation typical for an overcontact configuration. The phase coverage is also excellent. The fits are even better than those of MACHO 513, with the residuals showing no signs of systematic deviations at any phase.

Using the method described in 3.5.2, a primary temperature of 45000 K (corresponding to spectral type O5) is derived for MACHO 027. The temperature ratio is very close to 1, indicated by the identical depths of the primary and secondary light curve minima. The extremely high effective temperatures of both components are problematic with respect to the very short orbital period, though. Even if both stars were on the main sequence and therefore as compact as possible, the mass-radius relation gives a mass of $44M_\odot$ and a radius of $12R_\odot$ for O5 stars. With the observed orbital period and a total mass of $\approx 88M_\odot$ Kepler's Third Law gives an orbital separation of $\approx 16R_\odot$, whereas the light curve solution for $q = 1.0$ assigns radii of $0.4 \cdot a \approx 7R_\odot$ to both components.

There are three possible explanations for this discrepancy. First, one must keep in mind that the derivation of temperatures from the $V - R$ index for hot stars is very inaccurate and the temperatures could be overestimated. With the apparent system magnitude of

q	i [deg]	$T_{\text{eff},2}$ [K]	$L_1/(L_1 + L_2)$	$L_2/(L_1 + L_2)$	R_1/a	R_2/a
0.25	72.67 ± 0.18	52615 ± 306	0.757 ± 0.009	0.243 ± 0.009	0.5416 ± 0.0004	0.3095 ± 0.0007
0.30	71.79 ± 0.25	52116 ± 417	0.731 ± 0.013	0.269 ± 0.013	0.5231 ± 0.0015	0.3196 ± 0.0021
0.35	71.16 ± 0.17	51206 ± 252	0.708 ± 0.009	0.292 ± 0.009	0.5108 ± 0.0007	0.3324 ± 0.0010
0.40	70.55 ± 0.20	51420 ± 277	0.685 ± 0.009	0.315 ± 0.009	0.4983 ± 0.0008	0.3418 ± 0.0011
0.45	69.90 ± 0.13	51676 ± 253	0.661 ± 0.009	0.339 ± 0.009	0.4882 ± 0.0008	0.3515 ± 0.0010
0.50	69.80 ± 0.16	50399 ± 298	0.648 ± 0.010	0.352 ± 0.010	0.4749 ± 0.0010	0.3555 ± 0.0011
0.55	69.30 ± 0.13	51313 ± 236	0.625 ± 0.010	0.375 ± 0.010	0.4689 ± 0.0006	0.3658 ± 0.0007
0.60	69.23 ± 0.12	50680 ± 217	0.610 ± 0.009	0.390 ± 0.009	0.4585 ± 0.0006	0.3702 ± 0.0006
0.65	68.99 ± 0.15	50819 ± 263	0.593 ± 0.012	0.407 ± 0.012	0.4514 ± 0.0006	0.3768 ± 0.0007
0.70	68.66 ± 0.13	51013 ± 282	0.576 ± 0.013	0.424 ± 0.013	0.4455 ± 0.0006	0.3839 ± 0.0006
0.75	68.43 ± 0.12	51273 ± 241	0.560 ± 0.011	0.440 ± 0.011	0.4403 ± 0.0005	0.3905 ± 0.0005
0.80	68.50 ± 0.11	50982 ± 223	0.548 ± 0.011	0.452 ± 0.011	0.4327 ± 0.0006	0.3942 ± 0.0006
0.85	68.48 ± 0.15	51354 ± 232	0.533 ± 0.011	0.467 ± 0.011	0.4270 ± 0.0006	0.3988 ± 0.0006
0.90	68.48 ± 0.17	51498 ± 243	0.520 ± 0.012	0.480 ± 0.012	0.4211 ± 0.0008	0.4028 ± 0.0008
0.95	68.35 ± 0.19	51310 ± 292	0.510 ± 0.015	0.490 ± 0.015	0.4171 ± 0.0007	0.4081 ± 0.0007
1.00	68.34 ± 0.18	51357 ± 252	0.498 ± 0.014	0.502 ± 0.014	0.4129 ± 0.0007	0.4129 ± 0.0007

Table 3.2: Parameters of MACHO 027 (04:57:30.5–68:49:51) derived from the photometric analysis shown together with 1σ bootstrap errors.

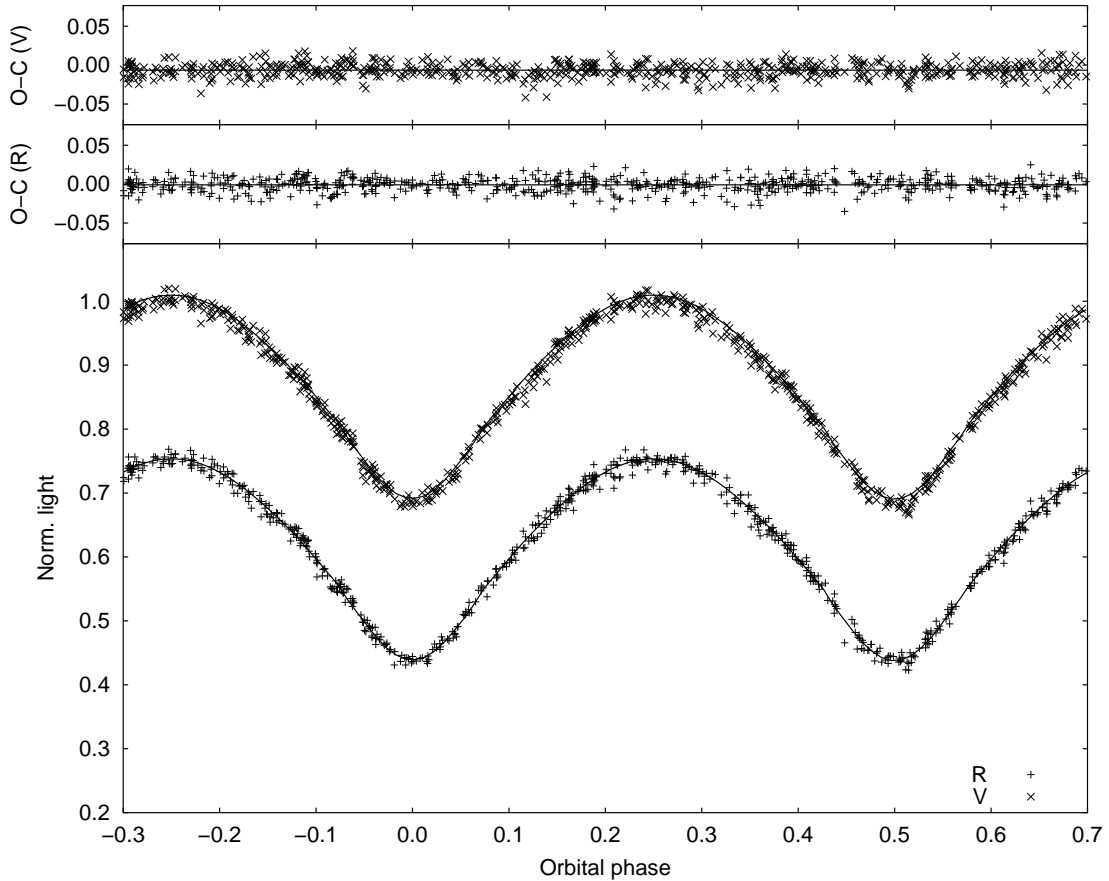


Figure 3.10: *V* and *R* light curves of MACHO 027 (04:57:30.5–68:49:51) shown together with best fits for mass ratio $q = 1.0$. For clarity, error bars of the individual data points are omitted and the *R* light curve is shifted down 0.25 light units.

$m_V = 15.4$, the distance modulus $m - M = 18.5$ of the LMC and the appropriate interstellar absorption, one can compute absolute magnitudes of $M_V \approx -2.7$ for the components (assuming equal radii) which indicates stars of spectral type B1 – B2 with an effective temperature between 22000 and 25000 K. The stellar sizes and separation would be much more compatible with these parameters, although with about $10M_\odot$ and $5.6R_\odot$ the components would still be somewhat larger than indicated by the light curve solution and the orbital separation of $a \approx 10R_\odot$.

It is also likely that the coarse resolution of the extinction map by Schwering & Israel (1991) smears out large extinction variations on small angular scales (as suggested by Oestreicher et al. 1995), occasionally leading to erroneous temperature determinations.

An alternative explanation would be the possibility that MACHO 027 may have been misclassified as a member of the LMC, and may in fact be a foreground system belonging to the Milky Way. While this would instantly alleviate any problems with the two components being too large for their separation, it would necessitate assuming effective temperatures in the 10000 to 11000 K range, in contrast to the observed color index.

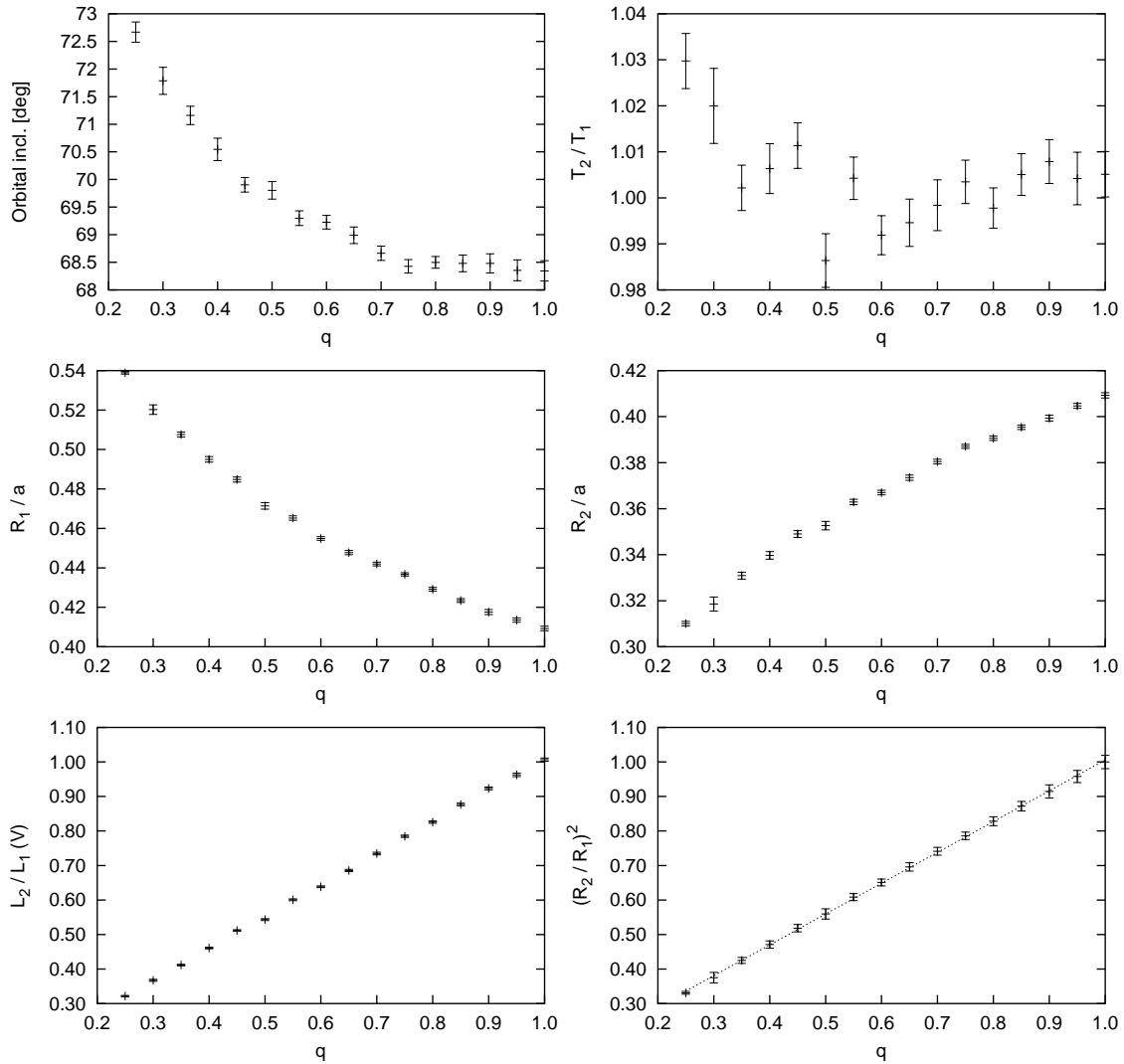


Figure 3.11: Final parameters of MACHO 027 (04:57:30.5–68:49:51) for different values of mass ratio q plotted together with their 1σ bootstrap errors. Note the same q -dependency of the parameters as with MACHO 513 (see Fig. 3.8).

It must be concluded that the most probable solution to the problem is the first alternative which suggests a faulty temperature determination. Unfortunately, it is the only way of determining temperatures for purely photometric data analyzed here. Since the light curve parameters react very weakly to a change in the absolute temperature scale (in contrast to the temperature ratio!), even a grossly wrong temperature determination should not much alter the light curve solutions. They remain valid in a wide temperature domain as long as the temperature ratio of the system is kept constant.

Regarding the analysis, only one region containing good solutions was found in the parameter space, as in the case of MACHO 513. The range of possible mass ratios q is even greater for this system (see Table 3.2). The parameter correlations are found identical

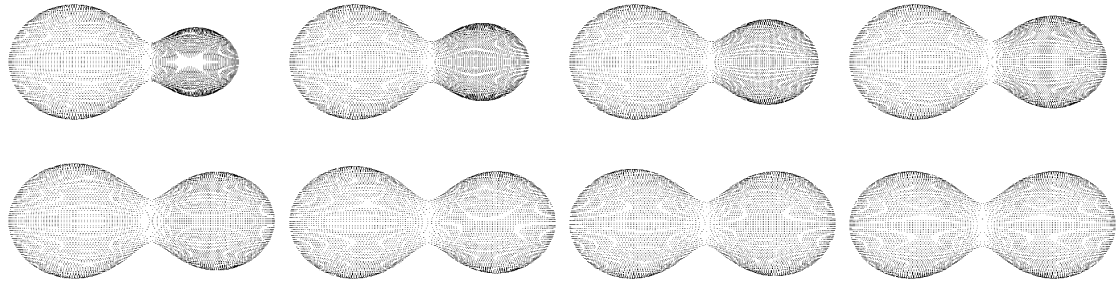


Figure 3.12: 3D plots of MACHO 027 (04:57:30.5–68:49:51) for mass ratio 0.3 (upper left) to 1.0 (lower right) with 0.1 increments.

to those of MACHO 513, especially with regard to the existence of a linear dependency of R_2^2/R_1^2 on the mass ratio (see Table 3.11).

MACHO 363 (05:22:55.8–69:51:13)

m_V [mag]	P [d]	σ	Conf.
15.3	0.7664386	0.006	OC
– marginal overcontact configuration – extreme range of photometrically possible mass ratio values – low orbital inclination			

MACHO 363 is another typical overcontact binary. Contrary to MACHO 513 and MACHO 027 (see Subsubsections 3.7.1 and 3.7.1), the state of overcontact is just marginal in this system, with a very narrow “bottleneck” connecting the two components (see Fig. 3.14). The scatter of the light curves is adequate for a $m_V = 15.3$ mag system, and the phase coverage is excellent in most parts. The derived orbital period is 0.7664386 days and therefore very similar to that of MACHO 027. Interestingly, despite the similar period and system configuration, the effective primary temperature of about 20000 K derived from the color index is much lower than that of MACHO 027, possibly alleviating some of the difficulties encountered in interpreting that system.

A surface temperature of ~ 20000 K corresponds to a spectral type of B2.5, in this case for both components, since the temperature ratio is near unity, as suggested by the identical depths of the light curve minima. In this region of the HRD, the changes in mass and radius with spectral type are drastic. From the main sequence relations component masses of $M_1 = M_2 \approx 6.5M_\odot$ can be inferred, corresponding to stellar radii of $R_1 = R_2 \approx 3.5R_\odot$. Together with the orbital period of 0.7664386 days, Kepler’s Third Law then gives an orbital separation of $a \approx 8.5R_\odot$. This fits well with the relative radii derived during the light curve solutions (see Fig. 3.15).

The light curves cover the whole phase range very well and are of good quality. As frequently encountered in MACHO data, the R light curve shows a slightly better S/N

q	i [deg]	$T_{\text{eff},2}$ [K]	$L_1/(L_1 + L_2)$	$L_2/(L_1 + L_2)$	R_1/a	R_2/a
0.15	65.15 ± 0.09	20582 ± 96	0.828 ± 0.007	0.172 ± 0.007	0.5665 ± 0.0001	0.2534 ± 0.0001
0.20	64.00 ± 0.34	19892 ± 183	0.803 ± 0.017	0.197 ± 0.017	0.5390 ± 0.0009	0.2687 ± 0.0011
0.25	63.50 ± 0.24	19460 ± 131	0.779 ± 0.013	0.221 ± 0.013	0.5157 ± 0.0006	0.2800 ± 0.0007
0.30	62.85 ± 0.27	19528 ± 105	0.750 ± 0.013	0.250 ± 0.013	0.4973 ± 0.0006	0.2906 ± 0.0007
0.35	62.13 ± 0.17	19670 ± 98	0.722 ± 0.012	0.278 ± 0.012	0.4834 ± 0.0004	0.3022 ± 0.0004
0.40	61.69 ± 0.24	19755 ± 121	0.696 ± 0.016	0.304 ± 0.016	0.4711 ± 0.0005	0.3124 ± 0.0005
0.45	61.69 ± 0.14	19345 ± 97	0.681 ± 0.012	0.319 ± 0.012	0.4581 ± 0.0003	0.3191 ± 0.0003
0.50	61.41 ± 0.15	19594 ± 96	0.655 ± 0.012	0.345 ± 0.012	0.4485 ± 0.0003	0.3276 ± 0.0003
0.55	61.08 ± 0.18	19481 ± 100	0.637 ± 0.013	0.363 ± 0.013	0.4403 ± 0.0002	0.3358 ± 0.0003
0.60	60.83 ± 0.21	19660 ± 95	0.616 ± 0.015	0.384 ± 0.015	0.4323 ± 0.0003	0.3428 ± 0.0003
0.65	60.59 ± 0.23	19528 ± 125	0.601 ± 0.018	0.399 ± 0.018	0.4255 ± 0.0004	0.3500 ± 0.0004
0.70	60.43 ± 0.26	19510 ± 105	0.585 ± 0.015	0.415 ± 0.015	0.4190 ± 0.0004	0.3565 ± 0.0004
0.75	60.52 ± 0.23	19732 ± 101	0.565 ± 0.018	0.435 ± 0.018	0.4122 ± 0.0004	0.3616 ± 0.0004
0.80	60.53 ± 0.22	19773 ± 111	0.550 ± 0.020	0.450 ± 0.020	0.4060 ± 0.0003	0.3668 ± 0.0003
0.85	60.52 ± 0.18	19812 ± 116	0.535 ± 0.022	0.465 ± 0.022	0.4008 ± 0.0003	0.3722 ± 0.0003
0.90	60.53 ± 0.19	19793 ± 106	0.522 ± 0.020	0.478 ± 0.020	0.3957 ± 0.0004	0.3772 ± 0.0004
0.95	60.62 ± 0.20	19834 ± 108	0.509 ± 0.021	0.491 ± 0.021	0.3907 ± 0.0004	0.3817 ± 0.0004
1.00	60.65 ± 0.21	19835 ± 135	0.497 ± 0.027	0.503 ± 0.027	0.3860 ± 0.0003	0.3860 ± 0.0003

Table 3.3: Parameters of MACHO 363 (05:22:55.8–69:51:13) derived from the photometric analysis shown together with 1σ bootstrap errors.

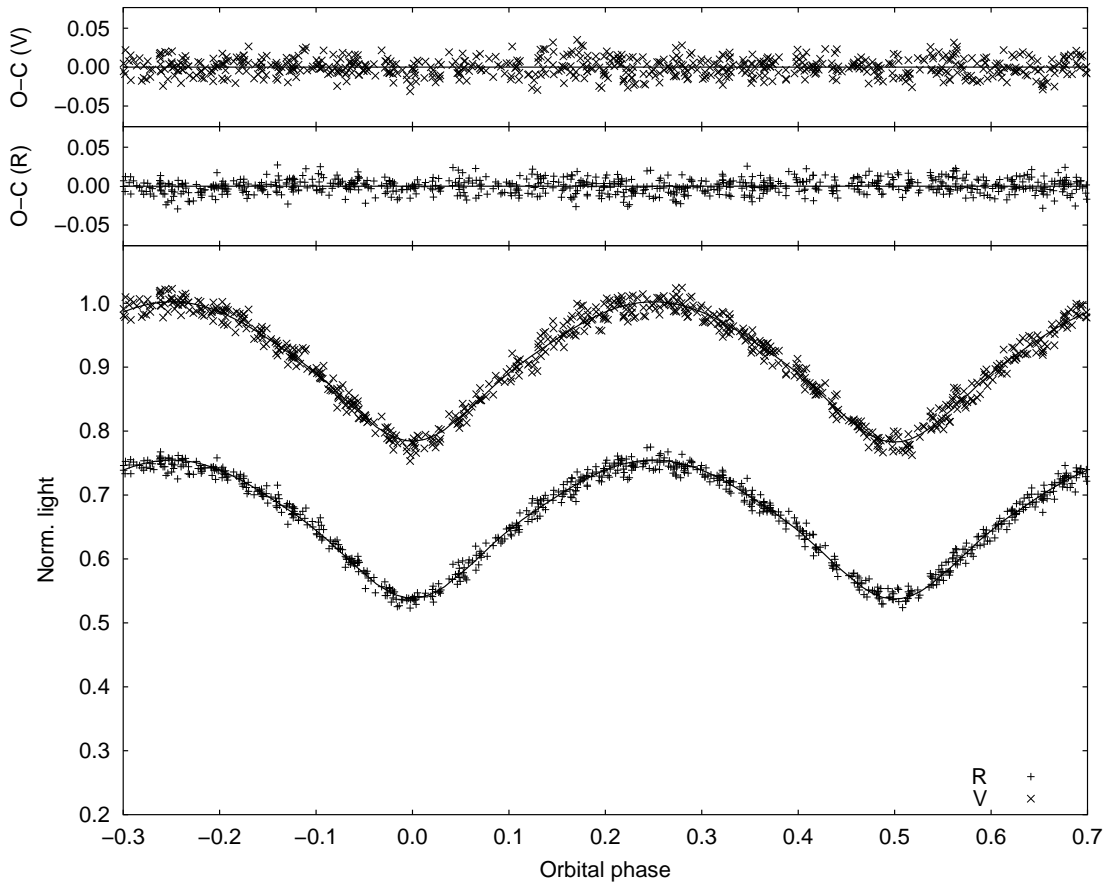


Figure 3.13: V and R light curves of MACHO 363 (05:22:55.8–69:51:13) shown together with best fits for mass ratio $q = 1.0$. For clarity, error bars of the individual data points are omitted and the R light curve is shifted down 0.25 light units.

ratio than the V light curve. The eclipse depths are not very large, with light losses of about 20% compared to quadrature phases. This is due to a low orbital inclination of hardly more than 60 degrees. There are no obvious systematic discrepancies of the residuals.

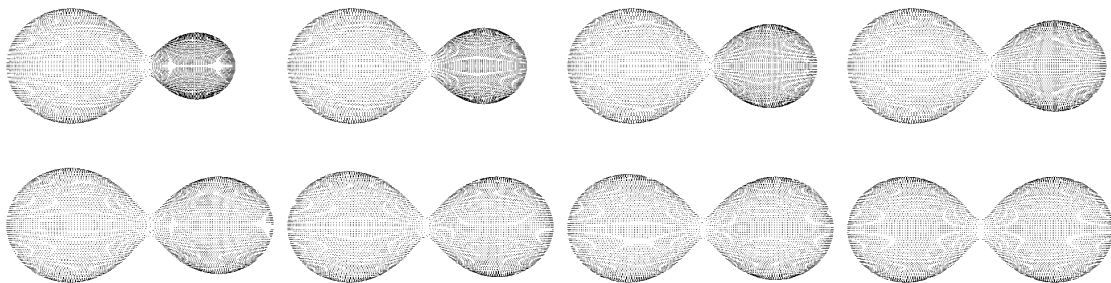


Figure 3.14: 3D plots of MACHO 363 (05:22:55.8–69:51:13) for mass ratio 0.3 (upper left) to 1.0 (lower right) with 0.1 increments.

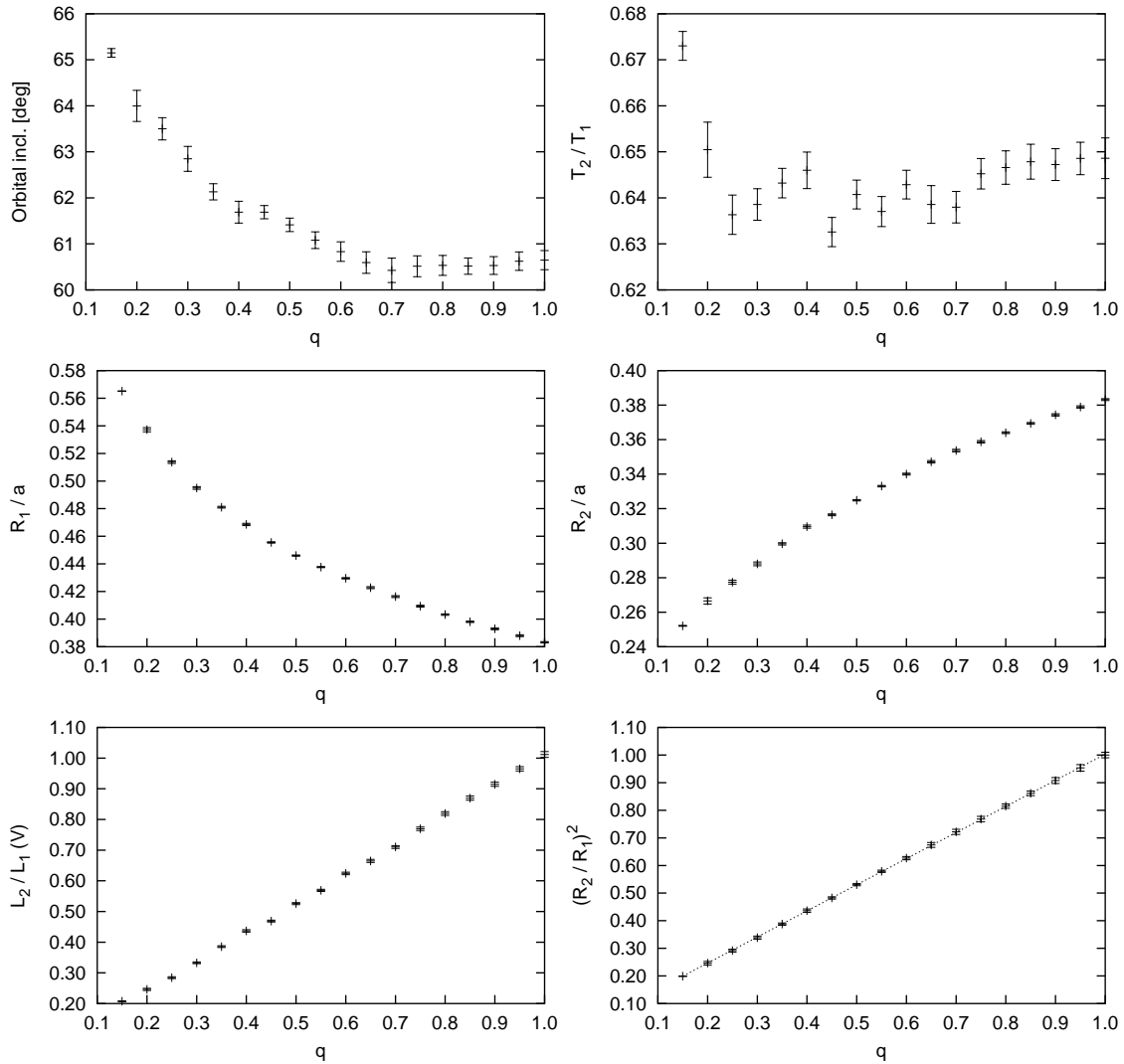


Figure 3.15: Final parameters of MACHO 363 (05:22:55.8–69:51:13) for different values of mass ratio q plotted together with their 1σ bootstrap errors.

The parameter correlations are again typical for an overcontact configuration. Solutions of practically identical quality have been found over a mass ratio range of $0.15 \leq q \leq 1.00$ which is truly remarkable if one keeps in mind the severe change in relative stellar sizes as a consequence of such a mass ratio variation. Since both ellipsoidal variation and eclipse depth become less distinct with decreasing orbital inclination, even a more extreme range of relative radii is compatible with the light curves. Probably, even mass ratios $q < 0.15$ would have yielded good solutions, but in this case the limit of the light curve grid described in Section 3.6.2 was hit, since it does not include smaller values of q . It must be noted, though, that such extreme values of the mass ratio are highly improbable to be encountered.

MACHO 304 (05:19:45.7–71:14:20)

m_V [mag]	P [d]	σ	Conf.
15.7	0.7960634	0.019	OC
– well-detached system			
– may contain evolved components			

MACHO 304 displays the most extreme overcontact configuration of all systems analyzed in this work. It is clear that both components must be significantly evolved and close-binary interactions must occur in this system. The light curves clearly indicate such a configuration by extremely large out-of-eclipse variations and smooth transitions to the eclipse minima. The large light loss of about 50% in both minima suggests a very high orbital inclination and components of similar size. The orbital period was determined as 0.7960634 days, while the apparent brightness during maximum is $m_V = 15.7$ mag. The light curves exhibit a large amount of scatter for this magnitude which can either be attributed to measurement problems encountered in too crowded fields or to intrinsic short-term stellar variations independent of orbital phase, which cannot be ruled out for such an extreme system.

From the configuration of this binary and the effective temperature of the primary component of about 35000 K it is immediately clear that no main sequence or even near-main sequence configurations can lead to reasonable results in this case. From the luminosity required at LMC distance to yield the observed apparent brightness, a very rough estimate can be made about the physical properties of the system. The most likely assumption would be that MACHO 304 is composed of two B2–B4 components which have left the main sequence and are evolving towards their first giant stage. The quoted temperature is at the upper end for this assumption, but as has already been discussed, the color index-derived temperatures should usually be considered as upper limits. In this case, the interstellar reddening has a relatively high value of $E(B - V) = 0.14$ which may be an artefact of the limited resolution of the reddening map provided by Schwing & Israel (1991).

The quality of the light curves is among the worst in this work in terms of scatter. Also, phase coverage is poorer compared with other systems. Again a slightly better

q	i [deg]	$T_{\text{eff},2}$ [K]	$L_1/(L_1 + L_2)$	$L_2/(L_1 + L_2)$	R_1/a	R_2/a
0.50	86.27 ± 1.02	34478 ± 375	0.644 ± 0.029	0.356 ± 0.029	0.4941 ± 0.0021	0.3763 ± 0.0028
0.55	85.67 ± 0.99	34123 ± 321	0.630 ± 0.026	0.370 ± 0.026	0.4826 ± 0.0022	0.3806 ± 0.0027
0.60	83.73 ± 0.81	34220 ± 314	0.611 ± 0.027	0.389 ± 0.027	0.4768 ± 0.0030	0.3895 ± 0.0037
0.65	82.85 ± 0.58	34307 ± 382	0.594 ± 0.033	0.406 ± 0.033	0.4709 ± 0.0033	0.3973 ± 0.0039
0.70	82.47 ± 0.47	34177 ± 328	0.580 ± 0.029	0.420 ± 0.029	0.4655 ± 0.0029	0.4045 ± 0.0033
0.75	82.27 ± 0.46	34070 ± 342	0.568 ± 0.032	0.432 ± 0.032	0.4576 ± 0.0037	0.4083 ± 0.0041
0.80	81.74 ± 0.43	34088 ± 313	0.554 ± 0.030	0.446 ± 0.030	0.4531 ± 0.0036	0.4149 ± 0.0040
0.85	81.66 ± 0.33	34157 ± 376	0.541 ± 0.036	0.459 ± 0.036	0.4482 ± 0.0034	0.4203 ± 0.0036
0.90	81.84 ± 0.56	34049 ± 360	0.530 ± 0.035	0.470 ± 0.035	0.4432 ± 0.0036	0.4252 ± 0.0037
0.95	81.66 ± 0.63	33883 ± 391	0.520 ± 0.039	0.480 ± 0.039	0.4388 ± 0.0040	0.4301 ± 0.0041
1.00	81.53 ± 0.39	33967 ± 372	0.509 ± 0.038	0.491 ± 0.038	0.4331 ± 0.0035	0.4331 ± 0.0035

Table 3.4: Parameters of MACHO 304 (05:19:45.7–71:14:20) derived from the photometric analysis shown together with 1σ bootstrap errors.

S/N can be observed in the R band than in the V band. The achieved fits match the observations satisfactorily with no systematic deviations whatsoever. Some problems may actually be masked by the large scatter of the measurements, though. Nevertheless, the overall characteristic light curve of this extreme overcontact configuration is very well reproduced.

The parameters are found to be subject to the same dependencies on q as observed in most overcontact binaries. The trends are extremely smooth, no outliers are present. The relatively large error bars are a direct consequence of the large scatter of the light curves. It is interesting to address the question why no mass ratio values below $q = 0.5$ have been found. For smaller mass ratios the secondary radius would be forced to decrease, thereby necessitating a larger orbital inclination. Increasing inclination in conjunction with an increasing difference in relative radii results in the formation of total minima with extended phases of near-constant light. This is definitely not compatible with the observed light curves (also because a light loss near 50% implies components of comparable size).

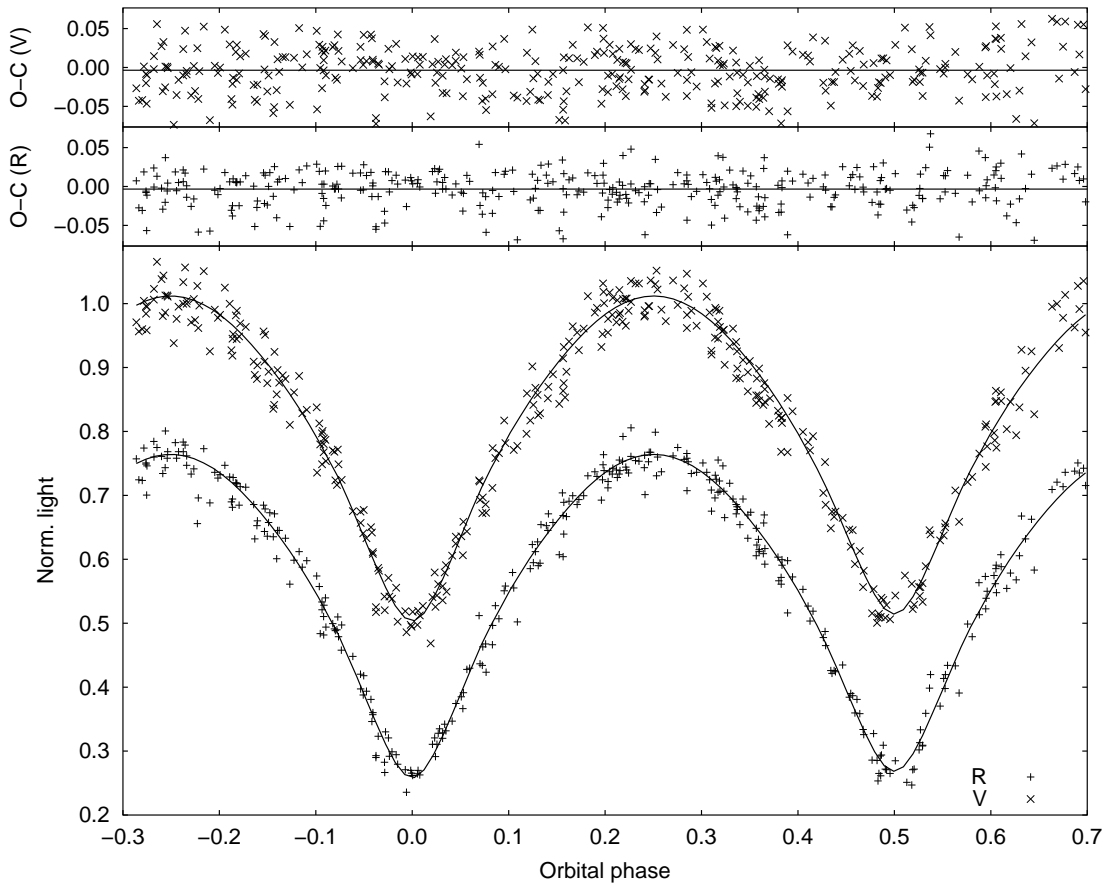


Figure 3.16: V and R light curves of MACHO 304 (05:19:45.7–71:14:20) shown together with best fits for mass ratio $q = 1.0$. For clarity, error bars of the individual data points are omitted and the R light curve is shifted down 0.25 light units.

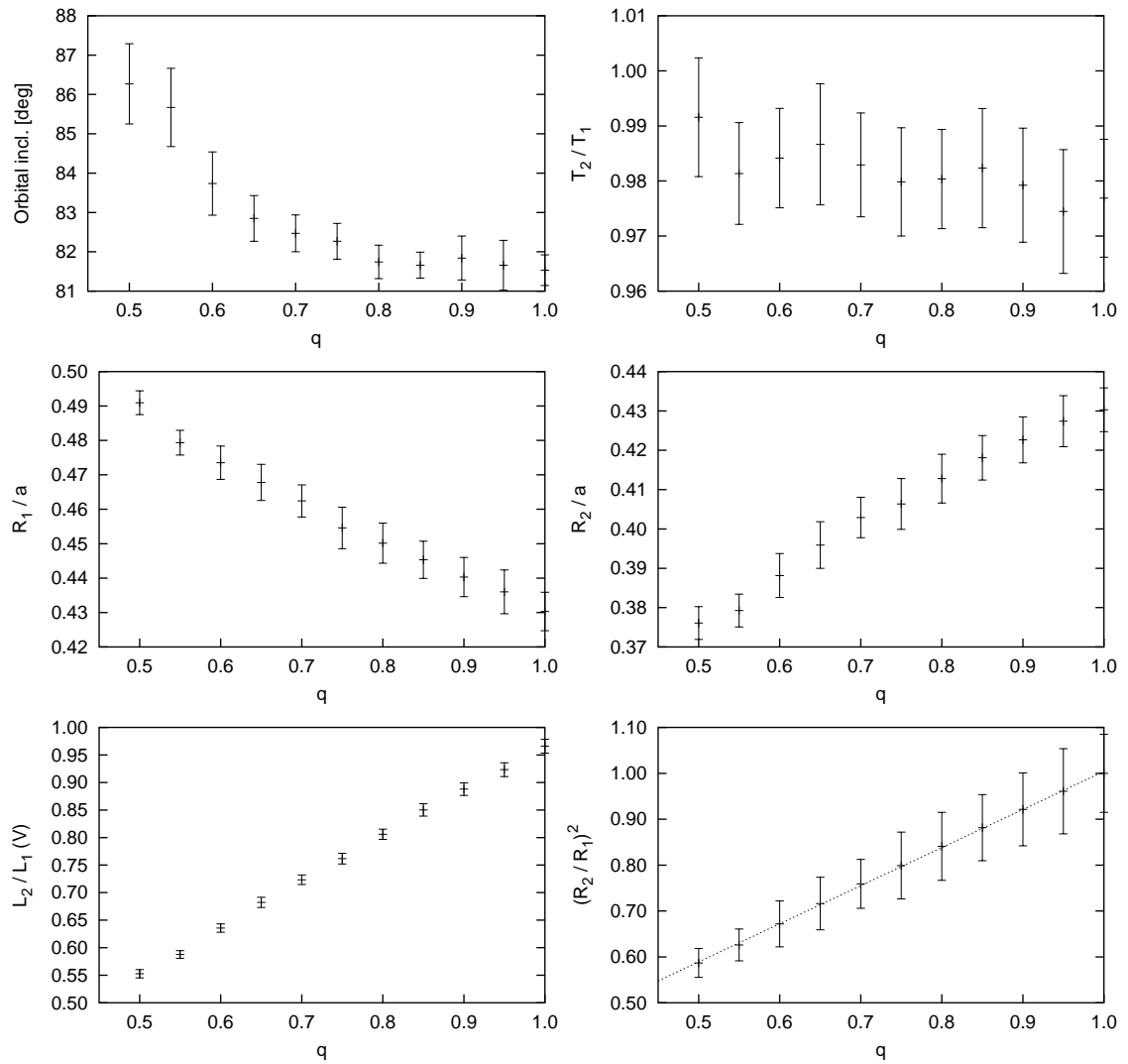


Figure 3.17: Final parameters of MACHO 304 (05:19:45.7–71:14:20) for different values of mass ratio q plotted together with their 1σ bootstrap errors.

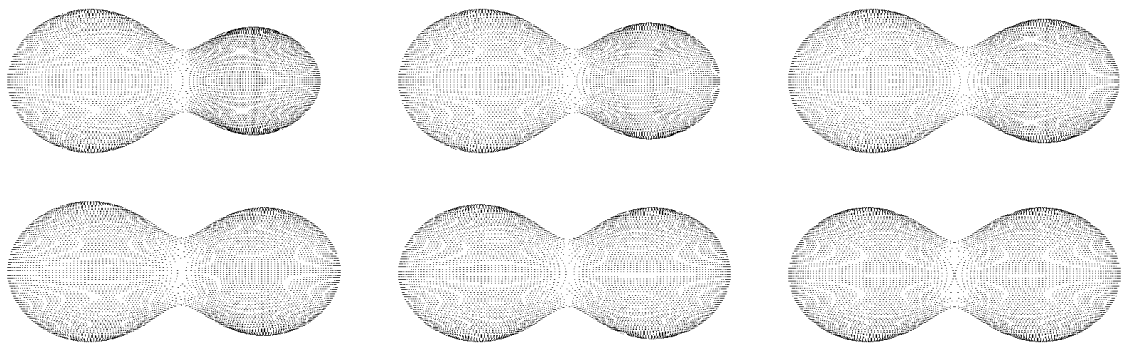


Figure 3.18: 3D plots of MACHO 304 (05:19:45.7–71:14:20) for mass ratio 0.5 (upper left) to 1.0 (lower right) with 0.1 increments.

3.7.2 Semi-detached systems

MACHO 529 (05 35 25.5–69 41 24)

m_V [mag]	P [d]	σ	Conf.
14.5	1.5771629	0.006	SD
– semi-detached system			
– case A mass transfer			

As illustrated in Fig. 3.21, MACHO 529 is unambiguously in a semi-detached state where the secondary component fills its Roche lobe. The light curves represent a typical example of this kind of binary configuration. They exhibit a continuous variation during all phases, but the ingress and egress points of the eclipse minima can still be discerned (e. g., see the primary eclipse ingress point of the R light curve at an orbital phase of about -0.1). The phase coverage of the light curves is reasonable and the scatter is quite low, owing to the system's brightness of $m_V = 14.5$ mag. The orbital period was determined to be 1.5771629 days, while the temperature determination yields a primary temperature of about 40000 K. If one assumes that both components are still on or at least near the main sequence, the photometrically derived temperature ratio suggests a mass ratio of 0.75. The primary star would have about $26M_\odot$ and $8.0R_\odot$, the secondary $20M_\odot$ and $7.6R_\odot$, with an orbital separation of $\approx 20R_\odot$. The associated relative radii derived through the analysis of the light curves are in excellent agreement with these values. MACHO 529 is a semi-detached system with possible mass transfer where none of the components seems to be significantly evolved. The secondary component has expanded just a little to fill its Roche lobe on the main sequence, suggesting that the system was very close right from the beginning of its existence and Case A mass transfer is taking place.

The effective temperatures derived from main sequence relations are 38000 K and 34000 K respectively. This corresponds to components of spectral types O7 and O9. Their absolute brightnesses together with the apparent magnitude of $m_V = 14.5$ mag place the binary at the correct distance to be an LMC member. In the case of the map given by Schwering & Israel (1991), overestimation of $E(B - V)$ seems much more likely than underestimation, since the values given in that publication usually tend to lie at the upper

q	i [deg]	$T_{\text{eff},2}$ [K]	$L_1/(L_1 + L_2)$	$L_2/(L_1 + L_2)$	R_1/a	R_2/a
0.45	64.26 ± 0.22	42299 ± 338	0.703 ± 0.021	0.297 ± 0.021	0.4274 ± 0.0024	0.3120 ± 0.0002
0.50	63.63 ± 0.18	42123 ± 306	0.689 ± 0.014	0.311 ± 0.014	0.4244 ± 0.0010	0.3203 ± 0.0008
0.55	63.71 ± 0.42	43390 ± 1077	0.657 ± 0.087	0.343 ± 0.087	0.4112 ± 0.0046	0.3279 ± 0.0015
0.60	63.06 ± 0.25	42163 ± 198	0.666 ± 0.015	0.334 ± 0.015	0.4174 ± 0.0014	0.3301 ± 0.0014
0.65	62.86 ± 0.25	42333 ± 403	0.636 ± 0.016	0.364 ± 0.016	0.4031 ± 0.0015	0.3414 ± 0.0013
0.70	63.18 ± 0.25	43068 ± 329	0.602 ± 0.021	0.398 ± 0.021	0.3865 ± 0.0016	0.3488 ± 0.0001
0.75	63.04 ± 0.26	42937 ± 307	0.591 ± 0.019	0.409 ± 0.019	0.3838 ± 0.0018	0.3547 ± 0.0004
0.80	62.74 ± 0.22	42741 ± 263	0.583 ± 0.014	0.417 ± 0.014	0.3825 ± 0.0012	0.3595 ± 0.0013
0.85	62.84 ± 0.24	42908 ± 281	0.566 ± 0.015	0.434 ± 0.015	0.3750 ± 0.0015	0.3648 ± 0.0011
0.90	62.86 ± 0.21	42718 ± 280	0.550 ± 0.018	0.450 ± 0.018	0.3674 ± 0.0013	0.3704 ± 0.0007
0.95	62.85 ± 0.19	42639 ± 219	0.537 ± 0.016	0.463 ± 0.016	0.3616 ± 0.0012	0.3751 ± 0.0007
1.00	62.98 ± 0.17	42603 ± 300	0.521 ± 0.018	0.479 ± 0.018	0.3543 ± 0.0008	0.3798 ± 0.0004

Table 3.5: Parameters of MACHO 529 (05 35 25.5–69 41 24) derived from the photometric analysis shown together with 1σ bootstrap errors.

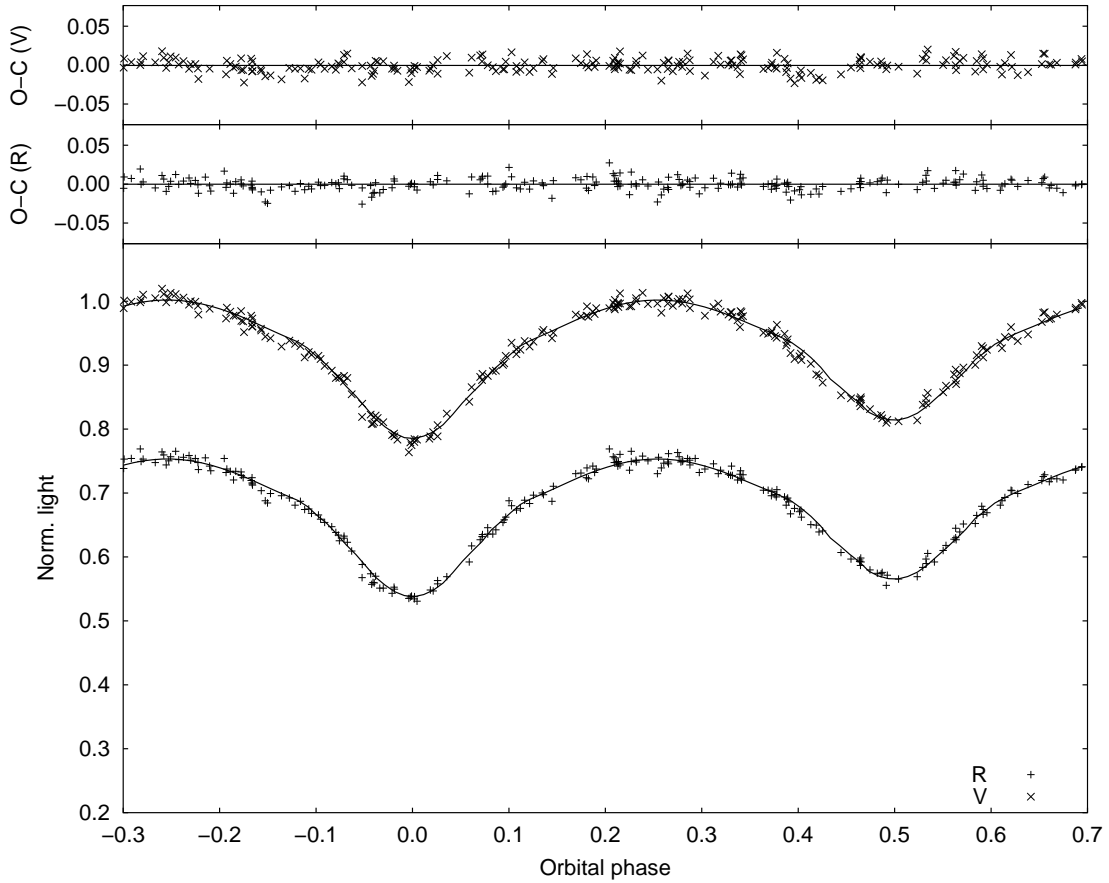


Figure 3.19: *V* and *R* light curves of MACHO 529 (05 35 25.5–69 41 24) shown together with best fits for mass ratio $q = 0.75$. For clarity, error bars of the individual data points are omitted and the *R* light curve is shifted down 0.25 light units.

end of those given by various authors for the LMC. Given the limited angular resolution, one should therefore expect the derived temperatures to be upper limits.

The light curves are represented nicely with no systematic deviations of the residuals in the whole phase range except for one small dip between orbital phases -0.2 and -0.1 just before ingress to primary eclipse. It is observed in both passbands and may be caused by a mass stream from the secondary component to the primary star, occulting a certain fraction of the primary stellar disk at this phase. The correlations of the parameters are similar to those of the overcontact systems described in Subsections 3.7.1 and 3.7.1, yet it is obvious that the additional free parameter, the surface potential of the primary component, makes the solutions less definitive. Nevertheless, the expected opposite trends of the relative radii with changing mass ratio can be observed, as well as the associated increase in secondary luminosity and the small reduction of orbital inclination i with increasing q , owing to $(R_2/R_1)^2$ getting closer to 1 and the associated increase in eclipse depths. The temperature ratio is generally close to a value of around 0.85 – 0.86.

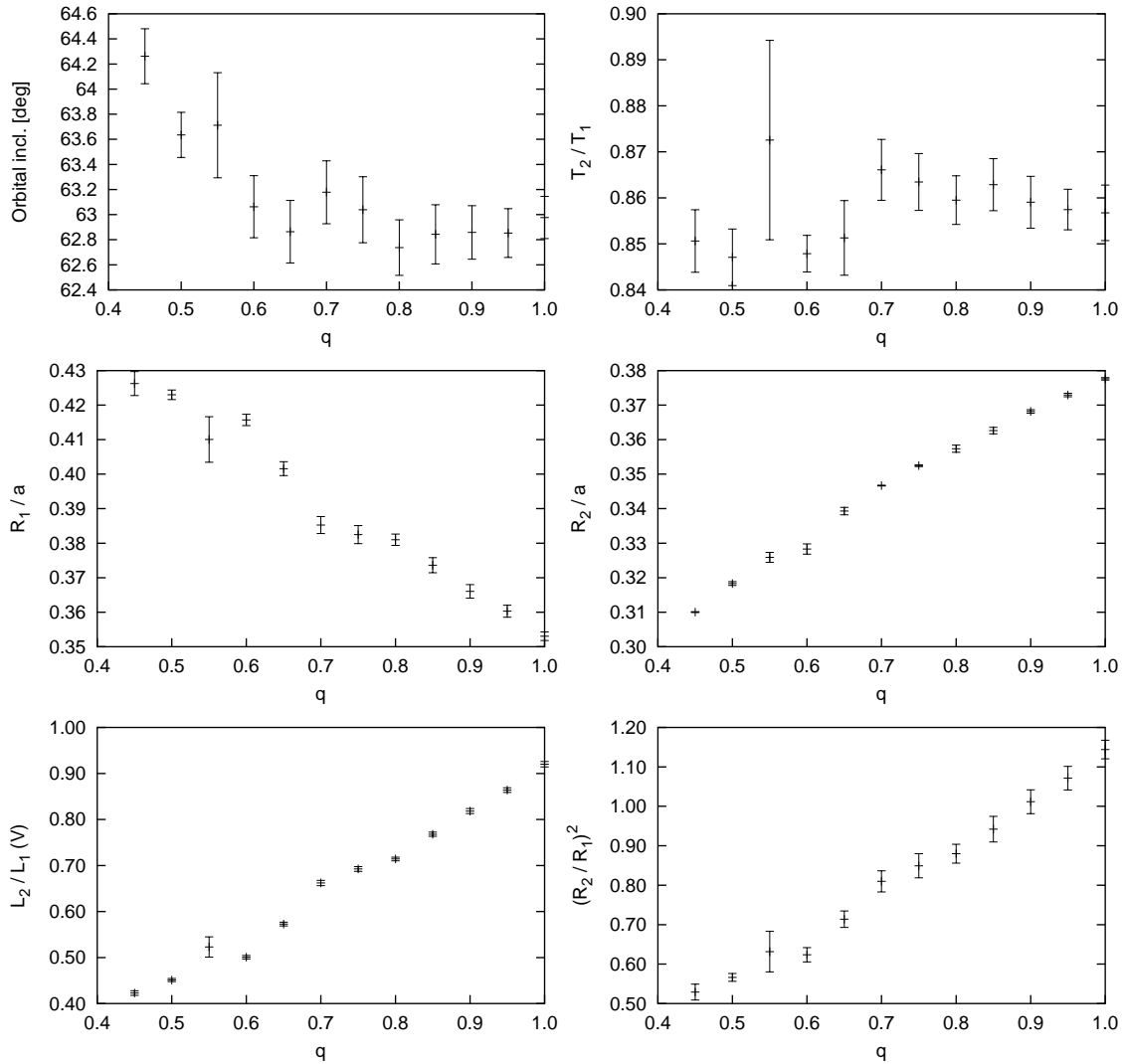


Figure 3.20: Final parameters of MACHO 529 (05 35 25.5–69 41 24) for different values of mass ratio q plotted together with their 1σ bootstrap errors.

There is one result with considerably increased error margins for $q = 0.55$, where especially T_2/T_1 and the relative radii deviate from the otherwise clearly defined trend of the parameters with the mass ratio. It is probably due to the simplex solution process being trapped in a local minimum of parameter space during the initial phase of the solution-finding process (see Section 3.6.3). From there, also the second MORO run could not escape. It is however clear that this result does not constitute part of an alternative solution regime, as its error margins as displayed in Fig. 3.20 are far above those of the other solutions found. It was therefore decided not to repeat the solution process for this particular mass ratio, as it is not a physically probable solution, and no further insights could be expected, since the trend of the parameters with changing mass ratio is obvious. It should be noted that this otherwise frequently met phenomenon of convergence to a local minimum in parameter space happened only sporadically in the course of this work.

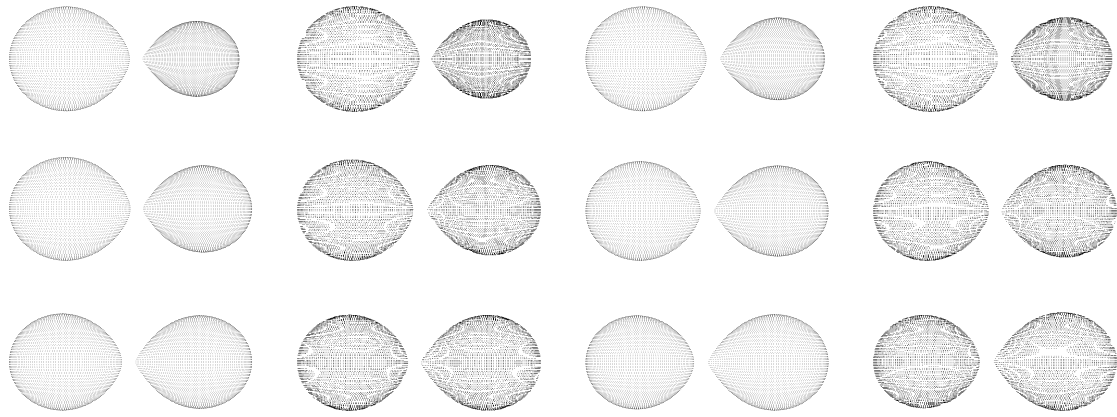


Figure 3.21: 3D plots of MACHO 529 (05 35 25.5–69 41 24) for mass ratio 0.45 (upper left) to 1.0 (lower right) with 0.05 increments.

Obviously, the special method applied here with which the whole parameter space is first scanned and the found parameter combinations are then rigorously subjected to multiple MORO runs can effectively avoid problems connected with the indeterminacy of multiple solutions of purely photometric analyses. Of course, it can also not guarantee to find the global minimum and one still has to take care and check for physically consistent results. The bootstrap-derived errors are a good indication of the trustworthiness of a given solution, as has been clearly shown in this case.

MACHO 082 (05:05:08.4–67:59:23)

m_V [mag]	P [d]	σ	Conf.
14.8	1.3689654	0.015	SD
– large temperature discrepancy – noisy light curves			

MACHO 082 is a good example for an Algol-type system, which started its evolution from a detached state. Subsequently one component slightly evolved to produce a semi-detached configuration, possibly with on-going mass transfer. In this case the evolved component is the secondary, less massive one, indicating that a mass ratio reversal has occurred due to mass exchange. The light curve is relatively flat during quadrature phases and shows eclipses of moderate depths, suggesting a relatively low inclination angle. The apparent brightness is $m_V = 14.8$, yet the light curves show a considerable amount of scatter in both passbands. Due to the good phase coverage they are still reasonably well defined, though.

If both stars are near the main sequence, the observed temperature ratio of about 0.81 implies a mass ratio of $q \approx 0.8$. Component masses of $M_1 \approx 12M_\odot$ and $M_2 \approx 10M_\odot$ follow. The stellar radii can be found as $R_1 \approx 4.9R_\odot$ and $R_2 \approx 5.5R_\odot$ respectively. This would be compatible with an orbital separation of $a \approx 14.5R_\odot$. These values are consistent with components of spectral types B0.5 and B1. Effective temperatures around 28000 K and 25000 K should be expected from this classification. Yet the color-temperature calibration of Section 3.5.2 gives an unrealistic effective temperature for the primary component of ≈ 81000 K, a huge discrepancy even when taking into account the large errors associated with the method. If one assumes that no interstellar reddening was present at all at the position of MACHO 082, the derived temperature would still be higher than suggested by the main sequence relations. Therefore, until no spectroscopic measurements are available for this particular object, it must be assumed that a severe error occurred during magnitude extraction from the raw data. On contrast, the expected absolute luminosities of B0.5 and B1 components are very well compatible with the LMC distance modulus.

Despite the considerable scatter found in both filter light curves, the synthetic curves fit the observations well and without any visible systematic deviations of the residuals.

q	i [deg]	$T_{\text{eff},2}$ [K]	$L_1/(L_1 + L_2)$	$L_2/(L_1 + L_2)$	R_1/a	R_2/a
0.55	72.25 ± 0.38	67856 ± 1806	0.587 ± 0.111	0.413 ± 0.111	0.3456 ± 0.0042	0.3283 ± 0.0008
0.60	71.62 ± 0.29	65553 ± 567	0.594 ± 0.021	0.406 ± 0.021	0.3518 ± 0.0010	0.3356 ± 0.0006
0.65	72.04 ± 0.20	66528 ± 702	0.548 ± 0.039	0.452 ± 0.039	0.3283 ± 0.0015	0.3425 ± 0.0003
0.70	71.64 ± 0.25	66596 ± 1097	0.540 ± 0.046	0.460 ± 0.046	0.3337 ± 0.0015	0.3486 ± 0.0008
0.75	71.35 ± 0.28	65110 ± 724	0.536 ± 0.033	0.464 ± 0.033	0.3315 ± 0.0008	0.3543 ± 0.0011
0.80	71.04 ± 0.33	64761 ± 622	0.531 ± 0.025	0.469 ± 0.025	0.3324 ± 0.0008	0.3593 ± 0.0019
0.85	70.86 ± 0.39	65869 ± 468	0.519 ± 0.021	0.481 ± 0.021	0.3294 ± 0.0010	0.3645 ± 0.0019
0.90	70.92 ± 0.41	65489 ± 675	0.501 ± 0.033	0.499 ± 0.033	0.3241 ± 0.0016	0.3692 ± 0.0020
0.95	71.89 ± 0.25	66892 ± 621	0.447 ± 0.033	0.553 ± 0.033	0.2950 ± 0.0009	0.3752 ± 0.0006
1.00	71.71 ± 0.25	66348 ± 569	0.441 ± 0.028	0.559 ± 0.028	0.2968 ± 0.0008	0.3797 ± 0.0006

Table 3.6: Parameters of MACHO 082 (05:05:08.4–67:59:23) derived from the photometric analysis shown together with 1σ bootstrap errors.

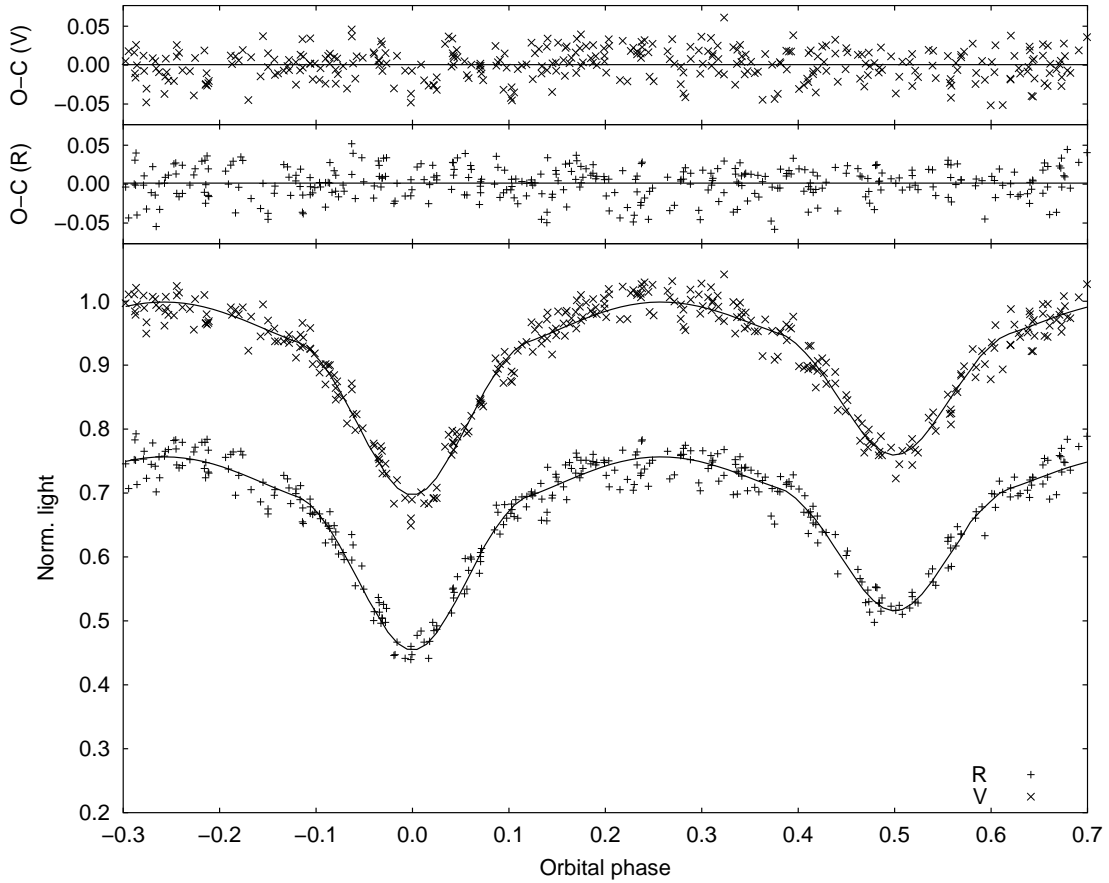


Figure 3.22: *V* and *R* light curves of MACHO 082 (05:05:08.4–67:59:23) shown together with best fits for mass ratio $q = 0.8$. For clarity, error bars of the individual data points are omitted and the *R* light curve is shifted down 0.25 light units.

Only during the primary minimum there seems to be a dip in the *V* residuals, but since this effect is not observed in the *R* light curve, it can probably be attributed to the general level of noise in the measurements.

Three different of solution regimes do exist, manifesting themselves via different values of the relative radius of the primary component. For $q \leq 0.6$ it is $R_1 \approx 0.35a$, for the large range of values between $0.6 < q \leq 0.9$ it is almost constant at $R_1 \approx 0.33a$, while for $q > 0.9$ it drops to $R_1 \approx 0.30a$. The reason for this is not clear, especially as the radius of the secondary component follows an almost linear relationship with q .

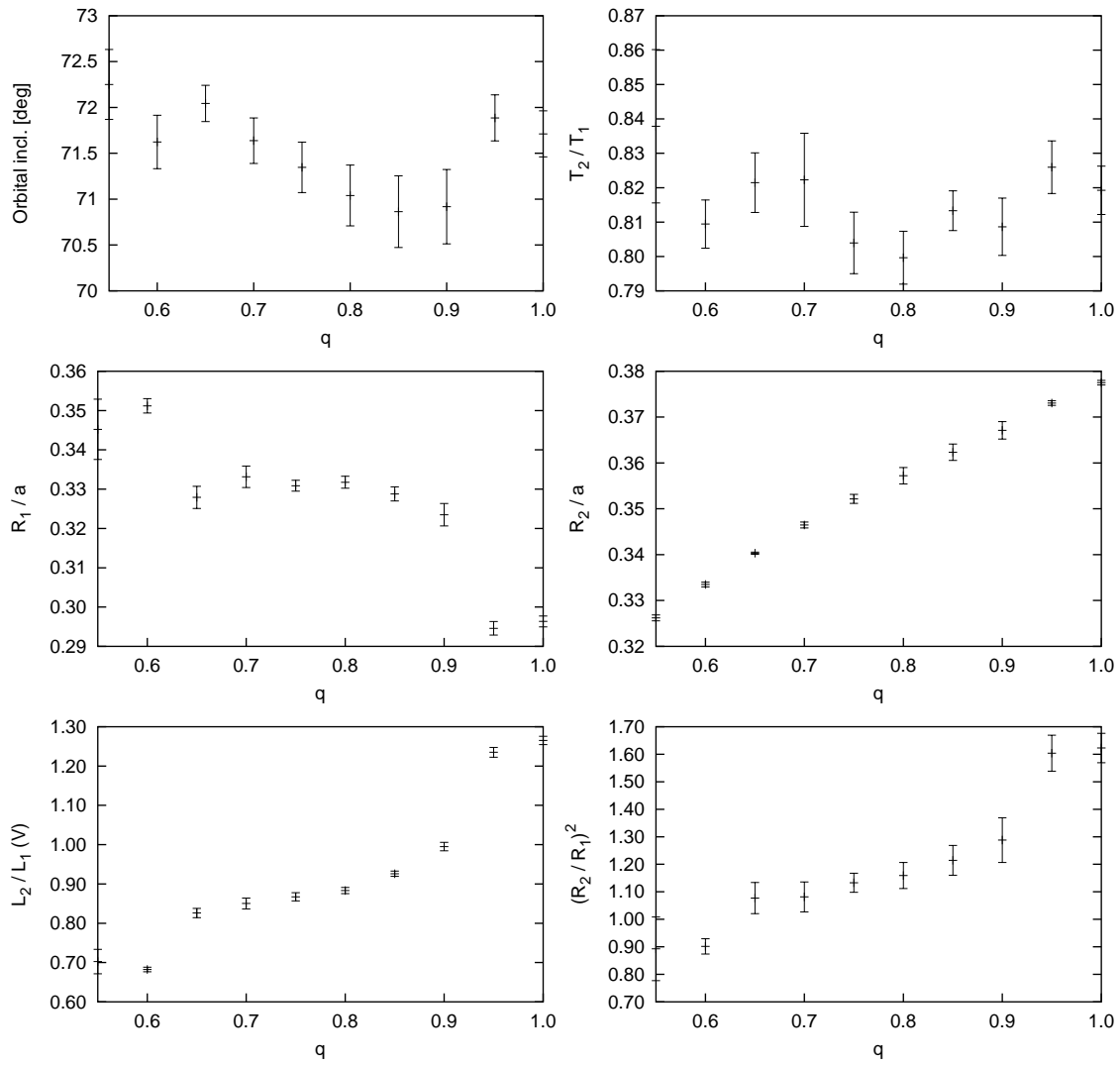


Figure 3.23: Final parameters of MACHO 082 (05:05:08.4–67:59:23) for different values of mass ratio q plotted together with their 1σ bootstrap errors.

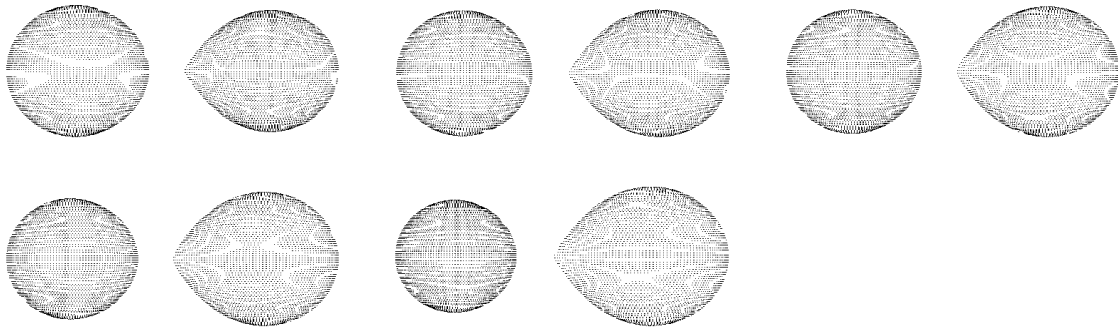


Figure 3.24: 3D plots of MACHO 082 (05:05:08.4–67:59:23) for mass ratio 0.6 (upper left) to 1.0 (lower right) with 0.1 increments.

MACHO 579 (05:38:40.5–69:29:22)

m_V [mag]	P [d]	σ	Conf.
15.0	1.5249987	0.005	SD
– system close to or actually in semi-detached configuration – evolved components suggested – light curves of excellent quality			

MACHO 579 is very similar to MACHO 082 (see Section 3.7.2) regarding its configuration and light curve shape. The secondary component almost or completely fills its Roche lobe. Mass transfer may be taking place, although no signature can be detected in the light curves. Interestingly, the light curve of this $m_V = 15.0$ mag system has a much higher S/N than that of MACHO 082, in spite of MACHO 579 being the fainter system. This is possibly due to different degrees of crowding in the two fields. The phase coverage is reasonable but not as good as for many other MACHO objects.

Assuming main sequence or near-main sequence stars with a mass ratio of $q = 0.7$ (implied by the observed temperature ratio), one can derive an orbital separation of $a \approx 19R_\odot$. Masses of $M_1 \approx 22M_\odot$ and $M_2 \approx 15M_\odot$ follow, as well as radii of $R_1 \approx 7.1R_\odot$ and $R_2 \approx 6.8R_\odot$. These parameters correspond to components of spectral types O8 and B0. The associated effective temperatures should be $T_1 \approx 35000$ K and $T_2 \approx 31000$ K. The observed color index yields a primary temperature of about 24000 K, this time lower than suggested by the main sequence relations. In this case, overestimation of the foreground extinction does not seem to be a problem. Since the derived temperature is too low for main sequence star companions, it is suggested that both components may actually be lower-mass stars in a slightly evolved state. The orbital period of 1.5249987 is larger than that of MACHO 082, so with similar relative radii, somewhat larger components are a distinct possibility.

The fit to the light curves is excellent, with the residuals being evenly distributed around 0. If any signs of mass transfer were present in the light curves, they are probably too weak to be noticed due to the limited phase coverage. Of course, the system may not be in a real semi-detached configuration, but only just before the onset of Roche lobe overflow as evident from the 3D plot for $q = 1.0$, which shows that the secondary does not yet really

q	i [deg]	$T_{\text{eff},2}$ [K]	$L_1/(L_1 + L_2)$	$L_2/(L_1 + L_2)$	R_1/a	R_2/a
0.55	69.28 ± 0.14	19148 ± 102	0.693 ± 0.020	0.307 ± 0.020	0.3997 ± 0.0010	0.3278 ± 0.0012
0.60	69.01 ± 0.14	19263 ± 103	0.672 ± 0.019	0.328 ± 0.019	0.3914 ± 0.0012	0.3352 ± 0.0009
0.65	68.85 ± 0.18	19173 ± 90	0.668 ± 0.027	0.332 ± 0.027	0.3909 ± 0.0016	0.3375 ± 0.0019
0.70	68.58 ± 0.13	19305 ± 91	0.635 ± 0.018	0.365 ± 0.018	0.3753 ± 0.0010	0.3486 ± 0.0008
0.75	68.43 ± 0.15	19377 ± 80	0.624 ± 0.022	0.376 ± 0.022	0.3733 ± 0.0016	0.3525 ± 0.0015
0.80	68.36 ± 0.12	19459 ± 98	0.599 ± 0.018	0.401 ± 0.018	0.3619 ± 0.0007	0.3603 ± 0.0003
0.85	68.20 ± 0.14	19401 ± 66	0.589 ± 0.010	0.411 ± 0.010	0.3584 ± 0.0007	0.3653 ± 0.0007
0.90	68.20 ± 0.12	19431 ± 62	0.573 ± 0.011	0.427 ± 0.011	0.3523 ± 0.0007	0.3704 ± 0.0007
0.95	68.19 ± 0.14	19426 ± 44	0.561 ± 0.012	0.439 ± 0.012	0.3478 ± 0.0006	0.3750 ± 0.0008
1.00	68.29 ± 0.17	19593 ± 77	0.552 ± 0.020	0.448 ± 0.020	0.3470 ± 0.0009	0.3771 ± 0.0015

Table 3.7: Parameters of MACHO 579 (05:38:40.5–69:29:22) derived from the photometric analysis shown together with 1σ bootstrap errors.

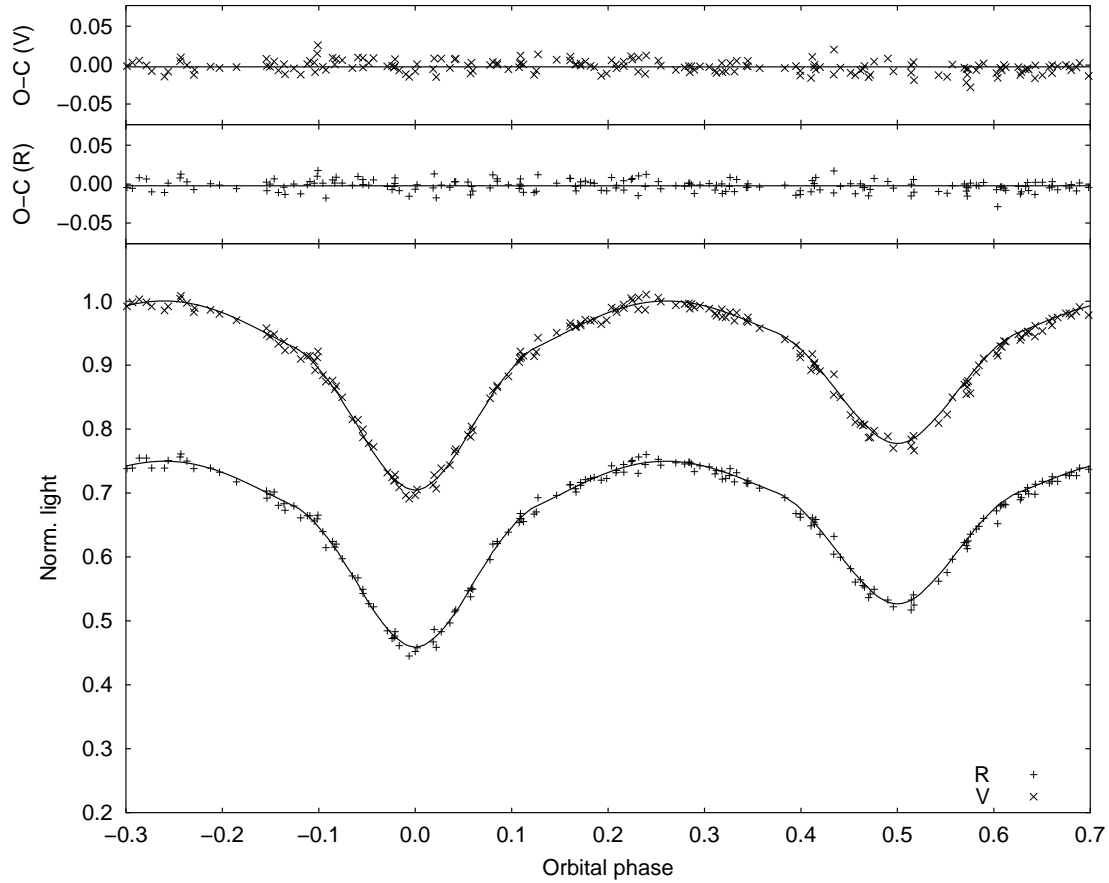


Figure 3.25: *V* and *R* light curves of MACHO 579 (05:38:40.5–69:29:22) shown together with best fits for mass ratio $q = 0.7$. For clarity, error bars of the individual data points are omitted and the *R* light curve is shifted down 0.25 light units.

touch the inner Lagrangian point, which is the case for most other mass ratios (see Fig. 3.27).

The derived parameters show the usual correlation with the mass ratio. The error bars generally are very small, undoubtedly owing to the excellent definition of both light curves without much scatter. There is a little deviation of the parameters for $q = 0.75$ which is probably due to a local minimum in parameter space very close to the actual solution. Neither does it disrupt the parameter trends, nor are the error bars considerably larger, so it can still be considered as a valid, if not optimal solution. It is interesting to note how the primary component is smaller than the secondary for low mass ratios, and then gradually becomes the larger component as the mass ratio is increased. It is a perfect example to demonstrate that the light curves are insensitive to a reversal of the relative sizes of both components: the eclipse depths only depend on the relative component sizes. The orbital inclination reaches a minimum for $(R_2/R_1)^2 = 1$, where eclipses are strongest, and slowly increases for $(R_2/R_1)^2$ values departing from unity to counteract the weakening of the eclipse minima (see Fig. 3.26).

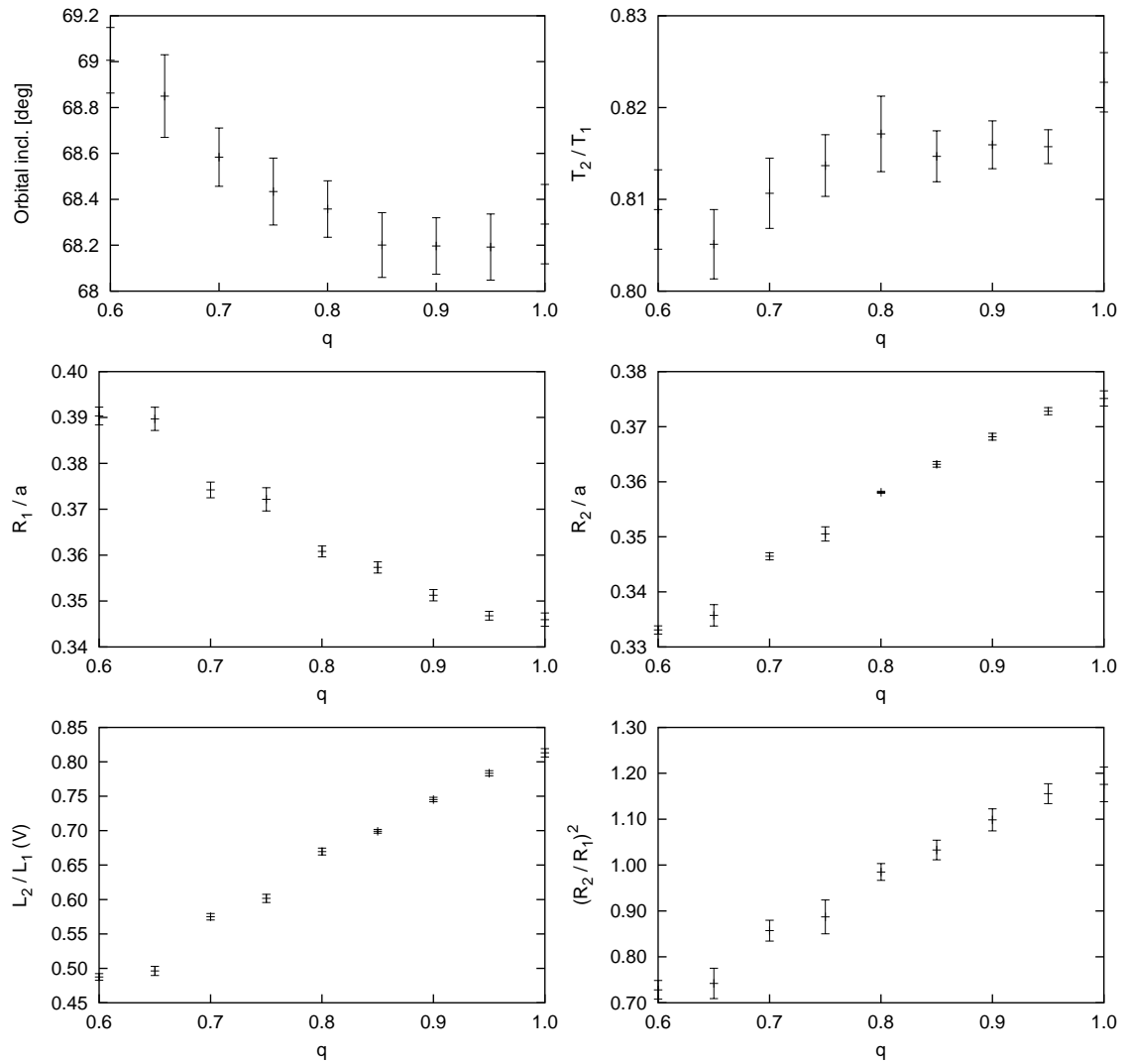


Figure 3.26: Final parameters of MACHO 579 (05:38:40.5–69:29:22) for different values of mass ratio q plotted together with their 1σ bootstrap errors.

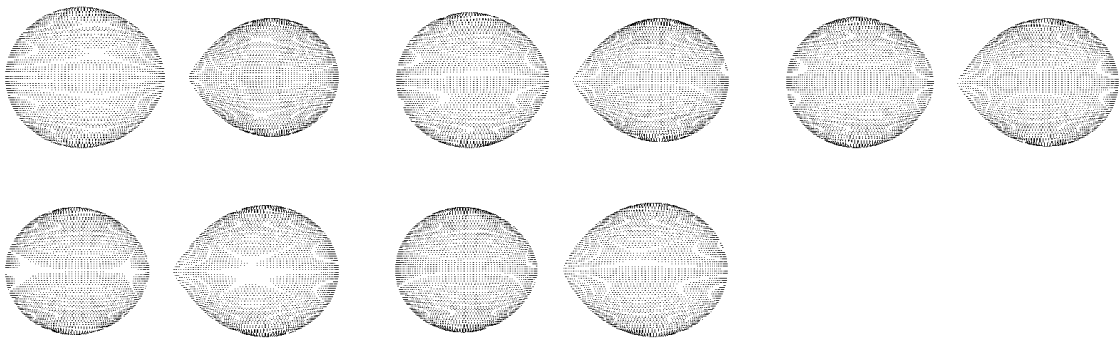


Figure 3.27: 3D plots of MACHO 579 (05:38:40.5–69:29:22) for mass ratio 0.6 (upper left) to 1.0 (lower right) with 0.1 increments.

MACHO 020 (04:56:11.4–69:11:55)

m_V [mag]	P [d]	σ	Conf.
15.5	1.7320187	0.008	SD
– system close to or actually in semi-detached configuration – evolved components suggested – light curves of excellent quality			

MACHO 020 is an eclipsing binary which is clearly in a semi-detached configuration. Its light curves are of adequate quality for an apparent brightness during quadrature phases of $V = 15.5$ mag. They display the classical shape of a semi-detached system with very strong out-of-eclipse variation, but clearly visible ingress and egress points of the eclipse minima. The different depths of the minima point to a significant difference in effective temperature of the components. The orbital period of the system was determined to be 1.7320187 days, and from the color index calibration again an unrealistic primary temperature of 63000 K would be suggested.

It is clear that the main sequence relations cannot be used in this case. The photometrically derived temperature ratio of the order 0.7 would imply grossly different stellar masses and radii. As can be seen in Table 3.29 and Fig. 3.30, the relative radii of both components are however comparable. To satisfy the photometric temperature ratio constraint, the secondary component, which is also the Roche lobe-filling one, must be in an evolved state. Since it is the less massive component, a significant amount of mass may already have been transferred to the primary star. Additionally, the color index-based temperature of 63000 K seems way too high to be physically realistic. It is very likely that with a value of $E(B - V) = 0.15$ the foreground reddening is largely overestimated at the position of MACHO 020. A still very high $E(B - V)$ value of 0.13 would immediately cut the temperature to 44000 K. This is due to the extremely low sensitivity of the $V - R$ color index against temperature change in this very hot regime. Since a probable mass ratio cannot be derived without the assumption of main sequence components, the light curves were plotted for $q = 0.75$ (see Fig. 3.28) which lies in the middle of the possible mass ratio range.

The observational data are fitted very well by the synthetic light curves. There are no clear systematic deviations of the residuals, although some small deviations are observed,

q	i [deg]	$T_{\text{eff},2}$ [K]	$L_1/(L_1 + L_2)$	$L_2/(L_1 + L_2)$	R_1/a	R_2/a
0.55	73.03 ± 0.21	41855 ± 280	0.718 ± 0.013	0.282 ± 0.013	0.3982 ± 0.0015	0.3277 ± 0.0014
0.60	72.94 ± 0.17	42661 ± 306	0.690 ± 0.016	0.310 ± 0.016	0.3863 ± 0.0011	0.3354 ± 0.0009
0.65	79.60 ± 0.86	36451 ± 261	0.860 ± 0.027	0.140 ± 0.027	0.4177 ± 0.0009	0.2340 ± 0.0028
0.70	72.79 ± 0.18	43977 ± 482	0.635 ± 0.046	0.365 ± 0.046	0.3613 ± 0.0021	0.3488 ± 0.0002
0.75	72.25 ± 0.11	43735 ± 322	0.632 ± 0.019	0.368 ± 0.019	0.3642 ± 0.0010	0.3548 ± 0.0001
0.80	72.05 ± 0.14	43738 ± 345	0.621 ± 0.019	0.379 ± 0.019	0.3612 ± 0.0013	0.3601 ± 0.0007
0.85	71.86 ± 0.12	43514 ± 249	0.605 ± 0.011	0.395 ± 0.011	0.3535 ± 0.0008	0.3656 ± 0.0001
0.90	71.92 ± 0.14	43864 ± 216	0.584 ± 0.012	0.416 ± 0.012	0.3443 ± 0.0007	0.3706 ± 0.0001
0.95	71.94 ± 0.18	43917 ± 205	0.571 ± 0.011	0.429 ± 0.011	0.3397 ± 0.0006	0.3754 ± 0.0001
1.00	72.07 ± 0.11	44439 ± 261	0.551 ± 0.015	0.449 ± 0.015	0.3325 ± 0.0006	0.3799 ± 0.0000

Table 3.8: Parameters of MACHO 020 (04:56:11.4–69:11:55) derived from the photometric analysis shown together with 1σ bootstrap errors.

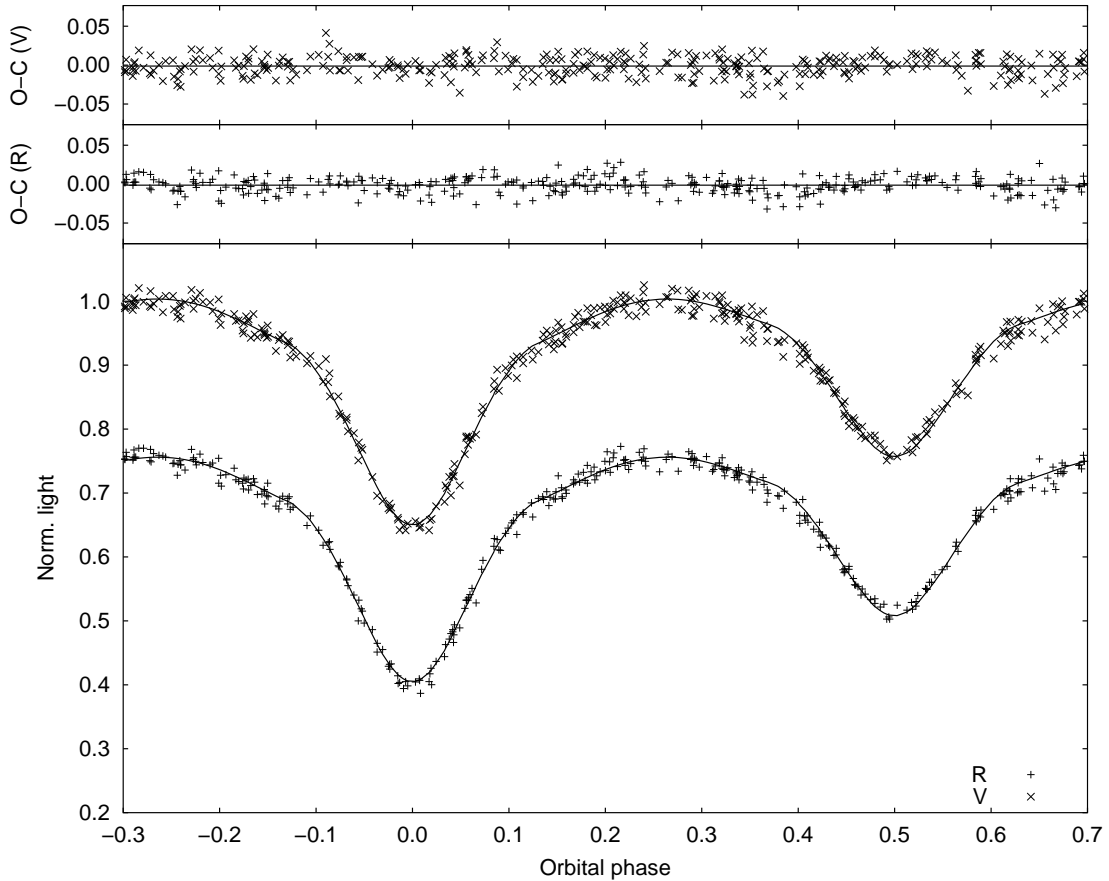


Figure 3.28: *V* and *R* light curves of MACHO 020 (04:56:11.4–69:11:55) shown together with best fits for mass ratio $q = 0.75$. For clarity, error bars of the individual data points are omitted and the *R* light curve is shifted down 0.25 light units.

which can be explained by poor phase sampling in some regions of the light curves. On the other hand there is a shallow dip in both light curves just before the onset of the secondary minimum, which may be caused by a stream of mass falling onto the secondary component via the inner Lagrangian point.

The parameter correlations are found similar to those of the other semi-detached binaries analyzed in this work. The temperature ratio stays nearly constant and the radii shift their values according to the changing tidal distortion with increasing mass ratio. This has to happen while at the same time retaining a semi-detached configuration, therefore the parameters are determined quite well. There is an exception for mass ratio $q = 0.65$, where the simplex algorithm probably got stuck in a local minimum which is actually far away in parameter space from the global minimum. The only common feature of this solution with the rest is the semi-detached configuration, but the roles of primary and secondary component are interchanged and the difference in size is much more drastic. Accordingly, the orbital inclination is much higher.

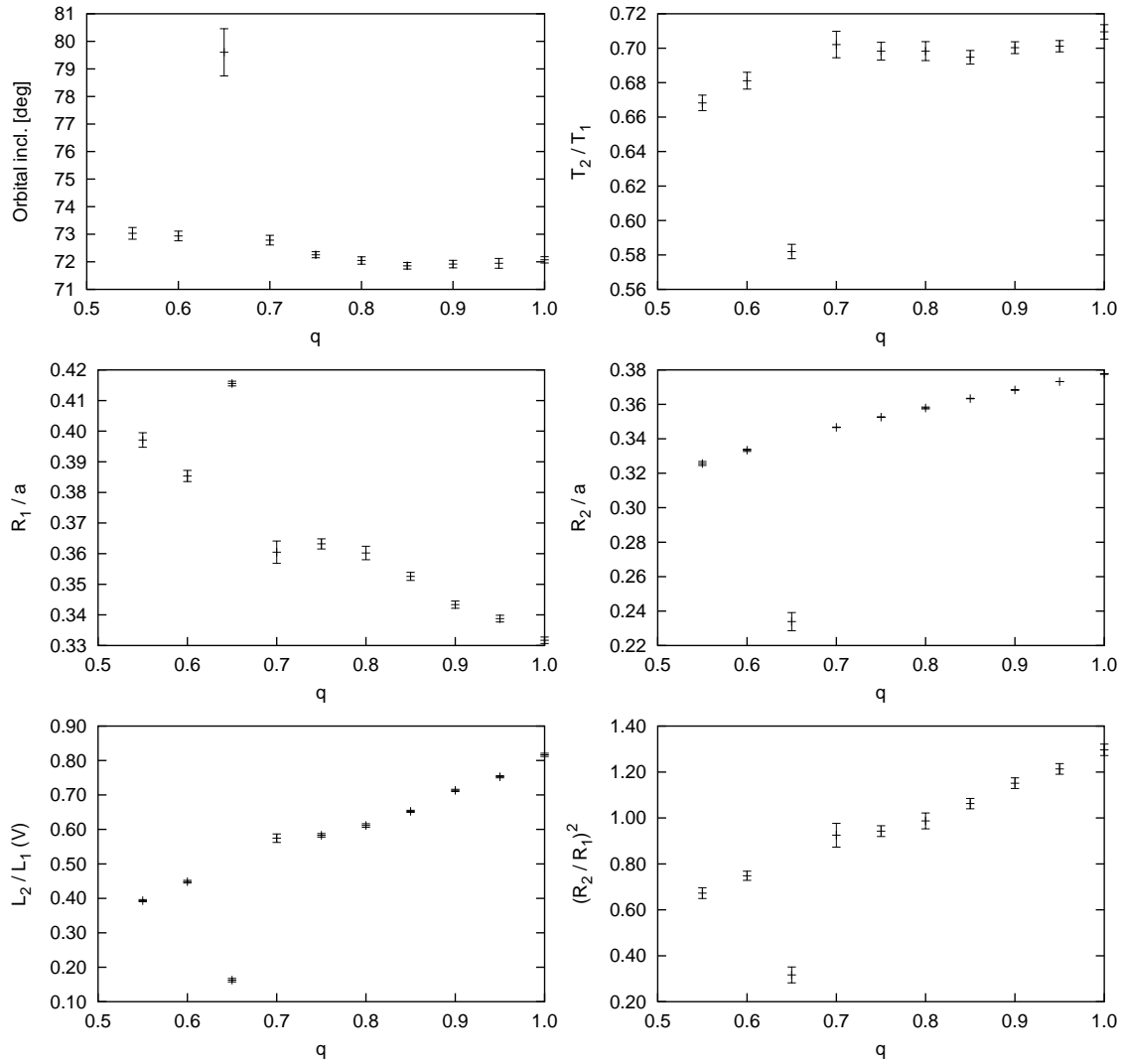


Figure 3.29: Final parameters of MACHO 020 (04:56:11.4–69:11:55) for different values of mass ratio q plotted together with their 1σ bootstrap errors.

This problem probably occurred, because the Roche lobe-filling condition of the secondary star was not explicitly set as boundary condition which is in principle possible to do in MORO. In order to search the largest possible region of parameter space this was not usually done during the analyses of this work, though. In this case, it opened up the possibility of the simplex getting trapped in a completely different configuration, which does not yield a fit quality as good as the rest of the parameter sets. It is however very instructive to see how this kind of problem arises and manifests itself, therefore the respective results are shown in Figs. 3.29 and 3.30. One has to keep in mind that the traditional procedure of guessing initial parameters and initiating trial fitting runs from these start values is very dangerous because of the local minimum problem. Usually, if the fit is of reasonable quality, one would not even doubt the result. If there are no obvious physical arguments against it (and with the lack of spectroscopic data these are generally

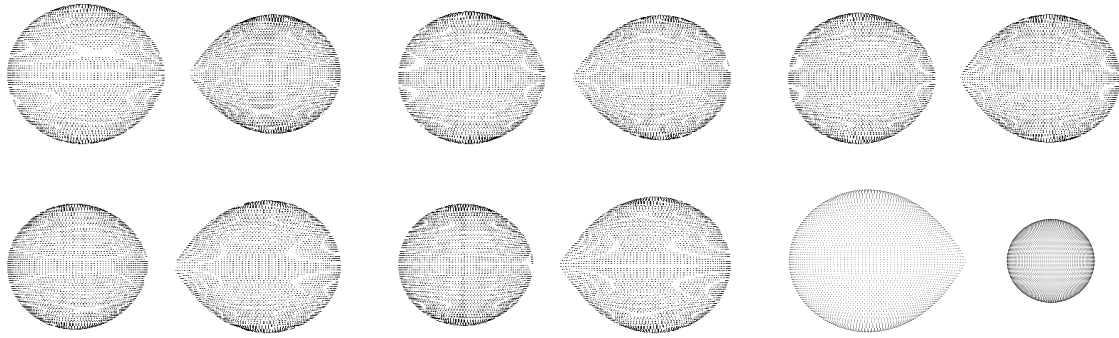


Figure 3.30: 3D plots of MACHO 020 (04:56:11.4–69:11:55) for mass ratio 0.6 (upper left) to 1.0 (lower middle) with 0.1 increments. The “freak” configuration for $q = 0.65$ which results from simplex entrapment in a local minimum is shown at the lower right.

rarely accessible), the error may not be discovered. Only a complete and thorough scan of the relevant parameter space, like it was performed for every system in this work, can help to reveal such a problem and find the most probable solution.

3.7.3 Detached systems

MACHO 468 (05:31:30.3–69:17:40)

m_V [mag]	P [d]	σ	Conf.
14.4	1.1972837	0.009	DE
– detached system with some tidal distortion			
– configuration change at $q = 0.9$			

The eclipsing binary MACHO 468 is shown to be in a very close, yet detached configuration. An inspection of the light curves clearly reveals a strong out-of-eclipse variation, while at the same time ingress and egress points of the eclipse minima are discernible without problems. An orbital period of 1.1972837 days was derived. The phase coverage of this $m_V = 14.4$ mag system is very good and the well-defined light curves exhibit only normal scatter. There is a pronounced dip in the light curve during the primary minimum which occurs just before phase 0. Therefore the expected symmetry around this point in phase is broken. The residuals, which are otherwise evenly scattered around their mean value, clearly show the deviation. The effect seems to be real, as it is observed in both passbands. Any problem related to weather, telescope or detector malfunction can be ruled out, since several independent measurements with long timespans in between form the dip. Since the rest of the light curves and especially the secondary minima exhibit very good symmetry, neither a phase-folding problem nor error of the orbital period can be the cause of the deviation.

An effective temperature of about 22500 K was derived for the primary component. The relative depths of the light curve minima give an approximate temperature ratio of $T_2/T_1 \approx 0.75$. Using this ratio, and again assuming a main sequence state for both stars a mass ratio of $q \approx 0.7$ is suggested. Primary and secondary masses of $11M_\odot$ and $8M_\odot$ follow, as well as radii of $R_1 \approx 4.7R_\odot$ and $R_2 \approx 3.9R_\odot$, respectively. In that case, the orbital separation would be $a \approx 12.7R_\odot$.

q	i [deg]	$T_{\text{eff},2}$ [K]	$L_1/(L_1 + L_2)$	$L_2/(L_1 + L_2)$	R_1/a	R_2/a
0.30	72.83 ± 0.37	21111 ± 207	0.731 ± 0.021	0.269 ± 0.021	0.3856 ± 0.0021	0.2762 ± 0.0018
0.35	72.53 ± 0.56	20971 ± 227	0.719 ± 0.021	0.281 ± 0.021	0.3822 ± 0.0019	0.2820 ± 0.0024
0.40	72.27 ± 0.47	21203 ± 203	0.676 ± 0.024	0.324 ± 0.024	0.3617 ± 0.0021	0.2941 ± 0.0018
0.45	72.03 ± 0.27	21321 ± 188	0.635 ± 0.026	0.365 ± 0.026	0.3436 ± 0.0012	0.3049 ± 0.0014
0.50	71.67 ± 0.24	21184 ± 140	0.634 ± 0.019	0.366 ± 0.019	0.3469 ± 0.0010	0.3087 ± 0.0014
0.55	71.37 ± 0.26	21162 ± 131	0.622 ± 0.015	0.378 ± 0.015	0.3435 ± 0.0011	0.3134 ± 0.0016
0.60	71.31 ± 0.36	20901 ± 175	0.641 ± 0.026	0.359 ± 0.026	0.3540 ± 0.0010	0.3109 ± 0.0019
0.65	71.96 ± 0.54	20497 ± 164	0.675 ± 0.028	0.325 ± 0.028	0.3639 ± 0.0014	0.2978 ± 0.0025
0.70	71.69 ± 0.53	20309 ± 143	0.670 ± 0.030	0.330 ± 0.030	0.3613 ± 0.0015	0.3011 ± 0.0028
0.75	71.46 ± 0.39	20393 ± 145	0.657 ± 0.023	0.343 ± 0.023	0.3572 ± 0.0015	0.3052 ± 0.0021
0.80	71.47 ± 0.37	20282 ± 155	0.658 ± 0.023	0.342 ± 0.023	0.3568 ± 0.0013	0.3040 ± 0.0020
0.85	71.70 ± 0.44	20140 ± 140	0.664 ± 0.029	0.336 ± 0.029	0.3562 ± 0.0016	0.3002 ± 0.0023
0.90	71.16 ± 0.28	21392 ± 218	0.504 ± 0.036	0.496 ± 0.036	0.3050 ± 0.0012	0.3496 ± 0.0018
0.95	70.91 ± 0.39	21093 ± 176	0.523 ± 0.036	0.477 ± 0.036	0.3135 ± 0.0016	0.3490 ± 0.0021
1.00	70.82 ± 0.36	21137 ± 176	0.515 ± 0.031	0.485 ± 0.031	0.3118 ± 0.0015	0.3513 ± 0.0021

Table 3.9: Parameters of MACHO 468 (05:31:30.3–69:17:40) derived from the photometric analysis shown together with 1σ bootstrap errors.

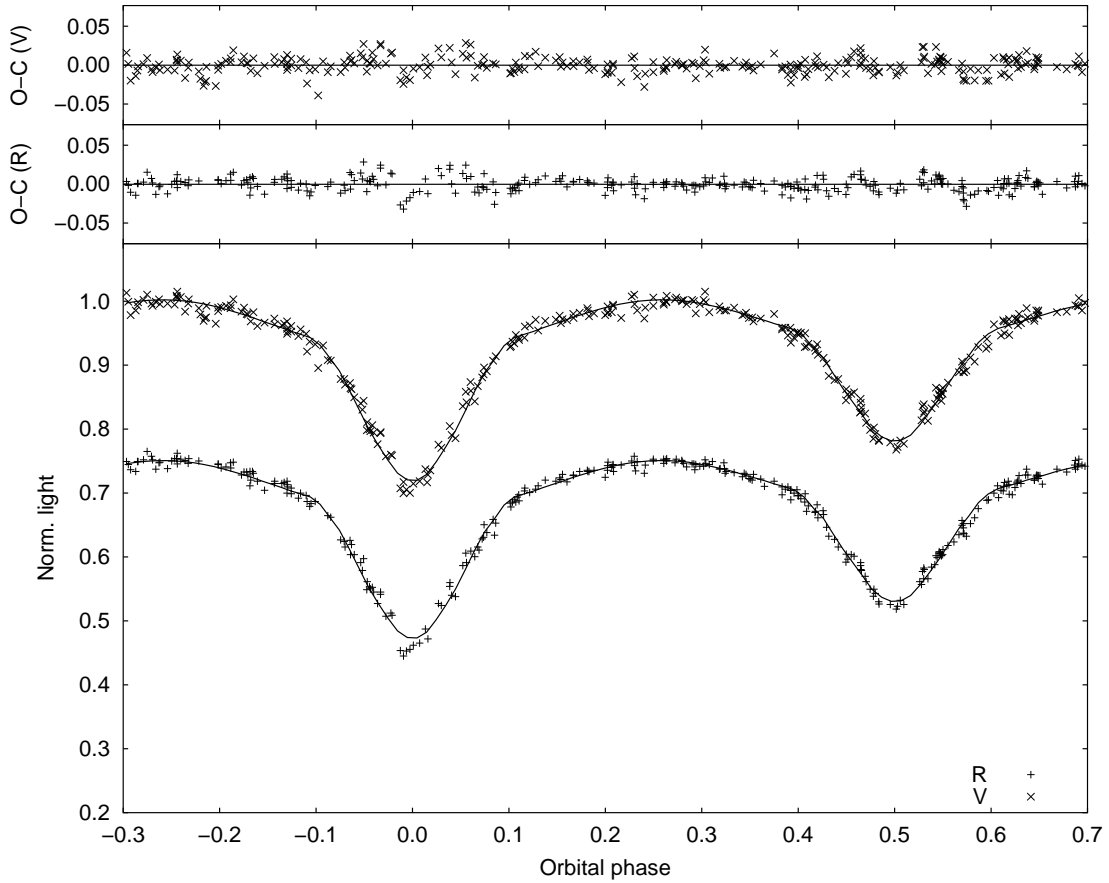


Figure 3.31: *V* and *R* light curves of MACHO 468 (05:31:30.3–69:17:40) shown together with best fits for mass ratio $q = 0.7$. For clarity, error bars of the individual data points are omitted and the *R* light curve is shifted down 0.25 light units.

These parameters are compatible with $T_1 \approx 27000$ K and $T_2 \approx 22000$ K (corresponding to spectral types B0.5 and B2), which is higher than the temperatures derived according to Section 3.5.2. Nevertheless, the discussion from Section 3.7.2 applies here as well: in addition to the well-known uncertainties of temperature determination via color indices, the interstellar extinction used is a major factor, and possibly cannot be determined with the accuracy that would be desirable. This problem is observed in this case, too, as the originally derived primary temperature of ≈ 22500 K shows.

The correlations of the derived light curve parameters are of course different from those of overcontact binaries. Naturally, since the secondary surface potential is not identical to that of the primary component, it is one additional free parameter which tends to make the solutions less definitive. As can be seen in Fig. 3.32, the parameter correlations are not as clear as in the overcontact case. The most striking phenomenon is the obvious existence of two different solution regions within the parameter space. From $q = 0.9$ upwards, the parameters shift to a somewhat different configuration. This can also be seen in the 3D plots (see Fig. 3.33): in the configurations for $q = 0.9$ and $q = 1.0$ the sizes

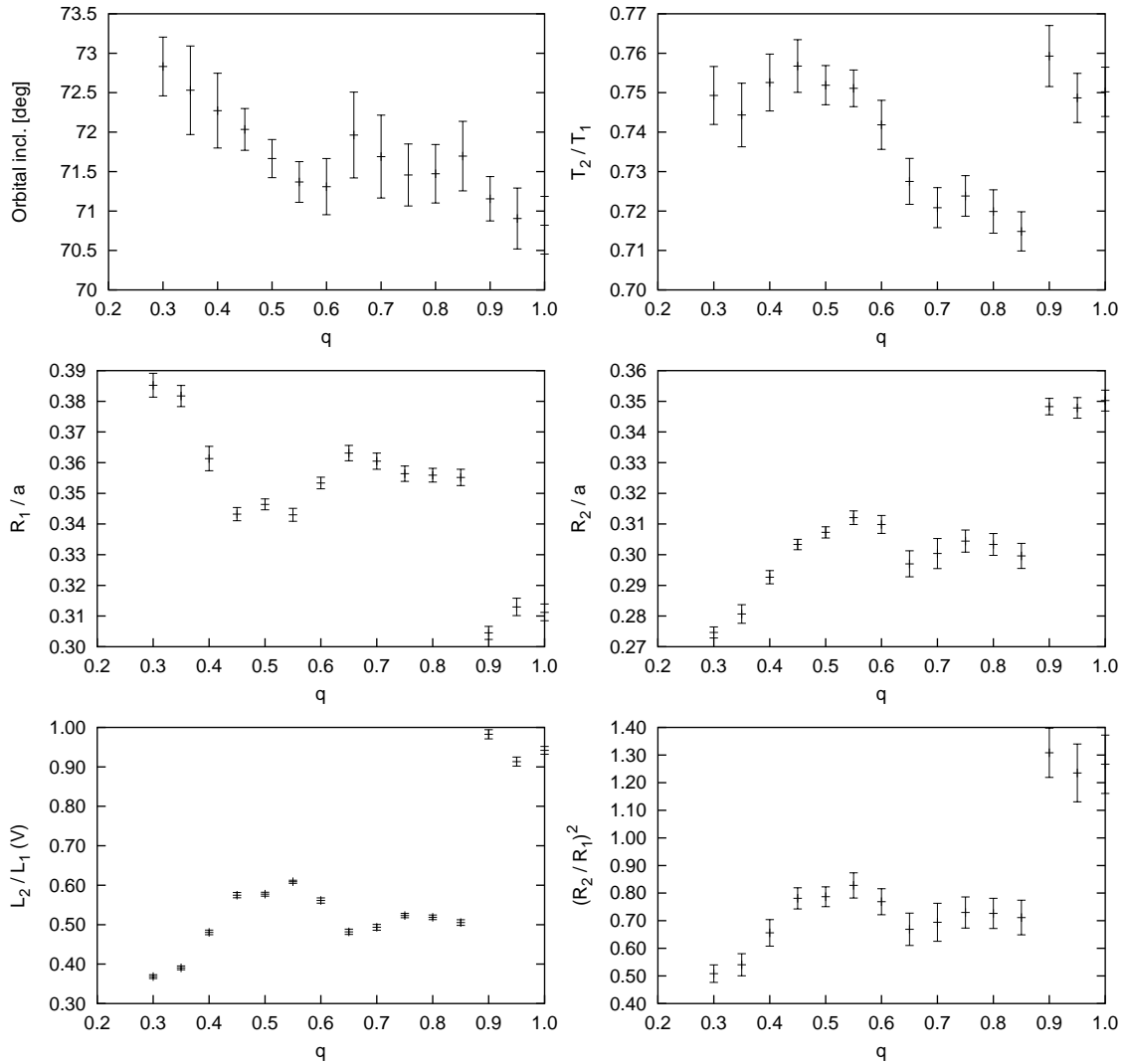


Figure 3.32: Final parameters of MACHO 468 (05:31:30.3–69:17:40) for different values of mass ratio q plotted together with their 1σ bootstrap errors.

of the components interchange and the secondary component becomes the larger one in this solution regime.

The temperature ratio stays fairly constant again because it is locked by the given relative depths of the eclipse minima. In the range $0.3 \leq q < 0.9$ one can clearly see how the compensation mechanisms for changing mass ratio work: since both surface potentials are adjusted independently, it is fairly easy for the light curve program to keep the radii of both stars constant for the different values of q . Nevertheless, there is a certain change in tidal distortion to be taken into account, as for increasing q the center of mass shifts away from the primary component. This results in a reduced distortion of the secondary component, which has to be counteracted by a slight increase of the relative radius R_2 . Equally, the increasing distortion of the primary component is compensated by a slightly reduced relative radius R_1 . The ratio $(R_2/R_1)^2$ gets closer to 1 for increasing q . The associated

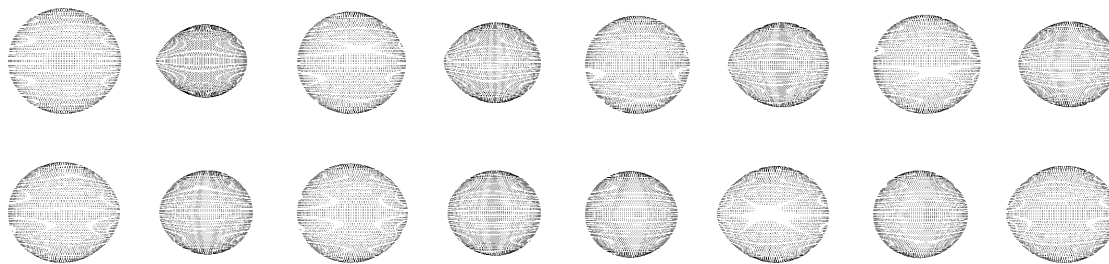


Figure 3.33: 3D plots of MACHO 468 (05:31:30.3–69:17:40) for mass ratio 0.3 (upper left) to 1.0 (lower right) with 0.1 increments.

increase in minimum depths is counteracted by a slightly decreasing orbital inclination. These tendencies can be clearly seen in Fig. 3.32. Also note that the errors of R_1 and R_2 are of course much larger than for overcontact systems (see Subsections 3.7.1 and 3.7.1).

As to the configuration change at $q = 0.9$, it is unclear why it happens. Most probably, a similar solution regime exists for smaller values of the mass ratio, but the configuration with the larger primary component seems to consistently yield lower χ^2 values here. Possibly due to some subtle features in the light curve, somewhere around $q = 0.9$ the configuration with larger secondary starts to produce slightly better results and is therefore favored by the light curve solution process.

MACHO 599 (05:40:11.7–69:55:04)

m_V [mag]	P [d]	σ	Conf.
14.6	1.2482550	0.012	DE
– deep eclipses – large light curve scatter			

Even though it is a very close system, MACHO 599 is still in a slightly detached configuration. It is similar to MACHO 468 (see Section 3.7.3) in many respects, including apparent brightness, orbital period and effective temperature. The light curve minima are much deeper, though, with a light loss of almost 50% between quadrature phases. This indicates a higher orbital inclination and possibly larger relative radii, although there is not much space to expand and at the same time still remain in a detached state. It is however evident from the light curve that MACHO 599 is not an overcontact system, as the ingress and egress points of the minima are clearly visible. The orbital period is 1.2482550 days, the system has an apparent brightness of 14.6 mag.

If one assumes both components to be on the main sequence or only slightly evolved, a mass ratio of $q \approx 0.85$ is implied by the observed temperature ratio. Taking into account the photometrically derived relative radii of the stars, an orbital separation of $a \approx 15.6R_\odot$ can be determined, with the primary component having $18M_\odot$ and $6.2R_\odot$, and the secondary component being a $15M_\odot$ star with $5.9R_\odot$. This corresponds nicely with the relative radii determined from the analysis of the light curves. These absolute parameters correspond to components of spectral types O9 and B0, respectively. The expected individual absolute brightnesses place this binary at the correct distance to be an LMC member.

The light curves are very well defined, although quite some scatter is present in the measurements, maybe owing to the very crowded stellar field. They are fitted nicely by the synthetic light curves, and no systematic deviations of the residuals are evident. As to the derived parameters, the temperature ratio is practically constant for every value of q considered, as can be expected. The other parameters show the classical correlations with R_1 and R_2 exhibiting opposite trends with changing mass ratio. The luminosity ratio changes accordingly, and a slightly decreasing orbital inclination compensates the

q	i [deg]	$T_{\text{eff},2}$ [K]	$L_1/(L_1 + L_2)$	$L_2/(L_1 + L_2)$	R_1/a	R_2/a
0.55	83.84 ± 0.43	16390 ± 83	0.680 ± 0.023	0.320 ± 0.023	0.4233 ± 0.0013	0.3252 ± 0.0019
0.60	83.02 ± 0.29	16329 ± 77	0.669 ± 0.021	0.331 ± 0.021	0.4183 ± 0.0013	0.3298 ± 0.0018
0.65	82.25 ± 0.23	16402 ± 69	0.647 ± 0.018	0.353 ± 0.018	0.4099 ± 0.0011	0.3381 ± 0.0020
0.70	82.29 ± 0.25	16217 ± 62	0.650 ± 0.015	0.350 ± 0.015	0.4089 ± 0.0013	0.3364 ± 0.0015
0.75	81.97 ± 0.27	16207 ± 70	0.637 ± 0.020	0.363 ± 0.020	0.4030 ± 0.0014	0.3416 ± 0.0018
0.80	81.67 ± 0.19	16244 ± 66	0.620 ± 0.019	0.380 ± 0.019	0.3963 ± 0.0013	0.3478 ± 0.0017
0.85	81.09 ± 0.15	16504 ± 64	0.583 ± 0.023	0.417 ± 0.023	0.3844 ± 0.0012	0.3616 ± 0.0018
0.90	81.10 ± 0.15	16333 ± 57	0.587 ± 0.017	0.413 ± 0.017	0.3849 ± 0.0011	0.3605 ± 0.0017
0.95	80.99 ± 0.17	16280 ± 59	0.582 ± 0.016	0.418 ± 0.016	0.3823 ± 0.0012	0.3618 ± 0.0016
1.00	80.82 ± 0.21	16280 ± 66	0.572 ± 0.020	0.428 ± 0.020	0.3787 ± 0.0010	0.3652 ± 0.0018

Table 3.10: Parameters of MACHO 599 (05:40:11.7–69:55:04) derived from the photometric analysis shown together with 1σ bootstrap errors.

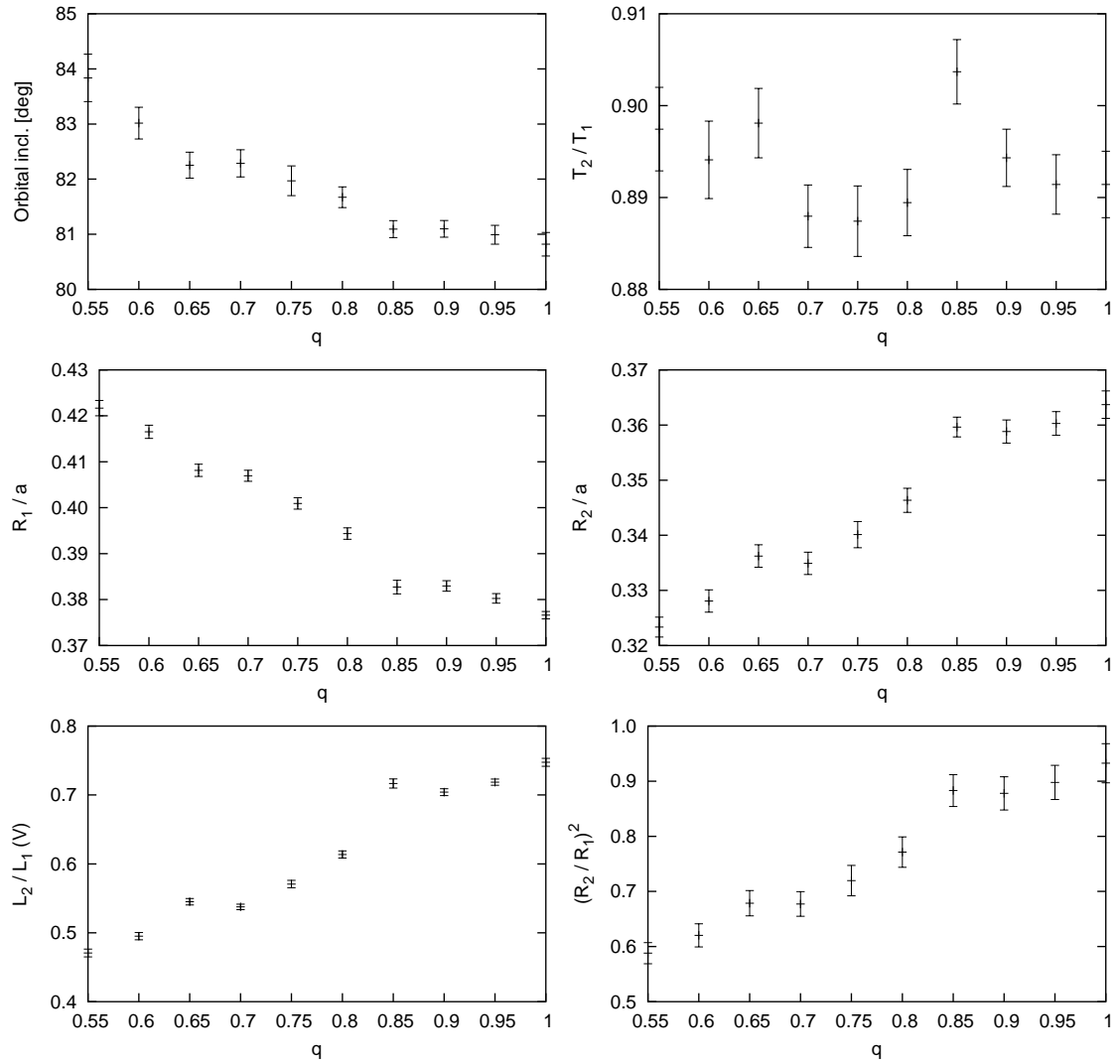


Figure 3.34: Final parameters of MACHO 599 (05:40:11.7–69:55:04) for different values of mass ratio q plotted together with their 1σ bootstrap errors.

increasing minimum depths caused by $(R_2/R_1)^2 \rightarrow 1.0$ for increasing q . Most solutions obey the overall trend and there are no unphysical exceptions. Just the solution for $q = 0.85$ seems to be slightly off, which manifests itself in an increased temperature ratio T_2/T_1 (but only by an amount of about 0.01 which is not much larger than the associated errors). Also a small “jump” can be observed at $q = 0.85$ for the other parameters as well which may be indeed due to the solution process again being trapped in a local minimum very close to the optimum solution. Nevertheless, the parameter trends look good and the values can be established with reasonably good accuracy.

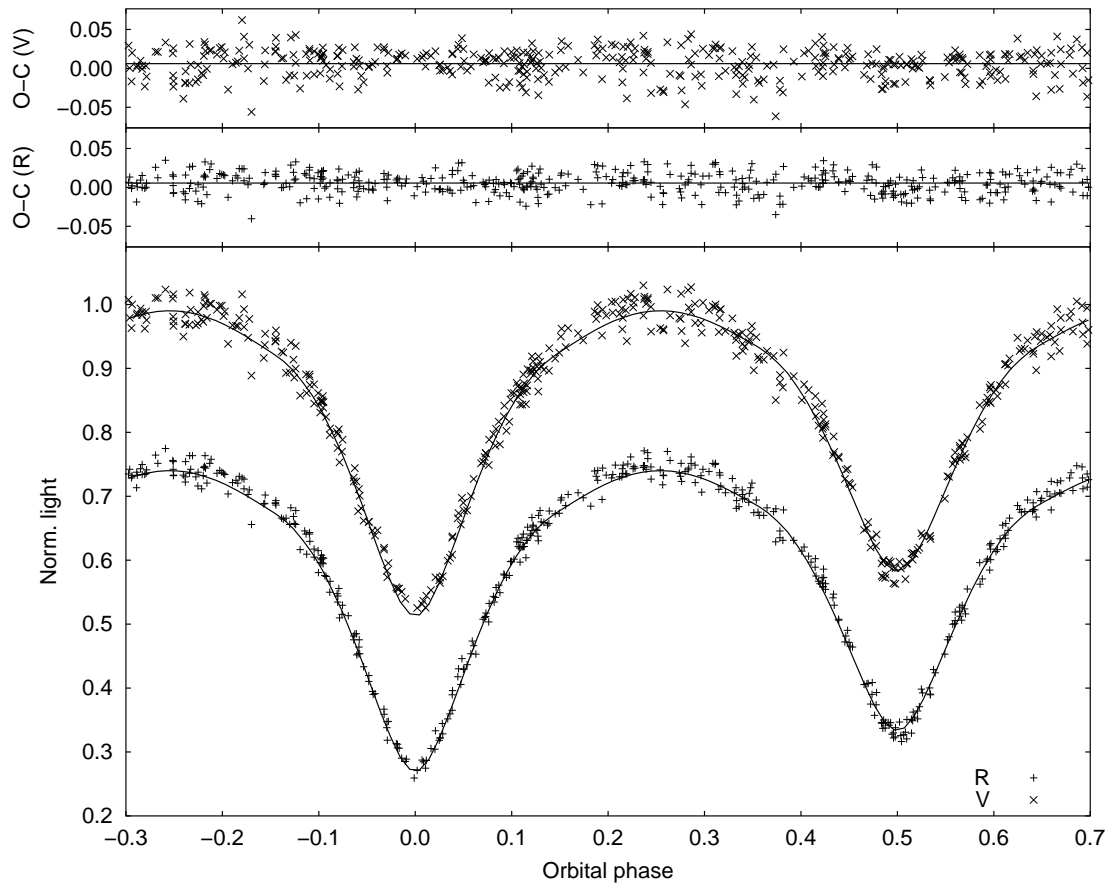


Figure 3.35: *V* and *R* light curves of MACHO 599 (05:40:11.7–69:55:04) shown together with best fits for mass ratio $q = 0.85$. For clarity, error bars of the individual data points are omitted and the *R* light curve is shifted down 0.25 light units.

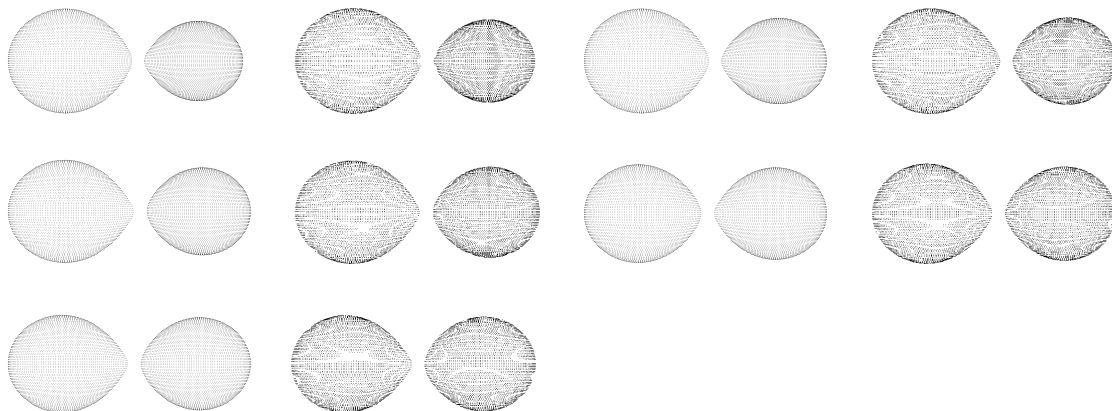


Figure 3.36: 3D plots of MACHO 599 (05:40:11.7–69:55:04) for mass ratio 0.55 (upper left) to 1.0 (lower right) with 0.05 increments.

MACHO 496 (05:33:01.8–69:26:47)

m_V [mag]	P [d]	σ	Conf.
14.7	1.7495007	0.012	DE
– well-detached system			
– may contain evolved components			

MACHO 496 is a typical example for a well-detached eclipsing binary with relatively little amount of tidal distortion. Ingress and egress of the light curve minima are defined clearly and there is only slight out-of-eclipse variability. The system has a total apparent brightness of $m_V = 14.7$ and an orbital period of 1.7495007 days, hinting at a substantial orbital separation a . Given a primary temperature of ≈ 31000 K (and a temperature ratio near 1) this suggests quite massive components.

Assuming both stars to be at or near the main sequence, the temperature ratio of about 1 (clearly seen from the almost equal depths of both eclipse minima) leads to a mass ratio of $q \approx 1$. With the main sequence relations given by component masses of $M_1 = M_2 \approx 18M_\odot$ and radii of $R_1 = R_2 \approx 6.4R_\odot$ can be derived. An orbital separation of $a \approx 20R_\odot$ can be assumed. The effective temperature for these kinds of stars would be in the 33000 K region. This is one of the cases where the temperatures seem to have been slightly underestimated. The discrepancy is not too large, though, and can easily explained by the inevitable uncertainties of the color-temperature calibration. Alternatively, the components may be evolved to some degree, in contrast to the assumption of main sequence components and thereby permitting lower effective temperatures.

A reasonable amount of scatter can be found in the light curves, with notably better S/N ratio in the R passband. The light curve fits are very good (see Fig. 3.38) and do not exhibit any major discrepancies from the observations. Only in the center of the primary minimum the residuals seem to be slightly biased towards the negative. Upon closer inspection, though, it is revealed that actually most of the R band residuals are ≈ 0 while in the V light curve, where the effect is noticed more prominently, the scatter is

q	i [deg]	$T_{\text{eff},2}$ [K]	$L_1/(L_1 + L_2)$	$L_2/(L_1 + L_2)$	R_1/a	R_2/a
0.30	79.49 ± 0.43	30056 ± 236	0.708 ± 0.023	0.292 ± 0.023	0.3773 ± 0.0013	0.2487 ± 0.0020
0.35	78.65 ± 0.41	30071 ± 202	0.689 ± 0.023	0.311 ± 0.023	0.3737 ± 0.0011	0.2567 ± 0.0019
0.40	78.56 ± 0.28	29726 ± 216	0.681 ± 0.019	0.319 ± 0.019	0.3683 ± 0.0010	0.2594 ± 0.0014
0.45	77.54 ± 0.19	30184 ± 201	0.622 ± 0.017	0.378 ± 0.017	0.3481 ± 0.0009	0.2776 ± 0.0014
0.50	77.54 ± 0.20	29982 ± 181	0.629 ± 0.019	0.371 ± 0.019	0.3523 ± 0.0007	0.2766 ± 0.0014
0.55	77.44 ± 0.23	29770 ± 186	0.624 ± 0.021	0.376 ± 0.021	0.3497 ± 0.0009	0.2781 ± 0.0016
0.60	77.59 ± 0.27	29252 ± 194	0.638 ± 0.023	0.362 ± 0.023	0.3531 ± 0.0009	0.2747 ± 0.0020
0.65	76.83 ± 0.34	29927 ± 203	0.585 ± 0.030	0.415 ± 0.030	0.3379 ± 0.0012	0.2905 ± 0.0026
0.70	77.71 ± 0.31	28852 ± 212	0.644 ± 0.025	0.356 ± 0.025	0.3521 ± 0.0012	0.2715 ± 0.0021
0.75	76.81 ± 0.29	30214 ± 195	0.519 ± 0.029	0.481 ± 0.029	0.3154 ± 0.0007	0.3091 ± 0.0019
0.80	76.76 ± 0.19	30406 ± 184	0.503 ± 0.023	0.497 ± 0.023	0.3111 ± 0.0006	0.3136 ± 0.0016
0.85	76.66 ± 0.29	29680 ± 197	0.549 ± 0.029	0.451 ± 0.029	0.3259 ± 0.0012	0.3021 ± 0.0021
0.90	76.84 ± 0.27	29461 ± 221	0.579 ± 0.028	0.421 ± 0.028	0.3344 ± 0.0011	0.2914 ± 0.0023
0.95	76.65 ± 0.21	29863 ± 148	0.511 ± 0.022	0.489 ± 0.022	0.3148 ± 0.0009	0.3143 ± 0.0018
1.00	76.56 ± 0.30	30177 ± 206	0.488 ± 0.034	0.512 ± 0.034	0.3082 ± 0.0011	0.3202 ± 0.0020

Table 3.11: Parameters of MACHO 496 (05:33:01.8–69:26:47) derived from the photometric analysis shown together with 1σ bootstrap errors.

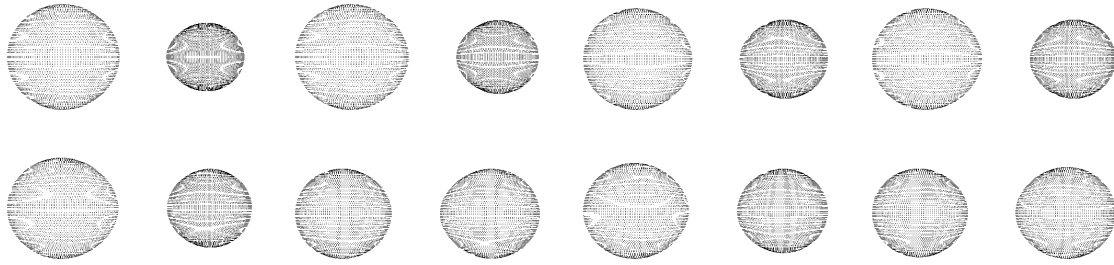


Figure 3.37: 3D plots of MACHO 496 (05:33:01.8–69:26:47) for mass ratio 0.3 (upper left) to 1.0 (lower right) with 0.1 increments.

much higher. Therefore the V data points are not fitted with the same weight as the R observations, resulting in the observed difference of fit quality in the primary minimum.

Moreover, there is quite some scatter in the parameters if different mass ratios are considered. It is obvious that the more detached a system becomes, the more local parameter space minima in the vicinity of the global minimum will arise while at the same time

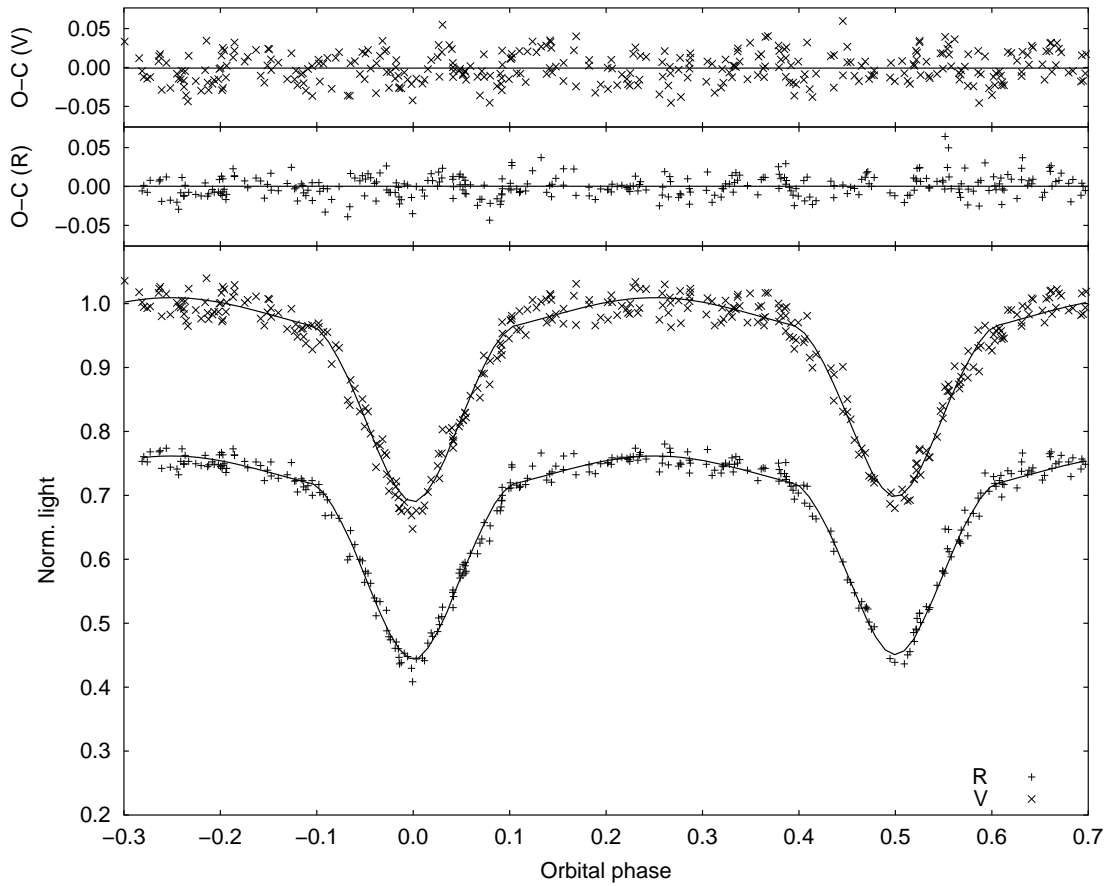


Figure 3.38: V and R light curves of MACHO 496 (05:33:01.8–69:26:47) shown together with best fits for mass ratio $q = 1.0$. For clarity, error bars of the individual data points are omitted and the R light curve is shifted down 0.25 light units.

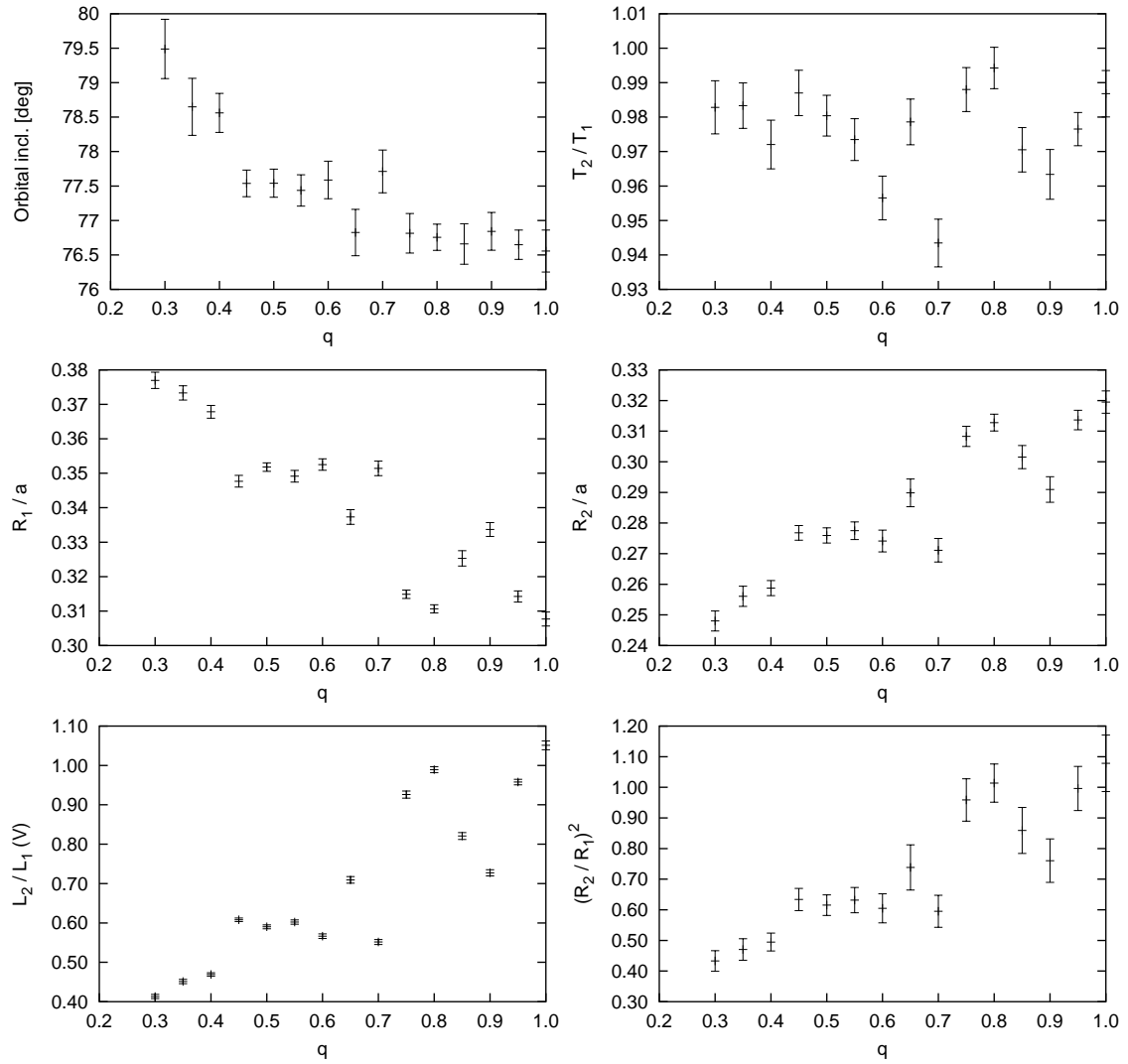


Figure 3.39: Final parameters of MACHO 496 (05:33:01.8–69:26:47) for different values of mass ratio q plotted together with their 1σ bootstrap errors.

the global minimum itself gets more difficult to identify. This is due to the light curve shape being not nearly as sensitive to small parameter changes in a well-detached system like MACHO 496 as it is in a system with strong tidal distortion, where minor parameter modifications change the physical appearance of the components considerably.

MACHO 325 (05:21:00.7–69:29:46)

m_V [mag]	P [d]	σ	Conf.
15.1	1.3007974	0.012	DE
– well-detached system			
– configuration change at $q = 0.5$			

The well-detached system MACHO 325 is very similar to MACHO 496 (see Section 3.7.3). However, it shows a greater variation in relative radii over the whole mass ratio range. Also the orbital inclination is much lower than for MACHO 496 which explains the shallower eclipse minima. The out-of-eclipse variability is similar, indicating a comparable tidal distortion of the components. With an apparent brightness of $m_V = 15.1$ mag and an orbital period of 1.3007974 days, the light curve shows larger scatter than MACHO 496.

If the assumption of main sequence components is made, the near-equal depths of the light curve minima suggest a temperature ratio and therefore a mass ratio near unity. Component masses $M_1 = M_2 \approx 6M_\odot$ and radii $R_1 = R_2 \approx 3.5R_\odot$ are derived from the main sequence relations, corresponding to stars of spectral type B3 and an orbital separation of $a \approx 11.4R_\odot$. Effective temperatures of about 18800 K would be expected for such stars. Keeping in mind that the color-based temperatures of the MACHO stars are generally to be considered upper limits, this value fits well with the 22000 K from the $V - R$ color index and lies within the error margin. The small remaining discrepancy can be explained by a local variation of interstellar extinction.

The light curves display a considerable amount of scatter with the R light curve showing a slightly better S/N than the V light curve. Field crowding is the most likely reason for the large scatter compared with some other systems of similar brightness. The fits are very good with no systematic deviations of the residuals.

The parameters themselves generally follow the usual trends with varying mass ratio. Between mass ratios $q = 0.50$ and $q = 0.55$ a “jump” in the parameter trends can be

q	i [deg]	$T_{\text{eff},2}$ [K]	$L_1/(L_1 + L_2)$	$L_2/(L_1 + L_2)$	R_1/a	R_2/a
0.30	72.83 ± 0.38	21599 ± 193	0.768 ± 0.020	0.232 ± 0.020	0.3906 ± 0.0015	0.2200 ± 0.0021
0.35	72.95 ± 0.46	21388 ± 229	0.772 ± 0.031	0.228 ± 0.031	0.3889 ± 0.0016	0.2170 ± 0.0026
0.40	72.39 ± 0.48	21485 ± 263	0.742 ± 0.038	0.258 ± 0.038	0.3766 ± 0.0016	0.2272 ± 0.0029
0.45	72.39 ± 0.44	21420 ± 223	0.739 ± 0.033	0.261 ± 0.033	0.3731 ± 0.0016	0.2267 ± 0.0027
0.50	72.45 ± 0.54	21450 ± 236	0.738 ± 0.046	0.262 ± 0.046	0.3708 ± 0.0021	0.2247 ± 0.0032
0.55	71.23 ± 0.34	21932 ± 223	0.633 ± 0.033	0.367 ± 0.033	0.3419 ± 0.0012	0.2637 ± 0.0024
0.60	71.07 ± 0.35	22024 ± 219	0.617 ± 0.037	0.383 ± 0.037	0.3382 ± 0.0012	0.2686 ± 0.0024
0.65	70.95 ± 0.36	22116 ± 205	0.566 ± 0.039	0.434 ± 0.039	0.3196 ± 0.0010	0.2833 ± 0.0023
0.70	70.89 ± 0.30	22182 ± 196	0.555 ± 0.032	0.445 ± 0.032	0.3173 ± 0.0009	0.2859 ± 0.0018
0.75	71.12 ± 0.38	22419 ± 259	0.501 ± 0.050	0.499 ± 0.050	0.2961 ± 0.0012	0.2966 ± 0.0024
0.80	70.86 ± 0.27	22110 ± 137	0.551 ± 0.030	0.449 ± 0.030	0.3159 ± 0.0010	0.2864 ± 0.0018
0.85	70.85 ± 0.28	22157 ± 148	0.547 ± 0.035	0.453 ± 0.035	0.3148 ± 0.0010	0.2871 ± 0.0020
0.90	70.81 ± 0.31	21953 ± 177	0.550 ± 0.028	0.450 ± 0.028	0.3152 ± 0.0014	0.2872 ± 0.0020
0.95	70.80 ± 0.37	22217 ± 211	0.511 ± 0.041	0.489 ± 0.041	0.3044 ± 0.0013	0.2981 ± 0.0027
1.00	70.94 ± 0.34	21756 ± 133	0.548 ± 0.036	0.452 ± 0.036	0.3121 ± 0.0014	0.2869 ± 0.0024

Table 3.12: Parameters of MACHO 325 (05:21:00.7–69:29:46) derived from the photometric analysis shown together with 1σ bootstrap errors.

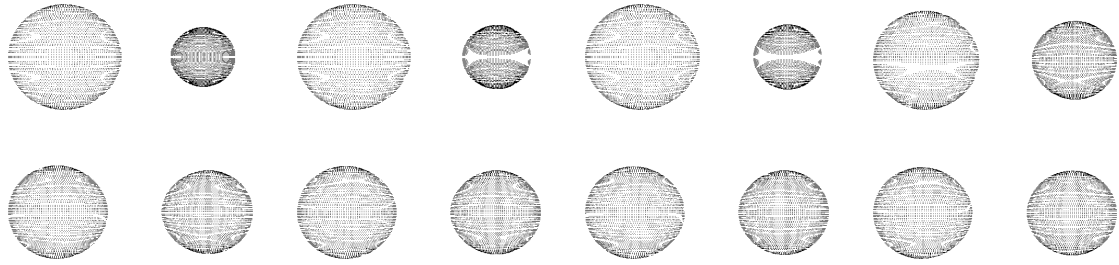


Figure 3.40: 3D plots of MACHO 325 (05:21:00.7–69:29:46) for mass ratio 0.3 (upper left) to 1.0 (lower right) with 0.1 increments.

recognized, corresponding to the region where lacking tidal distortion of the secondary component must be counteracted by its increase in relative size. The orbital inclination drops accordingly, as the rising value of $(R_2/R_1)^2$ results in deeper eclipse minima. Afterwards, the values remain more or less constant which is possible for well-detached systems, since for $q \rightarrow 1$ the variation in tidal distortion is not large enough to influ-

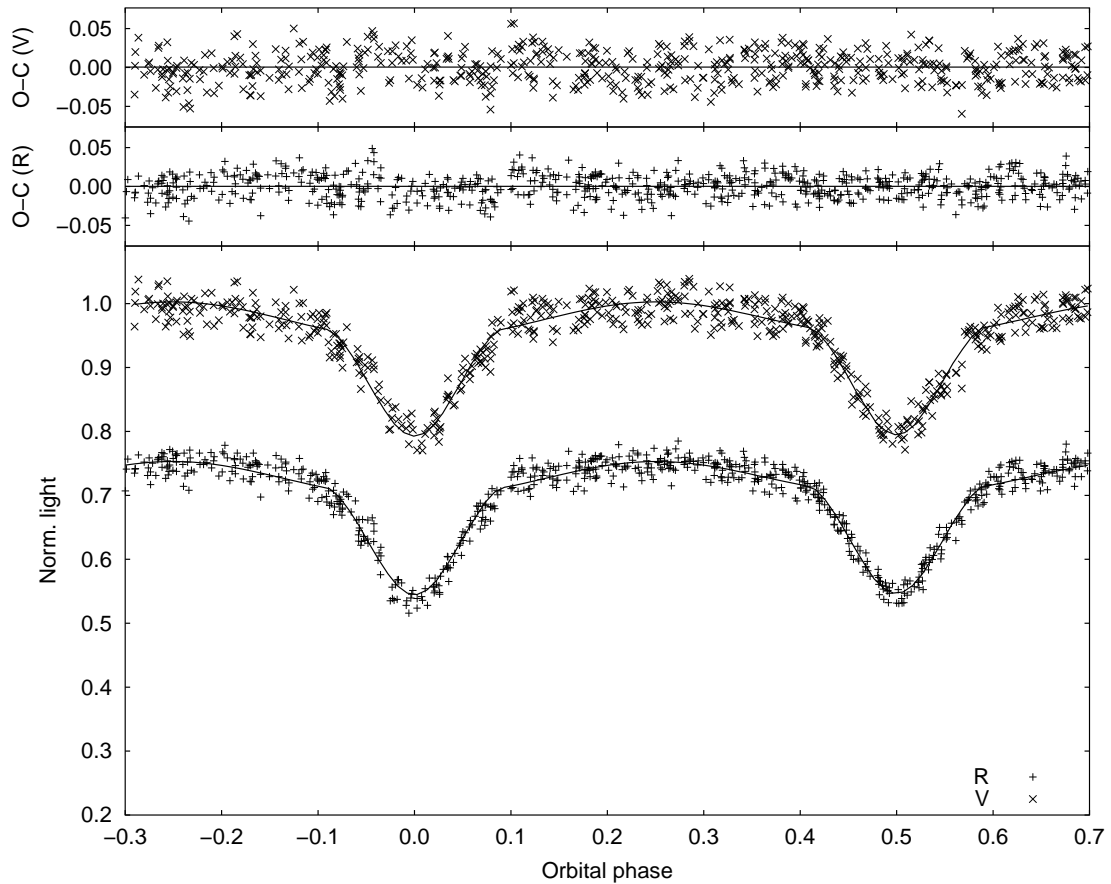


Figure 3.41: V and R light curves of MACHO 325 (05:21:00.7–69:29:46) shown together with best fits for mass ratio $q = 1.0$. For clarity, error bars of the individual data points are omitted and the R light curve is shifted down 0.25 light units.

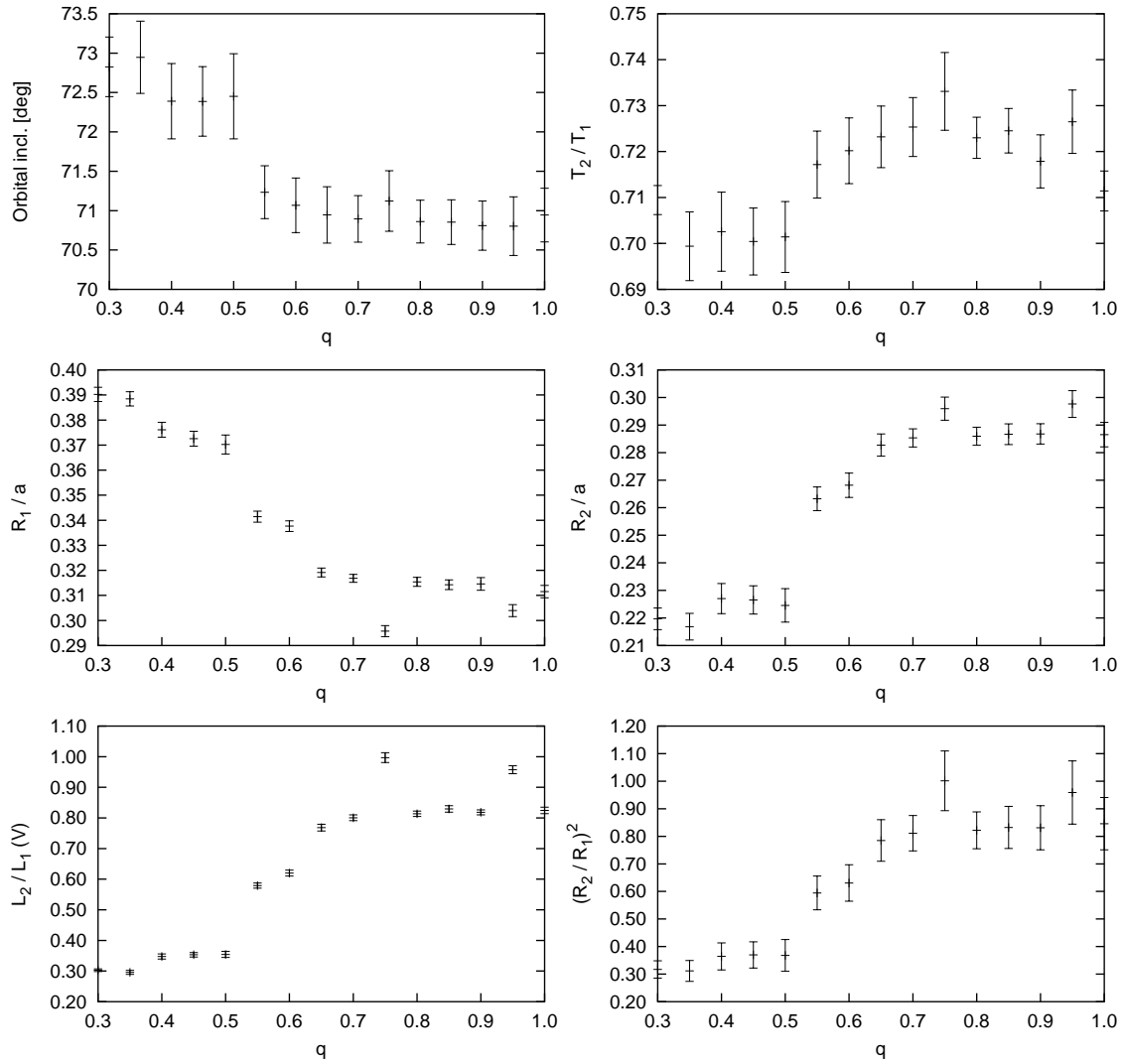


Figure 3.42: Final parameters of MACHO 325 (05:21:00.7–69:29:46) for different values of mass ratio q plotted together with their 1σ bootstrap errors.

ence the light curve shape very much. There is one deviating parameter set at $q = 0.75$ and another, less prominent one at $q = 0.95$. These can be attributed to local minima in parameter space.

MACHO 397 (05:26:03.5–69:26:38)

m_V [mag]	P [d]	σ	Conf.
15.2	1.9037204	0.004	DE
– well-detached system			
– probably contains evolved components			

MACHO 397 is a unique system with interesting peculiarities. First of all, it has the longest orbital period of all binaries analyzed in the photometric part of this work, namely 1.9037204 days. From the enormous difference in size between the components and the almost Roche lobe-filling configuration of the primary component it is clear that the primary is a significantly evolved star, while the secondary may still be on the main sequence. The light curves are of adequate quality for this system which has an apparent magnitude of 15.2 during quadrature phases. The phase coverage is excellent and turns out to be the best of all analyzed stars. The pronounced total eclipse is also unique in this work, due to the large size difference the flat bottoms of the minima are extremely extended. The strong out-of-eclipse variability points at strong tidal distortion of the very large primary component.

As the main sequence assumption is certainly not appropriate in this case, other means have to be found to guess the nature of the components of MACHO 397. In this case a moderate effective temperature of about 22000 K is found for the primary star. As the $V - R$ color index is still of acceptable accuracy in this temperature region and a relatively low interstellar extinction is given by Schwering & Israel (1991), this temperature can be – with proper caution – used as guideline for the physical properties of MACHO 397. A realistic assumption would be to classify the primary component as a giant of luminosity class III. An effective temperature of 22000 K would imply a B2 giant, the absolute luminosity of which would put it at approximately the correct distance to the LMC. From the photometrically derived temperature ratio of ~ 0.7 a secondary temperature of about 15400 K can be inferred, which would correspond to a main sequence star of spectral type B5. The masses would be approximately $M_1 \approx 12M_\odot$ and $M_2 \approx 6M_\odot$ yielding a mass ratio of $q \approx 0.5$ which is right in the middle of the mass ratio values found suitable by the photometric solutions. With these values Kepler’s Third Law (Eq. 1.1) gives an orbital separation of $a \approx 17R_\odot$. While the expected radius of $R_2 \approx 3.9R_\odot$ matches reasonably well the photometrically derived relative radius of about 0.17, $R_1 \approx 12R_\odot$ would be too

q	i [deg]	$T_{\text{eff},2}$ [K]	$L_1/(L_1 + L_2)$	$L_2/(L_1 + L_2)$	R_1/a	R_2/a
0.35	80.76 ± 0.20	20524 ± 119	0.908 ± 0.007	0.092 ± 0.007	0.4507 ± 0.0010	0.1817 ± 0.0004
0.40	81.49 ± 0.23	20283 ± 79	0.911 ± 0.005	0.089 ± 0.005	0.4397 ± 0.0007	0.1750 ± 0.0002
0.45	82.50 ± 0.30	20089 ± 97	0.913 ± 0.006	0.087 ± 0.006	0.4293 ± 0.0007	0.1697 ± 0.0004
0.50	83.29 ± 0.28	20068 ± 102	0.916 ± 0.006	0.084 ± 0.006	0.4204 ± 0.0006	0.1638 ± 0.0003
0.55	86.33 ± 0.10	20074 ± 98	0.917 ± 0.005	0.083 ± 0.005	0.4096 ± 0.0006	0.1579 ± 0.0002
0.60	88.58 ± 0.07	19592 ± 101	0.919 ± 0.005	0.081 ± 0.005	0.4014 ± 0.0006	0.1567 ± 0.0003
0.65	88.69 ± 0.07	19518 ± 99	0.920 ± 0.005	0.080 ± 0.005	0.3947 ± 0.0007	0.1534 ± 0.0003
0.70	87.69 ± 0.14	19647 ± 117	0.921 ± 0.006	0.079 ± 0.006	0.3892 ± 0.0007	0.1488 ± 0.0004

Table 3.13: Parameters of MACHO 397 (05:26:03.5–69:26:38) derived from the photometric analysis shown together with 1σ bootstrap errors.

large for this separation. Therefore it can be concluded that the primary probably has not yet reached the tip of the giant stage, but is definitely on its way up the first giant branch in the Hertzsprung-Russell diagram.

As can be seen in Fig. 3.43, the light curves are of good quality with the *R* band displaying less scatter than the *V* band. Also, the phase coverage is extremely good and allows to judge the quality of the fit throughout the entire orbital phase. The synthetic light curves match the observations very well, with the exception of the ascending branch of the secondary minimum. There the residuals are biased towards the negative in both passbands. Sometimes this kind of light curve distortion is ascribed to extinction by a mass transfer stream seen projected onto the primary surface, but this system is definitely well separated and there are no reasons to assume the presence of mass exchange. Due to the excellent definition of the light curves and the very satisfactory fit at all other phases, it is not likely that this problem will have significant effects on the validity of parameter determination.

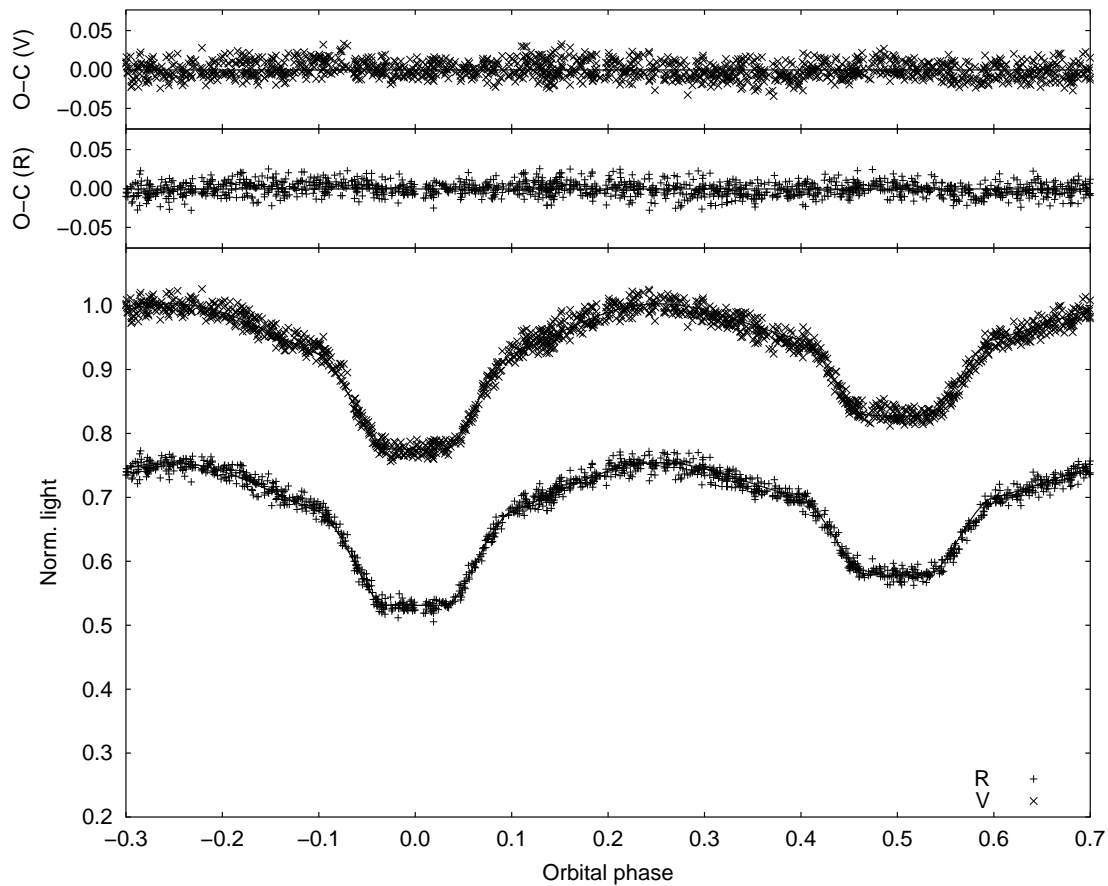


Figure 3.43: *V* and *R* light curves of MACHO 397 (05:26:03.5–69:26:38) shown together with best fits for mass ratio $q = 0.5$. For clarity, error bars of the individual data points are omitted and the *R* light curve is shifted down 0.25 light units.

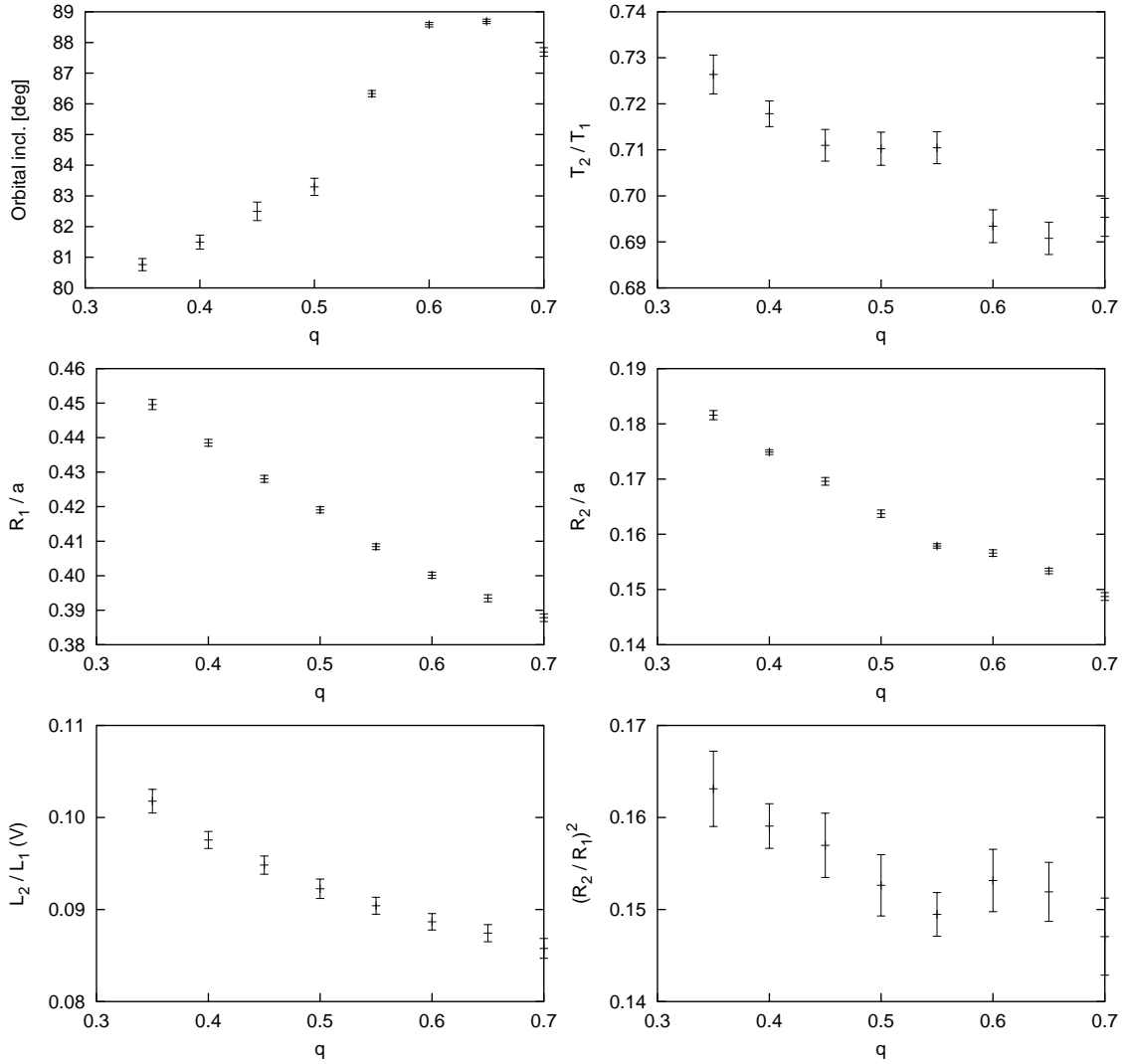


Figure 3.44: Final parameters of MACHO 397 (05:26:03.5–69:26:38) for different values of mass ratio q plotted together with their 1σ bootstrap errors.

The q -dependencies of the parameters show very interesting departures from the usual relationships (See Fig. 3.44). The relative radius of the primary component behaves in a conventional way, i. e. it decreases with increasing mass ratio in order to counteract growing tidal distortion. The other parameters however exhibit a completely unusual behavior, which is mainly caused by the large difference in size and the presence of total eclipses. As can be seen from the near-constant $(R_2/R_1)^2$ value, the relative stellar sizes cannot vary with changing mass ratio. This is due to the duration of the total and annular eclipses defining these relative sizes. Therefore, R_2 must decrease simultaneously with R_1 . This leads to a larger orbital separation of the components. With constant orbital inclination, this would result in a reduction of the depth of both eclipse minima. Counteraction of this effect is accomplished by the inclination to rise with increasing q , producing the correct minimum depths. From this consideration it is clear why no solutions were found for

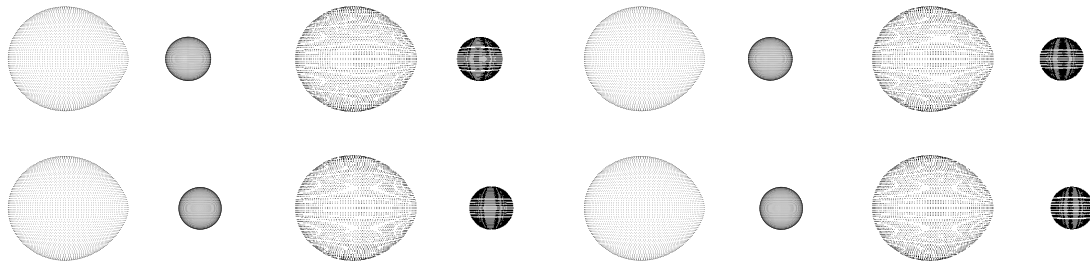


Figure 3.45: 3D plots of MACHO 397 (05:26:03.5–69:26:38) for mass ratio 0.35 (upper left) to 0.70 (lower right) with 0.05 increments.

$q > 0.7$: the inclination rises to nearly 90° at this mass ratio. A further decrease of the radii can therefore not be compensated by increasing orbital inclination anymore.

This is a very instructive example for how much insight into an eclipsing binary system can be gained by careful photometric analysis of the light curves and how much can be learned by a careful screening of the entire relevant parameter space. The favorable definition of the solution parameters in systems exhibiting total eclipses like this one make the discovery and thorough analysis of such binaries a top priority task.

MACHO 383 (05:25:02.5–68:31:12)

m_V [mag]	P [d]	σ	Conf.
15.2	0.9922025	0.007	DE & OC
– detached system just at inner contact – high orbital inclination – almost total eclipses – excellent definition of solutions			

MACHO 383 is a very interesting system due to the fact that it is at the edge of the classic “contact” configuration where both binary components accurately fill their Roche lobes, but do not have a common envelope yet. Moreover, the high orbital inclination yields almost total eclipses, which result in a parameter determination of unprecedented accuracy. The light curves show a significant out-of-eclipse variability and almost no well-defined ingress and egress points of the minima, indicating this system is indeed extremely close to an overcontact configuration. The measurements do not suffer from much scatter and the phase coverage is reasonably dense. An orbital period of 0.9922025 days was derived for this $m_V = 15.2$ mag eclipsing binary, along with a color index-based primary temperature of about 22000 K.

The assumption of main sequence components is not very likely to be correct in this case. Nevertheless, the temperature ratio of about 0.9 would be consistent with a mass ratio of roughly $q \approx 0.85$. Stars of spectral types B0.5 and B1 follow, with component masses of $M_1 \approx 12M_\odot$ and $M_2 \approx 10M_\odot$. The corresponding radii are $R_1 \approx 4.9R_\odot$ and $R_2 \approx 4.5R_\odot$, with an orbital separation of $a \approx 11.8R_\odot$, in close coincidence with the photometrically derived relative radii of the components. Of course, the expected effective temperatures of these kind of stars would lie in the region of 26000–28000 K. The reasons for the discrepancy to the color index-based temperatures must be sought in a possible underestimation of the local interstellar extinction and the limits of the empirical main sequence relations in application to close binary stars.

The light curve fits are mostly very good with a slight exception shortly after the primary minimum. In both passbands, there is a distinct rise of the observed light level over the synthetic light curves. Since this effect is asymmetric (it does not exist right before the primary minimum), it is probably due to a “hot spot” on the primary component, indicating possible slight mass transfer from the secondary component, hitting the primary

q	i [deg]	$T_{\text{eff},2}$ [K]	$L_1/(L_1 + L_2)$	$L_2/(L_1 + L_2)$	R_1/a	R_2/a
0.55	83.83 ± 0.28	19974 ± 105	0.678 ± 0.014	0.322 ± 0.014	0.4333 ± 0.0002	0.3283 ± 0.0004
0.60	82.75 ± 0.24	19995 ± 108	0.659 ± 0.015	0.341 ± 0.015	0.4255 ± 0.0002	0.3357 ± 0.0003
0.65	82.17 ± 0.15	20024 ± 94	0.642 ± 0.014	0.358 ± 0.014	0.4183 ± 0.0002	0.3424 ± 0.0004
0.70	81.58 ± 0.12	20059 ± 99	0.625 ± 0.015	0.375 ± 0.015	0.4116 ± 0.0003	0.3488 ± 0.0002
0.75	81.22 ± 0.13	20048 ± 109	0.610 ± 0.017	0.390 ± 0.017	0.4054 ± 0.0002	0.3547 ± 0.0002
0.80	81.12 ± 0.19	20071 ± 108	0.595 ± 0.017	0.405 ± 0.017	0.3996 ± 0.0003	0.3601 ± 0.0005
0.85	80.86 ± 0.21	20068 ± 110	0.582 ± 0.018	0.418 ± 0.018	0.3941 ± 0.0004	0.3655 ± 0.0004
0.90	80.74 ± 0.10	20122 ± 100	0.567 ± 0.017	0.433 ± 0.017	0.3891 ± 0.0003	0.3705 ± 0.0002
0.95	80.65 ± 0.10	20147 ± 92	0.555 ± 0.016	0.445 ± 0.016	0.3843 ± 0.0002	0.3750 ± 0.0005
1.00	80.54 ± 0.22	20169 ± 101	0.542 ± 0.018	0.458 ± 0.018	0.3797 ± 0.0002	0.3794 ± 0.0007

Table 3.14: Parameters of MACHO 383 (05:25:02.5–68:31:12) derived from the photometric analysis shown together with 1σ bootstrap errors.

at a spot being obscured during primary minimum ingress and becoming visible during egress. Otherwise, no discrepancies are found in the light curve fits.

Due to the special nature of this system, its parameters can be determined with excellent accuracy. The light curves in this marginally detached configuration is most sensitive against minimal parameter adjustments, since they have a great influence on component shapes. Additionally, the high orbital inclination amplifies the sensitivity of the light curves because any geometrical change is directly reflected by corresponding light curve changes and not dampened out through the $\sin i$ law. Unfortunately, the system does not have total eclipses, otherwise according to Terrell & Wilson (2005) a mass ratio could be deduced from the light curves alone, which is a very rarely met situation. Nevertheless, the range of mass ratio values is smaller in this case than it is usual for detached or overcontact systems of lower orbital inclination. To cover all possible cases, multiple runs of the light curve analysis procedure have been conducted for this system. Especially a possible (if slight) overcontact configuration was investigated thoroughly. Good solutions were indeed found when applying this restriction, too, but they consistently were of worse

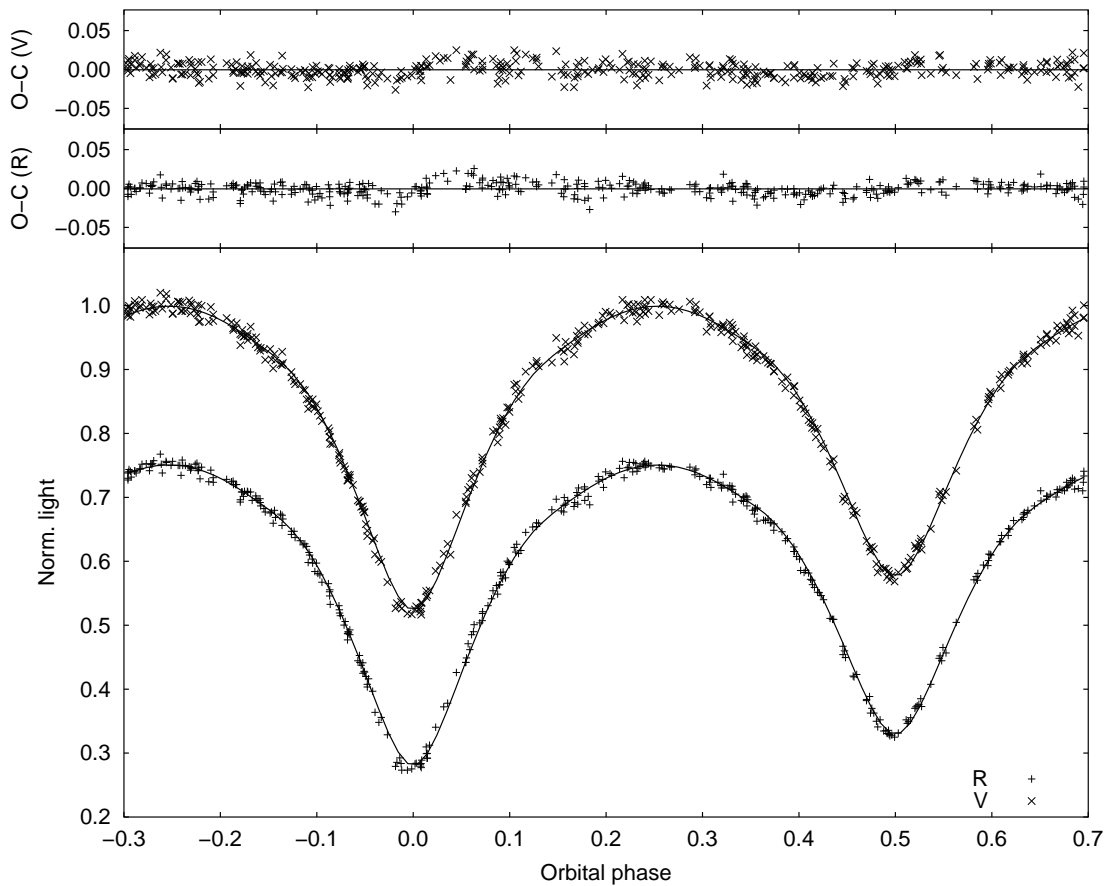


Figure 3.46: *V* and *R* light curves of MACHO 383 (05:25:02.5–68:31:12) shown together with best fits for mass ratio $q = 0.85$. For clarity, error bars of the individual data points are omitted and the *R* light curve is shifted down 0.25 light units.

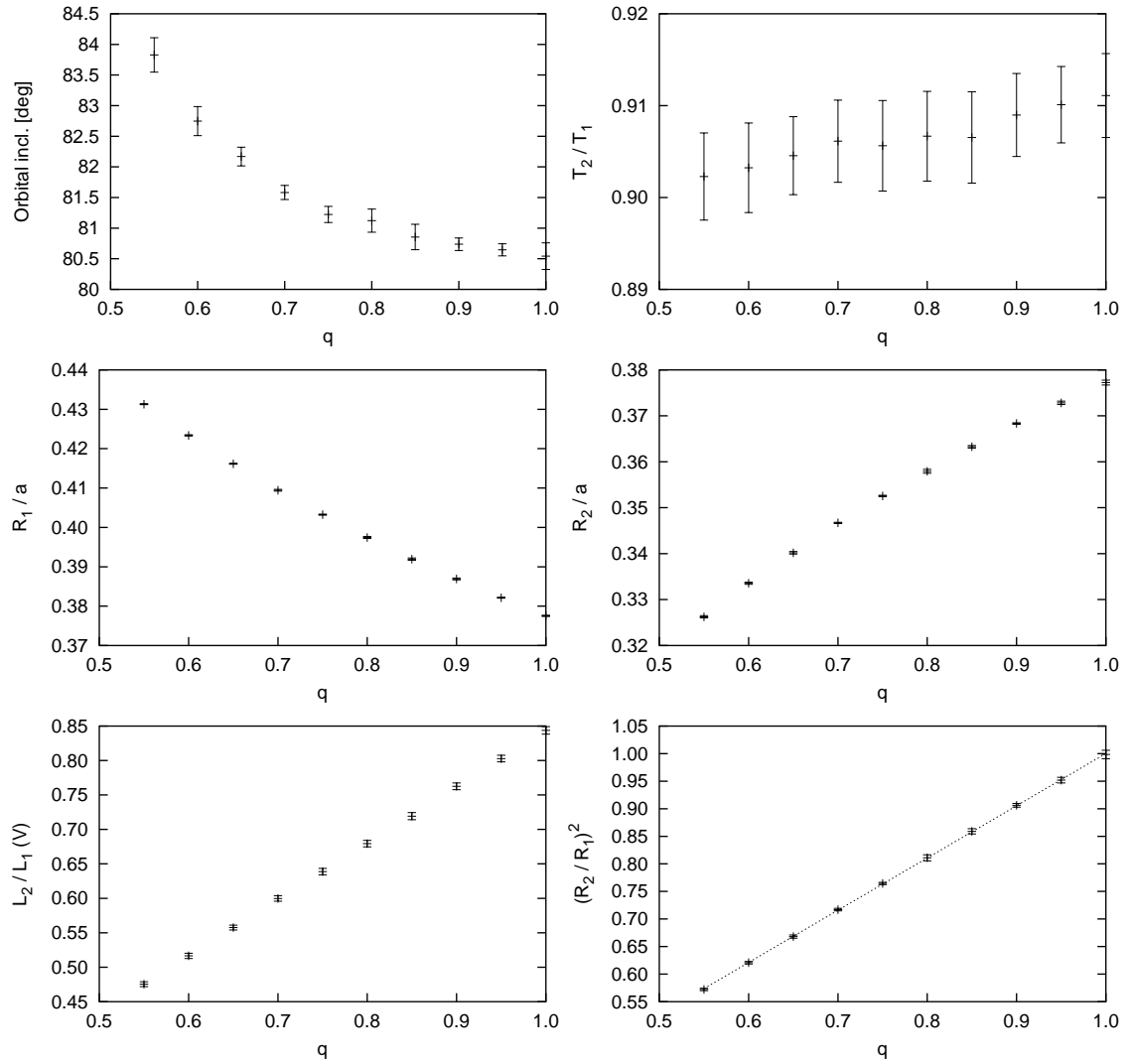


Figure 3.47: Final parameters of MACHO 383 (05:25:02.5–68:31:12) for different values of mass ratio q plotted together with their 1σ bootstrap errors.

numerical quality than those computed for the detached configuration. Also, they always tended to extremely marginal overcontact states where practically no “bottleneck” exists between the components. Therefore, the final solutions were calculated for a detached configuration, not ruling out a complete filling of both Roche lobes, though. 3D plots for both configurations are compared in Fig. 3.48.

The parameters follow the standard correlation with the mass ratio. There are no outliers and the bootstrap-derived error bars are extremely small, indicating a very high definiteness of the solutions. The fact that the light curves are not significantly above average (neither in scatter nor in phase coverage) drastically demonstrates the utmost importance of the actual configuration of the system when deriving parameters from the light curves. Or the other way around: even perfect light curves cannot resolve the multiple correlations of various stellar parameters if the system is in a well-detached configuration. Fur-

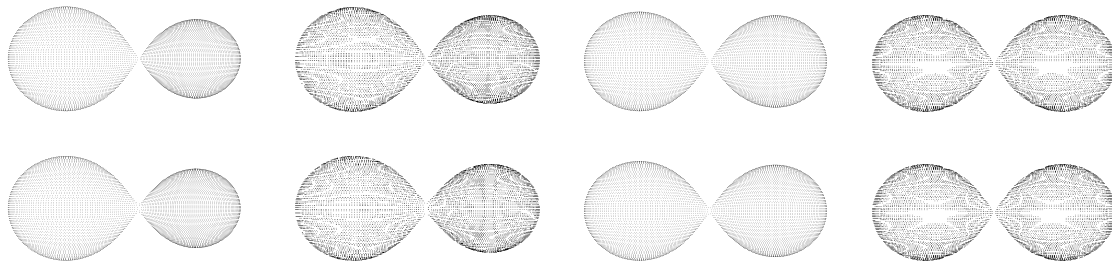


Figure 3.48: 3D plots of MACHO 383 (05:25:02.5–68:31:12) for mass ratio 0.55 to 1.00 and detached configuration (upper row) with 0.15 increments. Comparison plots with identical mass ratios are shown for overcontact configuration in the lower row.

ther constraints are always needed which are only found in unique systems like MACHO 383.

MACHO 002 (04:49:52.1–67:42:10)

m_V [mag]	P [d]	σ	Conf.
15.2	1.6330514	0.006	DE
– well-detached system			
– may contain evolved components			

MACHO 002 is a widely detached system. This becomes already clear upon a cursory inspection of the light curve, as it shows only little out-of-eclipse variability, indicating only slight tidal distortion. Additionally, the sizes of the components must be comparable and the orbital inclination must be high, since the eclipse minima show a light loss of almost 50%. Due to the similar components, no broad total eclipse minimum can be expected. With 1.6330514 days, the orbital period is relatively long. The apparent brightness of 15.2 mag yields light curves of good quality, with a little more scatter in the V than in the R band.

If main sequence or near-main sequence stars are assumed, a mass ratio of $q \approx 1$ seems appropriate due to the temperature ratio being near unity (both eclipses having equal depths). The main sequence relations fit best for a relatively wide system of orbital separation $a \approx 17R_\odot$. The relative radii derived through the photometric analysis yield component masses of $M_1 = M_2 \approx 13M_\odot$ and radii of $R_1 = R_2 \approx 5.2R_\odot$, corresponding to spectral type B0. The corresponding effective temperatures would lie around 29000 K. From the color index a primary temperature of 53000 K was derived which is of course way too high. Since the $V - R$ index becomes very insensitive against temperature variations in this range, a large temperature error follows even for small $E(B - V)$ variations. Additionally, the temperature difference can be explained by the likely overestimation of interstellar extinction.

The light curves are of reasonable quality with S/N being marginally better in R than in V . The derived fits are very satisfactory, no systematic errors seem to be present in the residuals. The good reproduction of both light curves throughout the whole phase range indicates that no complications like mass accretion or hot spots exist in the system. This is to be expected for a well-detached binary, of course. Small effects may be hidden in

q	i [deg]	$T_{\text{eff},2}$ [K]	$L_1/(L_1 + L_2)$	$L_2/(L_1 + L_2)$	R_1/a	R_2/a
0.50	87.03 ± 0.29	54670 ± 374	0.598 ± 0.026	0.402 ± 0.026	0.3290 ± 0.0008	0.2678 ± 0.0007
0.55	86.89 ± 0.21	54677 ± 178	0.595 ± 0.014	0.405 ± 0.014	0.3287 ± 0.0005	0.2685 ± 0.0007
0.60	86.26 ± 0.25	54581 ± 194	0.583 ± 0.014	0.417 ± 0.014	0.3250 ± 0.0004	0.2723 ± 0.0008
0.65	85.96 ± 0.18	54489 ± 213	0.573 ± 0.013	0.427 ± 0.013	0.3219 ± 0.0004	0.2751 ± 0.0006
0.70	85.41 ± 0.15	54708 ± 188	0.541 ± 0.013	0.459 ± 0.013	0.3125 ± 0.0003	0.2848 ± 0.0007
0.75	86.06 ± 0.21	53767 ± 206	0.582 ± 0.012	0.418 ± 0.012	0.3239 ± 0.0006	0.2731 ± 0.0007
0.80	85.28 ± 0.14	54314 ± 149	0.538 ± 0.011	0.462 ± 0.011	0.3119 ± 0.0003	0.2864 ± 0.0007
0.85	85.77 ± 0.20	53464 ± 188	0.570 ± 0.014	0.430 ± 0.014	0.3200 ± 0.0005	0.2769 ± 0.0007
0.90	85.50 ± 0.10	53609 ± 124	0.553 ± 0.010	0.447 ± 0.010	0.3152 ± 0.0004	0.2820 ± 0.0005
0.95	85.53 ± 0.10	53236 ± 173	0.556 ± 0.010	0.444 ± 0.010	0.3152 ± 0.0005	0.2810 ± 0.0005
1.00	85.14 ± 0.16	53754 ± 171	0.524 ± 0.013	0.476 ± 0.013	0.3071 ± 0.0006	0.2909 ± 0.0008

Table 3.15: Parameters of MACHO 002 (04:49:52.1–67:42:10) derived from the photometric analysis shown together with 1σ bootstrap errors.

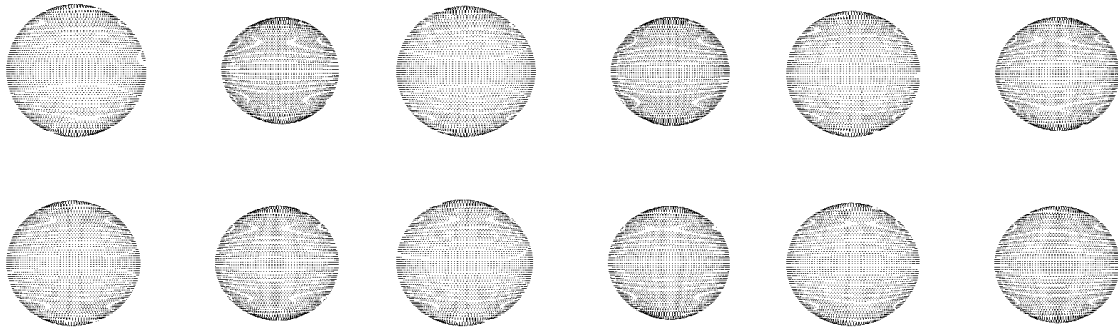


Figure 3.49: 3D plots of MACHO 002 (04:49:52.1–67:42:10) for mass ratio 0.5 (upper left) to 1.0 (lower right) with 0.1 increments.

the general scatter of the data points, but are not relevant to an analysis at this level of precision.

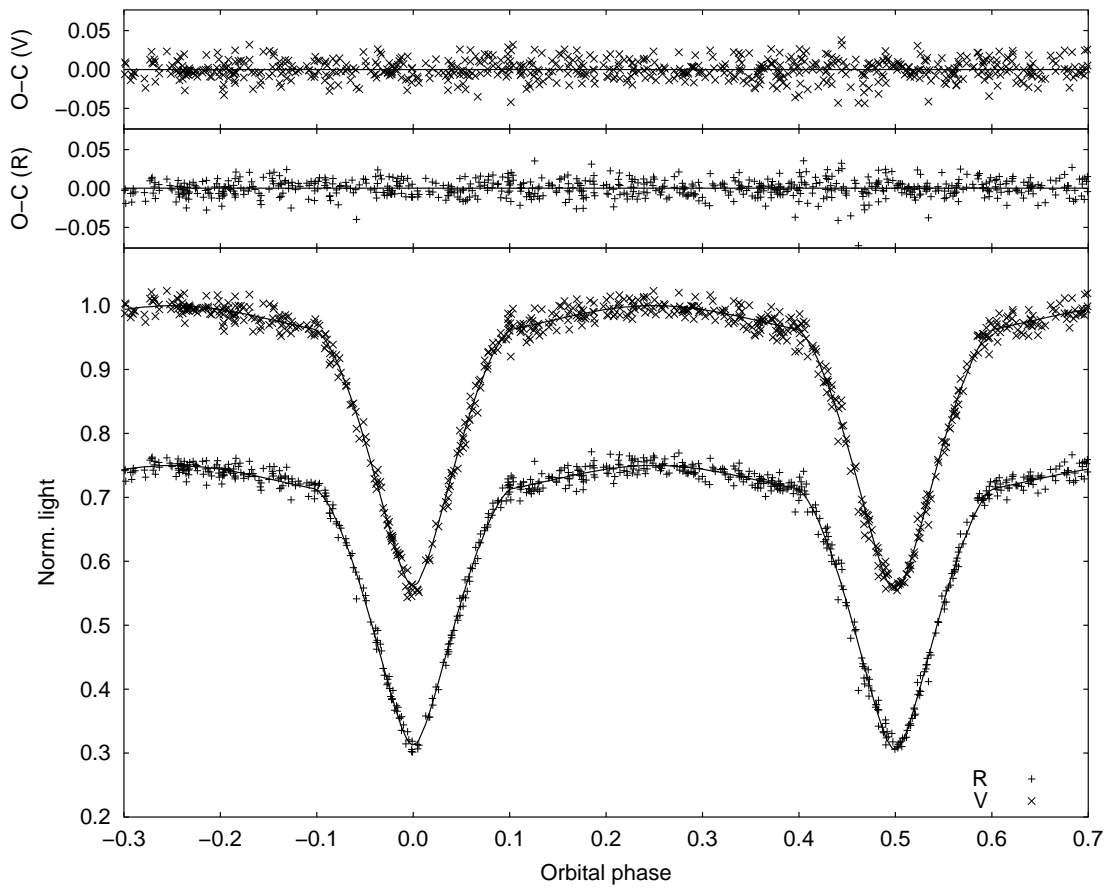


Figure 3.50: V and R light curves of MACHO 002 (05:21:00.7–69:29:46) shown together with best fits for mass ratio $q = 1.0$. For clarity, error bars of the individual data points are omitted and the R light curve is shifted down 0.25 light units.

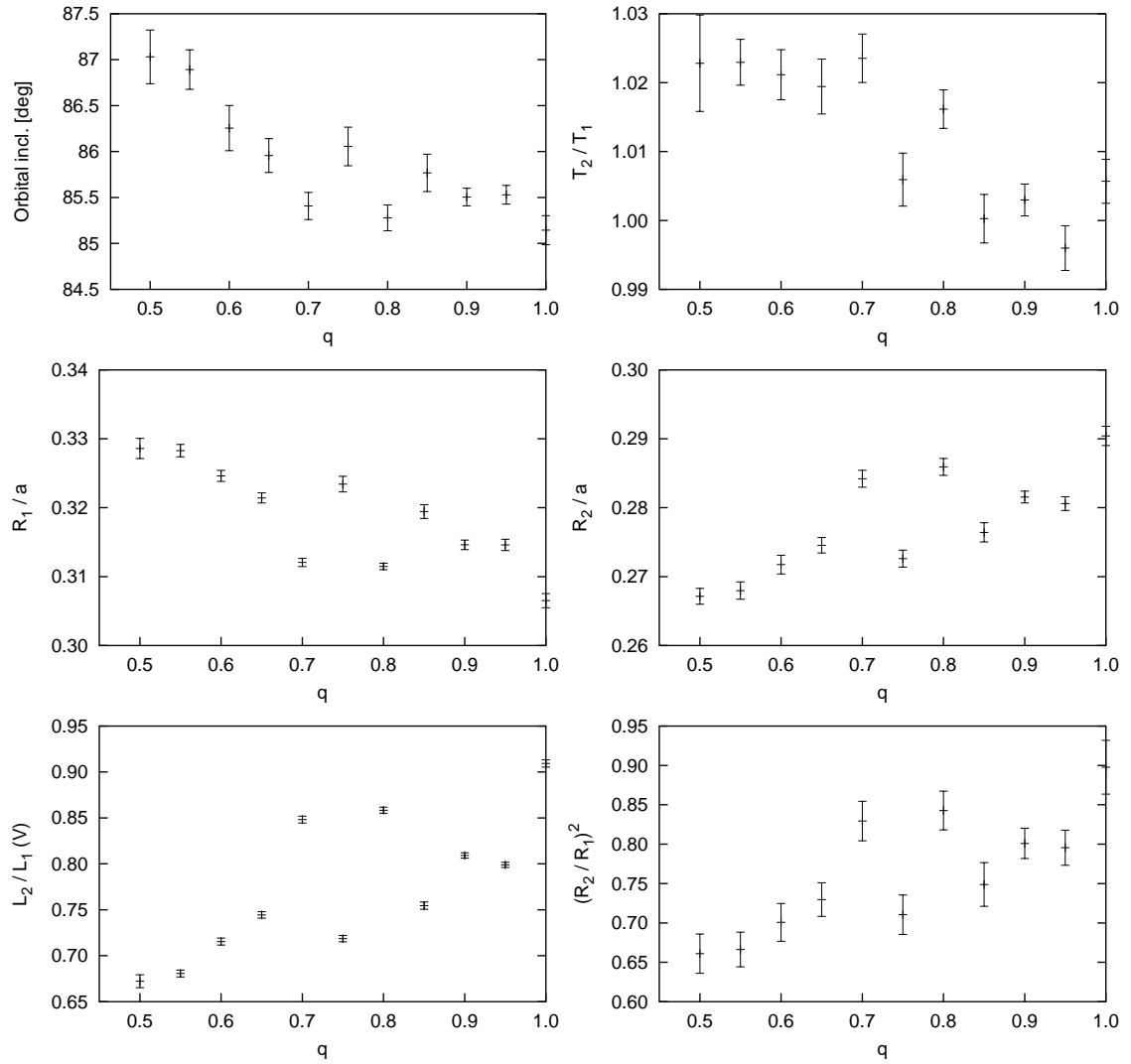


Figure 3.51: Final parameters of MACHO 002 (04:49:52.1–67:42:10) for different values of mass ratio q plotted together with their 1σ bootstrap errors.

The derived parameters show some interesting deviations from the usual q -dependencies. A slight tendency of the primary radius to decrease with increasing q can be observed, and vice versa for the radius of the secondary. Nevertheless, these changes remain small. Aside from the constraint of similar-sized components, large changes in radii are not necessary to compensate an increasing mass ratio, as not much tidal distortion is present in this system. Two departures from the optimal solution can be observed at $q = 0.75$ and $q = 0.85$ which are due to local minima in parameter space. The results and their small error bars show that even for a well-detached system well-defined solutions can be achieved when the light curves are sensitive to small adjustments, which is the case for this system with high orbital inclination and components of nearly equal size.

MACHO 530 (05:35:26.2–69:37:20)

m_V [mag]	P [d]	σ	Conf.
15.5	1.4739979	0.009	DE
– well-detached system – significant light curve scatter – possible slight eccentricity			

Just like MACHO 002 (see Section 3.7.3), MACHO 530 is a clearly detached system, as can be seen from the light curves which do not show strong signs of tidal distortion or other effects indicative of a closely interacting binary. Unlike MACHO 002, though, MACHO 530 shows relatively shallow eclipse minima of unequal depths. It is therefore obvious that the orbital inclination is lower and the components are of different size. The orbital period of 1.4739979 days shows that this well-detached system cannot consist of significantly evolved stars, while the apparent brightness of 15.5 mag explains at least in part the relatively high scatter of both available light curves, with R again displaying a slightly better quality than V .

It is reasonable to assume both components to be on or at least still near the main sequence. For this premise, the observed temperature ratio which was extracted from the relative depths of the eclipse minima points to a mass ratio of $q \approx 0.7$, which is well inside the covered mass ratio range. The photometrically derived relative radii are compatible with component masses of $M_1 \approx 7M_\odot$ and $M_2 \approx 5M_\odot$ with the appropriate radii of $R_1 \approx 3.7R_\odot$ and $R_2 \approx 3.1R_\odot$. With an orbital separation of $a \approx 11.5R_\odot$, the radii of the main sequence relations are actually somewhat larger than those derived by photometry. These values belong to stars of spectral types B2 and B4, corresponding to effective temperatures of about 21500 K and 17000 K. The temperatures found from the color index calibration are much higher, with a primary temperature of about 37000 K. The luminosity of a star with this temperature would of course not be compatible with the observed apparent brightness of $V = 15.5$ at the distance of the LMC. The reason for the discrepancy in

q	i [deg]	$T_{\text{eff},2}$ [K]	$L_1/(L_1 + L_2)$	$L_2/(L_1 + L_2)$	R_1/a	R_2/a
0.30	77.09 ± 0.26	28807 ± 230	0.790 ± 0.019	0.210 ± 0.019	0.3303 ± 0.0010	0.2061 ± 0.0016
0.35	77.05 ± 0.32	28396 ± 229	0.791 ± 0.022	0.209 ± 0.022	0.3284 ± 0.0008	0.2059 ± 0.0019
0.40	76.36 ± 0.20	28661 ± 234	0.770 ± 0.016	0.230 ± 0.016	0.3238 ± 0.0008	0.2147 ± 0.0013
0.45	75.60 ± 0.22	29110 ± 188	0.721 ± 0.018	0.279 ± 0.018	0.3071 ± 0.0006	0.2295 ± 0.0015
0.50	76.05 ± 0.22	28461 ± 186	0.757 ± 0.017	0.243 ± 0.017	0.3181 ± 0.0009	0.2188 ± 0.0014
0.55	75.97 ± 0.19	28346 ± 161	0.754 ± 0.013	0.246 ± 0.013	0.3159 ± 0.0009	0.2195 ± 0.0013
0.60	75.17 ± 0.24	29043 ± 213	0.694 ± 0.019	0.306 ± 0.019	0.2987 ± 0.0008	0.2380 ± 0.0017
0.65	74.93 ± 0.21	29393 ± 192	0.665 ± 0.019	0.335 ± 0.019	0.2914 ± 0.0008	0.2464 ± 0.0016
0.70	74.58 ± 0.21	29549 ± 179	0.606 ± 0.021	0.394 ± 0.021	0.2738 ± 0.0006	0.2632 ± 0.0016
0.75	74.85 ± 0.26	29312 ± 231	0.652 ± 0.024	0.348 ± 0.024	0.2872 ± 0.0009	0.2496 ± 0.0018
0.80	74.53 ± 0.22	29394 ± 227	0.611 ± 0.026	0.389 ± 0.026	0.2758 ± 0.0007	0.2624 ± 0.0016
0.85	74.58 ± 0.20	29406 ± 197	0.591 ± 0.026	0.409 ± 0.026	0.2693 ± 0.0009	0.2670 ± 0.0016
0.90	74.73 ± 0.24	29317 ± 284	0.587 ± 0.036	0.413 ± 0.036	0.2660 ± 0.0014	0.2662 ± 0.0017
0.95	74.46 ± 0.18	29457 ± 187	0.591 ± 0.029	0.409 ± 0.029	0.2710 ± 0.0007	0.2676 ± 0.0017
1.00	74.55 ± 0.23	29091 ± 211	0.608 ± 0.025	0.392 ± 0.025	0.2737 ± 0.0009	0.2628 ± 0.0018

Table 3.16: Parameters of MACHO 530 (05:35:26.2–69:37:20) derived from the photometric analysis shown together with 1σ bootstrap errors.

temperatures must again be sought in a probable overestimation of interstellar reddening due to the limited resolution of the extinction map provided by Schwering & Israel (1991). Also, the color-temperature-relation is of course very inaccurate for high temperatures like in this case.

MACHO 530 has light curves of acceptable quality with quite some scatter throughout the whole range of orbital phase. The synthetic light curves fit the observations generally well. Only during the secondary minimum there are some discrepancies which are indicative of a slight eccentricity of the system: both observed light curves seem to be shifted upwards in phase, indicated by the residuals during the entire secondary minimum. The deviation is not very strong, though, considering the significant scatter of the light curves.

The photometrically derived parameters show a conventional behavior with regard to the variation in mass ratio q . The slight tidal distortion of both stars necessitates a change of radii with increasing mass ratio, as the projected surface during quadrature phase of the primary component grows, while that of the secondary component decreases. The declining orbital inclination counteracts the eclipse minima becoming more equal in depth.

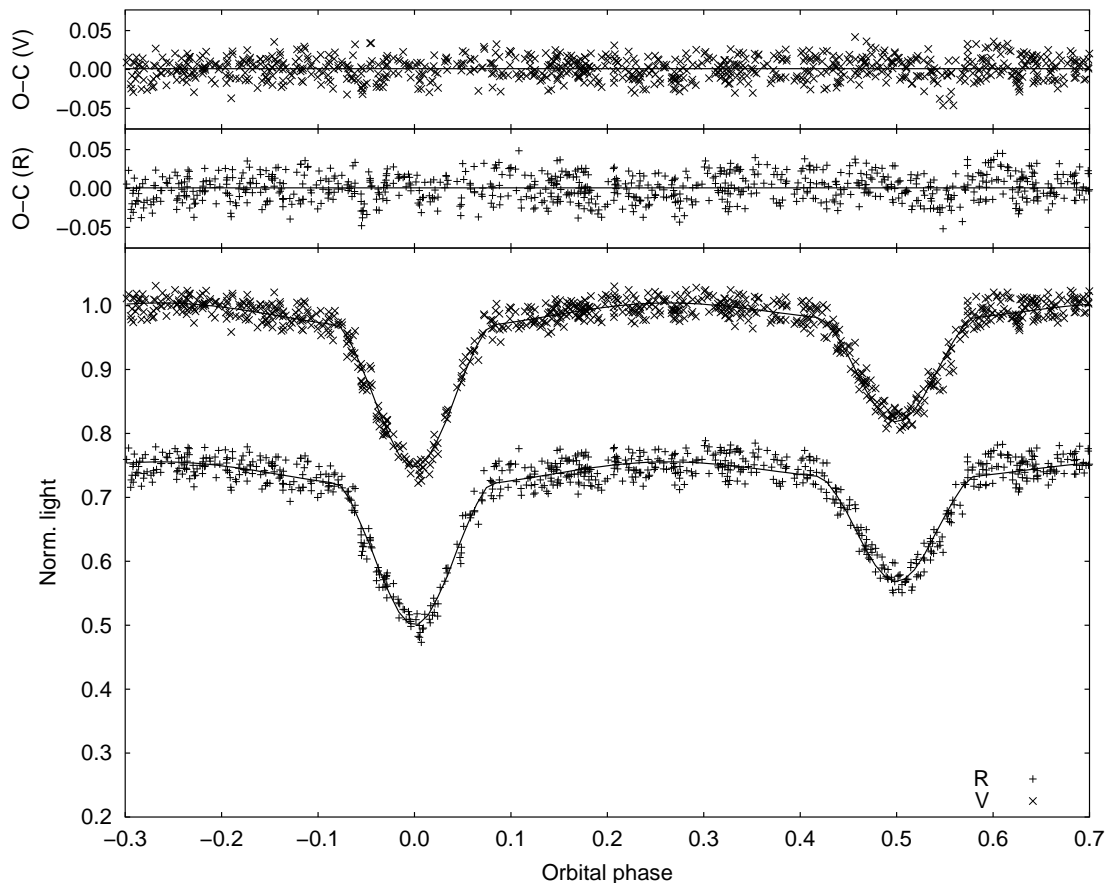


Figure 3.52: V and R light curves of MACHO 530 (05:35:26.2–69:37:20) shown together with best fits for mass ratio $q = 0.7$. For clarity, error bars of the individual data points are omitted and the R light curve is shifted down 0.25 light units.

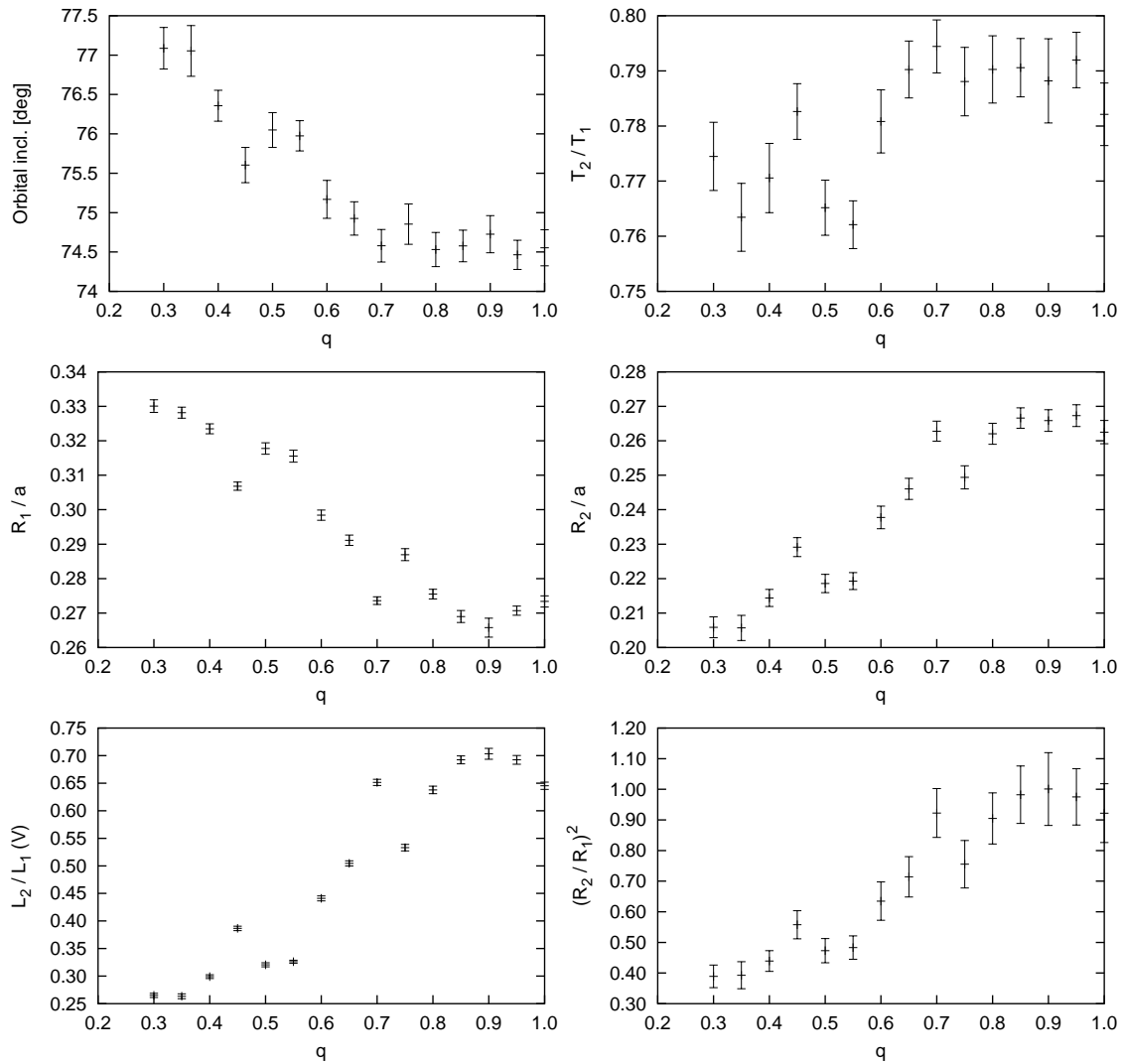


Figure 3.53: Final parameters of MACHO 530 (05:35:26.2–69:37:20) for different values of mass ratio q plotted together with their 1σ bootstrap errors.

for $q \rightarrow 1$. There are two sets of solution parameters at mass ratios $q = 0.45$ and

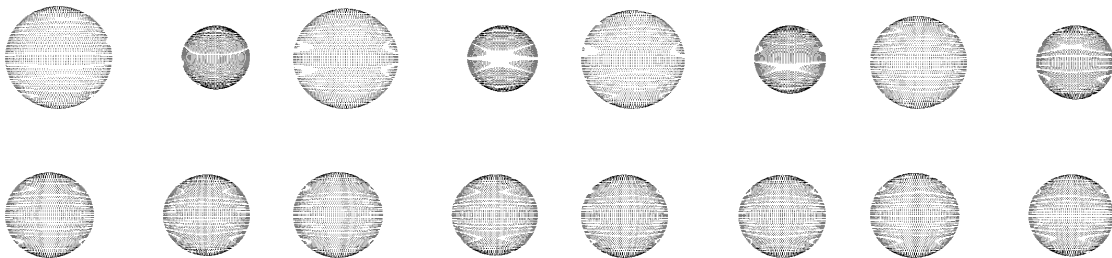


Figure 3.54: 3D plots of MACHO 530 (05:35:26.2–69:37:20) for mass ratio 0.3 (upper left) to 1.0 (lower right) with 0.1 increments.

$q = 0.70$ which somewhat deviate from the observed trends of the parameters. For many well-detached binaries, especially with noisier light curves, there is a tendency to end up in some local minimum of the parameter space near the optimum solution. It is a problem which cannot be easily alleviated due to the complex multiple parameter correlations. Light curves of better quality would help, but better constraints can be set in the less rugged parameter space of semi-detached and overcontact binaries. Nevertheless, in spite of relatively low orbital inclination, a possible slight eccentricity, and significant light curve scatter the definiteness of almost all parameters is still very good and again shows the power of photometric analysis if well-covered light curves like the MACHO ones are used.

MACHO 075 (05:04:51.0–70:08:59)

m_V [mag]	P [d]	σ	Conf.
15.4	1.1668692	0.005	DE
– marginally detached configuration – large temperature discrepancy – very low orbital inclination			

Like MACHO 383 (see Section 3.7.3), MACHO 075 is a good example for a system in a marginally detached configuration. In fact, it is so close that it cannot be decided unambiguously whether the system is detached or in a semi-detached state, and if the latter is the case, which of the components is filling its Roche lobe. In contrast to MACHO 383, part of this uncertainty may be due to the very low orbital inclination of $\sim 60^\circ$, apparent from the shallow minima with a light loss of only about 20%. Most of the solutions tend towards a slightly detached configuration. The components should be of similar temperature, due to the equal depths of the light curve minima. The period of this 15.4 mag system was determined as 1.1668692 days.

The extremely high effective temperature of about 86000 K derived for the primary component is certainly unrealistic because of the previously discussed problems with the applicability of the color-temperature relation to very early-type stars. In this case it is also unlikely that an overestimation of interstellar reddening can be claimed as a reason for the excessively high temperature. The value used is not much different from most other stars in this work. Like with MACHO 082 (see Section 3.7.2), the problem here could be in part due to the calibration of the observations.

If the assumption is made that both components are main sequence or near-main sequence components, more realistic values can be derived. The observed temperature ratio would then suggest a mass ratio of $q \approx 0.95$, leading to a binary with an orbital separation of $a \approx 15R_\odot$ and component masses of $M_1 \approx 17M_\odot$ and $M_2 \approx 16M_\odot$. The associated radii can be determined as $R_1 \approx 6.0R_\odot$ and $R_2 \approx 5.8R_\odot$. These values together with the or-

q	i [deg]	$T_{\text{eff},2}$ [K]	$L_1/(L_1 + L_2)$	$L_2/(L_1 + L_2)$	R_1/a	R_2/a
0.30	62.94 ± 0.21	81474 ± 1811	0.763 ± 0.034	0.237 ± 0.034	0.4864 ± 0.0013	0.2796 ± 0.0013
0.35	62.42 ± 0.14	80131 ± 510	0.741 ± 0.011	0.259 ± 0.011	0.4732 ± 0.0006	0.2912 ± 0.0009
0.40	61.67 ± 0.19	81232 ± 1063	0.713 ± 0.021	0.287 ± 0.021	0.4614 ± 0.0010	0.3021 ± 0.0008
0.45	61.58 ± 0.16	80588 ± 366	0.694 ± 0.009	0.306 ± 0.009	0.4506 ± 0.0006	0.3104 ± 0.0009
0.50	61.32 ± 0.20	81014 ± 328	0.672 ± 0.012	0.328 ± 0.012	0.4409 ± 0.0007	0.3184 ± 0.0012
0.55	61.16 ± 0.39	82282 ± 1153	0.642 ± 0.045	0.358 ± 0.045	0.4279 ± 0.0039	0.3280 ± 0.0010
0.60	60.63 ± 0.22	81496 ± 398	0.629 ± 0.012	0.371 ± 0.012	0.4234 ± 0.0009	0.3353 ± 0.0006
0.65	60.57 ± 0.20	81902 ± 482	0.610 ± 0.014	0.390 ± 0.014	0.4161 ± 0.0009	0.3418 ± 0.0009
0.70	60.49 ± 0.17	82553 ± 527	0.591 ± 0.015	0.409 ± 0.015	0.4087 ± 0.0008	0.3480 ± 0.0010
0.75	60.60 ± 0.18	82068 ± 198	0.585 ± 0.012	0.415 ± 0.012	0.4050 ± 0.0006	0.3496 ± 0.0013
0.80	60.37 ± 0.17	81757 ± 317	0.562 ± 0.010	0.438 ± 0.010	0.3961 ± 0.0009	0.3596 ± 0.0007
0.85	60.30 ± 0.17	81767 ± 279	0.548 ± 0.009	0.452 ± 0.009	0.3904 ± 0.0007	0.3652 ± 0.0007
0.90	60.25 ± 0.18	82373 ± 372	0.533 ± 0.012	0.467 ± 0.012	0.3858 ± 0.0009	0.3700 ± 0.0009
0.95	60.30 ± 0.19	82637 ± 392	0.524 ± 0.013	0.476 ± 0.013	0.3826 ± 0.0008	0.3725 ± 0.0013
1.00	60.44 ± 0.17	81943 ± 141	0.518 ± 0.010	0.482 ± 0.010	0.3795 ± 0.0004	0.3751 ± 0.0010

Table 3.17: Parameters of MACHO 075 (05:04:51.0–70:08:59) derived from the photometric analysis shown together with 1σ bootstrap errors.

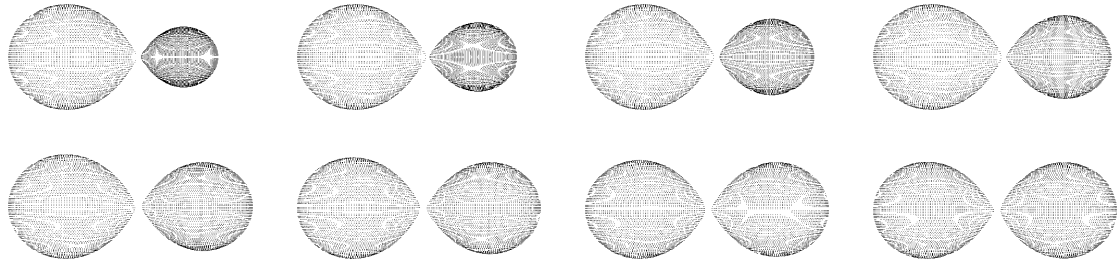


Figure 3.55: 3D plots of MACHO 075 (05:04:51.0–70:08:59) for mass ratio 0.3 (upper left) to 1.0 (lower right) with 0.1 increments.

bital separation nicely comply with the relative stellar radii derived from the photometric solution.

The light curves of MACHO 075 fit the observations with high precision. The measurements are of very good quality with only a small amount of scatter and excellent phase coverage. The residuals are evenly distributed and do not show any systematic trends.

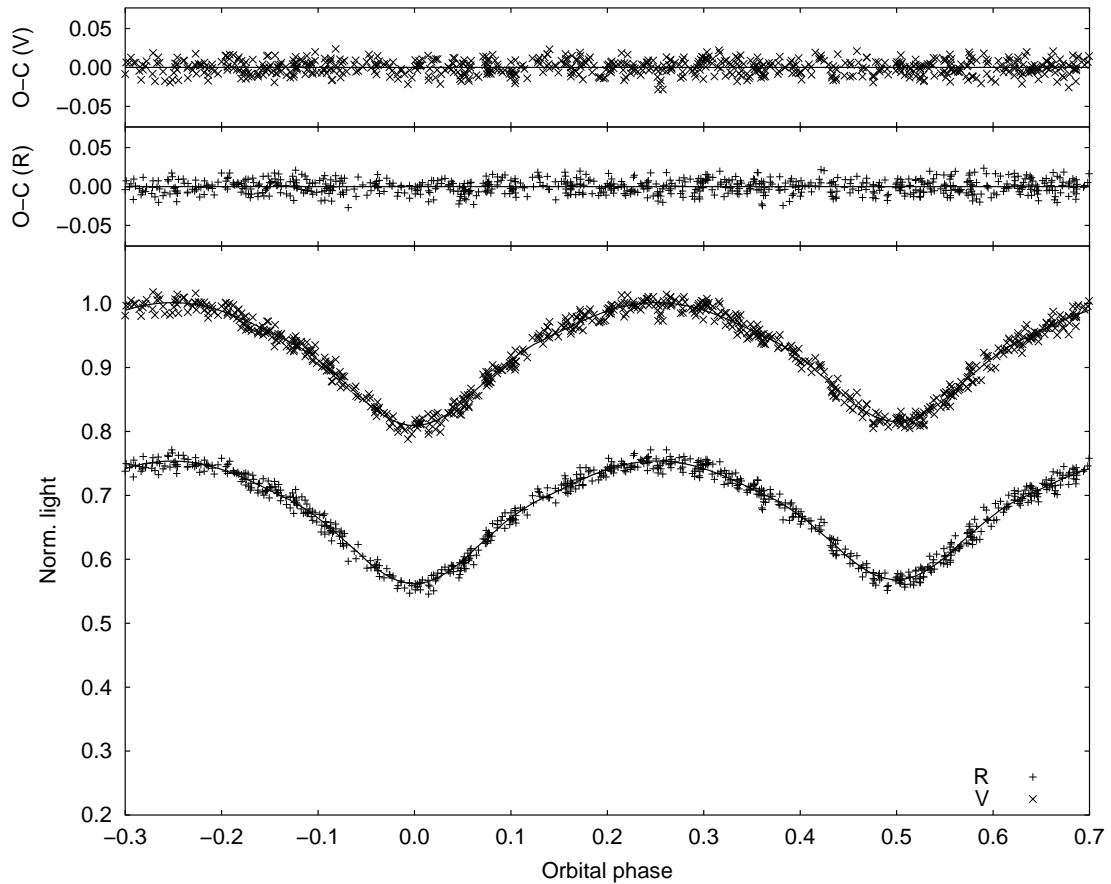


Figure 3.56: *V* and *R* light curves of MACHO 075 (05:04:51.0–70:08:59) shown together with best fits for mass ratio $q = 0.95$. For clarity, error bars of the individual data points are omitted and the *R* light curve is shifted down 0.25 light units.

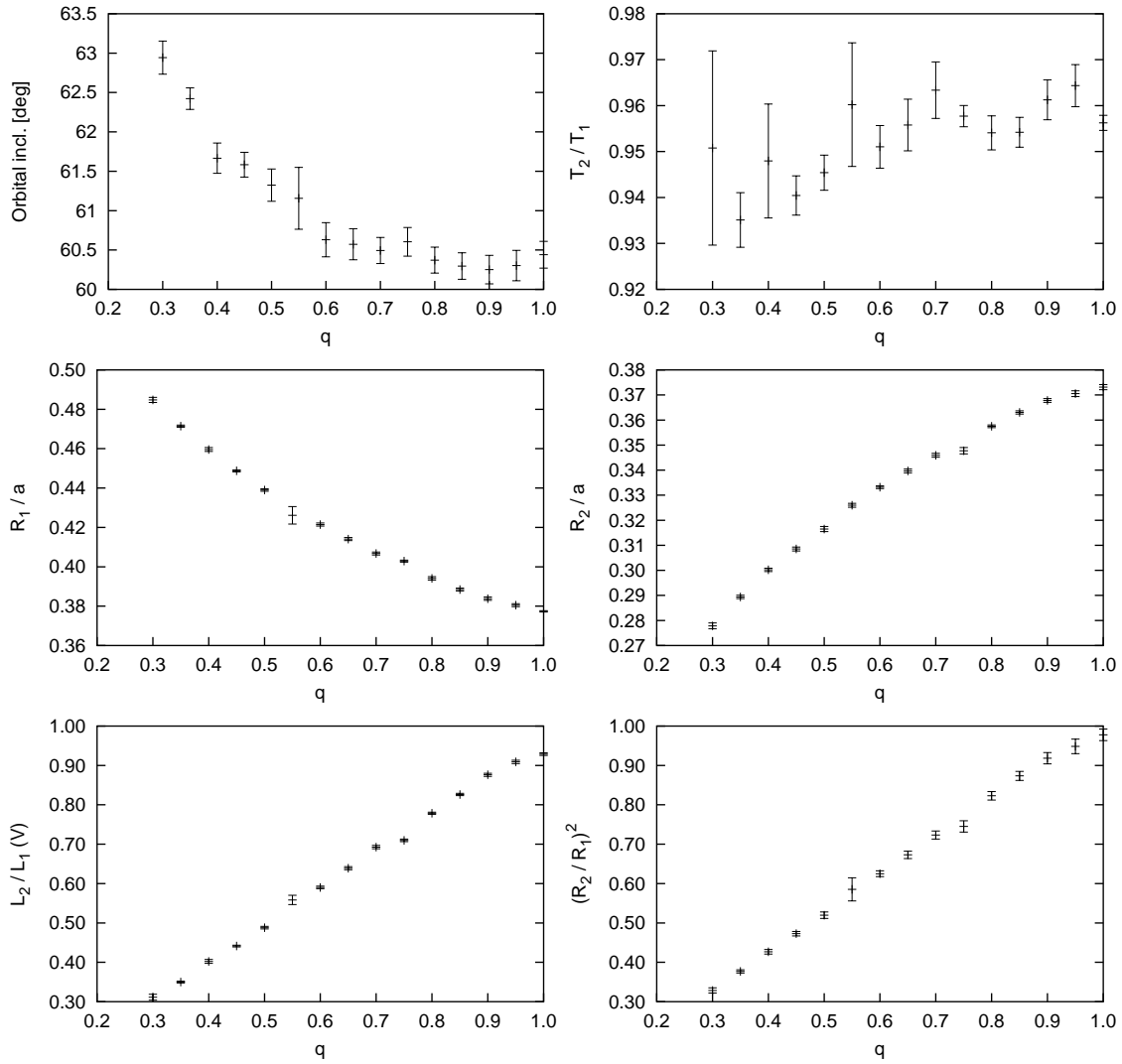


Figure 3.57: Final parameters of MACHO 075 (05:04:51.0–70:08:59) for different values of mass ratio q plotted together with their 1σ bootstrap errors.

The parameters exhibit the usual dependencies on the mass ratio. Very small error bars are also caused by the fortuitous fact that the system is found in a near-contact configuration. Due to the large tidal distortions, the light curves react sensitively to changes in the radii. Therefore these can be precisely determined, while other parameters like the orbital inclination and the temperature ratio are more uncertain, probably due to the low inclination which reduces the light curve sensitivity against variations of these parameters. Convergence to local minima in the parameter space becomes more likely, as can be seen for $q = 0.30$, $q = 0.40$ and $q = 0.55$.

MACHO 240 (05:15:41.5–70:04:39)

m_V [mag]	P [d]	σ	Conf.
15.5	1.7610180	0.008	DE
– well-detached configuration			
– total eclipse minima			
– constraints for relative stellar radii			

MACHO 240 is a very interesting example of a well-detached binary. Together with MACHO 397 it is the only binary analyzed in this work which unambiguously exhibits total eclipses. Their presence greatly supports the definiteness of the photometric analysis. Of course, due to the total eclipses the system must be seen at very high orbital inclination. The moderate light loss during minima therefore points to components with quite a large difference in size. The apparent brightness during quadrature phases is $V = 15.5$ mag and the orbital period was determined as 1.7610180 days which is long enough to accommodate the massive components within their Roche lobes. The color index suggests a primary temperature of about 50000 K.

Assuming near-main sequence components the observed ratio of temperatures suggests a mass ratio of $q \approx 0.7$. This yields massive stars with $M_1 \approx 30M_\odot$ and $M_2 \approx 21M_\odot$ and associated radii of $R_1 \approx 8.8R_\odot$ and $R_2 \approx 5.6R_\odot$. These values correspond well with the relative radii derived from the photometric analysis. The high temperatures of O7 and O8 stars indicated by the mass values match reasonably well the color index calibration: 39000 K and 35000 K would be expected, while a primary temperature of 50000 K was derived. The deviation might be due to an overestimated interstellar reddening. A high value of $E(B - V) = 0.12$ is found at the particular position of MACHO 240.

The observations of MACHO 240 are somewhat noisy at all orbital phases. Like is often the case, the R band data is of slightly better quality than the V band data. The phase coverage is very good. It is therefore possible to judge deviations from the optimum fit quite easily. Generally the fits are good.

q	i [deg]	$T_{\text{eff},2}$ [K]	$L_1/(L_1 + L_2)$	$L_2/(L_1 + L_2)$	R_1/a	R_2/a
0.35	84.04 ± 0.70	49443 ± 255	0.690 ± 0.016	0.310 ± 0.016	0.3888 ± 0.0011	0.2631 ± 0.0013
0.40	84.03 ± 0.70	48674 ± 222	0.694 ± 0.016	0.306 ± 0.016	0.3891 ± 0.0012	0.2622 ± 0.0013
0.45	84.11 ± 0.58	47785 ± 183	0.702 ± 0.013	0.298 ± 0.013	0.3911 ± 0.0009	0.2603 ± 0.0011
0.50	84.12 ± 0.42	47556 ± 200	0.705 ± 0.011	0.295 ± 0.011	0.3905 ± 0.0008	0.2581 ± 0.0008
0.55	88.53 ± 0.17	46790 ± 224	0.711 ± 0.011	0.289 ± 0.011	0.3805 ± 0.0008	0.2495 ± 0.0007
0.60	84.36 ± 0.56	46587 ± 178	0.711 ± 0.012	0.289 ± 0.012	0.3859 ± 0.0010	0.2535 ± 0.0010
0.65	84.58 ± 0.64	46332 ± 208	0.714 ± 0.015	0.286 ± 0.015	0.3838 ± 0.0009	0.2505 ± 0.0011
0.70	85.55 ± 0.67	46250 ± 158	0.715 ± 0.018	0.285 ± 0.018	0.3789 ± 0.0008	0.2462 ± 0.0011
0.75	86.01 ± 0.46	45815 ± 147	0.719 ± 0.013	0.281 ± 0.013	0.3759 ± 0.0008	0.2431 ± 0.0008
0.80	79.71 ± 0.24	48080 ± 214	0.583 ± 0.015	0.417 ± 0.015	0.3539 ± 0.0006	0.3043 ± 0.0014
0.85	79.66 ± 0.29	48146 ± 211	0.573 ± 0.018	0.427 ± 0.018	0.3502 ± 0.0008	0.3069 ± 0.0015
0.90	79.43 ± 0.18	49636 ± 179	0.468 ± 0.015	0.532 ± 0.015	0.3156 ± 0.0004	0.3395 ± 0.0011
0.95	79.41 ± 0.18	49467 ± 216	0.469 ± 0.016	0.531 ± 0.016	0.3164 ± 0.0004	0.3398 ± 0.0011
1.00	79.53 ± 0.22	49724 ± 219	0.458 ± 0.016	0.542 ± 0.016	0.3134 ± 0.0005	0.3426 ± 0.0011

Table 3.18: Parameters of MACHO 240 (05:15:41.5–70:04:39) derived from the photometric analysis shown together with 1σ bootstrap errors.

This system offers a good opportunity to recognize the constraints, which the presence of total eclipses places on all the parameters, especially on the mass ratio q . Though good fits were only found in the range $0.35 \leq q \leq 0.75$, the results of some trial runs for higher mass ratio values are also shown in Table 3.18 and Fig. 3.59 as they are highly instructive. Only in the lower mass ratio range the synthetic light curves yield total eclipses. In this region the orbital inclination has high values around 84 to 85 deg with one exception at $q = 0.55$, which is probably again caused by a local minimum of the parameter space.

Due to the presence of total eclipses the relative radii are strongly determined, as is indicated by the near-constant value of $(R_2/R_1)^2$. For increasing mass ratio, the inner Lagrangian point shifts towards the primary component, which suffers a stronger tidal distortion. Therefore the radius must get gradually smaller to compensate for this change. On the other hand, due to the $(R_2/R_1)^2 = \text{const}$ constraint, R_2 cannot grow to counteract the diminishing distortion of the secondary star, but must decrease along with R_1 . At some point between $0.75 < q < 0.80$ in this case, the primary component would reach a Roche lobe-filling configuration. If q was increased beyond that point, $(R_2/R_1)^2$ could no longer

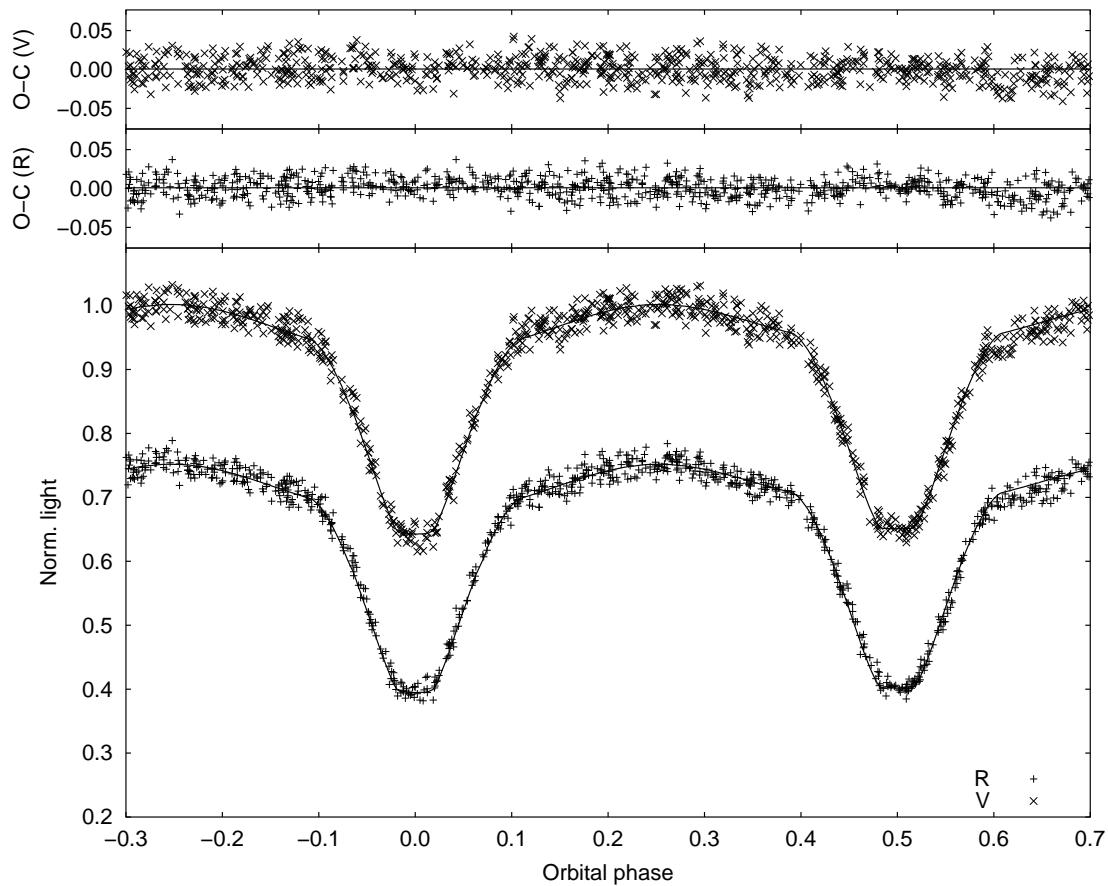


Figure 3.58: V and R light curves of MACHO 240 (05:15:41.5–70:04:39) shown together with best fits for mass ratio $q = 0.7$. For clarity, error bars of the individual data points are omitted and the R light curve is shifted down 0.25 light units.

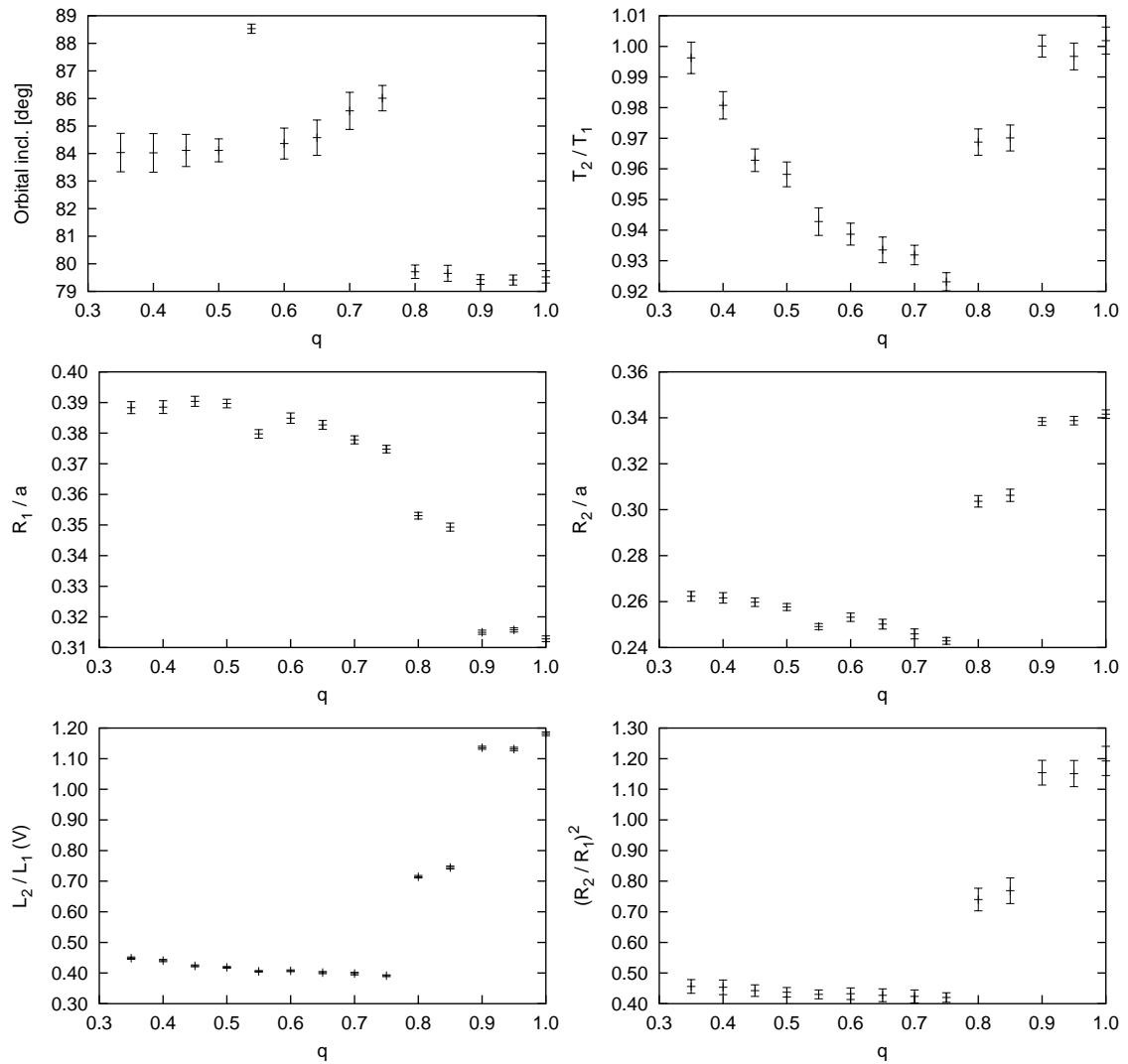


Figure 3.59: Final parameters of MACHO 240 (05:15:41.5–70:04:39) for different values of mass ratio q plotted together with their 1σ bootstrap errors.

be held constant. At this point, no fit of competitive quality can be achieved anymore. The

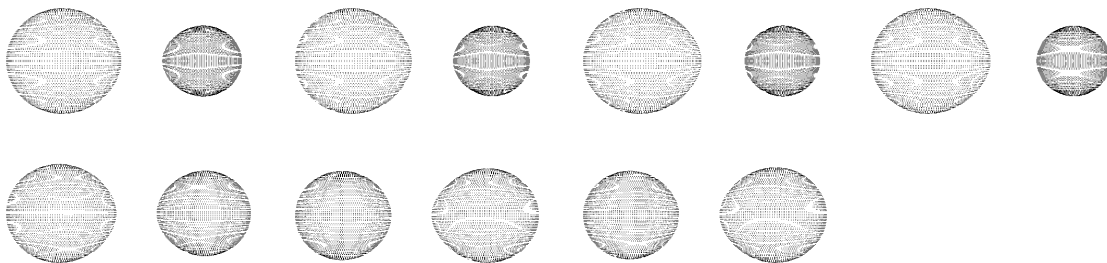


Figure 3.60: 3D plots of MACHO 240 (05:15:41.5–70:04:39) for mass ratio 0.4 (upper left) to 1.0 (lower right) with 0.1 increments.

best-fitting synthetic light curves are then produced after a drastic configuration change with components of similar size, but at a much lower inclination (see Fig. 3.59), which does not lead to total eclipses anymore. Therefore a solution in this region can be ruled out by the nature of the eclipse minima.

MACHO 074 (05:04:45.4–69:01:48)

m_V [mag]	P [d]	σ	Conf.
15.6	1.8176111	0.007	DE
– very close system with strong tidal distortion			
– high orbital inclination			
– relative stellar radii tightly constrained			

MACHO 074 is in a very close configuration where one of the stars almost fills its Roche lobe. Via the large loss of light during eclipses the light curves suggest a high orbital inclination (but not high enough to warrant total eclipses) and stellar companions of comparable size. The ingress and egress points of the minima are clearly defined, therefore the system must still be far from a contact configuration. For the observed apparent brightness of $V = 15.6$ mag the quality of the light curves is quite satisfactory. The relatively large orbital period of 1.8176111 days makes the orbit compatible with large, massive components.

If main sequence components are assumed, a mass ratio of $q \approx 1$ must be inferred due to the photometrically derived temperature ratio near unity. From the main sequence relations stars with high masses $M_1 = M_2 \approx 19M_\odot$ can be derived, which would require stellar radii of $R_1 = R_2 \approx 7.3R_\odot$. These values correspond to a spectral type of O9 with effective temperatures of about 33600 K. The color index calibration gives a primary temperature of 34000 K, which is in excellent agreement with the temperature derived from the standard main sequence relations.

The light curves of MACHO 074 are well-defined and show an acceptable amount of scatter for the observed brightness. The fits are mostly very good. During the eclipse minima the residuals exhibit a slight systematic trend which points at a somewhat inaccurate determination of minimum time. The effect is extremely small, though, and especially during the secondary minimum barely visible in the light curves. It surely does not affect the accuracy of the parameter determination which is dominated by other problems here.

q	i [deg]	$T_{\text{eff},2}$ [K]	$L_1/(L_1 + L_2)$	$L_2/(L_1 + L_2)$	R_1/a	R_2/a
0.35	84.71 ± 0.29	34421 ± 200	0.641 ± 0.019	0.359 ± 0.019	0.3813 ± 0.0011	0.2919 ± 0.0004
0.40	83.80 ± 0.23	34278 ± 165	0.626 ± 0.013	0.374 ± 0.013	0.3793 ± 0.0009	0.3001 ± 0.0012
0.45	83.15 ± 0.20	34158 ± 170	0.609 ± 0.012	0.391 ± 0.012	0.3751 ± 0.0007	0.3076 ± 0.0012
0.50	82.63 ± 0.15	34051 ± 146	0.590 ± 0.012	0.410 ± 0.012	0.3680 ± 0.0006	0.3146 ± 0.0010
0.55	82.58 ± 0.14	33708 ± 165	0.597 ± 0.013	0.403 ± 0.013	0.3734 ± 0.0005	0.3149 ± 0.0009
0.60	82.59 ± 0.18	33471 ± 154	0.592 ± 0.012	0.408 ± 0.012	0.3706 ± 0.0007	0.3168 ± 0.0008
0.65	82.05 ± 0.12	34067 ± 150	0.540 ± 0.013	0.460 ± 0.013	0.3513 ± 0.0006	0.3316 ± 0.0010
0.70	82.27 ± 0.14	33186 ± 146	0.569 ± 0.012	0.431 ± 0.012	0.3617 ± 0.0005	0.3251 ± 0.0009
0.75	82.09 ± 0.15	33266 ± 126	0.553 ± 0.011	0.447 ± 0.011	0.3563 ± 0.0005	0.3307 ± 0.0011
0.80	82.65 ± 0.15	32195 ± 168	0.613 ± 0.015	0.387 ± 0.015	0.3747 ± 0.0009	0.3100 ± 0.0009
0.85	82.67 ± 0.16	32012 ± 164	0.613 ± 0.013	0.387 ± 0.013	0.3729 ± 0.0008	0.3090 ± 0.0010
0.90	82.17 ± 0.19	32375 ± 164	0.565 ± 0.017	0.435 ± 0.017	0.3583 ± 0.0009	0.3273 ± 0.0013
0.95	82.89 ± 0.21	31395 ± 129	0.626 ± 0.012	0.374 ± 0.012	0.3722 ± 0.0008	0.3023 ± 0.0011
1.00	82.73 ± 0.18	31432 ± 140	0.617 ± 0.015	0.383 ± 0.015	0.3683 ± 0.0010	0.3046 ± 0.0011

Table 3.19: Parameters of MACHO 074 (05:04:45.4–69:01:48) derived from the photometric analysis shown together with 1σ bootstrap errors.

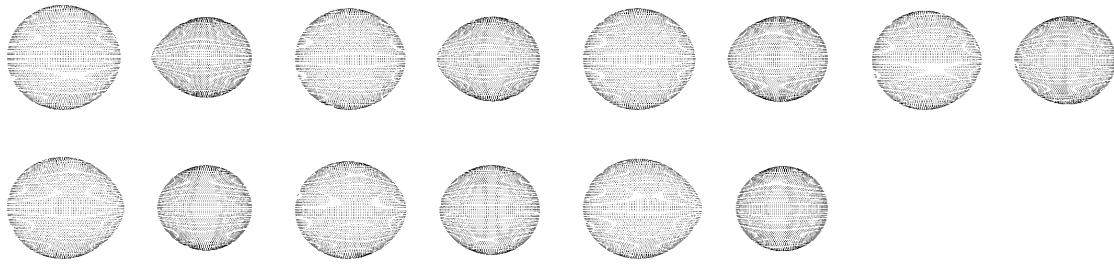


Figure 3.61: 3D plots of MACHO 074 (05:04:45.4–69:01:48) for mass ratio 0.4 (upper left) to 1.0 (lower right) with 0.1 increments.

The trends of the parameters with mass ratio q are generally normal, but especially the values of the relative radii are disrupted by many deviations from the expected scheme, mainly for medium values of the mass ratio. However, these discrepancies are small. This is due to the high inclination near the point of occurrence of total eclipses – where the radii are confined to a narrow range. Therefore the temperature ratio must change

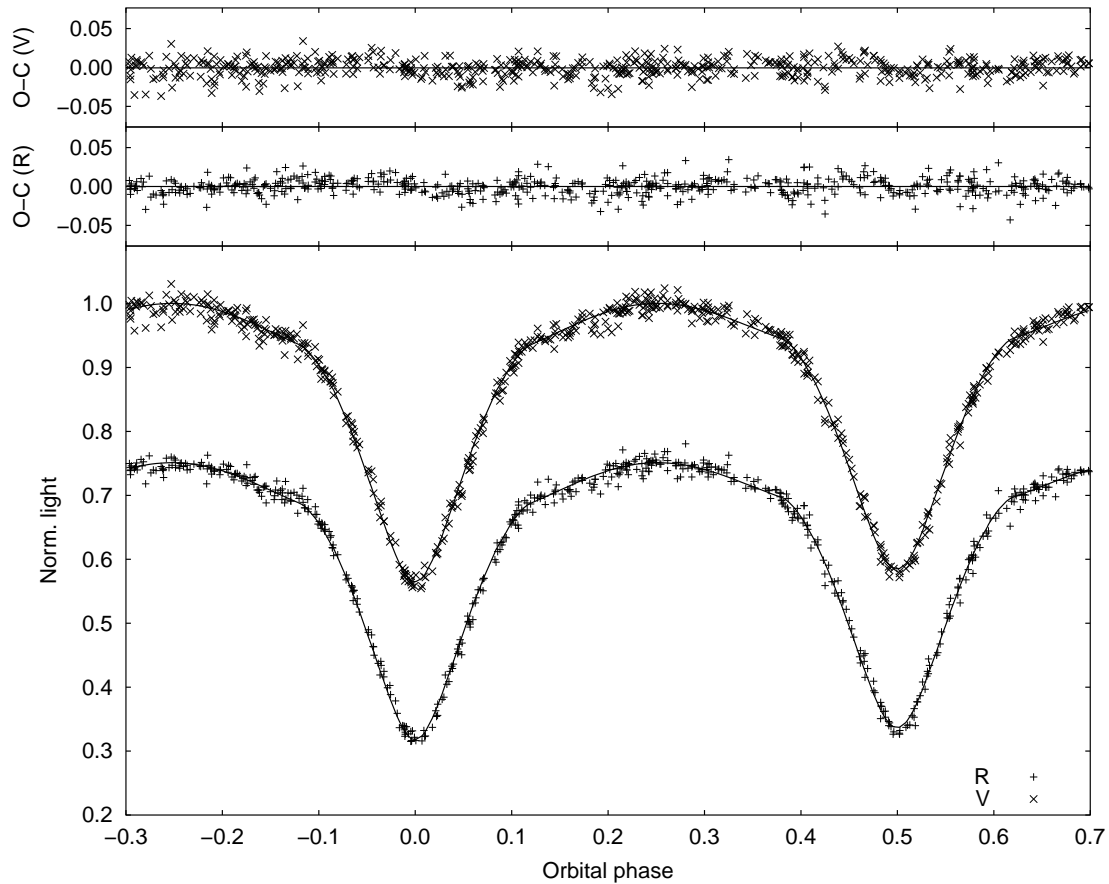


Figure 3.62: V and R light curves of MACHO 074 (05:04:45.4–69:01:48) shown together with best fits for mass ratio $q = 1.0$. For clarity, error bars of the individual data points are omitted and the R light curve is shifted down 0.25 light units.

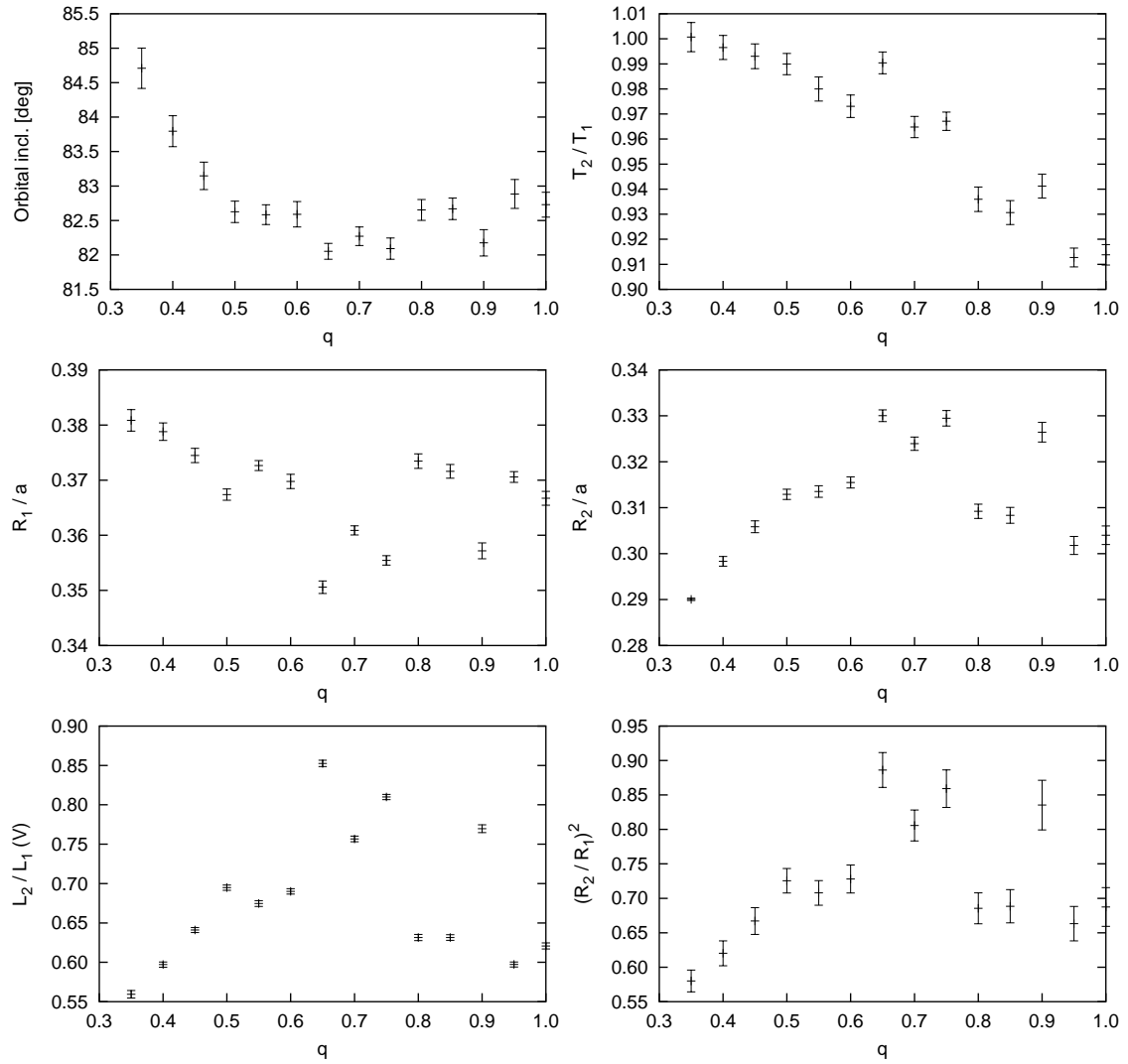


Figure 3.63: Final parameters of MACHO 074 (05:04:45.4–69:01:48) for different values of mass ratio q plotted together with their 1σ bootstrap errors.

to counteract the varying tidal distortion with increasing q in this case. Of course, the influence of this parameter is very limited due to the relative eclipse depths constraining its value. With increasing q , the secondary becomes less distorted, while the shape of the primary approaches gradually its critical lobe.

MACHO 421 (05:28:08.9–69:27:35)

m_V [mag]	P [d]	σ	Conf.
15.7	1.5778154	0.006	DE
– widely detached system – very good light curve fits – only weak parameter constraints possible			

MACHO 421 shows a distinctly detached configuration where the two components are very well separated. It is clear that this configuration will somewhat hamper precise parameter determination without spectroscopic data, since the ambiguity of the light curves with respect to many stellar parameters increases with separation, due to the lack of sensitivity of tidal distortion against parameter changes. With stellar radii of similar size, it is obvious that the light loss of only about 20% during both minima implies quite a low orbital inclination. The quality of the light curves is good, considering the apparent brightness of $V = 15.7$ mag. The phase coverage is not complete, with a few gaps in the descending branches of both eclipse minima.

With the derived orbital period of 1.5778154 days and under the assumption of both components being close to the main sequence, the photometrically derived temperature ratio suggests a probable mass ratio of $q \approx 0.85$. Stellar masses of $M_1 \approx 12M_\odot$ and $M_2 \approx 10M_\odot$ follow, resulting in component radii of $R_1 \approx 4.8R_\odot$ and $R_2 \approx 5.3R_\odot$. With an orbital separation of $a \approx 16R_\odot$ inferred from Kepler’s Third Law (1.1), the relative radii derived from the light curves are rather well compatible with these values. It is doubtful whether the main sequence assumption holds in this case. It is well possible that both components may be evolved to a certain degree. There are other indications for this assumption: the estimated absolute stellar parameters imply hot stars of spectral types B0.5 and B1 in contrast to the color-based temperature calibration which gives a primary temperature of only 21000 K. Nevertheless, this may also be a problem connected with interstellar reddening. With a value of $E(B - V) = 0.08$ it is relatively low at the coordinates of

q	i [deg]	$T_{\text{eff},2}$ [K]	$L_1/(L_1 + L_2)$	$L_2/(L_1 + L_2)$	R_1/a	R_2/a
0.30	71.28 ± 0.17	19268 ± 90	0.648 ± 0.010	0.352 ± 0.010	0.3310 ± 0.0007	0.2687 ± 0.0008
0.35	70.79 ± 0.19	19000 ± 90	0.663 ± 0.015	0.337 ± 0.015	0.3460 ± 0.0010	0.2728 ± 0.0012
0.40	70.64 ± 0.13	19073 ± 87	0.617 ± 0.017	0.383 ± 0.017	0.3256 ± 0.0007	0.2835 ± 0.0009
0.45	70.55 ± 0.16	19310 ± 142	0.583 ± 0.050	0.417 ± 0.050	0.3155 ± 0.0016	0.2913 ± 0.0011
0.50	70.16 ± 0.15	18970 ± 50	0.603 ± 0.015	0.397 ± 0.015	0.3268 ± 0.0005	0.2925 ± 0.0011
0.55	70.10 ± 0.17	18985 ± 70	0.595 ± 0.018	0.405 ± 0.018	0.3258 ± 0.0005	0.2951 ± 0.0012
0.60	70.17 ± 0.19	19191 ± 89	0.535 ± 0.014	0.465 ± 0.014	0.3019 ± 0.0005	0.3082 ± 0.0012
0.65	70.04 ± 0.17	19133 ± 85	0.527 ± 0.018	0.473 ± 0.018	0.3013 ± 0.0005	0.3123 ± 0.0011
0.70	69.84 ± 0.16	18940 ± 71	0.546 ± 0.017	0.454 ± 0.017	0.3109 ± 0.0005	0.3109 ± 0.0010
0.75	69.85 ± 0.16	19044 ± 70	0.515 ± 0.014	0.485 ± 0.014	0.2996 ± 0.0004	0.3185 ± 0.0010
0.80	69.91 ± 0.16	19001 ± 70	0.500 ± 0.013	0.500 ± 0.013	0.2940 ± 0.0005	0.3231 ± 0.0012
0.85	69.76 ± 0.17	18952 ± 78	0.507 ± 0.015	0.493 ± 0.015	0.2991 ± 0.0005	0.3232 ± 0.0013
0.90	69.73 ± 0.16	18971 ± 59	0.490 ± 0.017	0.510 ± 0.017	0.2942 ± 0.0004	0.3282 ± 0.0012
0.95	69.68 ± 0.15	18896 ± 51	0.499 ± 0.016	0.501 ± 0.016	0.2981 ± 0.0004	0.3270 ± 0.0011
1.00	70.19 ± 0.14	19267 ± 54	0.431 ± 0.018	0.569 ± 0.018	0.2737 ± 0.0004	0.3401 ± 0.0011

Table 3.20: Parameters of MACHO 421 (05:28:08.9–69:27:35) derived from the photometric analysis shown together with 1σ bootstrap errors.

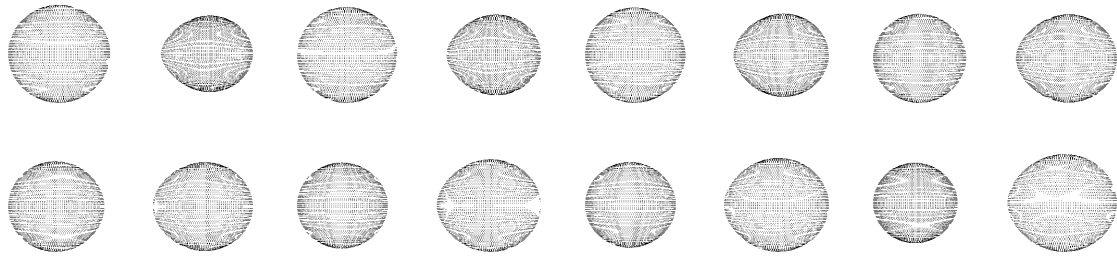


Figure 3.64: 3D plots of MACHO 421 (05:28:08.9–69:27:35) for mass ratio 0.3 (upper left) to 1.0 (lower right) with 0.1 increments.

MACHO 421. Due to the limited resolution of the reddening map used and a probably very low reddening in the immediate vicinity, the value may well be underestimated here. A higher reddening value would of course result in higher temperatures.

MACHO 421 shows light curves of good quality. As far as it can be judged, the fits are very good and do not show any systematic deviations from the observations. It can

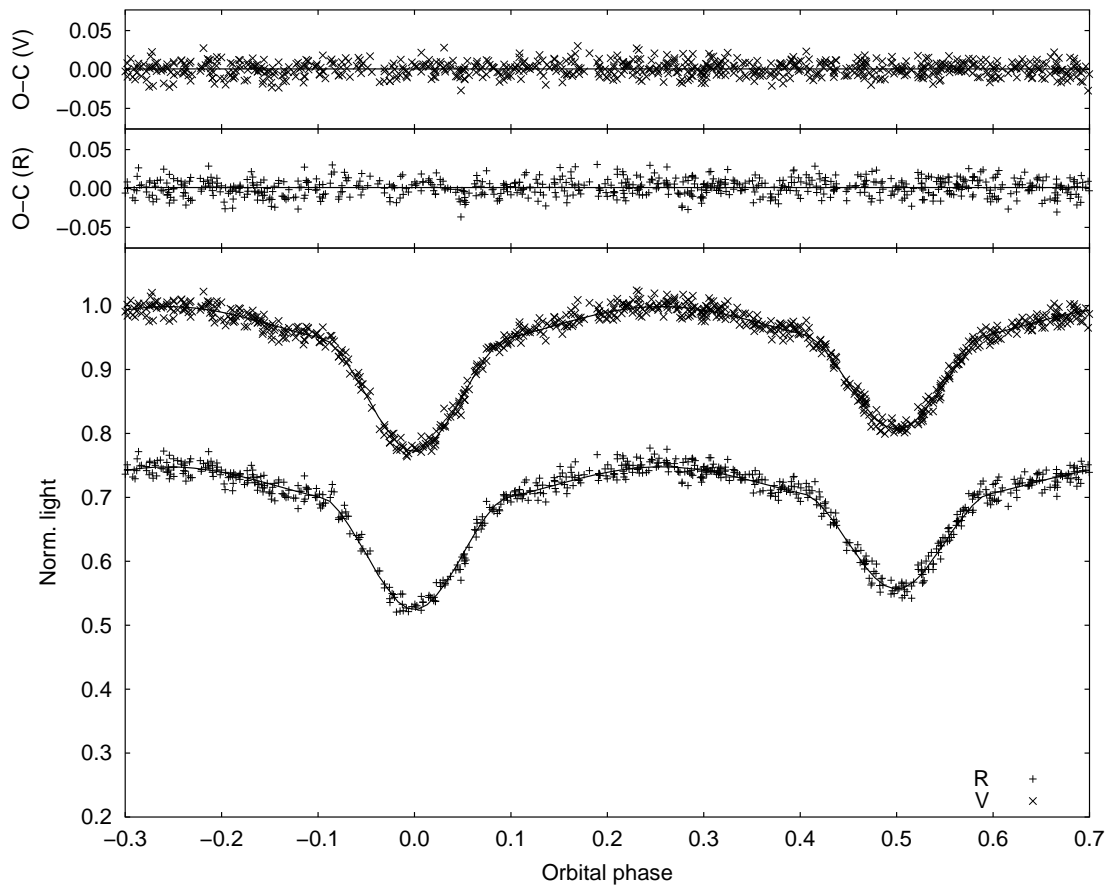


Figure 3.65: *V* and *R* light curves of MACHO 421 (05:28:08.9–69:27:35) shown together with best fits for mass ratio $q = 0.85$. For clarity, error bars of the individual data points are omitted and the *R* light curve is shifted down 0.25 light units.

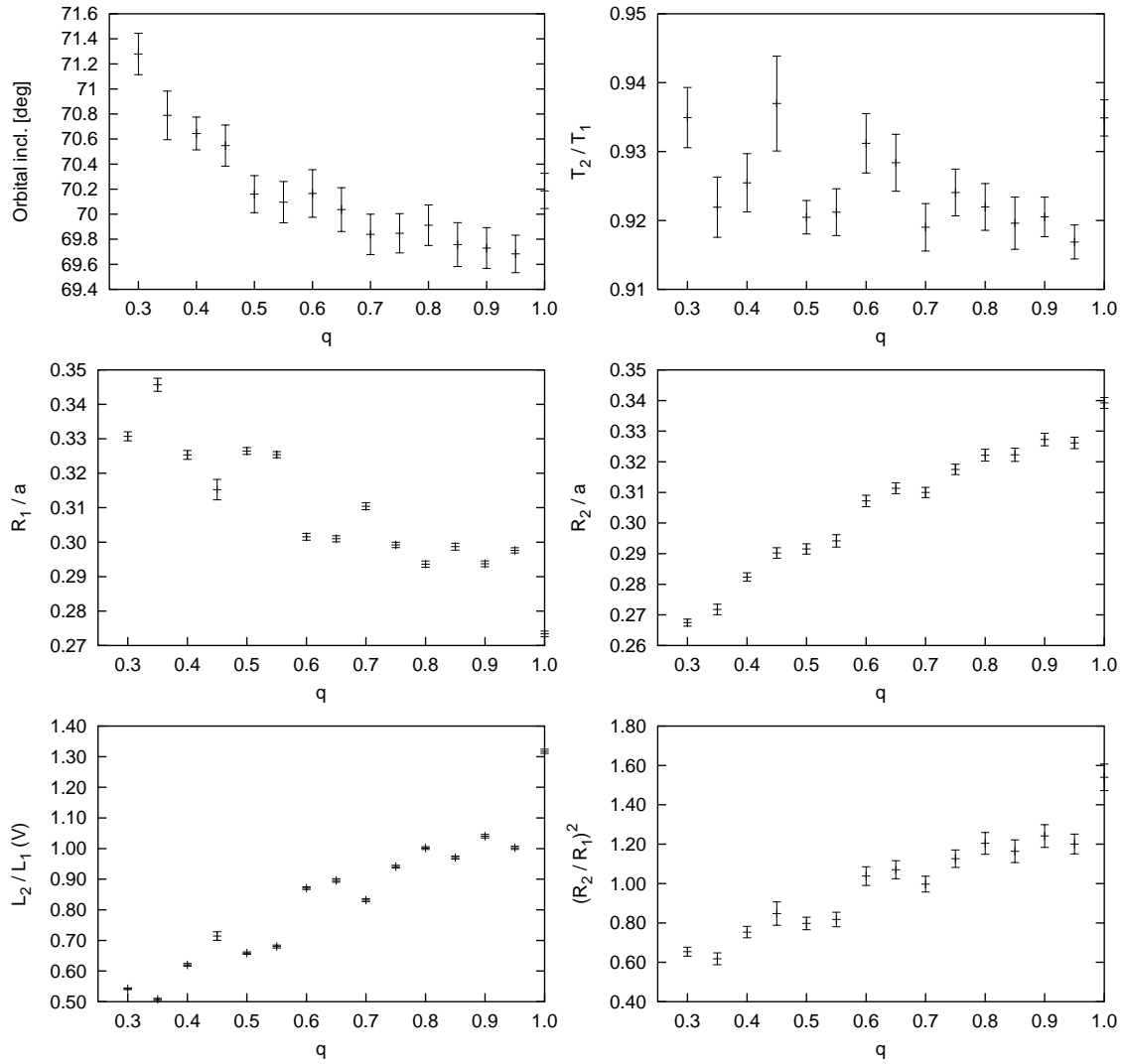


Figure 3.66: Final parameters of MACHO 421 (05:28:08.9–69:27:35) for different values of mass ratio q plotted together with their 1σ bootstrap errors.

therefore be safely concluded that no interaction effects are evident as expected in a widely separated binary like MACHO 421.

The parameters follow the usual trends with no conspicuous deviations except the larger error bars for $q = 0.45$. It is however clear that this type of system does not allow a definite determination of parameters due to the complicated structure of its parameter space. Additional constraints from the spectroscopic side would be necessary to achieve a unique solution.

MACHO 337 (05:21:34.4–69:31:28)

m_V [mag]	P [d]	σ	Conf.
15.9	1.1419771	0.008	DE
– very close, but still detached system – secondary component nearly filling Roche lobe – weak phase coverage, compared with other systems			

MACHO 337 is in a detached configuration, yet the secondary component suffers very strong tidal distortion and is very close to its Roche lobe at high mass ratios. The system has a relatively short orbital period of 1.1419771 days and shows light curves of good quality for its apparent quadrature brightness of $m_V = 15.9$ mag. However, there are a few gaps in phase. Actually, the phase coverage is among the worst of all systems analyzed in this work, but still adequate to allow for a detailed photometric analysis.

If once again main sequence stars are assumed, the observed temperature ratio implies a mass ratio of about $q \approx 0.7$. Through the main sequence relations and Kepler’s Third Law (1.1), stellar masses of $M_1 \approx 5.8M_\odot$ and $M_2 \approx 4.1M_\odot$ and radii of $R_1 \approx 3.3R_\odot$ and $R_2 \approx 3.6R_\odot$ can be derived. The orbital separation is $a \approx 10R_\odot$. These absolute parameters suggest the components to be stars with spectral types B3 and B6, corresponding to temperatures of about 18700 K and 14700 K. For the primary star a value of 20000 K follows from the color index, again being in line with the finding that the temperatures determined that way are usually to be regarded as upper limits.

The light curve fits are satisfactory and show no large-scale systematic discrepancies. More data points would be needed to better judge the actual quality of the fits in the ascending branch just after the primary minimum, and during the secondary minimum as well.

The parameters behave as expected for a close, yet detached system. The almost Roche lobe-filling condition of the secondary is reflected in the precise trends and small error

q	i [deg]	$T_{\text{eff},2}$ [K]	$L_1/(L_1 + L_2)$	$L_2/(L_1 + L_2)$	R_1/a	R_2/a
0.30	76.55 ± 0.22	15268 ± 98	0.793 ± 0.017	0.207 ± 0.017	0.4013 ± 0.0011	0.2801 ± 0.0006
0.35	75.54 ± 0.15	15339 ± 98	0.764 ± 0.018	0.236 ± 0.018	0.3859 ± 0.0010	0.2918 ± 0.0006
0.40	74.86 ± 0.21	15452 ± 102	0.731 ± 0.029	0.269 ± 0.029	0.3690 ± 0.0017	0.3025 ± 0.0004
0.45	74.40 ± 0.21	15495 ± 100	0.706 ± 0.029	0.294 ± 0.029	0.3584 ± 0.0016	0.3118 ± 0.0008
0.50	74.19 ± 0.14	15628 ± 88	0.672 ± 0.031	0.328 ± 0.031	0.3424 ± 0.0018	0.3202 ± 0.0008
0.55	73.67 ± 0.15	15604 ± 82	0.656 ± 0.020	0.344 ± 0.020	0.3384 ± 0.0013	0.3280 ± 0.0010
0.60	73.73 ± 0.22	15313 ± 68	0.685 ± 0.014	0.315 ± 0.014	0.3542 ± 0.0010	0.3240 ± 0.0021
0.65	73.21 ± 0.16	15715 ± 73	0.616 ± 0.015	0.384 ± 0.015	0.3256 ± 0.0010	0.3411 ± 0.0012
0.70	73.00 ± 0.18	15654 ± 66	0.617 ± 0.016	0.383 ± 0.016	0.3291 ± 0.0007	0.3443 ± 0.0015
0.75	72.84 ± 0.20	15497 ± 68	0.623 ± 0.022	0.377 ± 0.022	0.3329 ± 0.0007	0.3451 ± 0.0015
0.80	72.97 ± 0.27	15677 ± 64	0.594 ± 0.024	0.406 ± 0.024	0.3221 ± 0.0008	0.3517 ± 0.0020
0.85	72.91 ± 0.31	15712 ± 71	0.580 ± 0.025	0.420 ± 0.025	0.3180 ± 0.0007	0.3561 ± 0.0022
0.90	72.89 ± 0.31	15571 ± 61	0.595 ± 0.026	0.405 ± 0.026	0.3246 ± 0.0011	0.3533 ± 0.0023
0.95	72.79 ± 0.24	15733 ± 65	0.547 ± 0.026	0.453 ± 0.026	0.3058 ± 0.0009	0.3664 ± 0.0021
1.00	72.68 ± 0.25	15733 ± 68	0.530 ± 0.033	0.470 ± 0.033	0.2996 ± 0.0012	0.3720 ± 0.0023

Table 3.21: Parameters of MACHO 337 (05:21:34.4–69:31:28) derived from the photometric analysis shown together with 1σ bootstrap errors.

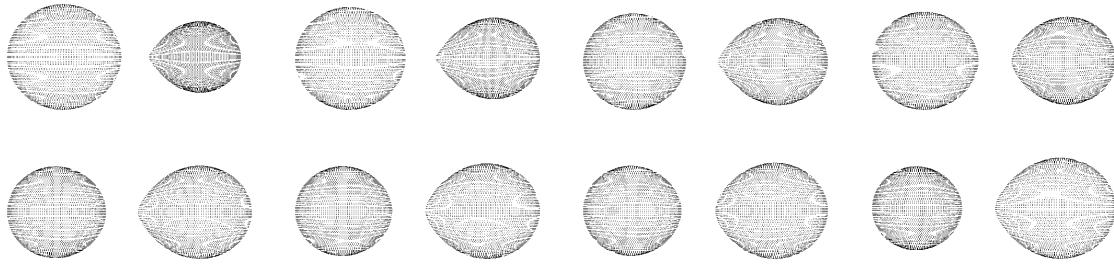


Figure 3.67: 3D plots of MACHO 337 (05:21:34.4–69:31:28) for mass ratio 0.3 (upper left) to 1.0 (lower right) with 0.1 increments.

bars of the relative radii. An outlier is observed at $q = 0.6$, but does not have large influence on the general trend.

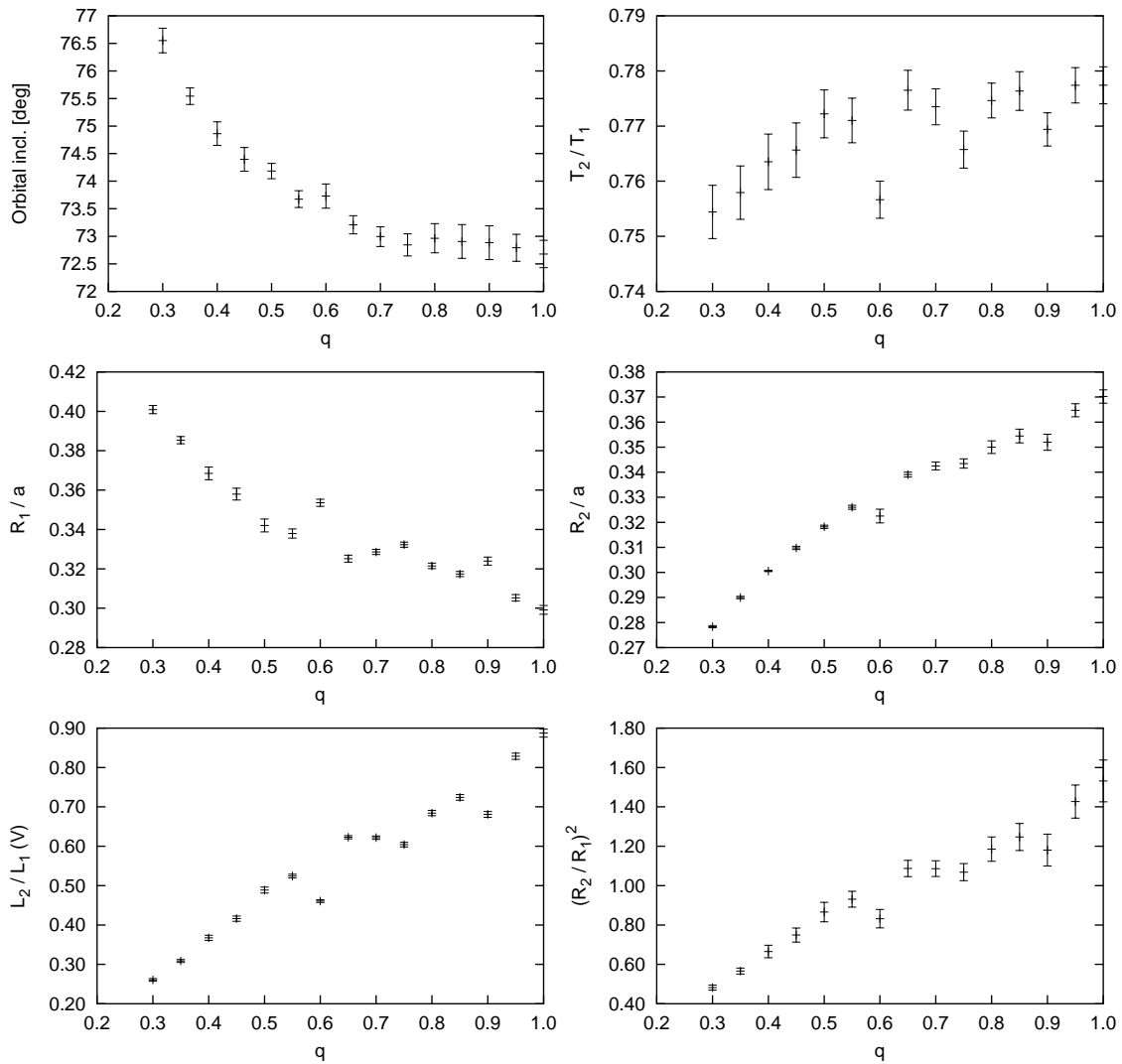


Figure 3.68: Final parameters of MACHO 337 (05:21:34.4–69:31:28) for different values of mass ratio q plotted together with their 1σ bootstrap errors.

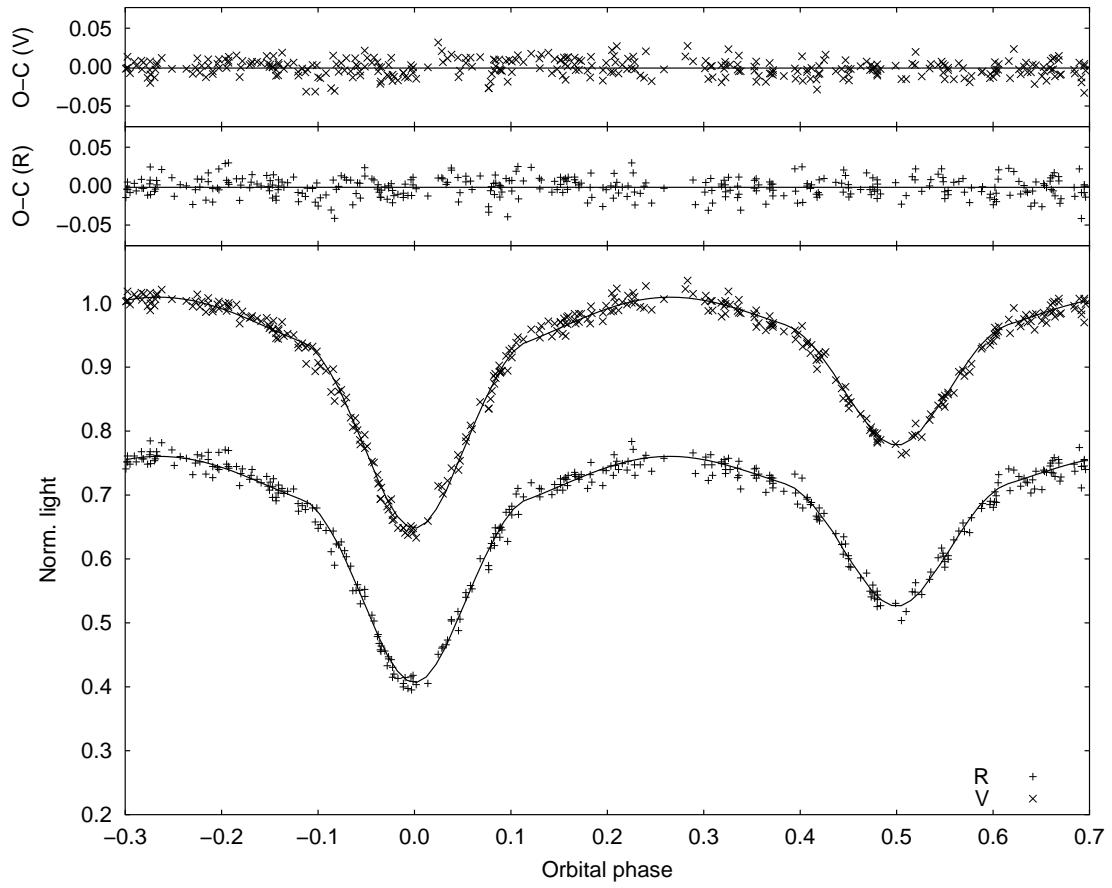


Figure 3.69: *V* and *R* light curves of MACHO 377 (05:21:34.4–69:31:28) shown together with best fits for mass ratio $q = 0.7$. For clarity, error bars of the individual data points are omitted and the *R* light curve is shifted down 0.25 light units.

3.7.4 Special cases

MACHO 547 (05:35:58.7–69:40:17)

m_V [mag]	P [d]	σ	Conf.
15.9	0.8046281	0.006	CO
– system exactly at inner contact			
– both components nearly completely filling Roche lobes			

Together with OGLE 9 175323 (see Section 4.7.1) MACHO 547 is a unique case among the binary systems analyzed in this work, since it is nearly exactly at inner contact where both components exactly fill their respective Roche lobes. Obviously, this is a very rare case, as any further expansion of one of the stars will result in an overcontact configuration with a common envelope. It is of course unlikely that MACHO 547 is in a perfect contact configuration, but it is certainly very close to it. Its orbital period is very short with only 0.8046281 days and it has an apparent brightness during quadrature phases of $m_V = 15.9$ mag. The orbital inclination is rather low and therefore eclipses are shallow. This is unfortunate since at higher inclination with possibly total eclipses MACHO 547 could be one of the best-determined systems of this entire work due to the sharp constraints on both surface potentials.

It is unlikely that MACHO 547 is constituted of main sequence components, because these would have too small luminosities to be compatible with the observed brightness at LMC distance. The primary temperature derived from the color index lies at about 30000 K. Because of the temperature ratio being near unity and the comparable sizes of both components, both stars are similar and belong to spectral type B0. Again, this should be regarded as an upper limit. According to the apparent brightness spectral type B3 seems a more likely possibility.

The light curves of MACHO 547 are of good quality and display only a moderate amount of scatter. With the currently available measurements, no systematic deviations of the residuals are observed. All parts of both light curves are fitted equally well and no asymmetries can be detected. Therefore it is likely that any complicating close-binary effects, should they exist, are relatively weak in this system.

q	i [deg]	$T_{\text{eff},2}$ [K]	$L_1/(L_1 + L_2)$	$L_2/(L_1 + L_2)$	R_1/a	R_2/a
0.45	65.61 ± 0.14	30515 ± 222	0.674 ± 0.017	0.326 ± 0.017	0.4515 ± 0.0001	0.3121 ± 0.0002
0.50	65.36 ± 0.13	30526 ± 209	0.652 ± 0.017	0.348 ± 0.017	0.4417 ± 0.0006	0.3206 ± 0.0003
0.55	65.06 ± 0.17	30435 ± 201	0.633 ± 0.017	0.367 ± 0.017	0.4333 ± 0.0003	0.3284 ± 0.0003
0.60	64.87 ± 0.13	30521 ± 190	0.614 ± 0.016	0.386 ± 0.016	0.4255 ± 0.0003	0.3357 ± 0.0005
0.65	64.77 ± 0.15	30524 ± 192	0.596 ± 0.017	0.404 ± 0.017	0.4182 ± 0.0003	0.3424 ± 0.0006
0.70	64.68 ± 0.13	30534 ± 181	0.579 ± 0.017	0.421 ± 0.017	0.4115 ± 0.0005	0.3485 ± 0.0010
0.75	64.84 ± 0.18	30275 ± 178	0.569 ± 0.021	0.431 ± 0.021	0.4054 ± 0.0002	0.3525 ± 0.0016
0.80	64.69 ± 0.16	30286 ± 179	0.553 ± 0.022	0.447 ± 0.022	0.3996 ± 0.0001	0.3587 ± 0.0013
0.85	64.50 ± 0.13	30383 ± 182	0.537 ± 0.020	0.463 ± 0.020	0.3942 ± 0.0002	0.3646 ± 0.0009
0.90	64.47 ± 0.12	30629 ± 142	0.521 ± 0.015	0.479 ± 0.015	0.3891 ± 0.0002	0.3700 ± 0.0005
0.95	64.33 ± 0.12	30553 ± 159	0.509 ± 0.017	0.491 ± 0.017	0.3843 ± 0.0003	0.3751 ± 0.0003
1.00	64.30 ± 0.11	30679 ± 181	0.495 ± 0.020	0.505 ± 0.020	0.3798 ± 0.0002	0.3797 ± 0.0004

Table 3.22: Parameters of MACHO 547 (05:35:58.7–69:40:17) derived from the photometric analysis shown together with 1σ bootstrap errors.

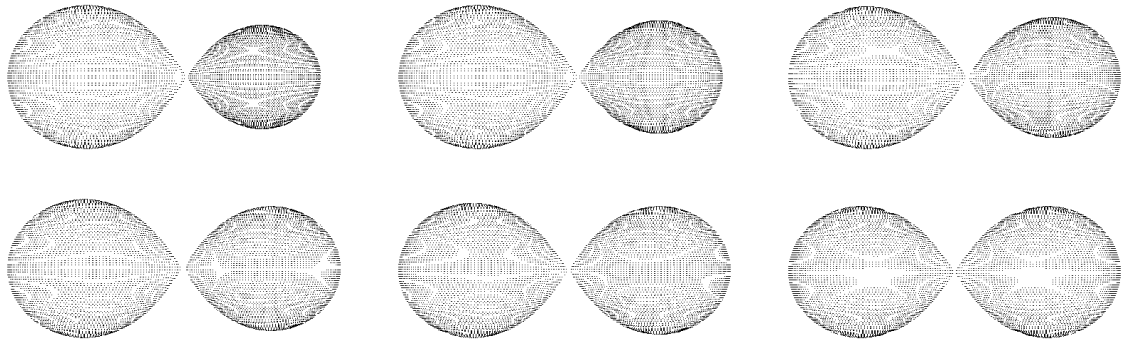


Figure 3.70: 3D plots of MACHO 547 (05:35:58.7–69:40:17) for mass ratio 0.5 (upper left) to 1.0 (lower right) with 0.1 increments.

The parameters are very well determined which can be expected for such a strongly constrained system. The Roche lobe-filling condition of both components severely restricts any variations in the relative radii for each fixed value of the mass ratio. The

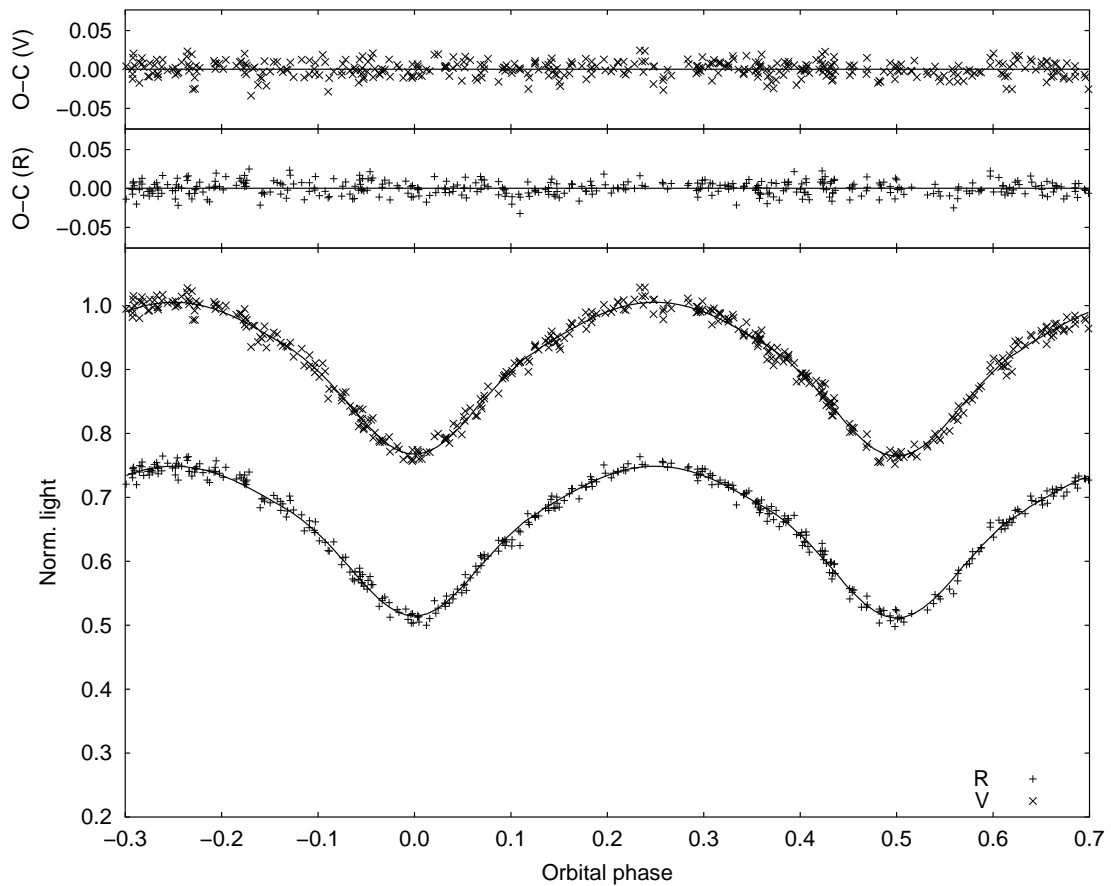


Figure 3.71: *V* and *R* light curves of MACHO 547 (05:35:58.7–69:40:17) shown together with best fits for mass ratio $q = 1.0$. For clarity, error bars of the individual data points are omitted and the *R* light curve is shifted down 0.25 light units.

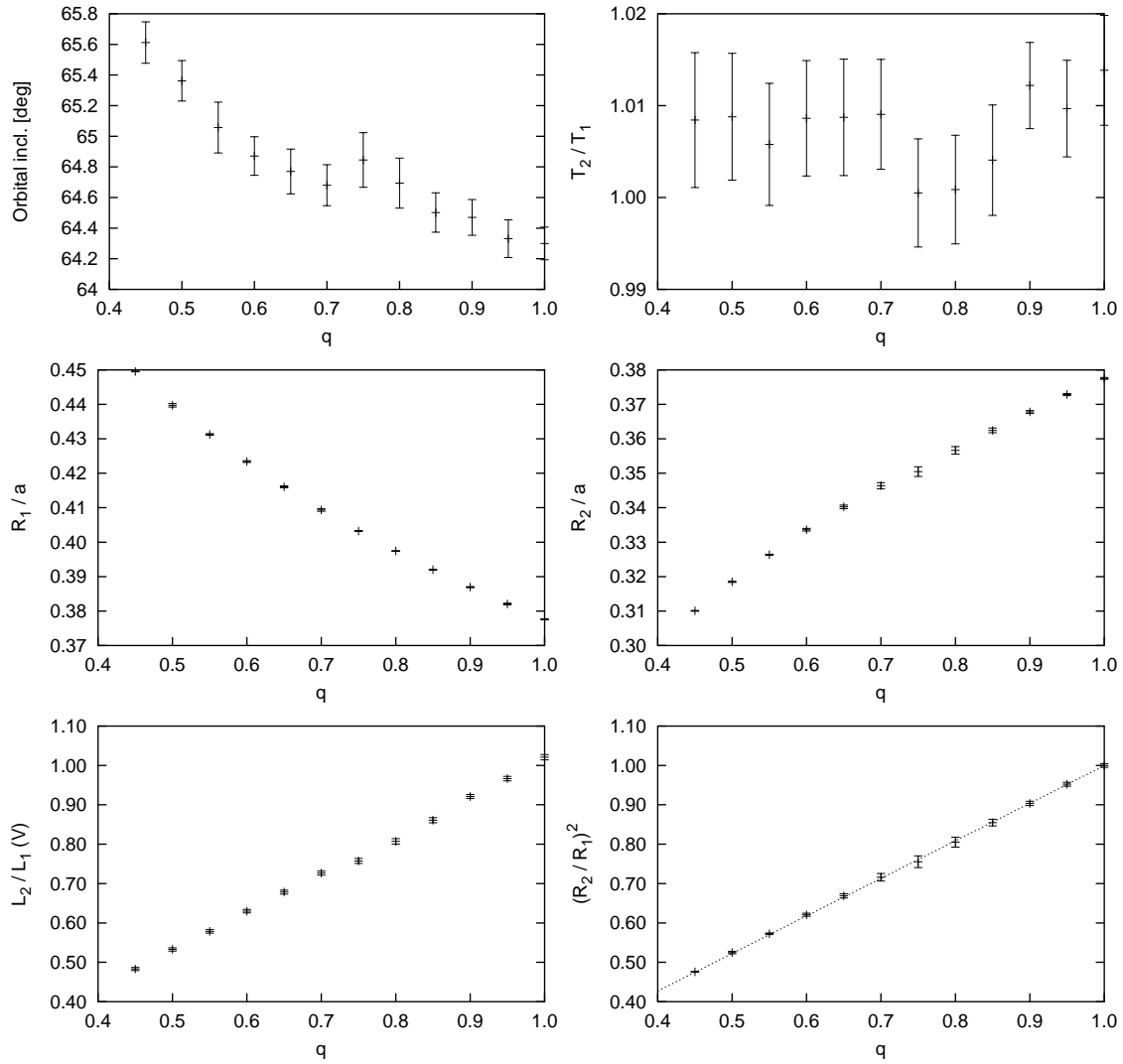


Figure 3.72: Final parameters of MACHO 547 (05:35:58.7–69:40:17) for different values of mass ratio q plotted together with their 1σ bootstrap errors.

radius changes caused by changes in mass ratio and the associated shifting of the inner Lagrangian point are compensated by slight variations of the orbital inclination. Since it is rather low, the sensitivity of the light curves against parameter changes is relatively weak. The low inclination therefore sets a definite limit to the accuracy with which parameter determination can be achieved for this system. Nevertheless, due to its unique configuration it is one of the most interesting and instructive binary stars analyzed in this work.

MACHO 307 (05:19:47.9–69:28:45)

m_V [mag]	P [d]	σ	Conf.
15.4	1.7185537	0.008	SD / DE
– two entirely different solution parameter sets – no main sequence stars – diversity of solutions			

Completely in contrast to MACHO 383 (see Section 3.7.3), MACHO 307 is one of the most ambiguous systems analyzed in this work. Two entirely different sets of parameters have been found in parameter space which yield solutions of comparable quality. Together with a relatively low orbital inclination and an above-average amount of scatter in the light curves it is again demonstrated how problematic the parameter determination from photometric data alone can be. In this case, even a spectroscopically determined mass ratio would not necessarily alleviate the problem, since good solutions have been found for exactly the same range of mass ratio values in both parameter regions. The orbital period of MACHO 307, having a maximum apparent brightness of $m_V = 15.4$ was found to be 1.7185537 days.

In this case the assumption that both components are main sequence stars is certainly not justified. The observed temperature difference of the components would require a mass ratio of $q < 0.5$, which is not covered by any of the solutions found, because no valid binary configuration exists for such a low mass ratio, which would be compatible with the observed light curves. Therefore, at least one of the components has to be an evolved star. The two parameter regions mainly differ by the fact, which of the components is the larger

q	i [deg]	$T_{\text{eff},2}$ [K]	$L_1/(L_1 + L_2)$	$L_2/(L_1 + L_2)$	R_1/a	R_2/a
0.65	68.97 ± 0.07	25949 ± 133	0.630 ± 0.014	0.370 ± 0.014	0.3339 ± 0.0006	0.3426 ± 0.0001
0.70	69.21 ± 0.09	26292 ± 140	0.592 ± 0.020	0.408 ± 0.020	0.3160 ± 0.0006	0.3489 ± 0.0000
0.75	69.55 ± 0.14	26438 ± 159	0.554 ± 0.027	0.446 ± 0.027	0.2985 ± 0.0011	0.3548 ± 0.0000
0.80	69.06 ± 0.13	26287 ± 165	0.555 ± 0.025	0.445 ± 0.025	0.3028 ± 0.0008	0.3604 ± 0.0000
0.85	69.02 ± 0.13	26283 ± 155	0.537 ± 0.023	0.463 ± 0.023	0.2961 ± 0.0005	0.3656 ± 0.0000
0.90	68.90 ± 0.16	26207 ± 154	0.529 ± 0.021	0.471 ± 0.021	0.2948 ± 0.0005	0.3706 ± 0.0000
0.95	69.57 ± 0.08	26531 ± 167	0.480 ± 0.028	0.520 ± 0.028	0.2728 ± 0.0004	0.3754 ± 0.0000
1.00	69.14 ± 0.08	26319 ± 116	0.484 ± 0.019	0.516 ± 0.019	0.2763 ± 0.0003	0.3799 ± 0.0000

Table 3.23: Parameters (semi-detached configuration) of MACHO 307 (05:19:47.9–69:28:45) derived from the photometric analysis shown together with 1σ bootstrap errors.

q	i [deg]	$T_{\text{eff},2}$ [K]	$L_1/(L_1 + L_2)$	$L_2/(L_1 + L_2)$	R_1/a	R_2/a
0.65	77.31 ± 0.36	18923 ± 179	0.910 ± 0.010	0.090 ± 0.010	0.4014 ± 0.0010	0.1946 ± 0.0012
0.70	76.88 ± 0.34	18806 ± 188	0.908 ± 0.009	0.092 ± 0.009	0.3959 ± 0.0009	0.1955 ± 0.0012
0.75	76.88 ± 0.39	18664 ± 181	0.908 ± 0.007	0.092 ± 0.007	0.3903 ± 0.0010	0.1934 ± 0.0014
0.80	75.95 ± 0.31	18825 ± 172	0.900 ± 0.009	0.100 ± 0.009	0.3858 ± 0.0009	0.1992 ± 0.0011
0.85	76.36 ± 0.36	18646 ± 194	0.903 ± 0.008	0.097 ± 0.008	0.3804 ± 0.0008	0.1945 ± 0.0016
0.90	76.70 ± 0.28	18433 ± 155	0.906 ± 0.006	0.094 ± 0.006	0.3755 ± 0.0007	0.1900 ± 0.0010
0.95	76.62 ± 0.26	18408 ± 165	0.905 ± 0.007	0.095 ± 0.007	0.3711 ± 0.0007	0.1895 ± 0.0011
1.00	74.94 ± 0.39	19053 ± 181	0.880 ± 0.016	0.120 ± 0.016	0.3678 ± 0.0009	0.2079 ± 0.0020

Table 3.24: Parameters (detached configuration) of MACHO 307 (05:19:47.9–69:28:45) derived from the photometric analysis shown together with 1σ bootstrap errors.

one. Since one set of solutions finds the secondary to fill its Roche lobe, it is designated the SD (semi-detached) set, while the other set shows a clearly detached configuration (with the primary suffering severe tidal distortion) and is therefore designated DE (see Fig. 3.76).

The light curve fits for both solution regimes are both not of best quality, indicating possible complications like mass transfer, accretion disks or other distortions by circumstellar matter, which prevent a truly global solution. In Fig. 3.73 typical solutions for both parameter regions are compared, in this case only in the R passband. Both light curves were computed for $q = 1.0$, since for evolved components no further information about this value can be extracted from the ratios of temperatures or radii. It is clear that both solutions have their individual strengths and weaknesses. While the SD solution fits the secondary minimum very well, particularly during the egress phase, this cannot be reproduced adequately by the DE solution. On the other hand, quadrature phases and the shoulders of the primary minimum are perfectly fitted by the DE solution, while the SD solution gives a poorer fit there. The primary minimum itself is not covered very well by

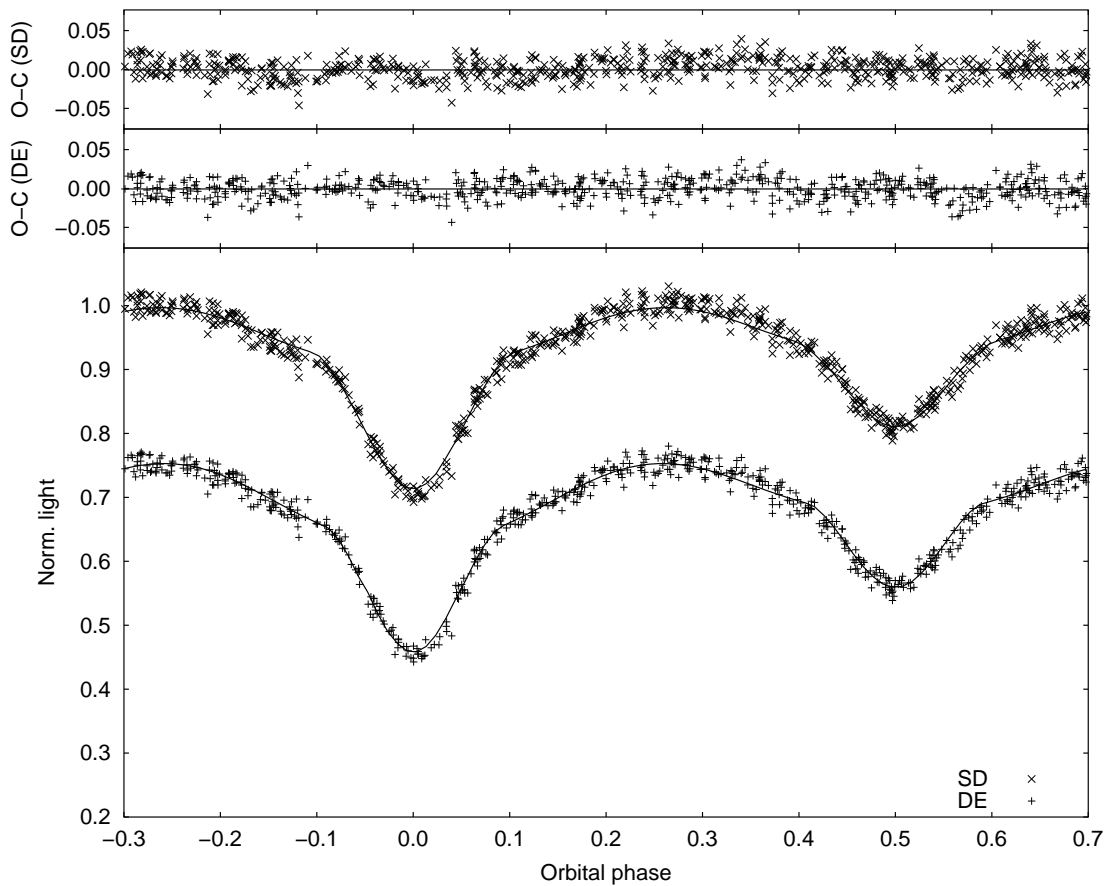


Figure 3.73: R light curves of MACHO 307 (05:19:47.9–69:28:45) for SD (top) and DE configuration (bottom) shown together with best fits for mass ratio $q = 1.0$. For clarity, error bars of the individual data points are omitted and the DE light curve is shifted down 0.25 light units.

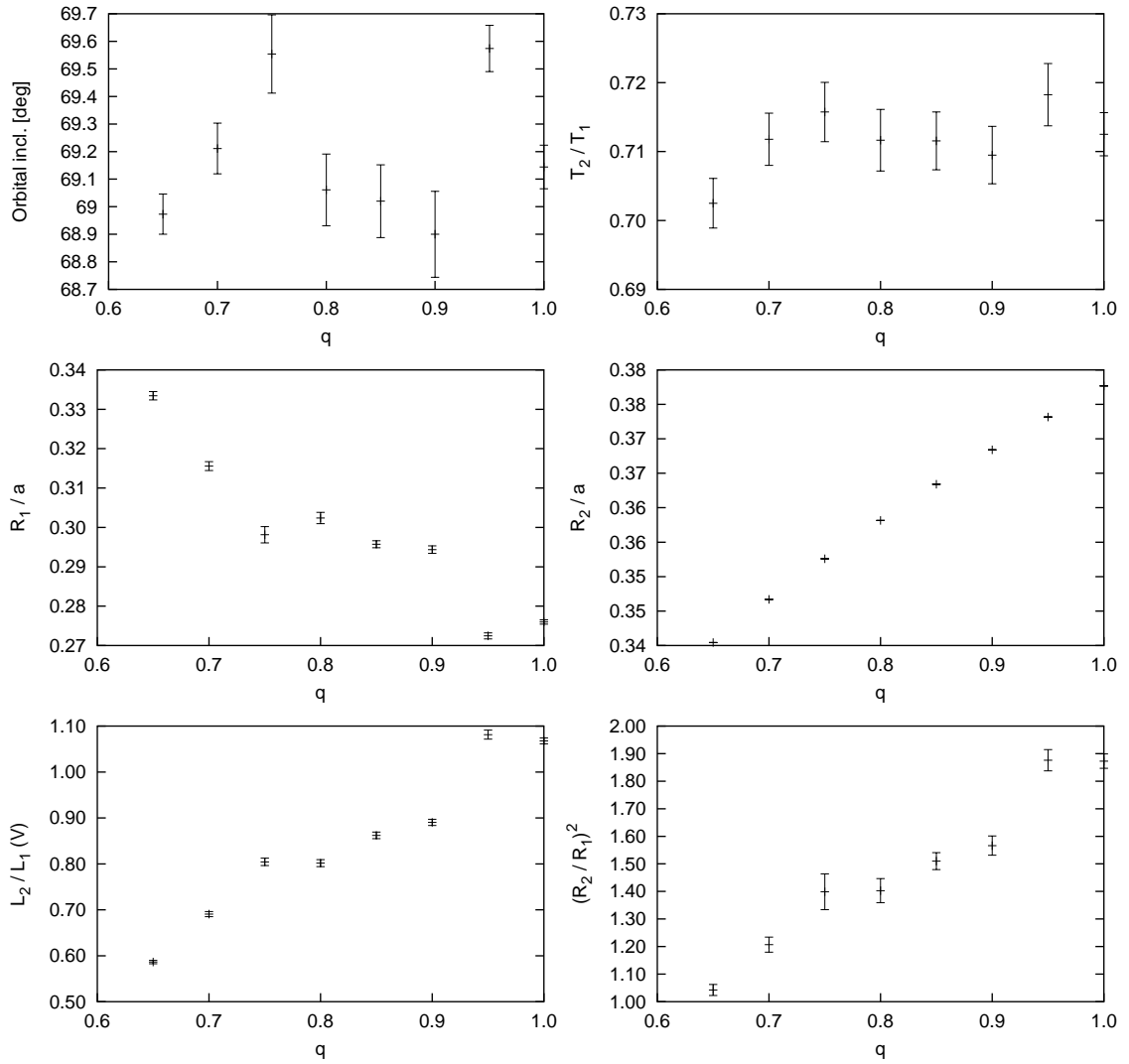


Figure 3.74: Final parameters of MACHO 307 (05:19:47.9–69:28:45) for different values of mass ratio q and SD configuration plotted together with their 1σ bootstrap errors.

either of the solutions, but this is due to a certain asymmetry in the profile which cannot be modelled by MORO whatsoever.

The parameters found in each of the solution regimes differ significantly from each other. Of course, the most obvious difference lies in the relative radii, which in the case of the SD solution follow the standard relations with the accurately determined secondary radius for each value of q due to the fact that its surface potential is fixed by the semi-detached component constraint. In the DE configuration the trends are not so clear. With the primary component being close to its Roche lobe, the primary radius does not have much freedom to vary and follows the usual trend. The relative radius of the secondary component, though, is nearly constant throughout the range of mass ratios. This is clear, since it has a comparably small value of $R_2/a \approx 0.2$ and small parameter changes will not result in a significant distortion of this component. Therefore changing its radius

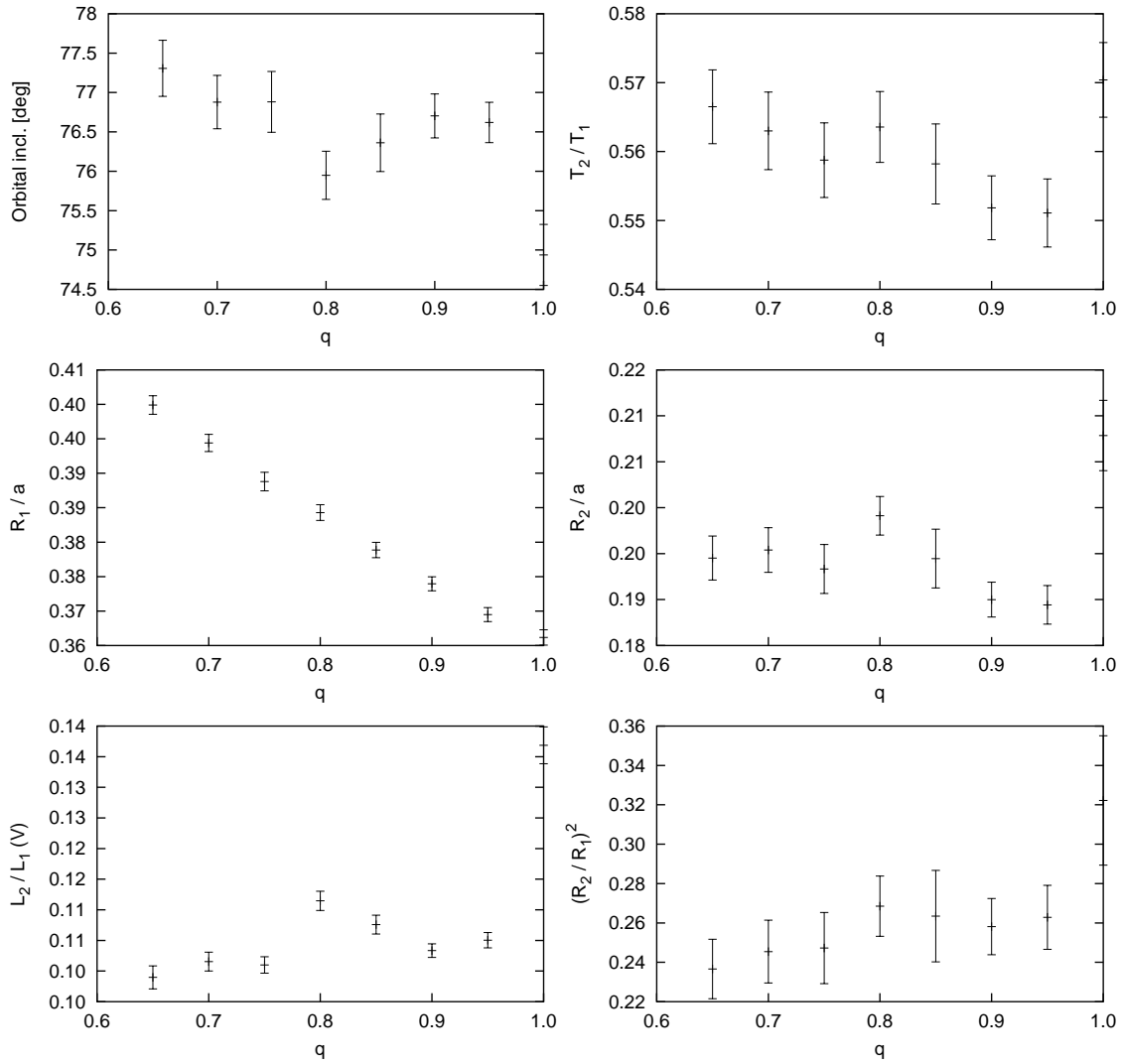


Figure 3.75: Final parameters of MACHO 307 (05:19:47.9–69:28:45) for different values of mass ratio q and detached configuration plotted together with their 1σ bootstrap errors.

cannot accomplish a sufficient compensation for variations of other parameters like orbital inclination. Interestingly, the temperature ratios found in both solution regimes differ from each other quite significantly. This effect is rather intricate and requires an in-depth discussion, which can be found in Section 3.7.4, where a very similar eclipsing binary is analyzed.

This example illustrates how poorer measurement quality combined with an assumed inadequate configuration can yield a satisfactory solution to the complete light curve, resulting in a serious indeterminacy of system parameters. It has to be mentioned that with the classic “guessing” method of determining initial parameters for light curve fits this kind of problem is easily overlooked. Only a thorough search of the entire relevant parameter space, as described in Section 3.6.2 and employed in this work, can effectively

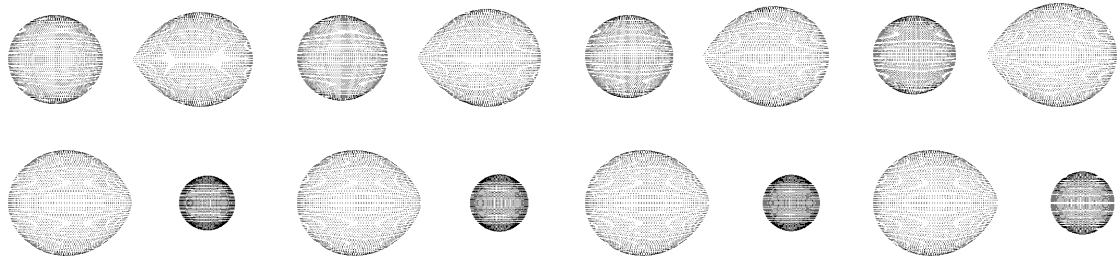


Figure 3.76: 3D plots of MACHO 307 (05:19:47.9–69:28:45) for mass ratio 0.7 to 1.0 and SD configuration (upper row) with 0.1 increments. Comparison plots with identical mass ratios are shown for DE configuration in the lower row.

alert the researcher to exercise even more caution than usually recommended when deriving stellar parameters from eclipsing binary light curves.

MACHO 443 (05:30:18.2–68:55:16)

m_V [mag]	P [d]	σ	Conf.
15.7	1.6690412	0.007	SD / DE
– two completely different solution parameter sets – very similar to MACHO 307 – ambiguity in temperature ratio			

Just like MACHO 307 (see Section 3.7.4), MACHO 443 is a system with two completely different sets of solutions. In fact, the light curves of both systems are very similar. Therefore the same kind of ambiguity is encountered, with one semi-detached (SD) and one detached (DE) set of solutions. A further similarity is the orbital period which in both cases lies around 1.7 days, giving room for evolved components in the systems. With $m_V = 15.7$ mag the apparent brightness of MACHO 443 is somewhat lower than that of MACHO 307. Nevertheless, the light curves are of comparable quality. The phase sampling is not as good MACHO 443, though.

Again, no main sequence components can be assumed for this stellar system. The temperature difference between primary and secondary stars is too large to yield a mass ratio which is covered by the photometric solutions. It is likely that one of the components has evolved far beyond its main sequence size. For the detached solution, the evolved star would be the primary component on its way to a Roche lobe-filling condition. In case of

q	i [deg]	$T_{\text{eff},2}$ [K]	$L_1/(L_1 + L_2)$	$L_2/(L_1 + L_2)$	R_1/a	R_2/a
0.55	70.02 ± 0.18	15302 ± 73	0.677 ± 0.024	0.323 ± 0.024	0.3381 ± 0.0013	0.3285 ± 0.0001
0.60	69.68 ± 0.10	15274 ± 57	0.662 ± 0.011	0.338 ± 0.011	0.3337 ± 0.0010	0.3357 ± 0.0002
0.65	69.58 ± 0.10	15405 ± 52	0.632 ± 0.014	0.368 ± 0.014	0.3218 ± 0.0007	0.3425 ± 0.0002
0.70	69.82 ± 0.15	15520 ± 76	0.595 ± 0.030	0.405 ± 0.030	0.3045 ± 0.0011	0.3488 ± 0.0003
0.75	69.51 ± 0.23	15454 ± 61	0.588 ± 0.034	0.412 ± 0.034	0.3044 ± 0.0015	0.3546 ± 0.0005
0.80	69.85 ± 0.15	15521 ± 56	0.552 ± 0.025	0.448 ± 0.025	0.2879 ± 0.0011	0.3603 ± 0.0003
0.85	69.51 ± 0.17	15499 ± 63	0.551 ± 0.038	0.449 ± 0.038	0.2911 ± 0.0017	0.3653 ± 0.0006
0.90	69.36 ± 0.09	15421 ± 58	0.541 ± 0.027	0.459 ± 0.027	0.2880 ± 0.0010	0.3702 ± 0.0008
0.95	69.21 ± 0.18	15502 ± 58	0.529 ± 0.022	0.471 ± 0.022	0.2858 ± 0.0010	0.3744 ± 0.0010
1.00	69.18 ± 0.11	15517 ± 56	0.517 ± 0.015	0.483 ± 0.015	0.2828 ± 0.0006	0.3786 ± 0.0011

Table 3.25: Parameters (semi-detached configuration) of MACHO 443 (05:30:18.2–68:55:16) derived from the photometric analysis shown together with 1σ bootstrap errors.

q	i [deg]	$T_{\text{eff},2}$ [K]	$L_1/(L_1 + L_2)$	$L_2/(L_1 + L_2)$	R_1/a	R_2/a
0.55	77.49 ± 0.42	12557 ± 123	0.914 ± 0.018	0.086 ± 0.018	0.4087 ± 0.0012	0.2041 ± 0.0016
0.60	77.82 ± 0.54	12486 ± 123	0.915 ± 0.022	0.085 ± 0.022	0.4014 ± 0.0012	0.2000 ± 0.0020
0.65	76.47 ± 0.75	12529 ± 96	0.906 ± 0.023	0.094 ± 0.023	0.3962 ± 0.0013	0.2080 ± 0.0027
0.70	75.25 ± 0.53	12633 ± 69	0.893 ± 0.021	0.107 ± 0.021	0.3912 ± 0.0011	0.2189 ± 0.0026
0.75	76.51 ± 0.42	12330 ± 97	0.908 ± 0.018	0.092 ± 0.018	0.3851 ± 0.0009	0.2037 ± 0.0016
0.80	74.16 ± 0.30	12873 ± 87	0.871 ± 0.019	0.129 ± 0.019	0.3798 ± 0.0009	0.2314 ± 0.0015
0.85	74.24 ± 0.33	12812 ± 87	0.871 ± 0.022	0.129 ± 0.022	0.3752 ± 0.0010	0.2294 ± 0.0018
0.90	73.74 ± 0.35	12914 ± 89	0.860 ± 0.026	0.140 ± 0.026	0.3704 ± 0.0010	0.2361 ± 0.0020
0.95	73.39 ± 0.24	13034 ± 94	0.848 ± 0.021	0.152 ± 0.021	0.3660 ± 0.0010	0.2418 ± 0.0013
1.00	73.43 ± 0.24	13032 ± 107	0.845 ± 0.026	0.155 ± 0.026	0.3620 ± 0.0009	0.2416 ± 0.0014

Table 3.26: Parameters (detached configuration) of MACHO 443 (05:30:18.2–68:55:16) derived from the photometric analysis shown together with 1σ bootstrap errors.

the semi-detached solution where both components are of similar size, it is possible that the secondary component originally was the more massive one, but has lost a significant amount of its mass during its evolution to the new primary component (see Fig. 3.80).

The fits of the light curves (see Fig. 3.77) are better than those of MACHO 307 (see Fig. 3.73). There are only subtle differences between the SD and the DE solutions. For example, the shoulders of the primary minimum are reproduced differently, but it is difficult to decide which of the two fits matches better in this range.

The parameters naturally exhibit a similar behavior as those of MACHO 443. The parameters of both solution sets are vastly different. Generally, the standard q -dependencies are followed very well. It is obvious that the determinateness of the radii is closely connected to the Roche lobe filling factor. For the semi-detached configuration in which the secondary star completely fills its Roche lobe, the variance of its radius is very small and the error bars nearly vanish. The same effect can also be noted for the second configuration where both stars are detached. The error bars are larger, of course, nevertheless

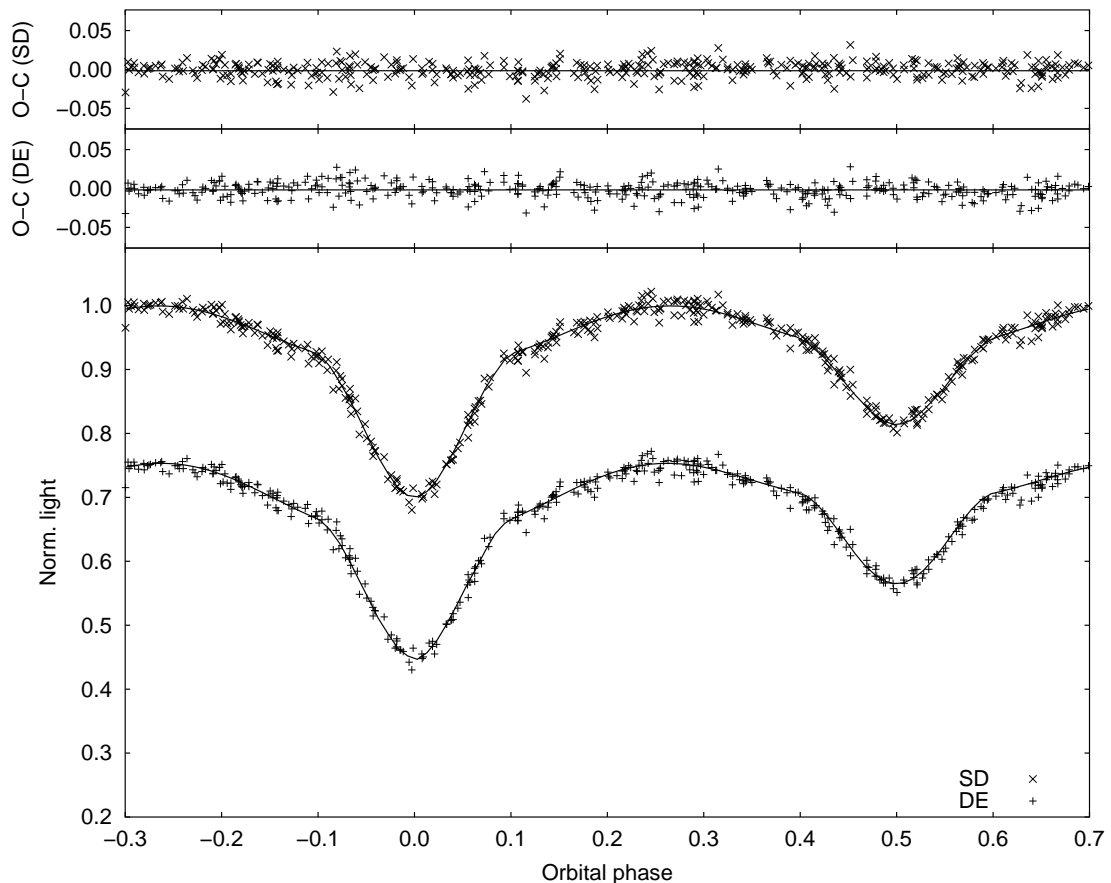


Figure 3.77: R light curves of MACHO 443 (05:30:18.2–68:55:16) for SD (top) and DE configuration (bottom) shown together with best fits for mass ratio $q = 1.0$. For clarity, error bars of the individual data points are omitted and the DE light curve is shifted down 0.25 light units.

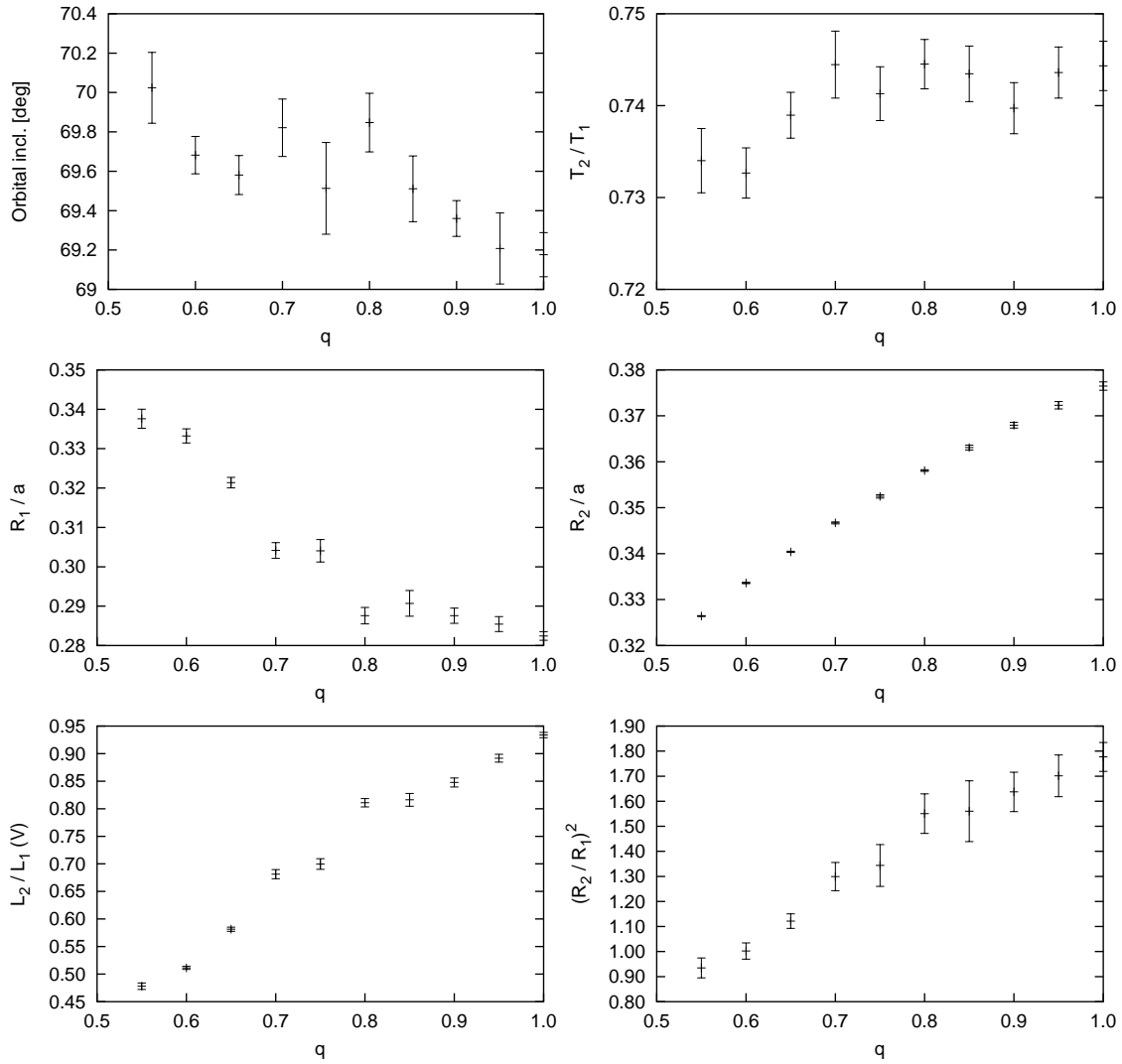


Figure 3.78: Final parameters of MACHO 443 (05:30:18.2–68:55:16) for different values of mass ratio q and SD configuration plotted together with their 1σ bootstrap errors.

the trend with q is much better defined than for the radius of the (very small) secondary component.

The question remains why a significant difference in temperature ratio can exist between the two solution sets, since it is the only parameter determined by the relative depths of the minima. The same effect was observed with MACHO 307. It is clear that the stellar temperatures must be seen as an average value over the whole stellar disk. Since the synthetic light curves must fit the observations identically for both configurations, it is necessary that the eclipsed parts have the same temperature in both cases. Since the (average) secondary temperature is derived significantly lower for the detached configuration, it must be concluded that the effect is due to irradiation by the primary star: the hemisphere of the secondary facing the primary component is heated by its radiation. The presence of this reflection effect can be detected in the light curves by comparing the

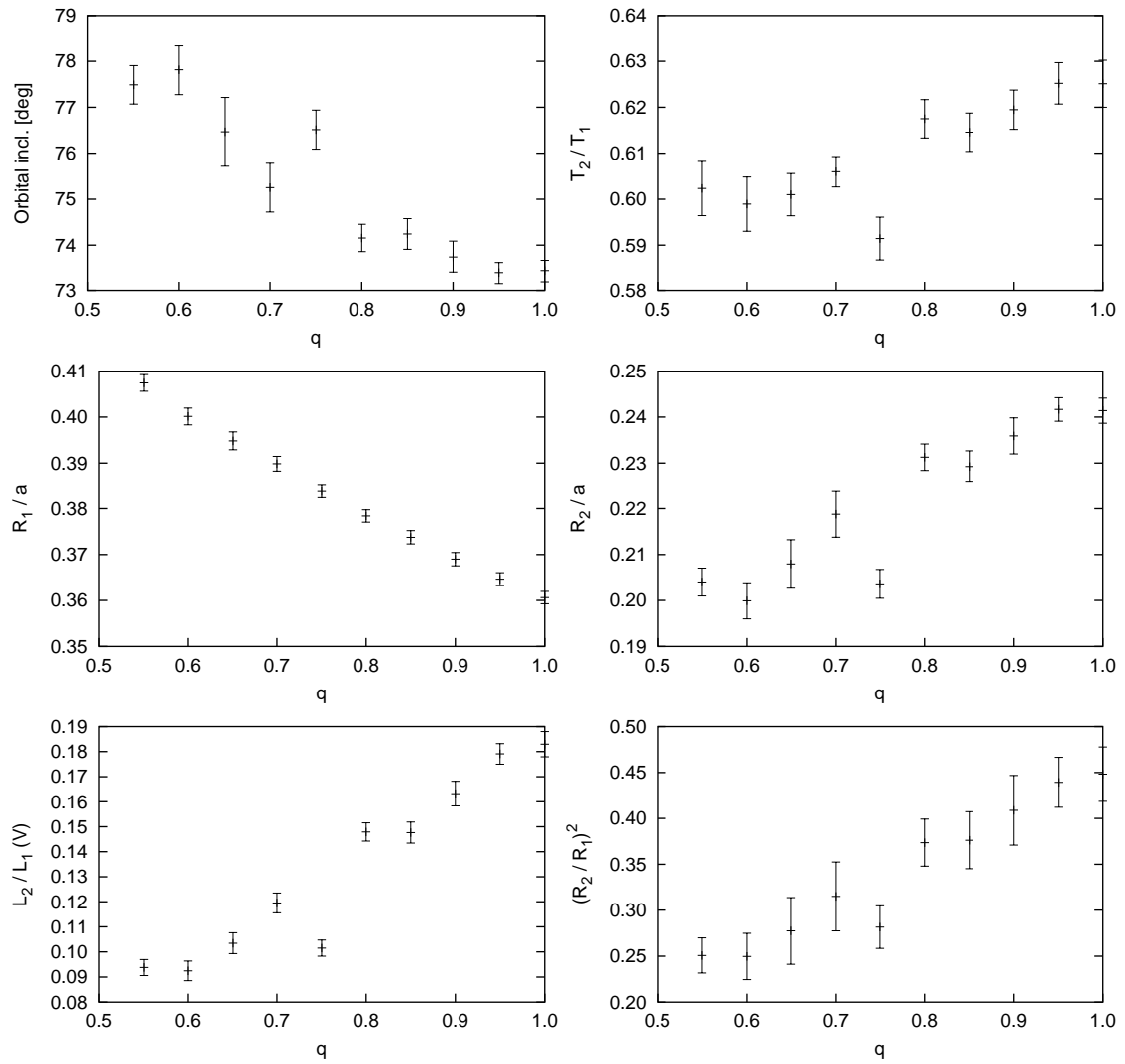


Figure 3.79: Final parameters of MACHO 443 (05:30:18.2–68:55:16) for different values of mass ratio q and detached configuration plotted together with their 1σ bootstrap errors.

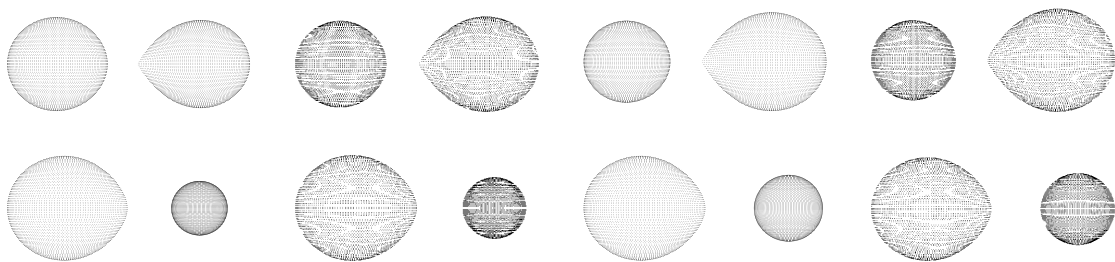


Figure 3.80: 3D plots of MACHO 443 (05:30:18.2–68:55:16) for mass ratio 0.55 to 1.00 and SD configuration (upper row) with 0.15 increments. Comparison plots with identical mass ratios are shown for DE configuration in the lower row.

ingress points of the primary and secondary minimum. The latter one is higher, indicating irradiation of the secondary component by the (hotter) primary star. It can clearly be seen that in the DE case the shoulder of the secondary minimum is higher than in the SD case, indicating a stronger reflection effect. This explains why temperature ratios can be derived differently from the same light curves for different stellar configurations. Otherwise, the temperature ratio can be precisely extracted, as has been demonstrated for numerous other binaries in this work.

MACHO 557 (05:36:26.8–69:35:19)

m_V [mag]	P [d]	σ	Conf.
15.7	0.8332756	0.009	DE / OC
– two slightly different solution parameter sets			
– very short orbital period			

Other than MACHO 307 and MACHO 443 (see Sections 3.7.4 and 3.7.4), MACHO 557 can be represented by two only slightly differing solution sets. The system consists of components of similar size which are either still detached or may also be in a slight overcontact configuration. For both cases solutions of identical quality can be derived and it cannot be decided from the fits which assumption is actually correct. The two results are discussed here individually not due to large differences between their parameters (as they are nearly identical), but because they are extremely instructive regarding the fundamental differences between detached and overcontact configurations in terms of parameter definiteness and correlations. The additional physical constraints valid even for the slightest overcontact configuration can be illustrated impressively by this example.

With only 0.8332756 days the orbital period of MACHO 557 is relatively short. The light curves are of very good quality for a system with $V = 15.7$ mag. If main sequence components are assumed, the observed temperature ratio corresponds to a mass ratio of about $q \approx 0.85$. Component masses come out as $M_1 \approx 7.3M_\odot$ and $M_2 \approx 6.2M_\odot$, and

q	i [deg]	$T_{\text{eff},2}$ [K]	$L_1/(L_1 + L_2)$	$L_2/(L_1 + L_2)$	R_1/a	R_2/a
0.60	81.53 ± 0.33	26593 ± 161	0.653 ± 0.014	0.347 ± 0.014	0.4223 ± 0.0012	0.3340 ± 0.0014
0.65	81.13 ± 0.31	26508 ± 162	0.643 ± 0.015	0.357 ± 0.015	0.4175 ± 0.0007	0.3377 ± 0.0015
0.70	80.48 ± 0.17	26978 ± 192	0.609 ± 0.022	0.391 ± 0.022	0.4046 ± 0.0011	0.3486 ± 0.0006
0.75	80.08 ± 0.20	27065 ± 191	0.591 ± 0.023	0.409 ± 0.023	0.3976 ± 0.0012	0.3547 ± 0.0003
0.80	79.85 ± 0.15	27008 ± 180	0.582 ± 0.021	0.418 ± 0.021	0.3953 ± 0.0009	0.3597 ± 0.0010
0.85	79.96 ± 0.24	26721 ± 180	0.585 ± 0.024	0.415 ± 0.024	0.3940 ± 0.0005	0.3577 ± 0.0019
0.90	79.61 ± 0.31	27055 ± 191	0.552 ± 0.026	0.448 ± 0.026	0.3831 ± 0.0013	0.3704 ± 0.0008
0.95	79.75 ± 0.18	27192 ± 175	0.534 ± 0.025	0.466 ± 0.025	0.3762 ± 0.0014	0.3752 ± 0.0006
1.00	79.72 ± 0.18	27093 ± 186	0.530 ± 0.028	0.470 ± 0.028	0.3751 ± 0.0011	0.3780 ± 0.0016

Table 3.27: Parameters (detached configuration) of MACHO 557 (05:36:26.8–69:35:19) derived from the photometric analysis shown together with 1σ bootstrap errors.

q	i [deg]	$T_{\text{eff},2}$ [K]	$L_1/(L_1 + L_2)$	$L_2/(L_1 + L_2)$	R_1/a	R_2/a
0.50	82.51 ± 0.33	26920 ± 315	0.690 ± 0.027	0.310 ± 0.027	0.4420 ± 0.0000	0.3207 ± 0.0000
0.55	81.80 ± 0.36	26848 ± 286	0.672 ± 0.026	0.328 ± 0.026	0.4334 ± 0.0000	0.3286 ± 0.0000
0.60	81.07 ± 0.39	26916 ± 272	0.653 ± 0.025	0.347 ± 0.025	0.4256 ± 0.0000	0.3358 ± 0.0000
0.65	80.58 ± 0.40	26941 ± 265	0.636 ± 0.026	0.364 ± 0.026	0.4183 ± 0.0000	0.3426 ± 0.0000
0.70	80.28 ± 0.24	26981 ± 266	0.619 ± 0.027	0.381 ± 0.027	0.4117 ± 0.0000	0.3489 ± 0.0000
0.75	79.87 ± 0.23	27049 ± 277	0.603 ± 0.029	0.397 ± 0.029	0.4055 ± 0.0000	0.3548 ± 0.0000
0.80	79.66 ± 0.14	27108 ± 249	0.587 ± 0.026	0.413 ± 0.026	0.3997 ± 0.0000	0.3604 ± 0.0000
0.85	79.41 ± 0.26	27164 ± 280	0.573 ± 0.030	0.427 ± 0.030	0.3943 ± 0.0000	0.3656 ± 0.0000
0.90	79.22 ± 0.27	27163 ± 282	0.560 ± 0.031	0.440 ± 0.031	0.3892 ± 0.0000	0.3706 ± 0.0000
0.95	79.20 ± 0.22	27201 ± 269	0.547 ± 0.031	0.453 ± 0.031	0.3844 ± 0.0000	0.3754 ± 0.0000
1.00	79.42 ± 0.29	27281 ± 257	0.534 ± 0.030	0.466 ± 0.030	0.3799 ± 0.0000	0.3799 ± 0.0000

Table 3.28: Parameters (overcontact configuration) of MACHO 557 (05:36:26.8–69:35:19) derived from the photometric analysis shown together with 1σ bootstrap errors.

stellar radii of $R_1 \approx 3.7R_\odot$ and $R_2 \approx 3.3R_\odot$ can be derived, along with an orbital separation of $a \approx 8.9R_\odot$. The photometrically derived relative radii match these values very well. However, the resulting temperatures of about 21400 and 19400 K, respectively, imply stars of spectral types B2 and B3. From the color index a primary temperature of about 30000 K is derived, corresponding to a B0 star. Therefore, it is unlikely that the main sequence assumption holds in this case, as was already doubtful for some other systems with very short periods. Only if no interstellar reddening was present at all at the position of MACHO 557, the color index calibration would yield a primary temperature consistent with the values derived from the main sequence relation.

The light curves of MACHO 557 have high S/N , but there are some phase ranges with gaps or poorer coverage. There are some problems, which are not successfully addressed by either of the solution regimes. The first and most obvious one is that both eclipse minima are not adequately fitted by the solutions. It is clear from direct inspection of the light curves that severe systematic errors are present in the V and R passbands. Fig. 3.81

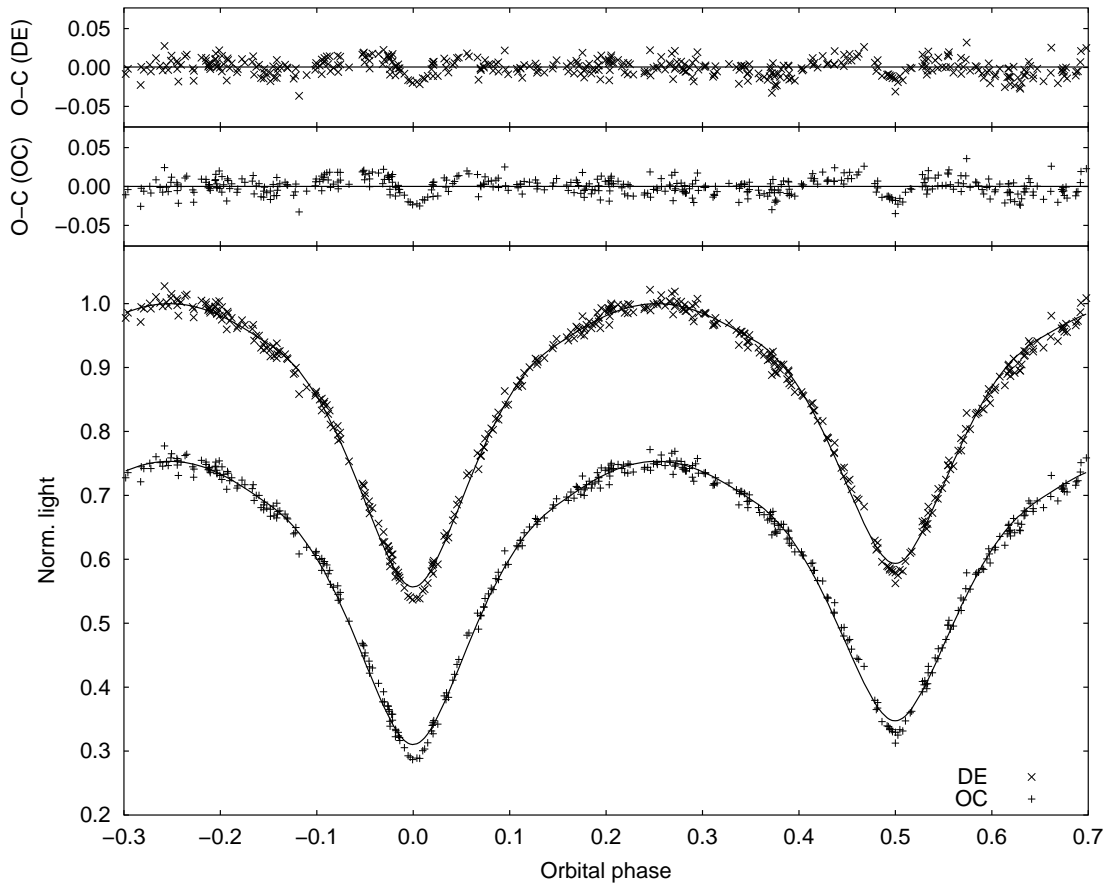


Figure 3.81: R light curves of MACHO 557 (05:36:26.8–69:35:19) for DE (top) and OC configuration (bottom) shown together with best fits for mass ratio $q = 0.85$. For clarity, error bars of the individual data points are omitted and the DE light curve is shifted down 0.25 light units.

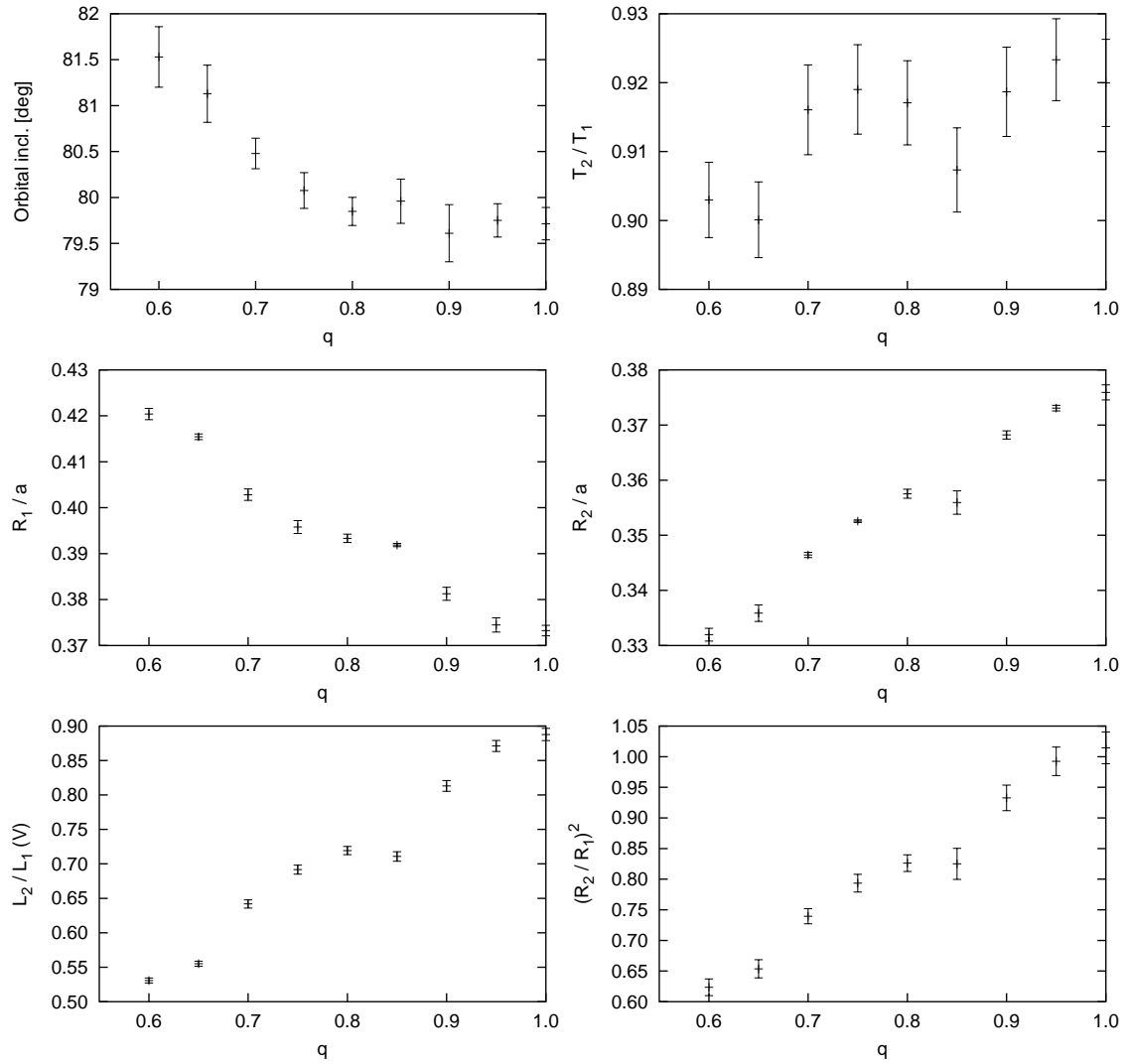


Figure 3.82: Final parameters of MACHO 557 (05:36:26.8–69:35:19) for different values of mass ratio q and DE configuration plotted together with their 1σ bootstrap errors.

shows the R light curves for a detached and an overcontact solution. Otherwise, the fits represent the measurements quite well.

It is most interesting to investigate the effect of the configuration change from detached to marginal overcontact a little closer. While the values of the derived parameters do not change in a significant way and the q -dependencies follow the generally established trends, the definiteness of the individual parameter determination differs appreciably between both configurations. While in the detached configuration they are already rather well-determined with small error bars (with the exception of a possible local minimum encountered at $q = 0.85$, see Fig. 3.82), the parameters found for an OC configuration are even more accurate. Especially the relative radii have extremely small errors, and the linear relation of $(R_2/R_1)^2$ vs. q is perfect, as indicated by the linear fit (see Fig. 3.84).

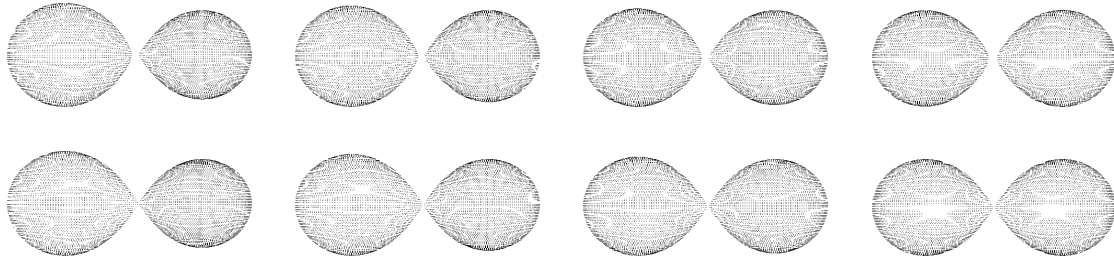


Figure 3.83: 3D plots of MACHO 557 (05:36:26.8–69:35:19) for mass ratio 0.7 to 1.0 and DE configuration (upper row) with 0.1 increments. Comparison plots with identical mass ratios are shown for OC configuration in the lower row.

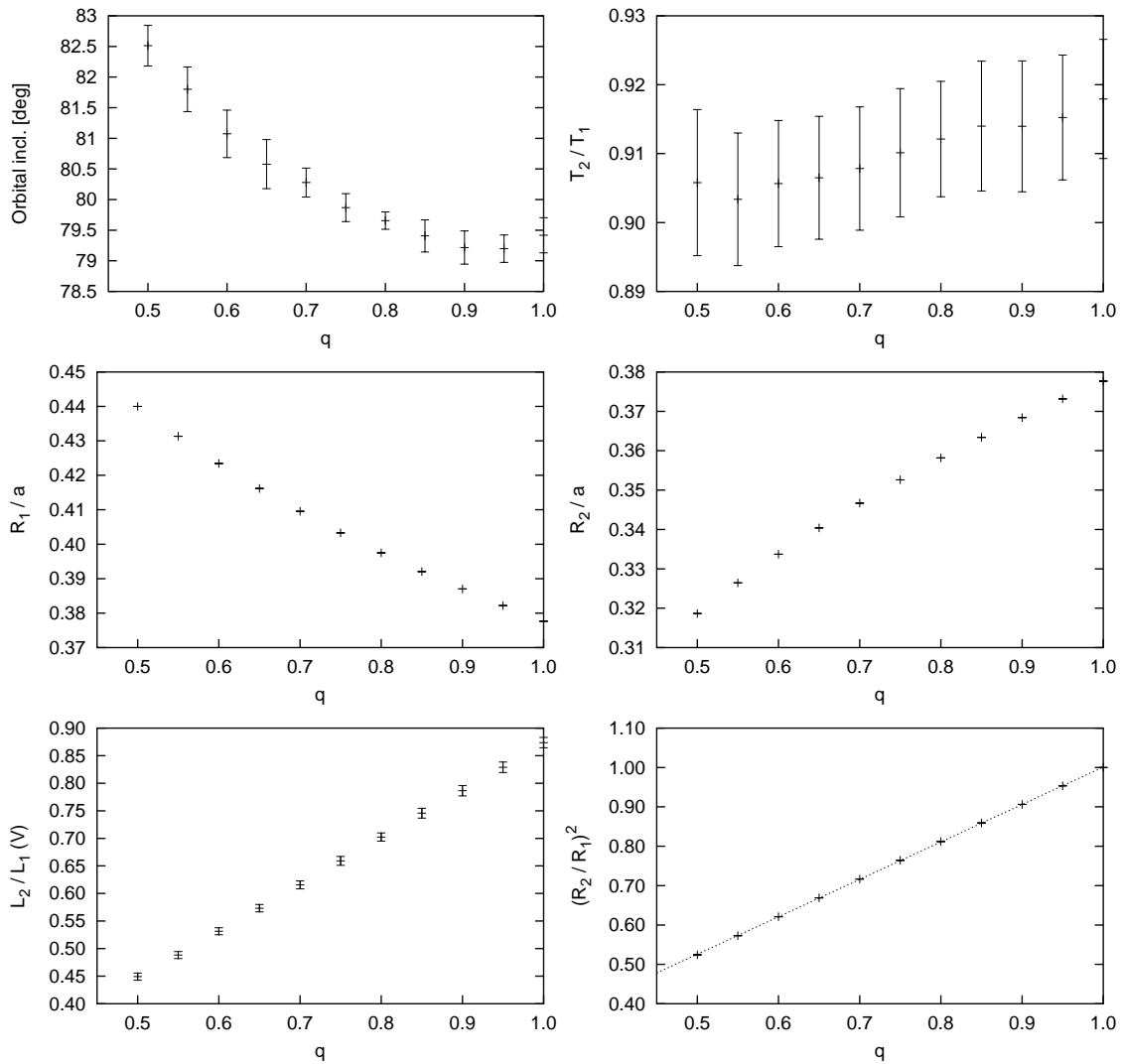


Figure 3.84: Final parameters of MACHO 557 (05:36:26.8–69:35:19) for different values of mass ratio q and OC configuration plotted together with their 1σ bootstrap errors.

In this case, the positive influence of an overcontact configuration on parameter determinateness is especially extreme, since the degree of overcontact is very small; also a high orbital inclination is present and light curves have very high S/N . There is no degree of freedom for the relative radii to change; together with the constraint that both surface potentials have to be identical, this serves as a powerful boundary condition for the light curve solutions by an effective reduction of the number of free parameters. Even the very slight variations of relative radii allowed by the marginally detached configuration instantly changes this situation and leads to a larger variance of the parameters. Unfortunately, none of the solution regimes is really favored by the light curves, so the question of the actual configuration of MACHO 557 remains unsolved so far.

4 Combined spectroscopic and photometric analysis of SMC binaries

4.1 Motivation

The goal of this work was to derive accurate absolute parameters for a sample of selected eclipsing binary stars in the LMC. The main idea was to combine the powerful new approach of simultaneous SB2 spectral analysis by means of the FITSB2 software with an analysis of excellent binary light curves from the MACHO archive of long-term photometric observations of the LMC. With state-of-the-art instruments like the multi-object spectrographs 2dF at the Anglo-Australian Observatory or FLAMES at ESO's VLT in Chile, it is possible to secure a reasonable amount of spectra for between 50 and 150 objects within a few nights. The combined photometric and spectroscopic approach outlined in Chapter 2 can then yield precise fundamental stellar quantities for the early-type program stars.

As explained earlier in the motivation for the purely photometric analysis in Section 3.1, during the the past two years, no spectroscopic time could be secured for various reasons not to be anticipated at the start of the project. Between 2004 and 2006, six proposals were submitted for use of the following powerful instruments: the UK Schmidt telescope at the Anglo-Australian Observatory (AAO) equipped with the 6dF multi-object spectrograph, the NTT telescope at ESO La Silla with its EMMI spectrograph, the ESO 10 m Very Large Telescope (VLT) with its FLAMES instrument, the 3.9 m AAT telescope at AAO with the 2dF spectrograph and later with its follow-up 2dF/AAOMEGA instrument, and finally the new 11 m Southern African Large Telescope (SALT) with its PFIS spectrograph.

The major part of the available observing time with all of these large telescopes and instruments is allocated to extragalactic projects, leaving only few space for stellar astronomical work. Nevertheless, our proposal for use of the 3.9 m AAT telescope with the multi-object 2dF spectrograph was allocated time in November 2005 provided that the follow-up AAOMEGA instrument was not yet ready for its science verification phase at that date. However, it was delivered shortly before the scheduled observations. Finally, the author participated in a collaboration with a research group of Göttingen University which has guaranteed observing time at the new 11 m SALT telescope. The proposal to obtain time-resolved spectroscopy of OB systems in the LMC with the PFIS spectrograph was accepted as part of the Göttingen projects. Though first light of SALT could be achieved as scheduled, it shortly later turned out that there were severe technical problems

with the main focus of the new-technology telescope and also with various instruments. These problems could not be solved to date.

Nevertheless, besides the “fall-back” program of photometric analysis, the results of which were discussed in Chapter 3, the combined analysis method is so promising, that it was decided to show its potential and effectiveness by use of archive data, in this case binary stars in the SMC. With our new method the absolute parameters of the stars could be derived to very good accuracy. Also, the results can be used to derive a value for the distance of the individual stars within the SMC, which is an important step in the so-called cosmic “distance ladder”, still under debate today. So methods independent of the classical Cepheid period-luminosity relation are needed to finally ascertain the distance to our nearest neighbor galaxies.

Another reason for demonstrating the power of the approach is the urgent need of precise stellar parameters of early-type stars, and especially early-type binaries in metal-poor environments, for which only few reliable investigations are known today. One of the main problems is that these hot stars are rare and cannot be found in the solar neighborhood. Even more problematic is the metallicity content. Since all early-type stars must necessarily be young, they always exhibit relatively high metallicity in the Milky Way. Therefore the only chance to gather insight in these very special class of stars is in metal-poor environments like the LMC and especially the SMC, for which a metal content of about one fifth of the solar value is assumed. In this light the present work must be seen as a foundation to encourage future researchers to apply the proposed method to a much larger number of extragalactic early-type binaries, since its effectiveness and the validity of the results can be convincingly proven. As has been mentioned earlier, future researchers could greatly benefit from the photometric investigation of Chapter 3 by collecting spectra for the photometrically analyzed stars.

4.2 Previous work

Since new technology telescopes and instrumentation became powerful enough to conduct time-resolved spectroscopic observations of extragalactic binary stars, various authors attempted to derive absolute parameter of such systems. First important results were published by Guinan et al. (1998) and Ribas et al. (2000), who combined UV spectroscopy with photometric data to derive accurate parameters of a single LMC system.

Clausen et al. (2003) analyzed four eclipsing binaries in the LMC and SMC with uvby photometry combined with spectroscopic observations the VLT-UVES spectrograph.

Besides this pioneering work, a few other studies of specific individual systems were published; e. g. Ribas et al. (2002), Fitzpatrick et al. (2002) and Fitzpatrick et al. (2003) derived absolute parameters for binaries in the LMC.

Recently, Harries et al. (2003) and Hilditch et al. (2005) published the first large-scale studies of absolute parameters and distances of SMC binaries with 10 and 40 individually analyzed systems, respectively. Some of the caveats regarding these investigations were, however, mentioned earlier.

4.3 Available data

Since despite best efforts no observation time could be secured at suitable instruments, existing spectra had to be used to apply the FITSB2 software to determine atmospheric parameters. Since a pioneering group (Harries, Hilditch and Howarth) in the field of extragalactic binary research had secured suitable data of SMC binaries with the same instrument that had been proposed to be used for this work (2dF at AAO), it was decided to analyze their data with the approach described in this work and possibly derive parameters of better accuracy based on a more “physical” model. The published results of their work can be found in Harries et al. (2003), where they describe their method and present the analysis of the spectra of 10 SMC binaries and of light curves from the OGLE archive. Hilditch et al. (2005) extended the analyzed sample to 40 stars. Differences between this work and that of Harries et al. (2003) will be discussed in detail in the presentations of the analyzed stars (see Section 4.7) as well as in the conclusions in Chapter 5.

The spectra were gathered at the Anglo-Australian 3.9 m telescope with the 2dF multi-object spectrograph. With this instrument it is possible to secure 400 spectra simultaneously, distributed over two fields feeding two spectrographs via fiber links. With its 2° field of view it is predestined to observe a large number of objects spread-out over large areas like the Magellanic Clouds. Details about the instrument can be found in Lewis et al. (2002). Both fields, containing 124 SMC binaries, were integrated two times for 15 minutes, amounting to a 30 minute exposure of each observation. With these settings, typical S/N values of 30 can be achieved for these objects. Binaries contained in only one of the fields were observed about 16 to 18 times in total, objects within the overlapping part of both fields usually have more than 30 phase points. The spectrograph grating used in the observing runs resulted in a continuous wavelength coverage from 3900 Å to 4900 Å where many important absorption lines like $H\beta$, $H\gamma$, $H\delta$, several He I and in case of very hot stars also He II lines are found. The analysis of much weaker metal lines is not appropriate because of a too low S/N .

4.4 Data selection

For this work, binary spectra obtained by Harries et al. (2003) at the 3.9 m AAT telescope of the Anglo-Australian Observatory (AAO) equipped with the 2dF multi-object spectrograph were selected. These have been secured during a total of nine nights distributed over three observation runs in the years 2001, 2002 and 2003. Only data from seven nights in 2001 and 2003 could be used since the spectra from 2003 were focussed so poorly on the CCD plane that the reduction was difficult and the spectra were not usable. The other spectra usually have an adequate S/N ratio of about 30. The objects were selected such that a variety of systems with a broad range of orbital periods, relative sizes, masses and values of effective temperatures were covered.

After a two-year proprietary period all data secured at the AAT can be retrieved from the AAT archive or downloaded via FTP server upon user request. With prompt assistance by the very helpful staff, the raw data could be downloaded without problems. The OGLE

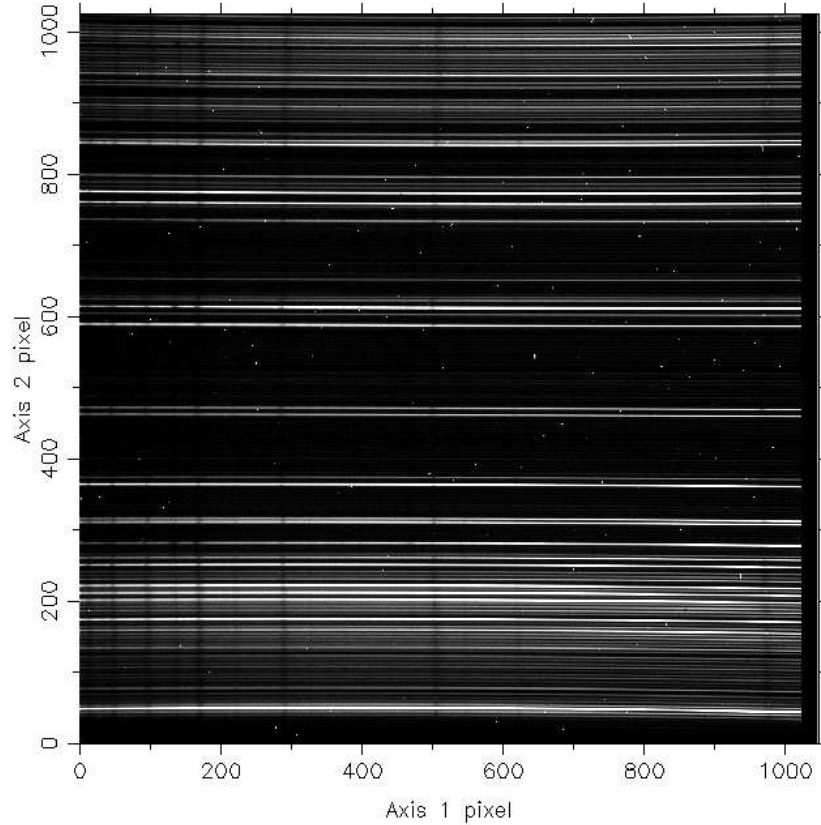


Figure 4.1: A typical raw image from the 2dF multi-object spectrographs. The spectra from different objects are visible with the wavelength dispersion acting in horizontal direction. The exact position of each spectrum has to be determined before its extraction from the image by using so-called “tramlines”.

I light curves associated with the selected systems were taken from the internet archive of the OGLE database (see Section 3.3.2). Additionally, the MACHO archive (see Section 3.3.3) was checked for light curves of the stars in question. Indeed, MACHO light curves did exist for some of the analyzed stars, so that in these lucky cases photometry in three different passbands (*I*, *R* and *V*) with very good phase coverage was available for light curve analysis.

4.5 Data preparation

4.5.1 Spectroscopic data

Since the spectroscopic data was still in raw format, it had to be reduced first. For this purpose a semi-automatic reduction software called 2DFDR is available from the AAT website. It has a graphical user interface and is relatively user-friendly. With some user interaction, it can reduce entire observation runs at once. In this case, the procedure was a little more problematic, since the data used for this work was some years old while

the 2DFDR software package is adjusted for the format of recent 2dF and AAOMEGA data. One special issue which required great care was the adjustment to the so-called “tramlines” before each reduction run. These are the coordinates of the lines on the CCD surface in which the spectra from the individual fibers are aligned. They tend to shift and bend between observations, so in order to accurately extract the individual spectra, one has to check and possibly adjust the coincidence of the tramlines with the actual positions of the spectra before the reduction of each observation (see Fig. 4.1). Once this step is complete, the software automatically extracts fiber flat fields, bias frames, spectra and calibration frames. They are processed accordingly and the two subsequent 15-minute science frames of each observation are automatically added up to one 30-minute frame containing the reduced spectra of all stars. From there, the data of the individual spectra can be extracted in ASCII format for further processing. The spectrum of the relevant star is extracted from each observation in which it is contained. If the star is situated in the overlap of both 2dF fields, it may be contained in ~ 35 single frames. The extracted ASCII files are modified by some additional data needed for orbit analysis (for example date and time of mid-exposure, exposure time and coordinates of the object) and then directly serve as input for FITSB2. Normalization of the continua is not necessary, since FITSB2 does this automatically via pre-defined “continuum windows” around the absorption lines chosen for fitting.

4.5.2 Photometric data

The preparation of the MACHO light curves was performed according to the description given in Section 3.5.1. The OGLE light curves were treated similarly, with some exceptions: for instance, it is not necessary to apply a calibration of instrumental magnitudes, since the data is readily available as standard *I* band photometry. The OGLE light curves were also not phase-binned, since the phase coverage is not as good as that of MACHO data, so too much information would have been lost by applying a binning procedure. Instead, the complete light curve data is used as input for MORO, along with the MACHO photometry. Due to the long time base of the MACHO photometry, it can be used to determine the orbital period very precisely. This way the periods given by Udalski et al. (1998), which were also used by Harries et al. (2003), could be considerably improved.

4.6 Combined spectroscopic and photometric analysis

The concept of this analysis was to use a purely physical approach whenever feasible. Some binary parameters can be derived from spectroscopic data alone, though mostly not with sufficient accuracy. However, one of the most important parameters, the orbital inclination, can only be determined by light curve analysis. This in turn requires a spectroscopically determined mass ratio. For data of relatively low signal-to-noise it is also desirable to constrain the temperature ratio during spectrum analysis to the value derived

from the light curves. As has been demonstrated in Chapter 3, the temperature ratio can be extracted from the light curves very precisely, even without knowledge of the mass ratio (which should be assigned a reasonable value, though).

4.6.1 Parameter adjustment

The technique used for parameter adjustment during photometric analysis was identical with the one described in Section 3.6, with the exception that the mass ratio q was input directly from the analysis of the spectra and not photometrically adjusted over a wide range of possible values. This reduced the computational demands significantly, of course. The reduced spectra were fed into FITSB2 along with a pre-defined set of spectral lines to be fitted and a list of start parameters. Usually the $H\beta$, $H\gamma$, $H\delta$ and $H\epsilon$ lines were fit together with the He I lines at 4026, 4388 and 4471Å. Only for very hot stars the He II line at 4686Å was taken into account. The parameters to be adjusted need to be set to reasonable initial values. These include the following:

- Effective temperatures T_1 and T_2 , as well as surface gravities $\log g_1$ and $\log g_2$ were taken from Harries et al. (2003). In that publication, the temperatures are assigned according to spectral type, while the surface gravities are calculated from stellar masses and radii. Both methods are not nearly as accurate as desirable, nevertheless the values serve as reasonable starting points.
- Approximate radial velocity amplitudes K_1 and K_2 and the system velocity γ were taken from Harries et al. (2003) as well.
- Rotational velocities of the stars were not considered by Harries et al. (2003), therefore these were initially calculated under the assumption of synchronous rotation of both components.

Parameters which are pre-defined and are not adjusted during the analysis:

- Heliocentric Julian Date HJD0 serves as designation of the zero point in phase and was taken from Udalski et al. (1998). In most cases, the published values proved sufficiently accurate and no further processing was required. Where necessary, small corrections were applied until all light curves had their primary minima exactly at phase 0. It is important to note that the zero-phase definitions of MORO and FITSB2 differ by exactly 0.5 in phase: while MORO expects the secondary component to be in front of the primary at phase 0 (primary minimum), FITSB2 assumes the primary in front of the secondary. Therefore HJD0 was set to differ by 0.5 times the orbital period between spectra and photometric data.
- Orbital periods P are newly determined for each star, as the values given by Udalski et al. (1998) and adopted by Harries et al. (2003) are not as accurate as possible, as discussed in Section 4.5.2.

- Scale factor L_2/L_1 (denoting the phase-dependent luminosity ratio of the binary components) was taken from the solution of the light curves. It had to be separately calculated for each point in phase for which a spectrum was available so that the changing relative line strengths (due to tidal distortion or eclipse effects) could be fitted accordingly.

After having checked that the start parameters give reasonably good fits to the observed spectra, the first step in the parameter adjustment was the determination of the systemic velocity γ and the radial velocity amplitudes K_1 and K_2 . Since the actual radial velocities of each spectrum depend on the Julian Date of observation and the orbital period in FITSB2's "orbit mode" (see Section 2.2.3), and just the maximum amplitude is a free variable, they can be determined quickly and unambiguously. From these, a very accurate mass ratio can be derived immediately as $q = M_2/M_1 = K_1/K_2$. This was then used to derive preliminary values of the photometrically accessible parameters (orbital inclination i and effective temperature ratio. In a next step, the rotational velocities $V_{\text{rot},1}$ and $V_{\text{rot},2}$ were adjusted. Initial values for the surface gravities which cause varying broadening of the spectral lines could be taken from Harries et al. (2003).

Then the parameter determination entered a computationally more demanding phase. The effective temperatures T_1 and T_2 , as well as the surface gravities $\log g_1$ and $\log g_2$ were adjusted. This is where the quality of the grid of synthetic spectra used for fitting came into play. For the analysis synthetic spectra were used which are based on state-of-the-art NLTE model atmospheres by Hubeny & Lanz (1995) specifically adjusted for the prevalent metallicity of the SMC, which is widely accepted as $\approx 1/5$ of the solar amount. The resulting synthetic spectra of O- and B-stars are discussed in detail in Lanz & Hubeny (2003, 2007). As a crosscheck another set of synthetic spectra was used based on the new models by Nieva & Przybilla (2007). These spectra based on the first method were provided by Przybilla (2007), while those by Lanz & Hubeny (2003, 2007) were downloaded from the WWW via the TLUSTY homepage <http://nova.astro.umd.edu/>. It became evident that the parameters derived from the different approaches are very consistent, with differences not exceeding their respective error margins.

Only after the first independent determination of effective temperatures these were constrained to the photometrically derived temperature ratio during all further iterations where it was necessary. An independent spectroscopic adjustment of both temperatures was always conducted and compared with the photometric temperature ratio before launching the full parameter adjustment. Mostly, photometrically and spectroscopically derived temperature ratios were very consistent, though.

After effective temperatures and surface gravities had been established to the desired accuracy, γ , K_1 , K_2 , $V_{\text{rot},1}$ and $V_{\text{rot},2}$ were reiterated to achieve an optimum fit, as the small changes caused by the adjustment of temperature and surface gravities could have influenced the values slightly. The resulting new (usually very similar) value of q again served as input for the light curve analysis procedure which was executed again to optimize the photometric fit, yielding a new value for the orbital inclination i as well as (very small) corrections for the temperature ratio. Along with the updated temperature ratio, in a final run all parameters were then adjusted simultaneously by FITSB2. During this last run

the bootstrap error assessment was activated (see Sections 2.2.4 and 3.6.4). This was by far the most time-consuming step in the entire analysis as the multiple runs of the fitting routine required by the bootstrap method typically took days or even weeks.

After completion of the FITSB2 run, a final MORO run of similar extent was executed with active bootstrap error processing routines as described in Section 3.6.4 in order to yield a final value of the orbital inclination i along with a realistic error.

4.6.2 Absolute parameter determination

From the combined spectroscopic and photometric analysis discussed in Section 4.6.1 all absolute parameters of the investigated binaries could be derived, including their orbital separation, masses, radii and distance. An overview of the necessary prerequisites has been given in Sections 1.3 and 1.4. The actual procedure used for parameter determination and especially distance determination is quite intricate and is now described in more detail.

From the spectrum analysis the velocity semi-amplitudes $k_1 = v_1 \sin i$ and $k_2 = v_2 \sin i$ can be derived while the analysis of the light curves yields the orbital inclination i . Substituted in Eq. (1.7) these parameters give the absolute mass of the secondary component. The primary mass is immediately obtained via the mass ratio $q = M_2/M_1 = k_1/k_2$.

From the sum of the absolute masses and the orbital period of the system the orbital separation can be derived in absolute units via Eq. (1.1). The radii of the components relative to the separation of the stars are determined via light curve analysis. Together with the orbital separation they yield the absolute radii of both stars. As has been discussed in Section 3.7, these are given as “volume radius”, i. e. as radius of a hypothetical sphere with the same volume that the (tidally deformed) star actually has.

With the effective temperatures derived directly from the spectroscopic analysis, all absolute parameters of the stars are known at this point. Based on the absolute luminosity the distance of the objects can be determined. It is commonly presented in the form of the distance modulus

$$m_I - M_I = -5 + 5 \log d + A_I \quad (4.1)$$

with the interstellar absorption A_I . This readily yields the distance in parsec (pc). m_I and M_I are to be evaluated in the same spectral passband, of course. OGLE photometry is taken in a proprietary I band and then converted to the standard I system defined in Bessell (1990). The details of the conversion can be found in Udalski et al. (2002). Great care has been taken to comply exactly with the standard I band, and especially for blue stars systematic deviations should be almost non-existent.

To derive m_I for each component of a given binary, the flux ratio in the I band is substituted into

$$m_I^n - m_I = -2.5 \log \frac{L_n}{L_1 + L_2}, \quad (4.2)$$

with n denoting the component index 1 or 2. The resulting value has then to be modified in order to account for interstellar absorption A_I . In principle, A_I is determined from the reddening $E(B - I)$. The measured colors and I band magnitudes taken from the OGLE

database show subtle differences from the values given by Harries et al. (2003), the reason for which is unknown. They should not be the cause for severe deviations, though. After the interstellar absorption has been properly taken into account, the resulting I magnitude has to be converted to the I band flux in order to be compared with the absolute flux emitted by the star. For this the zero-point calibrations given by Bessell et al. (1998) are used. The same relations were chosen by Harries et al. (2003), facilitating comparison between their work and the parameters derived here.

To be properly compared with the local flux, the absolute flux of each star in the I passband has to be calculated. This can be achieved by synthetic spectroscopy. First a synthetic spectrum is produced with the parameters derived from spectral analysis. For this purpose, the BSTAR2006 and OSTAR2002 grids by Lanz & Hubeny (2003, 2007) are used as they give absolute fluxes over a wide wavelength range. The actual T_{eff} and $\log g$ values are interpolated linearly in these grids. The resulting absolute-flux synthetic spectrum is then convolved with the standard I passband to yield the absolute flux being transmitted through this filter per unit surface area of the radiating star. To yield the total I band luminosity, this value is multiplied by the surface area of the star which is readily computed from the absolute radius derived earlier. The distance can then be calculated with Eq. 1.14 and substituted in Eq. 4.1 to yield the distance modulus. The procedure is repeated independently for both components of each analyzed binary. The mean value of both distance moduli is then accepted as the distance modulus of the binary in question. The results are given for each individual object in Section 4.7.

4.7 Results for individual objects

This section presents the results gathered from the combined analysis of photometric and spectroscopic data of five eclipsing binary systems in the SMC. The selected stars are examples to illustrate how powerful the presented method is to derive accurate absolute parameters. Each analyzed system will be presented in a similar fashion like the photometrically analyzed systems of Section 3.7. Light curves will be shown together with best fits, and pseudo-3D representations of their geometrical shapes will be displayed. Additionally, examples for fitted stellar absorption lines are shown. Since photometric and spectroscopic data has been analyzed simultaneously, tight constraints can be placed on the absolute parameters. These parameters will be given in tables together with the errors derived by application of the bootstrap method. The consistency between independently derived photometric and spectroscopic results will be discussed, such as the effective temperature ratio of the binary components.

Among the most important results will be the determined distances to the stars. The quality and reliability of these will be emphasized. The given errors are fully and consistently propagated from the bootstrap errors of the photometrically and spectroscopically determined relative and absolute parameters through to the distance and distance modulus, including effective temperatures, masses, radii, orbital separation, orbital inclination, apparent magnitude, luminosity ratio and interstellar absorption.

The OGLE stars will be designated with their identifiers from the OGLE catalogue. An example for these identifiers is OGLE 5 38089, which means that the object is No. 38089 in the 5th of 11 fields with which the OGLE survey covered the SMC.

4.7.1 OGLE 9 175323

m_I [mag]	P [d]	$T_{\text{eff},1}$ [K]	Conf.
13.8	2.206045	37474 ± 819	CO

Just like MACHO 547 (see Section 3.7.4) in the photometric part of this work, OGLE 9 175323 is one of the very rare examples of binary systems in which both components accurately fill their respective Roche lobes. It is very fortunate to have the opportunity to analyze two of this remarkable kind of star in this work. OGLE 9 175323 is similar in many respects to MACHO 547. Fortunately, in this case spectroscopic data is available in addition, so all parameters can be determined to very good precision. OGLE 9 175323 is an especially bright system with an I magnitude of about 13.8 mag. Therefore it is clear that this binary consists of very luminous components exhibiting high effective temperatures. Unfortunately, no light curves were available from the MACHO survey for this system, so the analysis had to be limited to the I band photometry of OGLE alone. The light curve is of good quality, the overall scatter is a bit larger than average for other OGLE data in this work, though (see Fig. 4.2). This is especially remarkable in light of the fact that it is one of the brightest of all systems analyzed. Possibly there is a problem with field crowding. The phase coverage, on the other hand, is quite favorable. The orbital period of the system was derived as 2.206045 days.

The fit of the I light curve is very good with no obvious systematic deviations through the entire phase range. The light curve displays all the characteristics expected for a contact system. A strong out-of-eclipse variation is present owing to the significant tidal distortion of both components; in this case it is however attenuated by the low orbital inclination which reduces the depths of the minima to only little more than 15%. Additionally, the ingress and egress points of the actual eclipses are barely discernible, but still visible upon close examination of the light curve at a light level just above 90%. It is remarkable that more than half of the complete light curve amplitude is caused by tidal distortion, while the impact of the eclipses is smaller. In a similar way other factors influencing the light curve shape become less significant with decreasing orbital inclination. Therefore

i [deg]	56.97 ± 0.22
T_1 [K] (fixed)	37474
T_2 [K]	36701 ± 589
R_1/a	$0.424 \pm \text{N/A}$
R_2/a	$0.337 \pm \text{N/A}$
$L_1/(L_1 + L_2)$ in I	0.618 ± 0.003
$L_2/(L_1 + L_2)$ in I	0.382 ± 0.003

Table 4.1: Parameters of OGLE 9 175323 derived from the photometric analysis shown together with 1σ bootstrap errors. Errors for the relative radii are not available because the surface potentials were fixed to a contact configuration and the radii are therefore entirely determined by the mass ratio inferred from spectroscopy.

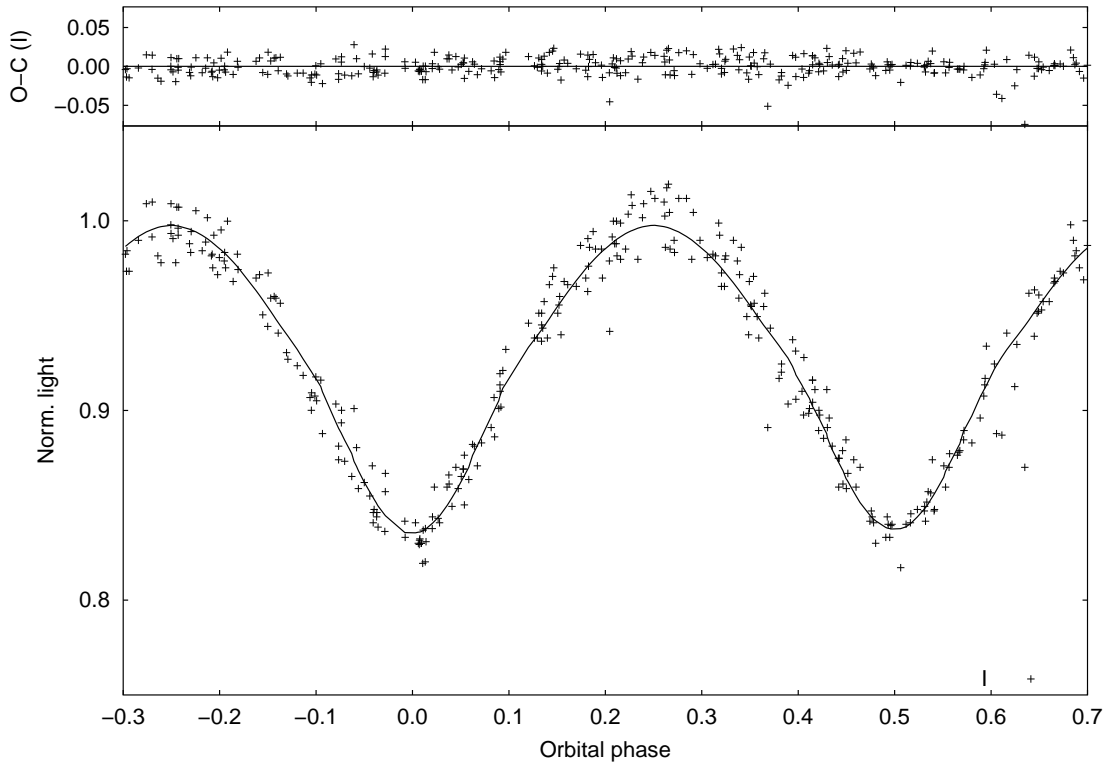


Figure 4.2: *I* light curve of OGLE 9 175323 shown together with best fit. For clarity, error bars of the individual data points are omitted. Note the scale of the ordinate is much larger than for the other systems in this work as the light change is quite small due to the low orbital inclination of OGLE 9 175323.

it is very important to check the photometrically derived parameters for consistency with the spectroscopic results.

As already indicated by its enormous brightness, spectral analysis confirmed that OGLE 9 175323 contains very hot stars of spectral types O7 and O8, respectively. These spectral types disagree with those found by Harries et al. (2003) through visual classification. Since this work is built on a quantitative analysis of the spectra and not just on a quali-

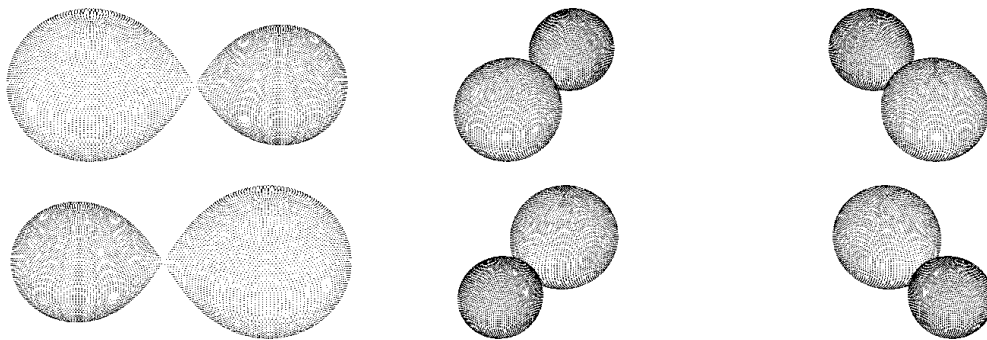


Figure 4.3: 3D plots of OGLE 9 175323 at different orbital phases.

T_1 [K]	37474 ± 819
T_2 [K]	36701
M_1 [M_\odot]	27.4 ± 1.4
M_2 [M_\odot]	16.6 ± 0.7
R_1 [R_\odot]	10.6 ± 0.1
R_2 [R_\odot]	8.4 ± 0.1
$\log g_1$ (from $g = GM/R^2$)	3.82 ± 0.03
$\log g_2$ (from $g = GM/R^2$)	3.80 ± 0.02
$\log g_1$ (from spectra)	4.02 ± 0.05
$\log g_2$ (from spectra)	3.41 ± 0.02
a [R_\odot]	25.0 ± 0.3
$v_1 \sin i$ [km/s]	182.0 ± 4.0
$v_2 \sin i$ [km/s]	301.2 ± 4.9
γ [km/s]	187.7 ± 3.05
$v_{\text{rot},1} \sin i$ [km/s]	208.5 ± 5.3
$v_{\text{rot},2} \sin i$ [km/s]	224.5 ± 5.1

Table 4.2: Absolute parameters of OGLE 9 175323 derived from spectroscopic and photometric analysis shown together with propagated 1σ bootstrap errors. The secondary temperature was fixed to the photometrically derived value in this case.

tative classification scheme, it seems reasonable to favor the temperatures and according spectral types derived here. One must keep in mind that the spectral type-temperature calibration becomes increasingly difficult for extremely early-type stars, therefore some discrepancies between different researchers and their methods must be expected. It is clear that these very hot stars exhibit He II absorption lines. As can be seen in Fig. 4.4, the contributions of both components to the superimposed line profile can be resolved in the spectra. The spectroscopic observations are of good quality with a high S/N ratio due to the relative brightness of the system. The spectroscopically derived temperature of the secondary component tended to be about 2000 K lower compared with the photometric value. Since temperature ratios determined from light curve analysis are very reliable and also showed smaller bootstrap errors in this case, the photometric values were preferred and the secondary temperature fixed in the spectroscopic fit process. Both components seem to rotate somewhat faster than would be expected for tidally locked stars. It is however reasonable to assume that both components actually do rotate synchronously and there were possibly some problems with extracting these parameters from the spectra in this case. One should bear in mind that the precision of quantities derived from Doppler shifts like the rotational velocities is reduced by the low orbital inclination of the system. Also, the values for $\log g$ derived from the spectra deviate somewhat from the ones derived from masses and radii. This is an indication to exercise caution with extracting parameters of more subtle influence from stellar spectra under these circumstances. The systemic velocity of about 188 km/s is perfectly consistent with the overall radial velocity of the SMC.

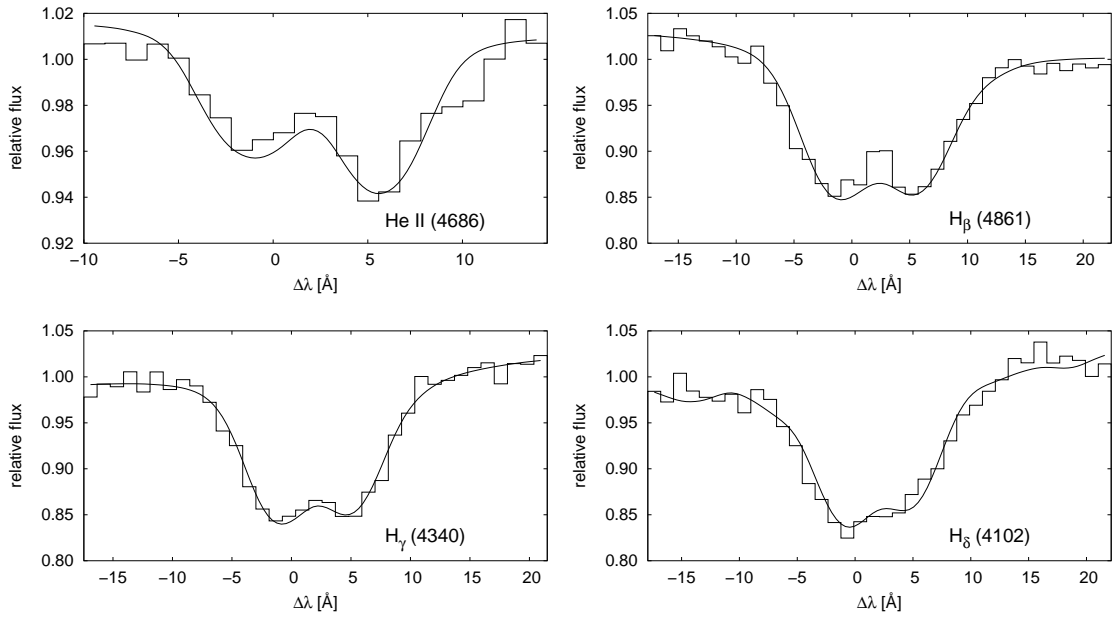


Figure 4.4: Spectral line fits of OGLE 9 175323 shown together with observational data for orbital phase 0.81 (between second quadrature and primary minimum).

The fits of the spectral lines generally are of good quality. The He II fits are not perfect, though, as can be seen in Fig. 4.4. It should be mentioned that in the case of extreme O-type systems like OGLE 9 175323 complicating factors like stellar winds and wind collision zones – which are not modelled by the fitting software – lead to distortions of

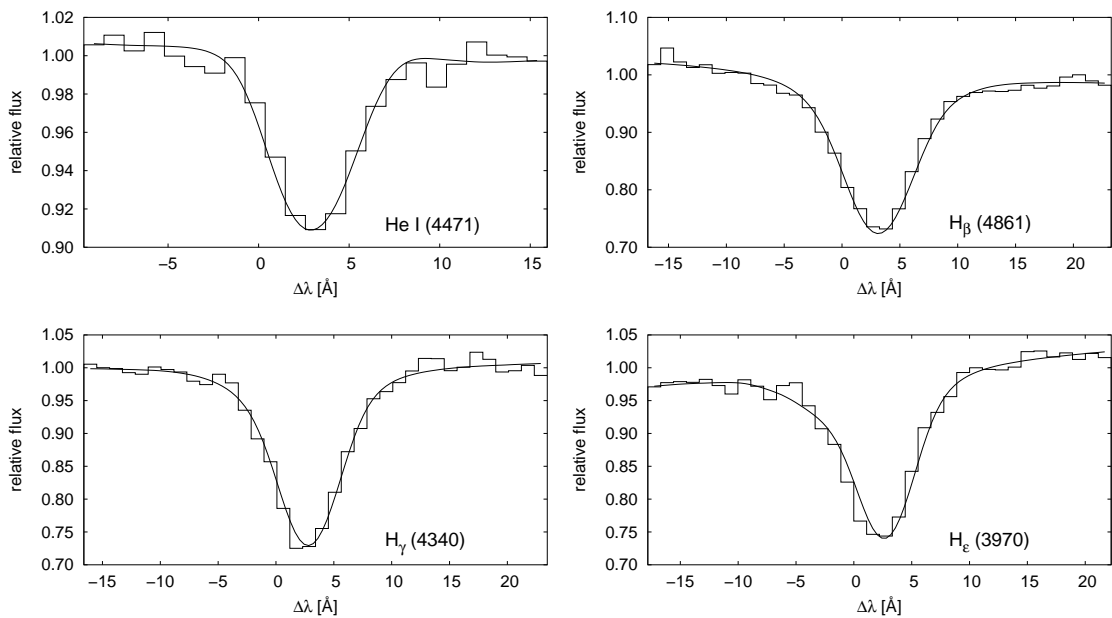


Figure 4.5: Spectral line fits of OGLE 9 175323 shown together with observational data for orbital phase 0.02 (during primary eclipse).

the light curve and also influence the line profiles. Some emission is seen in the center of the $H\beta$ line which may be caused by circumstellar matter or adjacent nebulosity like in the case of OGLE 5 38089 (see Section 4.7.4). It is much weaker in this case, though. Only 18 usable spectra were available for OGLE 9 175323, so it was necessary to use as many lines as possible to derive reliable parameter values. The fits in Fig. 4.5 show how good the method of a variable scale factor works even during eclipses. These spectra were taken right at the center of primary eclipse, and still the fits are very good and consistent with those of other orbital phases.

From the derived absolute parameters the distance was individually determined for both components of OGLE 9 175323. Note that the secondary temperature was fixed to the photometrically derived value. The excellent agreement between the independently derived distances to both stars shows that the photometric temperature ratio should normally be trusted if deviations from the spectroscopic value exist:

component	distance [kpc]	dist. mod.
primary	59.5 ± 1.9	18.87 ± 0.07
secondary	60.0 ± 1.0	18.89 ± 0.04
both	59.7 ± 1.1	18.88 ± 0.04

Had the spectroscopically derived secondary temperature been used, a discrepancy in the distances in excess of the error margins would appear. The distance derived is fully compatible with the general distance of the SMC and has a remarkably small uncertainty.

4.7.2 OGLE 11 30116

m_I [mag]	P [d]	$T_{\text{eff},1}$ [K]	Conf.
15.0	2.954203	27349 ± 513	SD

OGLE 11 30116 is clearly in a semi-detached configuration (see Fig. 4.7). No other configurations were compatible with the light curves of the system. The quality especially of the OGLE I band curve is quite good, in spite of a few phase gaps during both eclipses. Fortunately, the MACHO V and R light curves cover this region and also the secondary eclipse more densely. The scatter of these measurements is somewhat higher than that of the OGLE light curve, however. The semi-detached configuration is evident from the strong out-of-eclipse variations of the light curves while very deep primary eclipses with light loss of about 50% indicate components of comparable sizes and a high orbital inclination. The system reaches a brightness of $m_V = 14.6$ and $m_I = 15.0$. An orbital period of 2.954203 days is derived, leaving room for large, possibly evolved components.

The fits to the light curves are generally good. There are however two effects of close binary interaction apparent (see Fig. 4.6). First, there is an asymmetry of the shoulders of the primary minimum. Such a feature cannot be modelled by MORO, therefore systematically negative residuals are observed during ingress of the primary eclipse. This effect may be due to partial obscuration of the primary star's surface by a matter stream falling in from the Roche lobe-filling secondary component. It is certainly not a measurement artefact since it is clearly observable in all three light curves. There is also indication for the presence of the O'Connell effect causing a slightly unequal height of the maxima. During the first half of the primary minimum there is a slight negative trend of the residuals which is only visible in the I band curve. During the secondary minimum there is no such effect, and it cannot be reproduced in the V and R curves. Therefore it is probably not real and likely an observational artefact due to the poor phase coverage of the I curve.

The light curve solution indicates comparable radii of both stars, but a large temperature difference between the two components. Furthermore, the V band light ratio of $L_2/L_1 \approx 0.44$ indicates that the secondary is overluminous for its derived effective temperature (see Table 4.3). Therefore the cooler secondary star seems to be evolved to a certain

i [deg]	84.62 ± 0.14
T_1 [K] (fixed)	27349
T_2 [K]	20273 ± 64
R_1/a	0.356 ± 0.002
R_2/a	$0.312 \pm \text{N/A}$
$L_1/(L_1 + L_2)$ in I	0.675 ± 0.002
$L_2/(L_1 + L_2)$ in I	0.325 ± 0.002

Table 4.3: Parameters of OGLE 11 30116 derived from the photometric analysis shown together with 1σ bootstrap errors. An error for the relative radius of the secondary component is not available because the surface potential was fixed to a semi-detached configuration and the secondary radius is therefore entirely determined by the mass ratio inferred from spectroscopy.

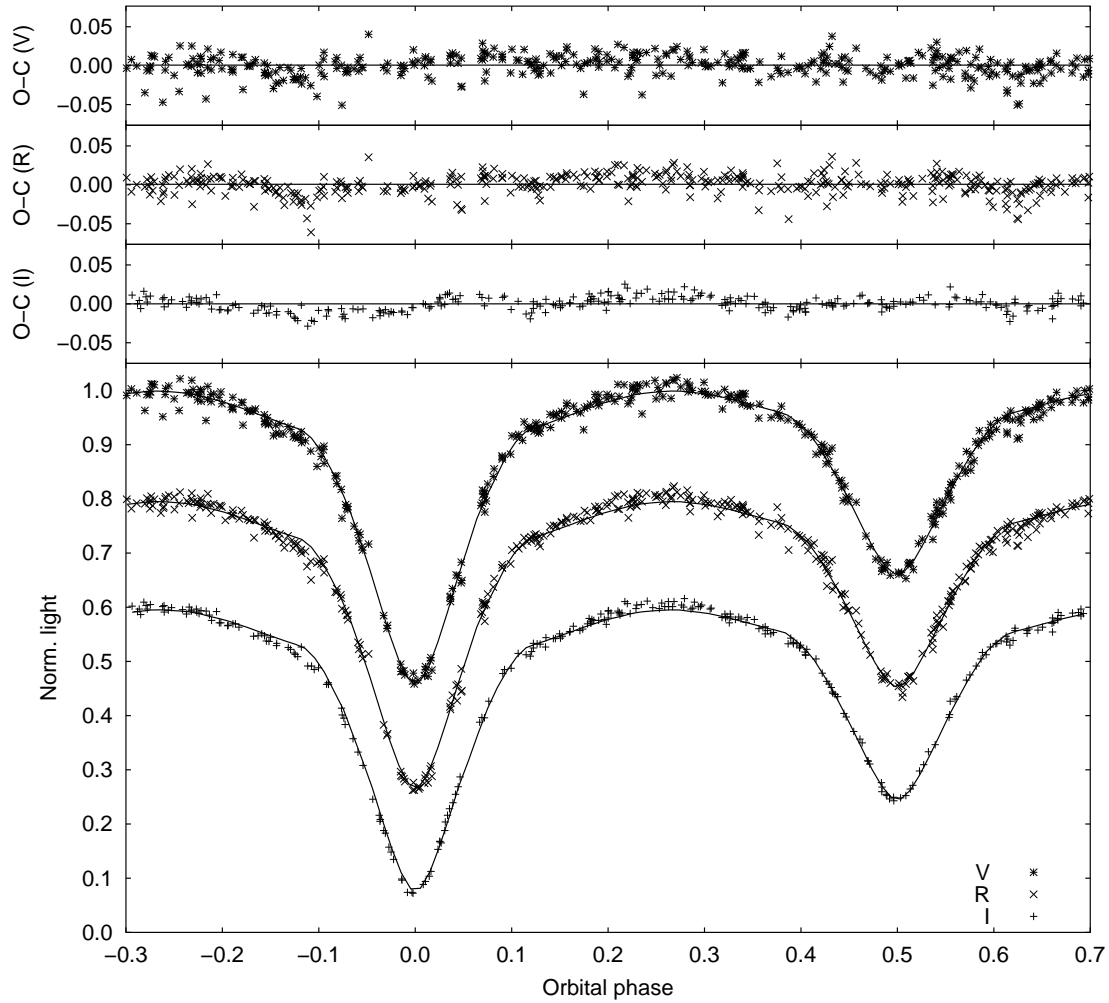


Figure 4.6: *V*, *R* and *I* light curves of OGLE 11 30116 shown together with best fits. For clarity, error bars of the individual data points are omitted and the *R* and *I* light curves are shifted down 0.2 and 0.4 light units, respectively.

degree. This is the typical situation usually met for Algol-type binaries, in which the original primary first evolved and started case A mass transfer until the mass ratio was reverted and primary and secondary exchanged their roles. This finding is confirmed by the analysis of the spectra where the temperature ratio of the stars is reproduced in excellent agreement (see Table 4.4 for absolute system parameters). In this case, it even proved unnecessary to fix the temperature ratio during spectral analysis, as the secondary temperature was derived exactly as suggested by the photometric temperature ratio. The photometrically derived value (with the primary temperature fixed from spectral analysis) of 20314 K is practically identical to the 20300 K determined by spectrum analysis. The temperature of the primary component has been derived as 27350 K, corresponding to spectral type B0.5, with the secondary being classified as spectral type B2. These results are consistent with the visual spectroscopic classification of Harries et al. (2003). The

T_1 [K]	27349 ± 513
T_2 [K]	20300 ± 709
M_1 [M_\odot]	14.5 ± 0.9
M_2 [M_\odot]	6.5 ± 0.3
R_1 [R_\odot]	8.5 ± 0.1
R_2 [R_\odot]	7.4 ± 0.1
$\log g_1$ (from $g = GM/R^2$)	3.74 ± 0.03
$\log g_2$ (from $g = GM/R^2$)	3.51 ± 0.03
$\log g_1$ (from spectra)	3.63 ± 0.04
$\log g_2$ (from spectra)	3.28 ± 0.07
a [R_\odot]	23.8 ± 0.4
$v_1 \sin i$ [km/s]	126.1 ± 3.7
$v_2 \sin i$ [km/s]	280.6 ± 4.8
γ [km/s]	172.3 ± 2.5
$v_{\text{rot},1} \sin i$ [km/s]	233.5 ± 6.5
$v_{\text{rot},2} \sin i$ [km/s]	151.4 ± 11.0

Table 4.4: Absolute parameters of OGLE 11 30116 derived from the spectroscopic and photometric analysis shown together with propagated 1σ bootstrap errors.

low surface gravities indicate that both stars are evolved since values of $\log g \approx 4.0$ would be normally expected for main sequence stars of the observed temperatures. The $\log g$ values derived from spectral analysis are consistently lower than those computed from $g = GM/R^2$. This has to be expected, since the spectroscopically derived values are determined with due account to centrifugal and tidal forces on the surfaces of the fast-rotating stars, yielding effectively lower surface gravities than encountered on a stationary star of same mass and radius.

The rotational velocity of the primary is higher than expected in the case of orbital synchronization. The value for the secondary component is roughly consistent with synchronized rotation, though. The ratio of the orbital radial velocity semiamplitudes yields

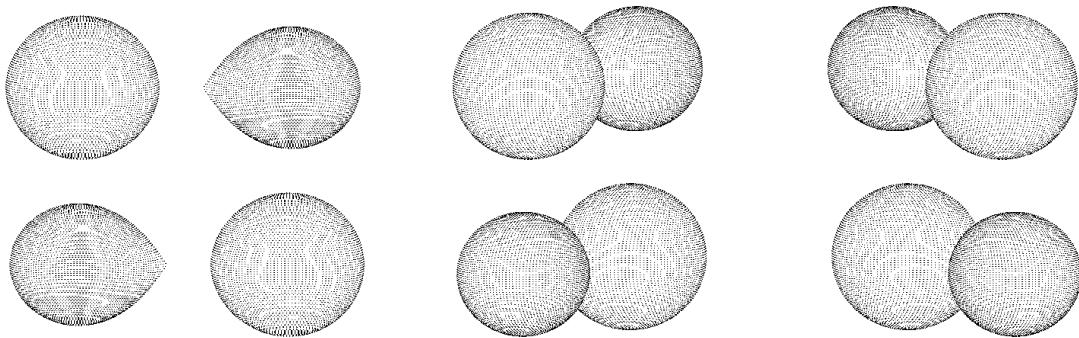


Figure 4.7: 3D plots of OGLE 11 30116 at different orbital phases.

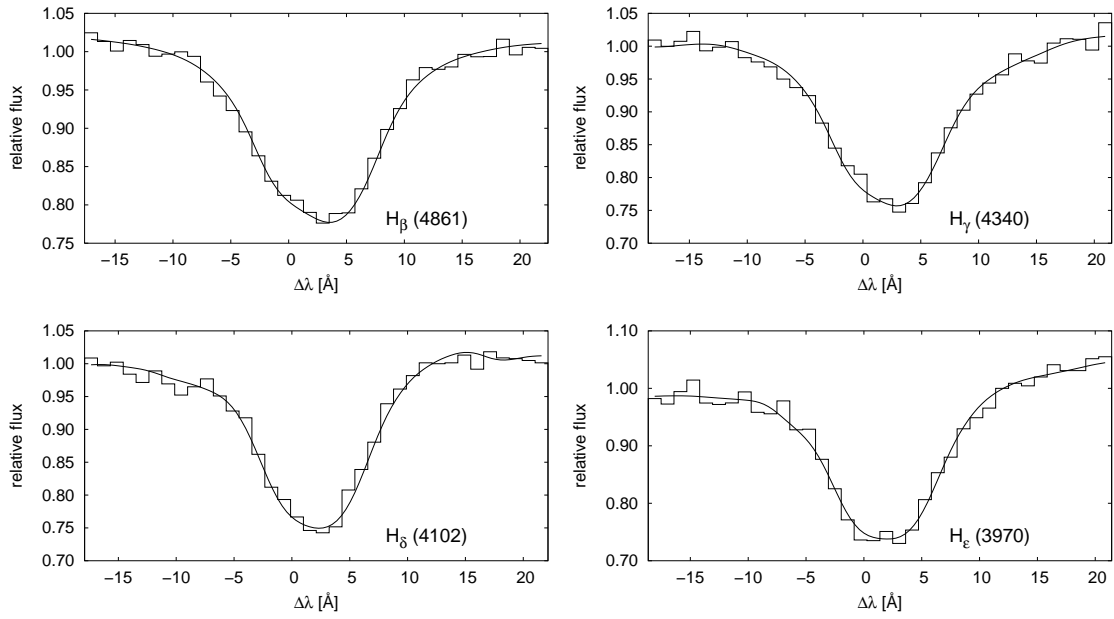


Figure 4.8: Spectral line fits of OGLE 11 30116 shown together with observational data for orbital phase 0.65 (between secondary eclipse and second quadrature).

a mass ratio of $q \approx 0.45$ which has been used as basis for the light curve analysis. The systemic velocity of about 172 km/s is well compatible with the mean redshift of the SMC of about 150 km/s.

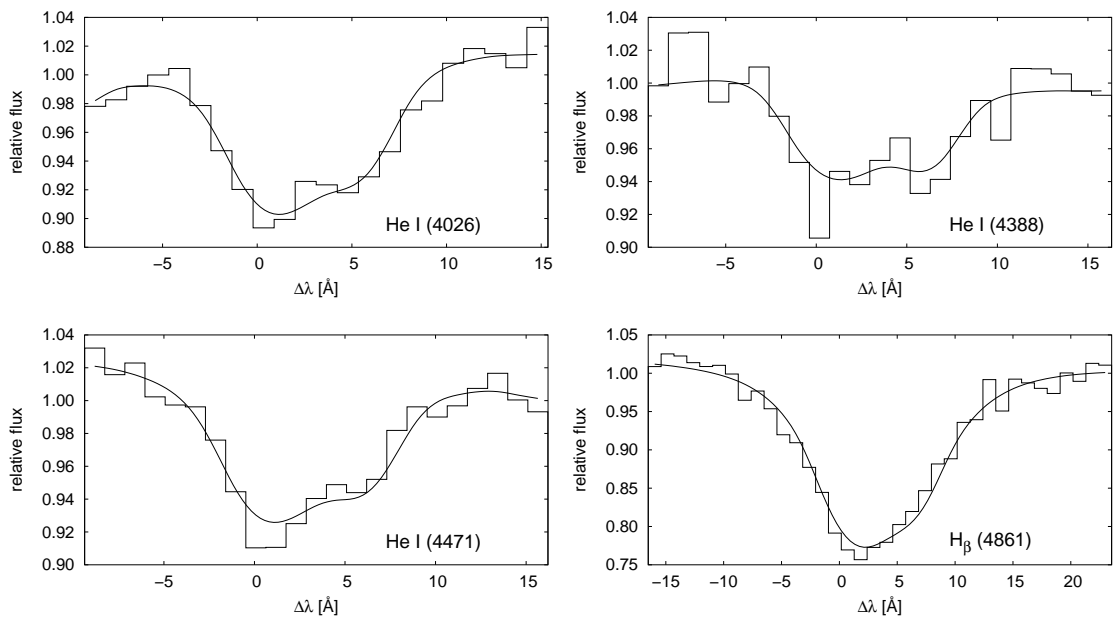


Figure 4.9: Spectral line fits of OGLE 11 30116 shown together with observational data for orbital phase 0.34 (between first quadrature and primary eclipse).

The fits to the spectral line profiles of OGLE 11 30116 are mostly excellent. As can be seen in Figs. 4.8 and 4.9, the lines show a strong rotational broadening so that especially the hydrogen lines of both components are severely blended. There are no systematic deviations of the fits neither with orbital phase nor wavelength. 22 single spectra were available, and all of them were used simultaneously during the fitting procedure.

From the absolute parameters found and its apparent brightness in the *I* band the distance to OGLE 11 30116 can be determined. Via the procedures described in Section 4.6.2 the following values are found:

component	distance [kpc]	dist. mod.
primary	60.0 ± 1.3	18.89 ± 0.05
secondary	59.4 ± 1.9	18.87 ± 0.07
both	59.7 ± 1.1	18.88 ± 0.04

As can be seen the values for both components agree to excellent accuracy and lie well within the error margins of each other.

4.7.3 OGLE 7 243913

m_I [mag]	P [d]	$T_{\text{eff},1}$ [K]	Conf.
14.9	2.631631	32131 ± 173	SD

OGLE 7 243913 is quite similar to OGLE 11 30116 (see Section 4.7.2) regarding its system configuration and light curve shape. It is a semi-detached binary with the second component filling its Roche lobe. Due to the much smaller depths of the eclipse minima it is obvious, however, that OGLE 7 243913 has a lower orbital inclination. The phase coverage of the light curves is reasonable. While the MACHO V and R measurements lack coverage especially in the branches of the primary minimum, the OGLE I band data points are distributed relatively evenly over the orbital phase. The quality of the data is good, with especially low scatter in the OGLE light curve. The strongest noise is found in the MACHO V band. The light curves display strong out-of-eclipse variations, the ingress and egress points of the minima are clearly defined, however. As a result the system cannot be extremely close and the primary star does not fill its Roche lobe. The orbital period was derived as 2.631631 days, the apparent quadrature phase brightness of the system is $m_I = 14.9$.

The light curve fits are convincing, aside from some minor problems (see Fig. 4.10). Just like with OGLE 11 30116, the synthetic light curves show some deviation right before ingress to the primary minimum. This effect is observed in all passbands and therefore certainly no observational artefact. The most likely explanation is again a possible mass stream from the Roche lobe-filling secondary component accreting on the primary component. The circumstellar material between the two stars obviously causes some extinction and the observed dip in the light curve. A similar effect can be noticed just before and after the secondary eclipse. The center of the secondary minimum shows a tendency towards positive residuals, but the effect is very small and its reality doubtful.

As in the case of OGLE 11 30116 the components of OGLE 7 243913 are comparable in size, but display a certain difference in effective temperatures. This effect is however not as large in the latter case, and there is also no significant overluminosity of the secondary component. It probably has evolved into its Roche lobe-filling state still on or very near

i [deg]	74.08 ± 0.07
T_1 [K] (fixed)	32131
T_2 [K]	26334 ± 120
R_1/a	0.357 ± 0.002
R_2/a	$0.311 \pm \text{N/A}$
$L_1/(L_1 + L_2)$ in I	0.639 ± 0.002
$L_2/(L_1 + L_2)$ in I	0.361 ± 0.002

Table 4.5: Parameters of OGLE 7 243913 derived from the photometric analysis shown together with 1σ bootstrap errors. An error for the relative radius of the secondary component is not available because the surface potential was fixed to a semi-detached configuration and the secondary radius is therefore entirely determined by the mass ratio inferred from spectroscopy.

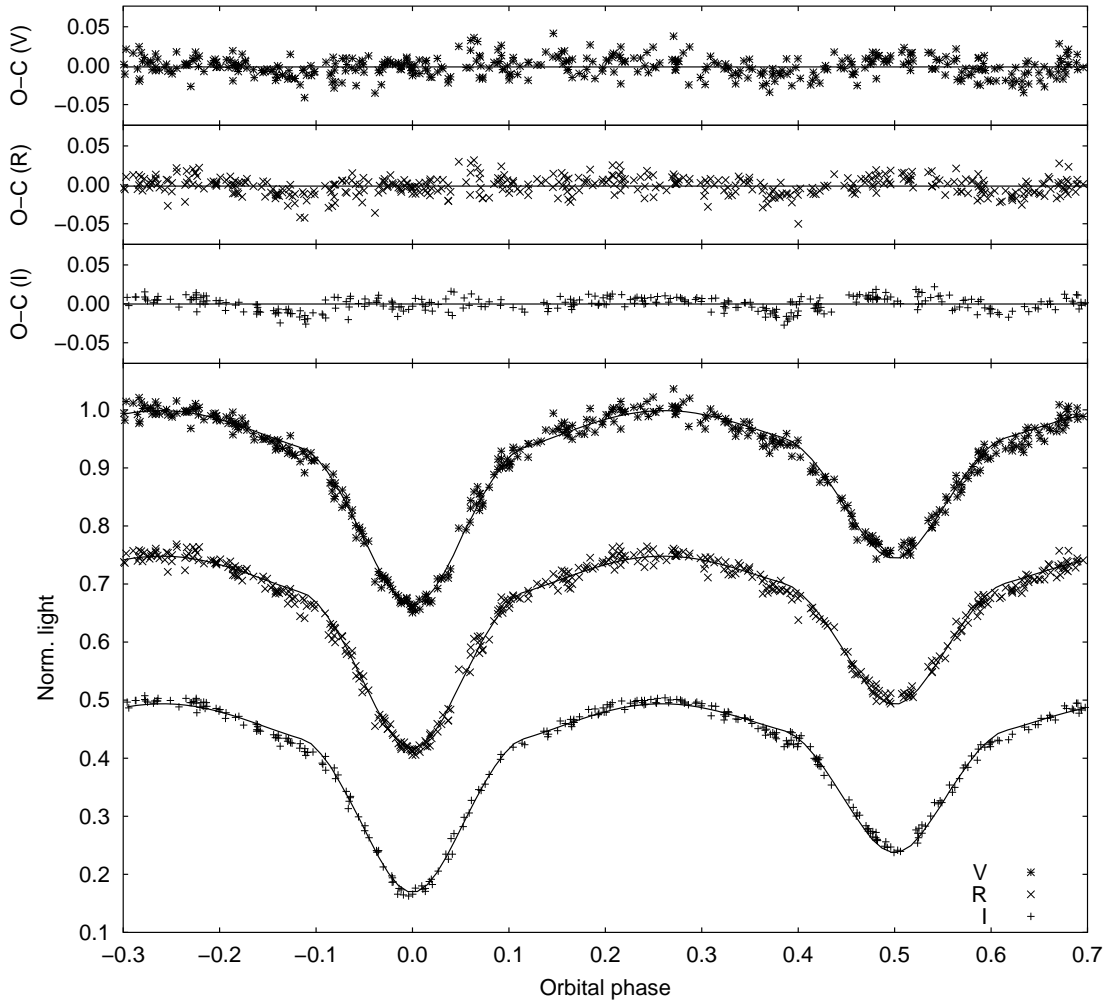


Figure 4.10: V , R and I light curves of OGLE 7 243913 shown together with best fits. For clarity, error bars of the individual data points are omitted and the R and I light curves are shifted down 0.25 and 0.5 light units, respectively.

the main sequence, indicating that it was close to its limiting radius right from the beginning of its existence. Unlike the previously analyzed systems, the photometrically derived temperature ratio could first not be unambiguously reproduced by spectral analysis. The spectroscopically determined value tended to be much too low. Instead of fixing it to the photometric value, it was first tried to solve the problem by a multiple parameter subset approach where not all physical parameters are adjusted simultaneously. Specifically, T_2 and $\log g_2$ were only adjusted in separate subsets. This helps avoid parameter correlation effects and alleviated the problem of the erroneous secondary temperature, leading to agreement between the photometric and spectroscopic values. With about 32000 K and 26000 K the components correspond to O9.5 and B1 stars, agreeing within half a spectral subclass with the classification by Harries et al. (2003). The rotational velocity of the secondary component is compatible with tidally locked rotation, which is to be expected for a

T_1 [K]	32131 ± 513
T_2 [K]	26352 ± 295
M_1 [M_\odot]	19.4 ± 0.7
M_2 [M_\odot]	8.4 ± 0.3
R_1 [R_\odot]	8.6 ± 0.1
R_2 [R_\odot]	7.5 ± 0.1
$\log g_1$ (from $g = GM/R^2$)	3.85 ± 0.02
$\log g_2$ (from $g = GM/R^2$)	3.61 ± 0.02
$\log g_1$ (from spectra)	3.93 ± 0.03
$\log g_2$ (from spectra)	3.66 ± 0.03
a [R_\odot]	24.2 ± 0.2
$v_1 \sin i$ [km/s]	135.8 ± 2.4
$v_2 \sin i$ [km/s]	312.9 ± 3.2
γ [km/s]	183.7 ± 2.1
$v_{\text{rot},1} \sin i$ [km/s]	206.8 ± 5.5
$v_{\text{rot},2} \sin i$ [km/s]	131.2 ± 7.6

Table 4.6: Absolute parameters of OGLE 7 243913 derived from spectroscopic and photometric analysis shown together with propagated 1σ bootstrap errors.

Roche lobe-filling star. The primary seems to rotate somewhat faster than synchronously, but since this component does not suffer from tidal distortion as much as the secondary, this is well possible. The systemic velocity of OGLE 7 243913 is about 180 km/s, which is consistent with the SMC redshift. A mass ratio of $q = 0.43$ can be derived from the radial velocity amplitudes of the stars. During photometric analysis the mass ratio has been fixed to this value. As can be seen in Tables 4.5 and 4.6, the photometrically and spectroscopically derived results are very consistent.

The spectral line fits of OGLE 7 243913 are quite good given the relatively low S/N of the spectra. It is readily apparent, though, that in this system the He I lines are quite affected by the general noise level, and especially the He II profile of the primary com-

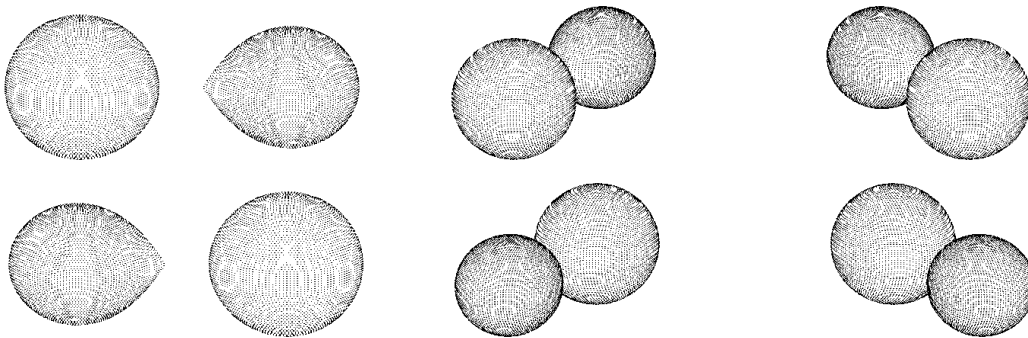


Figure 4.11: 3D plots of OGLE 7 243913 at different orbital phases.

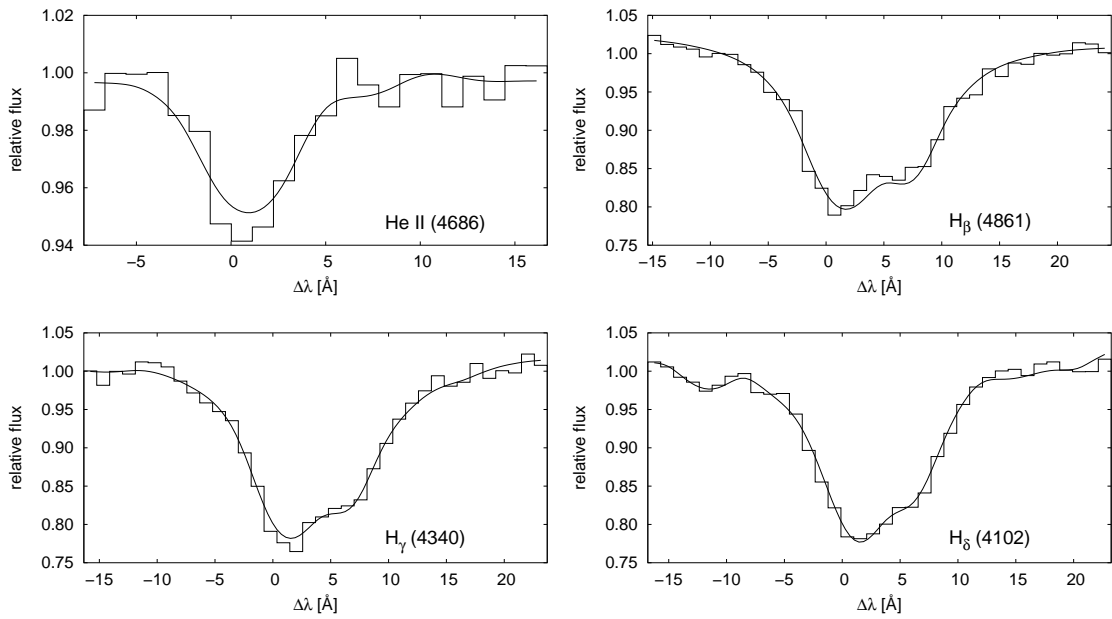


Figure 4.12: Spectral line fits of OGLE 7 243913 shown together with observational data for orbital phase 0.17 (between primary eclipse and first quadrature).

ponent is at some orbital phases barely discernible. 35 single spectra were available for fitting, as OGLE 7 243913 is located in the overlap of two observed fields. Only in rare cases the fits of all observed lines match perfectly at all phase points. Naturally the quality of the observations sets limits to how precise the fits can be. The hydrogen lines, which

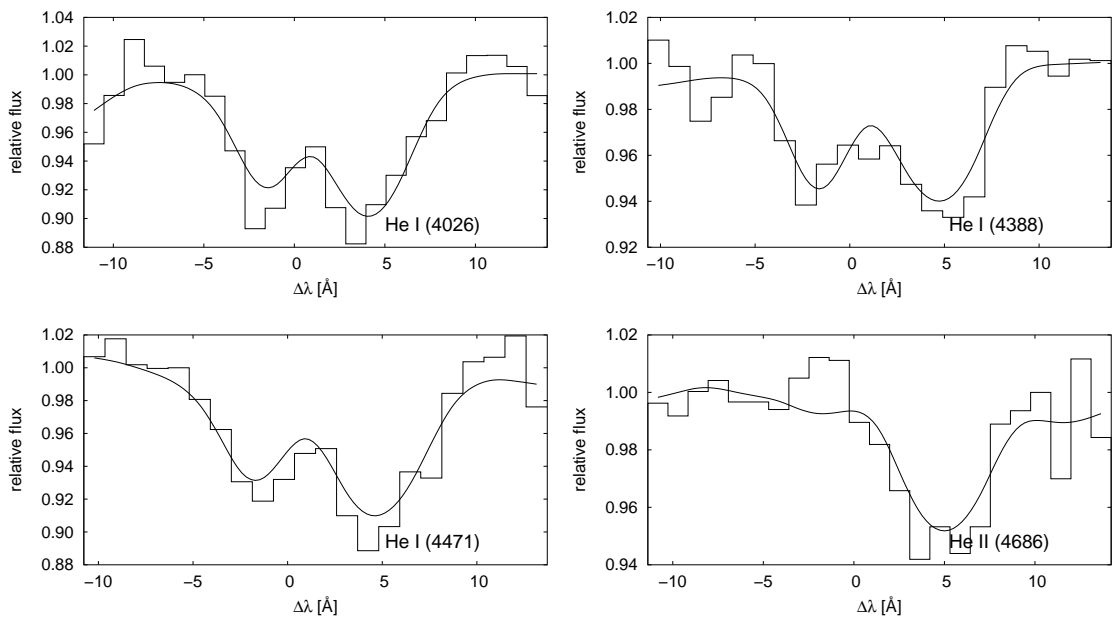


Figure 4.13: Spectral line fits of OGLE 7 243913 shown together with observational data for orbital phase 0.79 (between second quadrature and primary eclipse).

are much stronger than the helium lines, still produce adequate results. A comparison between the lines and the quality of the fits can be made in Figs. 4.12 and 4.13.

According to the procedures described in Section 4.6.2 the distance to OGLE 7 143913 was determined. The following values were derived:

component	distance [kpc]	dist. mod.
primary	67.1 ± 0.8	19.13 ± 0.03
secondary	65.6 ± 0.9	19.08 ± 0.03
both	66.3 ± 0.6	19.11 ± 0.02

Interestingly, the value derived for this system is much larger than the distances determined for the other OGLE stars in this work. Harries et al. (2003) also derive a larger distance to OGLE 7 243913. This is probably a real effect and caused by the system being located towards the far side of the line-of-sight depth of the SMC. As has been discussed in Section 4.7.4, this depth is nowadays assumed to be as large as 10 kpc, so the result is actually consistent with the present knowledge of the structure of the SMC galaxy and may provide valuable information for an even better understanding.

4.7.4 OGLE 5 38089

m_I [mag]	P [d]	$T_{\text{eff},1}$ [K]	Conf.
15.3	2.389431	30401 ± 264	DE

In contrast to most of the other binaries from the OGLE database analyzed in this work, OGLE 5 38089 is in a well-detached configuration. From a cursory inspection of the light curves this is immediately evident, since there is only a small amount of out-of-eclipse-variation and both minima are relatively narrow with well-defined ingress and egress points. The light loss during both eclipses is approximately equal, indicating components of similar temperature. The apparent brightness of the system is about 15.3 mag in both V and I bands and the orbital period amounts to 2.389431 days. The quality of the OGLE I observations is very good with little scatter and acceptable phase coverage, while the MACHO V and R measurements are worse in these respects. Especially the scatter of the R light curve is uncharacteristically large and cannot be compared with any of the systems analyzed in Chapter 3 of this work. The coverage during the secondary minimum is also particularly weak.

Nevertheless, the quality of the fits is very satisfactory, no obvious large discrepancies can be found anywhere through the entire phase range (see Fig. 4.14). There is a very slight tendency of the residuals towards positive values during the entire secondary minimum of the I curve. Although this effect is not discernible in the other passbands, it cannot be excluded, since the significant scatter of the R and V measurements does not allow a judgement of the fit quality in as much detail as in the I band. The effect is very small, though, and mainly concerns the temperature ratio of the components, which is very consistent with the spectroscopically derived value. It must be pointed out, however, that well-detached configurations with relatively low inclination angle do not facilitate a good determinateness of the photometrically derived parameters, especially if the quality of the observations is as low as in the V and R light curves of the present case. It is therefore very important to ascribe large weight on the outcome of the spectroscopic analysis. Therefore, in contrast to the method described in Section 4.6.1, the secondary temperature was not fixed to the photometrically derived value; instead it was freely adjusted by FITSB2. As pointed out above, the good agreement between both independently determined values is very encouraging.

i [deg]	76.99 ± 0.12
T_1 [K] (fixed)	30401
T_2 [K]	30613 ± 164
R_1/a	0.249 ± 0.001
R_2/a	0.253 ± 0.002
$L_1/(L_1 + L_2)$ in I	0.491 ± 0.002
$L_2/(L_1 + L_2)$ in I	0.509 ± 0.002

Table 4.7: Parameters of OGLE 5 38089 derived from the photometric analysis shown together with 1σ bootstrap errors.

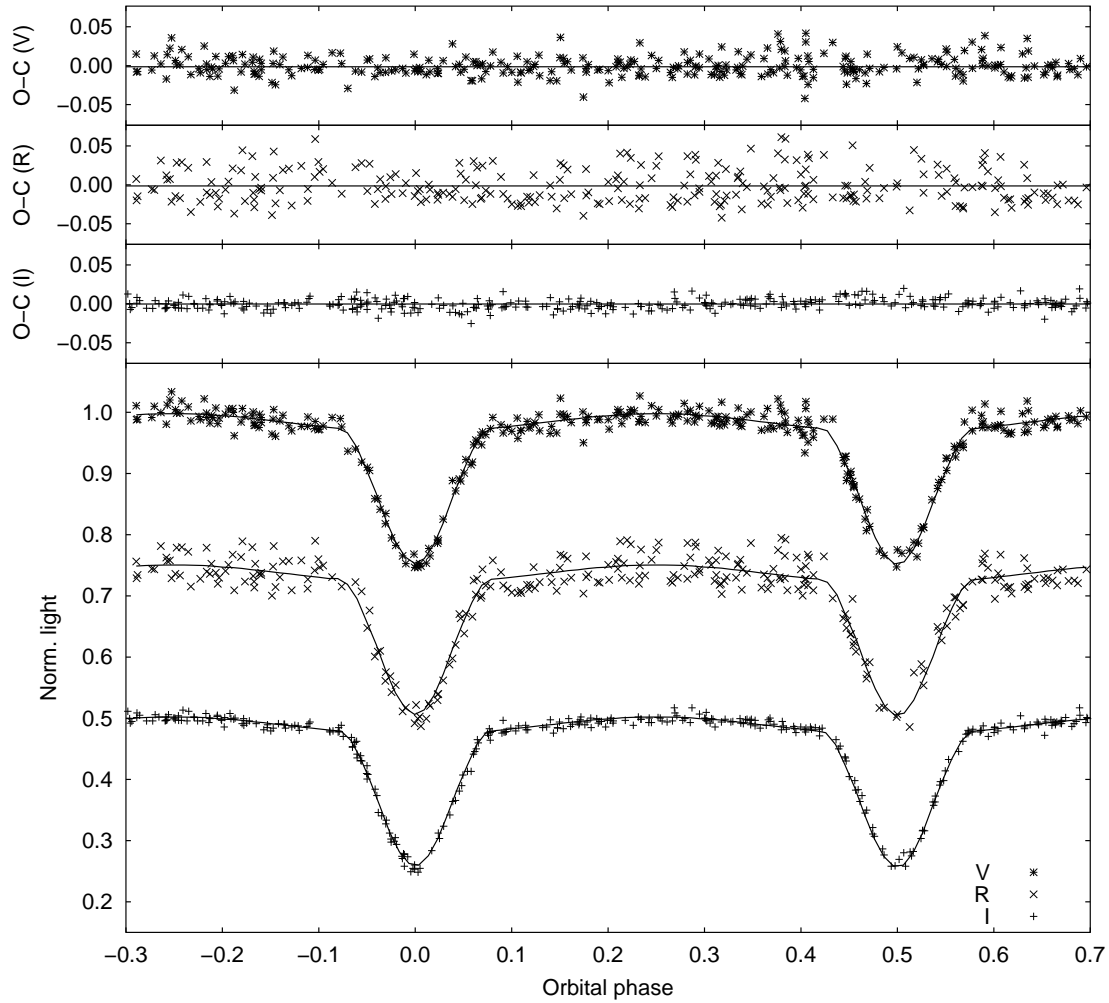


Figure 4.14: *V*, *R* and *I* light curves of OGLE 5-038089 shown together with best fits. For clarity, error bars of the individual data points are omitted and the *R* and *I* light curves are shifted down 0.25 and 0.5 light units, respectively.

Since OGLE 5 38089 consists of hot stars with spectral type B0, it seemed desirable to gain additional information from the spectra by fitting the He II line at 4686\AA . Of course, owing to the moderate S/N of the observations, this line was only weakly discernible in most spectra. Nevertheless, the fits found during all phases look quite reasonable and support the stability of the overall FITSB2 solution (see Figs. 4.16 and 4.17). For the primary star an effective temperature of 30401 K was derived, consistent with the B0 classification of Harries et al. (2003). While these authors have determined a slightly lower temperature of the secondary component upon visual classification of the disentangled spectrum of the companion, the FITSB2 and MORO runs consistently agree on a slightly higher secondary temperature. Nevertheless, the differences are small. Both stars can be classified as typical B0 main sequence stars. The spectroscopically derived values for the surface gravities support this finding, since they are both close to the $\log g \approx 4.0$ value

T_1 [K]	30401 ± 264
T_2 [K]	30709 ± 182
M_1 [M_\odot]	14.2 ± 0.6
M_2 [M_\odot]	12.9 ± 0.5
R_1 [R_\odot]	5.6 ± 0.1
R_2 [R_\odot]	5.7 ± 0.1
$\log g_1$ (from $g = GM/R^2$)	4.09 ± 0.02
$\log g_2$ (from $g = GM/R^2$)	4.04 ± 0.02
$\log g_1$ (from spectra)	4.14 ± 0.06
$\log g_2$ (from spectra)	4.01 ± 0.04
a [R_\odot]	22.5 ± 0.2
$v_1 \sin i$ [km/s]	222.0 ± 4.1
$v_2 \sin i$ [km/s]	243.6 ± 2.8
γ [km/s]	153.1 ± 2.4
$v_{\text{rot},1} \sin i$ [km/s]	228.3 ± 9.5
$v_{\text{rot},2} \sin i$ [km/s]	128.0 ± 6.9

Table 4.8: Absolute parameters of OGLE 5 38089 derived from spectroscopic and photometric analysis shown together with propagated 1σ bootstrap errors.

expected for this kind of star. With a mass ratio of $q > 0.9$ and luminosity ratios close to unity in all passbands they are obviously very similar also in the mass regime. The only significant difference between both components is their rotational velocity. While the value of the secondary is compatible with tidally locked rotation, the primary component clearly rotates faster than indicated by hypothetical orbital synchronization. The systemic velocity of OGLE 5 38089 amounts to 153 km/s, which is again in excellent agreement with the generally accepted value of the SMC's radial velocity.

The spectral line profiles of OGLE 5 38089 were fitted very well, although it is evident that the S/N is somewhat lower than for example that of OGLE 11 30116 (see Section 4.7.2). Near the quadrature phases a pronounced peak was often observed between the

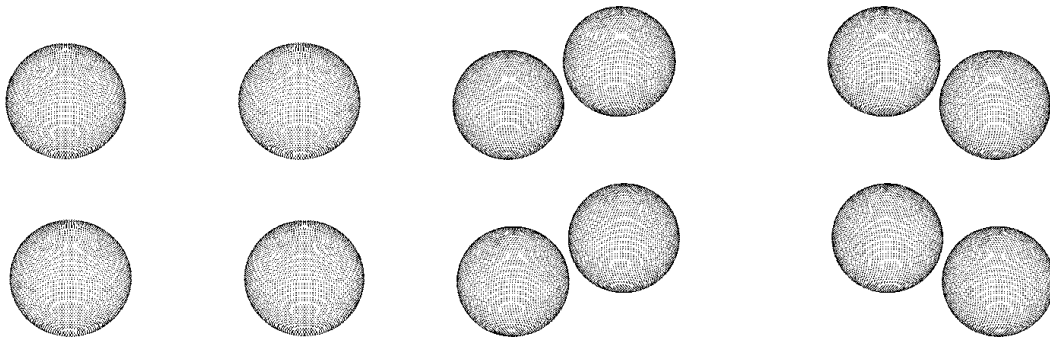


Figure 4.15: 3D plots of OGLE 5 38089 at different orbital phases.

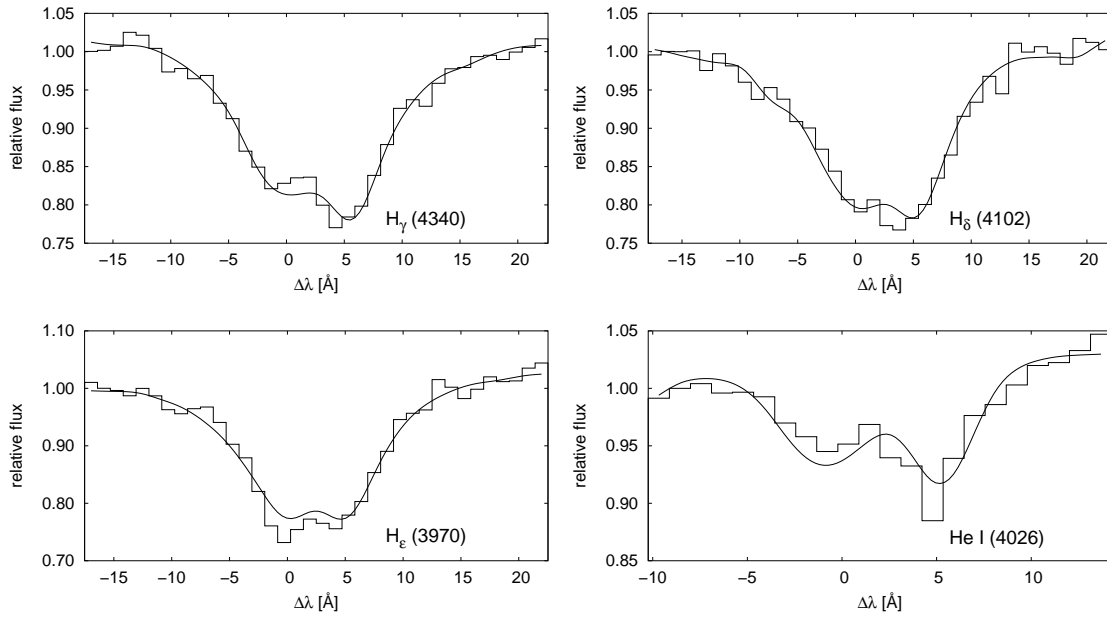


Figure 4.16: Spectral line fits of OGLE 5 38089 shown together with observational data for orbital phase 0.27 (first quadrature).

absorption line components of both stars in the $H\beta$ and $H\gamma$ profiles. It is associated with a redshift of about 2 \AA which indicates a velocity consistent with the SMC radial velocity. Therefore it can be assumed that the observed peak is due to emission from some

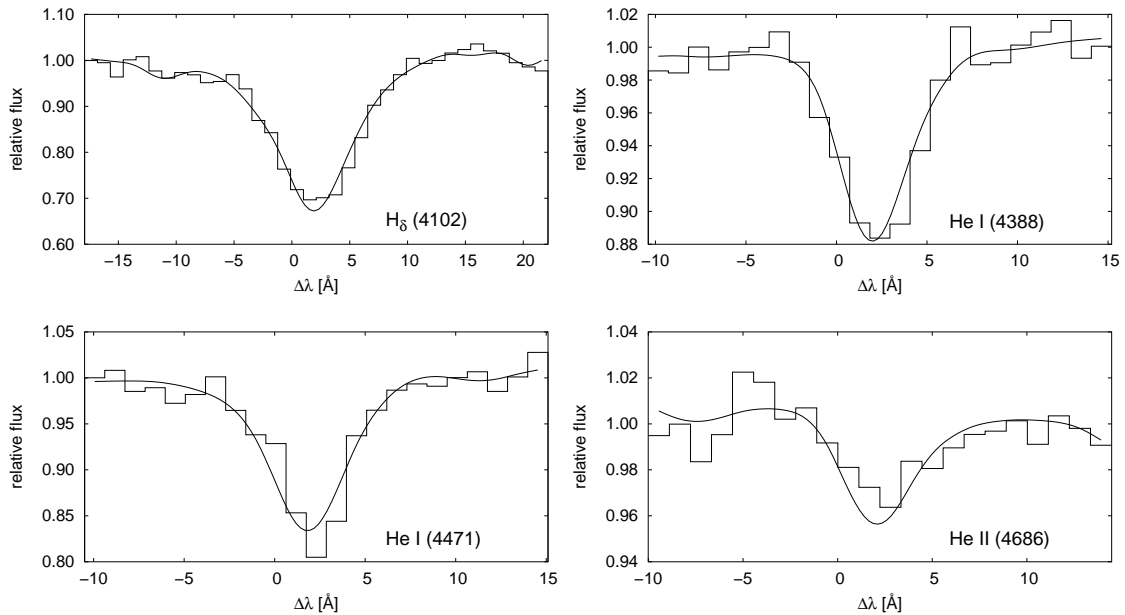


Figure 4.17: Spectral line fits of OGLE 5 38089 shown together with observational data for orbital phase 0.97 (during primary eclipse; note how good the fits are due to the consideration of the phase-dependent scaling factor L_2/L_1).

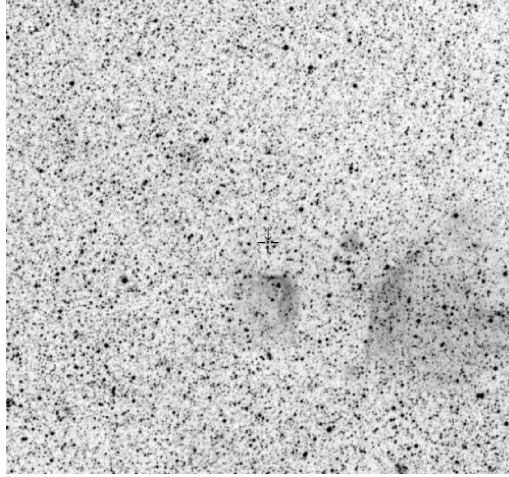


Figure 4.18: The vicinity of OGLE 5 38089 (marked near the center of the image) shows strong nebulosity in the R filter, explaining the emission lines observed at SMC systemic velocity. The frame has been taken from the ESO DSS-2 survey and is 15×15 arcminutes in size.

nebulosity localized in the SMC near OGLE 5 38089 (see Fig. 4.18). The $H\beta$ lines were not fitted due to the profile distortion caused by this emission. In $H\gamma$ the emission is only moderately strong, therefore it was considered safe to include this absorption line in the fit. Other lines do not seem to be affected at all. 36 spectra of OGLE 5 38089 were available, as the system was located in overlapping fields.

According to the outline given in Section 4.6.2 the following values can be derived for the distance and distance modulus of OGLE 5 38089:

component	distance [kpc]	dist. mod.
primary	57.2 ± 0.8	18.79 ± 0.03
secondary	57.7 ± 0.8	18.81 ± 0.03
both	57.5 ± 0.5	18.80 ± 0.02

The values for both individual stars agree very well and are exactly in the range which is to be expected for SMC members. It is stressed again that the SMC itself has a certain depth. All stars analyzed in this work lie very close to the center of the galaxy. One can assume that the line-of-sight depths for young stellar populations in this region is as large as about 10 kpc (see Martin et al. 1989; Crowl et al. 2001). If a sufficient number of these very bright objects are analyzed, they should yield an approximate mean distance to the center of the SMC. However, such an undertaking is beyond the scope of this work. For an attempt to establish the SMC distance see also Hilditch et al. (2005).

4.7.5 OGLE 6 215965

m_I [mag]	P [d]	$T_{\text{eff},1}$ [K]	Conf.
14.1	3.946078	26363	DE

OGLE 6 215965 is a well-separated eclipsing binary (see Fig. 4.20), in contrast to the majority of the SMC systems analyzed otherwise (see Sections 4.7.1, 4.7.2 and 4.7.3). From the light curve this configuration is evident, as clearly defined ingress and egress points of the minima exist, while out-of-eclipse variation is present, but relatively moderate compared to the closer binary systems. MACHO V and R light curves are available for this system, but due to unknown reasons they are of extremely bad quality and suffer from intolerable amounts of scatter and outliers, especially the observations in the V band. Therefore it was decided not to include these data sets in the analysis in order not to compromise the solution with the potentially damaging influence of bad data. Fortunately, the OGLE I light curve is of excellent quality with regard to scatter (see Fig. 4.19). On the other side, the phase density of points is low, especially so in the minima. Nevertheless, the available data proved to be sufficient to arrive at an unambiguous photometric solution. From the light loss of about 30% during primary minimum it is clear that the orbital inclination cannot be as low as that of OGLE 9 175323. The brightness of the I light curve reaches 14.1 mag during quadrature phases, which explains the good S/N of the measurements. With 3.946078 days it has by far the longest orbital period of all stars analyzed in this work.

The best fit of the light curve is presented in Fig. 4.19. The quality of the data can be judged well by means of the residuals: they are among the smallest found in all analyses contained in this work. Apart from that, the fit itself is excellent, no systematic deviations are present anywhere except for a short range of orbital phase during the onset of primary minimum. At that time a subtle trend towards positive values of the residuals can be detected. Due to the general lack of measurements it remains unclear whether it is a real effect or just an observational artefact. Due to both stars being well inside their Roche lobes, the presence of mass transfer and the associated light curve effects are very unlikely. Therefore the effect may indeed be caused by a random clustering of measurements, especially as nothing similar is present anywhere else in the otherwise perfectly symmetric light curve. Some uncertainty remains regarding the depth of the primary min-

i [deg]	75.40 ± 0.10
T_1 [K] (fixed)	26363
T_2 [K]	25482 ± 111
R_1/a	0.278 ± 0.001
R_2/a	0.339 ± 0.001
$L_1/(L_1 + L_2)$ in I	0.418 ± 0.002
$L_2/(L_1 + L_2)$ in I	0.582 ± 0.002

Table 4.9: Parameters of OGLE 6 215965 derived from the photometric analysis shown together with 1σ bootstrap errors.

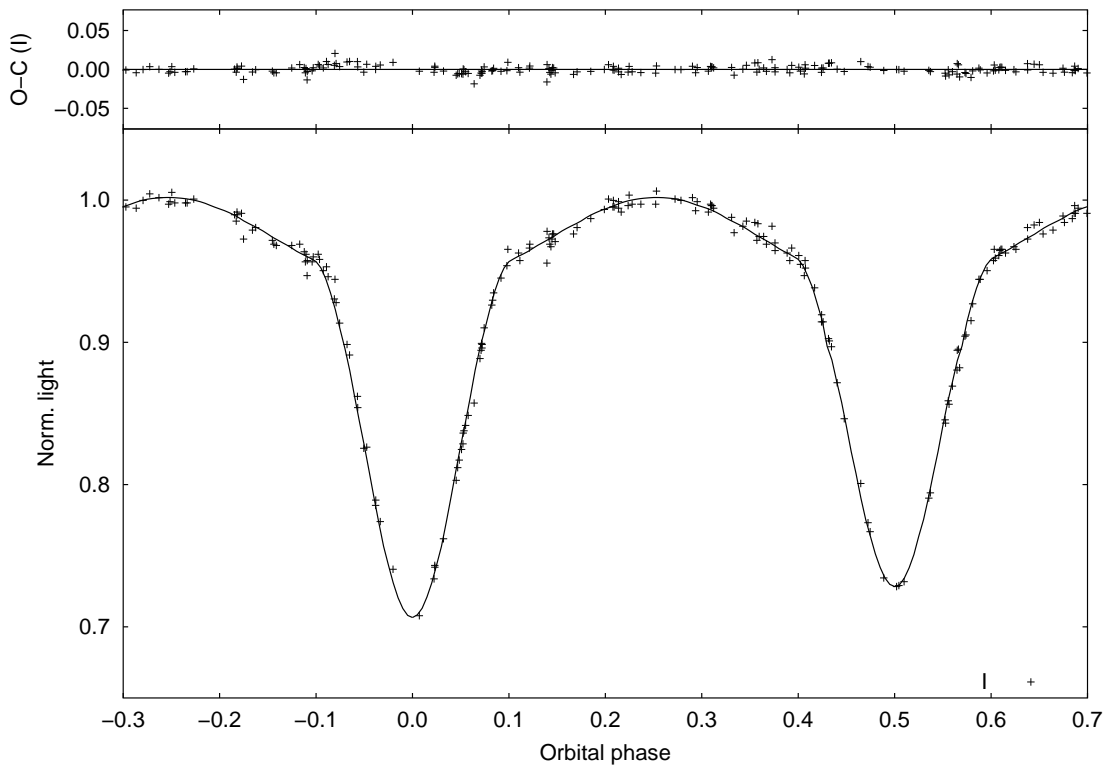


Figure 4.19: *I* light curve of OGLE 6 215965 shown together with best fit. For clarity, error bars of the individual data points are omitted.

imum, as phase coverage is particularly poor in that region. Basically, the bottom of the eclipse is established by a single data point. Since both minima must be identical in width and the gradients of the wings are reasonably well established, there is not as much scope for variation in minimum depth as one might think.

From the different depths of both light curve minima it is clear that there must be a certain temperature difference of both components. The star being eclipsed at phase 0 produces the deeper minimum and must be the hotter component. It is therefore considered the primary star. Interestingly, further analysis shows that in all other respects it is actually the secondary star. From the light curve solution in combination with the spectroscopically derived radial velocity semi-amplitudes it is evident that the “secondary component” is not only the more massive, but also the larger star of the system. This finding is of course consistent with an earlier departure of the secondary component from the main sequence caused by its higher mass. A comparison with the parameters of the primary component should allow a good age determination of the system. Indeed the two components are consistent with the same evolutionary isochrone, as can be seen in the comparison with the evolutionary tracks by Claret (2005) in Fig. 4.23 of Section 4.8.

The primary component shows much weaker absorption lines in the spectra due to its lower luminosity compared with the evolved secondary. Obviously, the constraints imposed by these lines are not enough to reliably determine the temperature and surface

T_1 [K]	26363
T_2 [K]	25369 ± 1124
M_1 [M_\odot]	14.7 ± 0.4
M_2 [M_\odot]	15.7 ± 0.3
R_1 [R_\odot]	9.1 ± 0.1
R_2 [R_\odot]	11.1 ± 0.1
$\log g_1$ (from $g = GM/R^2$)	3.69 ± 0.01
$\log g_2$ (from $g = GM/R^2$)	3.54 ± 0.01
$\log g_1$ (from spectra)	3.50 ± 0.02
$\log g_2$ (from spectra)	3.41 ± 0.08
a [R_\odot]	32.6 ± 0.2
$v_1 \sin i$ [km/s]	209.4 ± 2.0
$v_2 \sin i$ [km/s]	196.8 ± 1.7
γ [km/s]	135.6 ± 1.4
$v_{\text{rot},1} \sin i$ [km/s]	116.9 ± 6.1
$v_{\text{rot},2} \sin i$ [km/s]	141.1 ± 5.2

Table 4.10: Absolute parameters of OGLE 6 215965 derived from spectroscopic and photometric analysis shown together with propagated 1σ bootstrap errors. The primary temperature was fixed to the photometrically derived value in this case.

gravity of this component. Therefore the usual procedure with fixing one of the temperatures according to the photometrically derived temperature ratio was used, but the other way around than usually. In this case the secondary temperature was freely adjusted, while the primary temperature was set to the photometrically derived value during spectral analysis. The results are very consistent and do not have χ^2 values any larger than with the unreasonable solutions derived by adjusting the primary temperature, too. This shows that the secondary component dominates the spectra too much in order to unambiguously extract both temperatures without further boundary conditions. As effective temperatures of about 26200 K and 25400 K were derived, they can both be classified

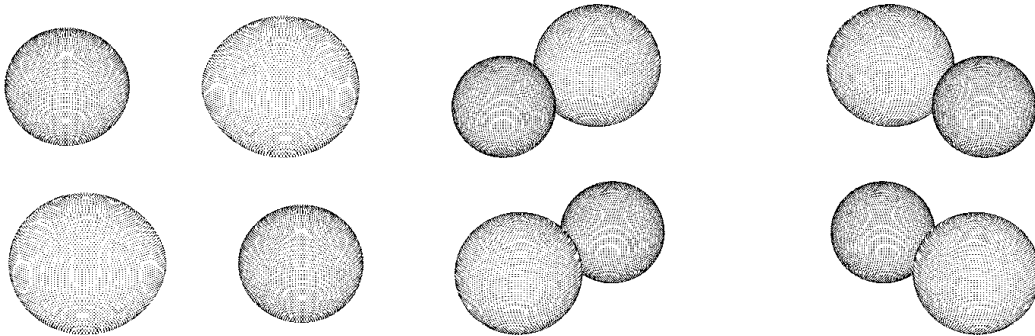


Figure 4.20: 3D plots of OGLE 6 215965 at different orbital phases.

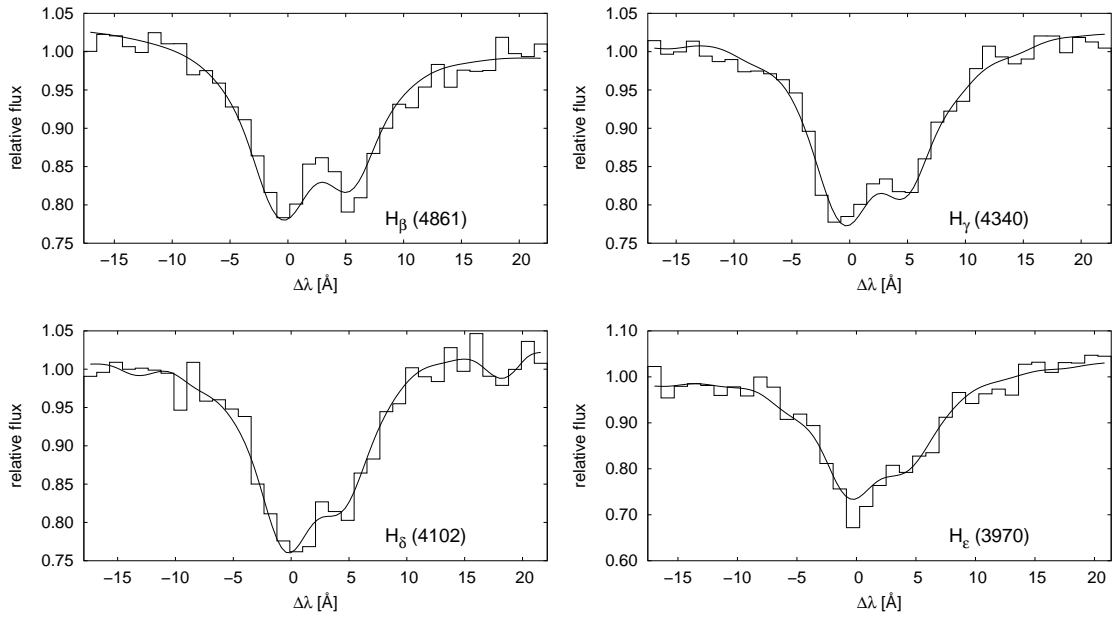


Figure 4.21: Spectral line fits of OGLE 6 215965 shown together with observational data for orbital phase 0.69 (between secondary eclipse and second quadrature).

as spectral type B1. This is only a 0.5 deviation in spectral type from the B0.5 classifications proposed by Harries et al. (2003). The rotational velocities of both stars are in excellent agreement with synchronous rotation which is consistent with OGLE 6 215965 being somewhat older than the other SMC systems analyzed. So tidal forces had plenty of

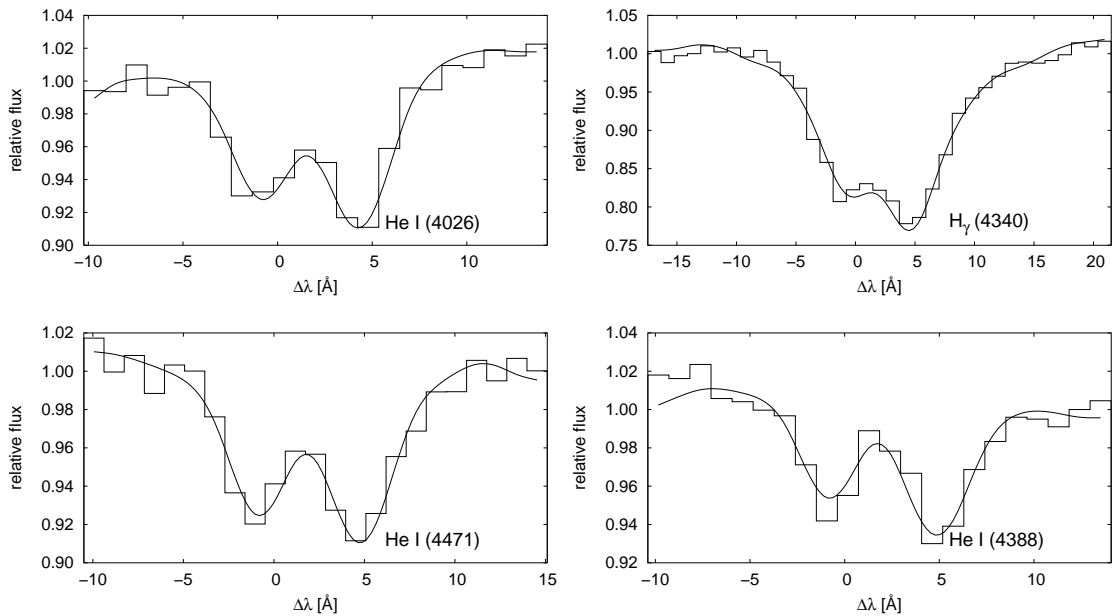


Figure 4.22: Spectral line fits of OGLE 6 215965 shown together with observational data for orbital phase 0.20 (between primary eclipse and first quadrature).

time to synchronize the rotation rate of both stars to the orbital period. With a systemic radial velocity of 136 km/s the binary shows no obvious discrepancy from the generally accepted radial velocity of the SMC.

The spectra of OGLE 6 215965 are fitted very well. Examples of considered absorption lines at different orbital phases are shown in Figs. 4.21 and 4.22. As can be seen, the primary component is clearly visible in the H β and He I lines, but appears somewhat weaker in H γ , H δ and H ϵ . This adds to the problem that the temperature of the primary component cannot be unambiguously extracted from the spectra, although 36 single frames were available covering all orbital phases.

Regarding the distance determination it can be noted that OGLE 6 215965 establishes the short end of the distance scale found in this work. With the derived values it still lies in the 10 kpc band of SMC line-of-sight depth proposed by Martin et al. (1989); Crowl et al. (2001):

component	distance [kpc]	dist. mod.
primary	54.0 ± 0.4	18.66 ± 0.02
secondary	54.1 ± 1.2	18.67 ± 0.07
both	54.0 ± 0.6	18.67 ± 0.04

The values of both binary components are perfectly consistent with each other. Harries et al. (2003) have found a distance modulus of 18.83 for this system. This discrepancy arises from the different temperatures determined. While Harries et al. (2003) fixed both temperatures (!) to the values corresponding to their spectral classification of the components, in this work the absolute temperature of the secondary component and the temperature ratio were physically determined from model spectra and light curve analysis. Therefore the value published here is clearly to be preferred.

4.8 Comparison with evolutionary tracks

The absolute parameters derived in Section 4.7 can be compared with the predictions by contemporary stellar evolution theory. Of course, one must keep in mind that practically all available evolutionary calculations are based on single stars. Close-binary evolution is a highly complicated matter and evolutionary tracks are only available for certain scenarios of mass transfer and initial boundary conditions. However, a comparison of the actual absolute parameters of the components of the studied systems with evolutionary tracks of single stars is still valuable to gain insights into close binary interaction effects and their consequences for the evolutionary state of the binary components, which can be quite different from what would be expected for conservative single star evolution. Here the recent stellar evolution calculations by Claret (2005) were used. These are based on a grid of stellar models for SMC metallicity of $Z = 0.004$ which cover a mass range from 0.8 to $125M_{\odot}$. They take into account mass loss caused by stellar winds (Nieuwenhuijzen & de Jager 1990) and convective core overshooting. The radiative opacities for hot stars

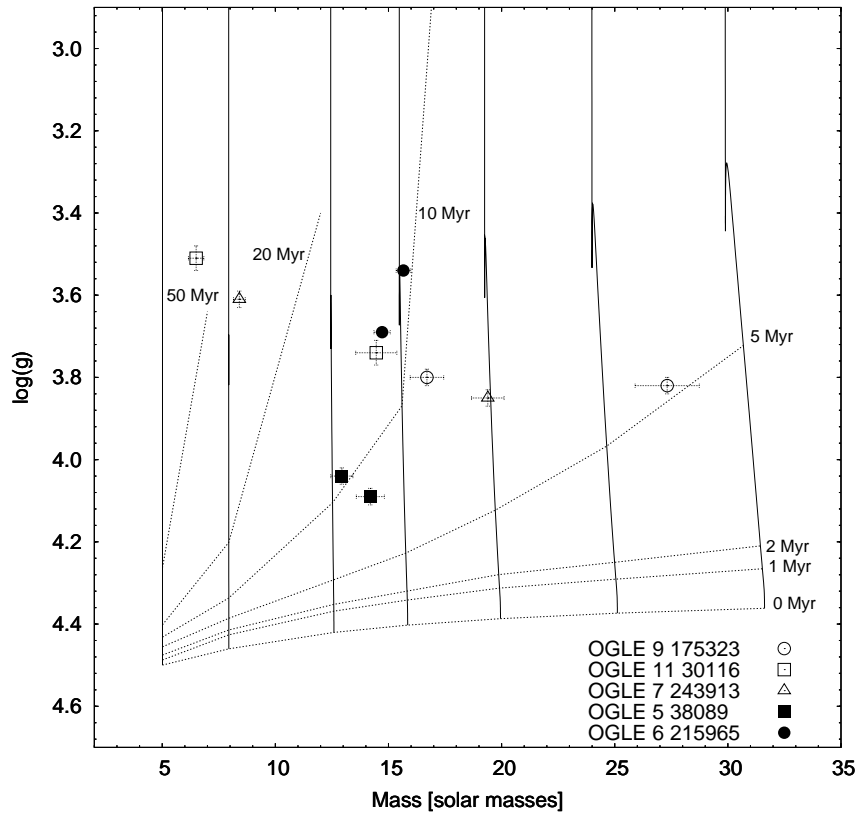


Figure 4.23: Position of the components of the five binaries for which absolute parameters were derived in the $\log g$ - M -plane, compared with evolutionary tracks and isochrones by Claret (2005). The components of the two detached binaries (filled symbols) display consistent ages, while the secondaries of the three semi-detached and contact binaries (open symbols) appear much too old due to the mass loss to their respective primaries.

are taken from Iglesias & Rogers (1996). The models follow the evolution of 13 isotopes from ^1H to ^{26}Mg and use the basic nuclear reaction rates published by Caughlan & Fowler (1988).

One must keep in mind, however, that the evolution especially of close binary star systems can be quite different from single-star evolution, mainly due to the many different stages of evolution which can force mass transfer from one component to the other, altering their physical properties and further development. In classical single-star evolution theory, three distinct stages are known where the stars expand in size: during the main sequence stage, the stellar radius usually increases by a factor of about 2, while during the quick transition from the terminal-age main sequence (TAMS) to the red-giant stage the size of a star may expand by a factor of 50. The final evolution to the asymptotic giant branch (AGB) of the red-supergiant stage is accompanied by another very quick expansion of the star. More information on this subject can be found in Hilditch (2001).

In binary systems, an expanding star may reach its Roche lobe during any of the three expansion phases described, resulting in the transfer of mass to its companion. Accordingly, there are three cases of mass transfer defined:

- Case A: The star already reaches its Roche lobe during the slow and moderate expansion caused by evolution on the main sequence. Systems with short orbital periods of up to a few days are prone to encounter this kind of mass transfer, since their components are usually already close to their Roche lobes in zero-age main sequence state (ZAMS).
- Case B: A longer orbital period between several and about 100 days will cause most stars to reach their Roche lobes during the fast transition between the TAMS and the first red-giant stage. Core helium ignition of the red giant may interrupt the mass transfer process, if it causes its radius to decrease enough to not longer fill its Roche lobe (case BB).
- Case C: In the case of long-period binaries (several 100 days), the separation is wide enough to allow evolution up to the red-giant stage without any mass transfer occurring. Mass is transferred not before the exhaustion of core helium burning, when the star evolves to the supergiant state with the associated further expansion.

The binary components of the five photometrically and spectroscopically analyzed systems, for which precise absolute quantities could be derived, are compared with the Claret tracks in Fig. 4.23. Two subgroups of objects can be easily distinguished. For the detached systems, OGLE 5 38089 and OGLE 6 215965, both components have apparently evolved like single stars without previous interaction and are found on or close to a single isochrone for an age of about 10 Myr.

The semi-detached and contact systems, however, are undergoing mass transfer or did so in the past. They are typical examples for the case A mass transfer discussed above. Moreover, they clearly are subject to what is known as the “Algol paradox”. This classical paradox refers to the eclipsing binary Algol which has been observed to contain a more massive primary star well within its Roche lobe, and an obviously more evolved secondary

filling its Roche lobe. According to single-star evolution theory this is not possible, as the more massive star always evolves faster than its companion. Therefore the primary component should be the large, Roche-lobe filling component. The paradox is only solved by taking into account the possibility of Roche-lobe overflow, i. e. the transfer of mass from one component to the other via the inner Lagrangian point. This way, the originally more massive (now secondary, less massive) star transferred or is still in the process of transferring enough mass to the originally less massive (now primary, more massive) star to reverse the mass ratio of the binary. This is clearly the case for OGLE 9 175323, OGLE 11 30116 and OGLE 7 243913.

The “paradox” clearly manifests itself in Fig. 4.23: the less massive secondary components appear much older than their primary companions due to the mass exchange they caused after having filled their respective Roche lobes. They are now less massive than in their ZAMS state and farther evolved than their actual mass would suggest. The ages of the primaries are in the range of 5 to 15 Myr.

4.9 Distance to the LMC

Finally, after having computed the absolute parameters and distances of individual systems, a mean value for the distance to the SMC can be determined. Here only five binaries were analyzed as exemplary cases. Therefore the mean distance given here can by no means be representative. Nevertheless, the good agreement with previously determined distance values by e. g. Harries et al. (2003) or Hilditch et al. (2005) shows the enormous potential of the approach used in this work. It must be stressed again that the self-consistency of the results achieved here is much better than in the above-mentioned studies, as has been discussed in much detail in Section 4.7. The distance to the SMC derived as the mean of the five eclipsing binaries analyzed photometrically and spectroscopically in this work, together with its 1σ standard error, is determined as follows:

distance [kpc]	distance modulus
59.5 ± 4.0	18.87 ± 0.15

5 Conclusions and outlook

Eclipsing binaries are among the most important objects from which we can gain in-depth knowledge about the properties and parameters of stars. In light of the huge photometric data bases which have become available as by-products of large microlensing surveys in recent years, this work was intended to explore the unique possibilities which the huge number of newly discovered eclipsing binaries offers and to determine fundamental stellar properties on an absolute scale for a large number of stars. In contrast to other approaches, which are based on statistical investigations or less physical models and assumptions, a concept is introduced to perform a simultaneous photometric and spectroscopic analysis of early-type OB binaries, which is capable to be applied to a large number of program stars with acceptable efforts. The main advantage of this method is that it is exclusively based on physical assumptions and models and does not leave scope for subjective estimates (e. g. temperatures derived from spectral types) or statistical presumptions (like, e. g. mass ratios simply fixed at $q = 1$), which are usually applied by other investigators when dealing with the task of stellar parameter determination for large binary samples. The approach used in this work is therefore superior in a sense to yield results of unprecedented accuracy, not only in individual cases, but for the major part of the whole bulk of objects. Also, another feature is the way of reckoning realistic error margins for the derived quantities based on the bootstrap method, which has to be preferred to the mostly supplied formal fitting errors, which do not include systematic error sources and hence are usually far too small.

The overall aim was to determine absolute parameters and distances of early-type eclipsing binaries in the LMC. The original plan was to select a number of eclipsing binary stars from the microlensing survey archives and analyze their light curves in combination with spectra obtained in one of our proposed observing runs. Spectroscopic observations with the 3.9 m AAT and the 2dF spectrograph in Australia were actually approved, but could finally not be carried out due to the early commissioning of the 2dF follow-up instrumentation AAOmega in October 2005. For another joint proposal with a group at Göttingen University guaranteed spectroscopic observing time at the new-technology 11 m SALT telescope in South Africa would have been used to observe the program stars, if not an unforeseen delay caused by technical problems with the main focus of this instrument would have prevented these observations to be carried out in due time for this thesis.

Due to reasons explained in Section 1.3 photometric data alone are not sufficient to determine absolute parameters of eclipsing binaries. So alternative ways had to be sought to meet the main objectives of this work. This was essentially achieved by splitting the working program into two parts: one to demonstrate the power of the photometric analysis method by means of numerous binaries of different configurations, and a second one to

illustrate the concept of combined photometric and spectroscopic analysis with the aid of archival spectra for especially interesting binaries with high quality data.

The first part was devoted to purely photometric analyses of originally selected program stars of early OB spectral type. The careful case studies of 25 systems with detached, semi-detached and (over-)contact configurations impressively demonstrate the degeneracy of photometric solutions with respect to one of the most essential parameters – the mass ratio q of both components (Neßlinger 2004). Mostly, equally good light curve fits can be found for a wide range of q values, and there is no way to pin down the right value of q from photometric data alone. By a multitude of solutions it is shown how other important system parameters closely correlate with the variation in q . It is not only very instructive and already provides important physical insights in the structure of a system to define these correlations quantitatively for systems of different type, but the q -dependent family of solutions also forms a valuable basis for future investigators of the program stars, once spectroscopic data will be available. The mass ratio can then easily be derived from the radial velocity curves, and absolute parameters are uniquely determined by the photometric solutions.

5.1 Results of the photometric analysis

Among the three largest available microlensing survey databases, MACHO, OGLE and EROS, MACHO was selected as primary source for the photometric data. After careful consideration of the pros and cons of each of the available projects, MACHO photometry simply offered the best compromise of the desired features: hundreds of light curves for suitable objects were available, and each of them has good to excellent phase coverage in two passbands, R and V . The OGLE archive even contains thousands of eclipsing binary light curves with S/N comparable to MACHO observations. Nevertheless, only in the I band were light curves available with acceptable phase coverage and sufficient number of data points. As for EROS, this survey offered only a very limited number of a few tens of eclipsing binaries with observations of mixed quality and phase coverage. So it was decided to select suitable objects from the MACHO survey and subject them to the most sophisticated photometric analysis possible.

Since the focus lay on close, early-type (OB) eclipsing binaries, the list of objects was narrowed down to 239 objects with color index $V - R < 0$ and orbital period $P < 2d$. From this sample, the 25 visually brightest objects were chosen for final analysis, as these promised to contain the maximum possible amount of information due to excellent S/N . The completion of several steps was necessary to prepare the raw MACHO data for light curve analysis. During this process it became obvious that the original period and minimum time search conducted by the MACHO collaboration (Alcock et al. 1997a) as an automated process did not provide the necessary precision. Therefore these parameters were newly determined before the photometric analysis could commence.

The analysis itself was conducted by means of MORO, a state-of-the-art light curve synthesis and optimization software originally described by Drechsel et al. (1995). Essentially, a synthetic light curve is computed from user-supplied initial parameters and

compared with the observations. An improved new set of parameters is then constructed by application of the simplex algorithm, again compared with the observations and so on. Due to the nature of the iterative simplex scheme, this approach cannot diverge and offers a great deal of numerical stability. This way, the parameter set which yields the best fit of the observations is finally found. The selection of suitable start parameters is one of the key ingredients to successful light curve solution. Most analyses published in the literature are based on individual user-supplied choices – essentially “best guesses” of more or less experienced researchers. In this work a different method was preferred. A dense grid of about 10^7 synthetic light curves was computed by a systematic variation of all essential parameters over a wide range. For each star it was systematically scanned for light curves matching closely the observations before the actual parameter optimization was started.

Due to the lack of spectroscopic data, no definite mass ratio could be assigned to any of the stars analyzed in this part of the work. Therefore each analysis was repeated for the entire physically reasonable range of mass ratio values in steps of 0.05.

Another fundamental improvement over existing binary light curve analyses is the accurate and realistic representation of the associated parameter errors. As it is not possible to propagate observational errors through the simplex algorithm, the time-consuming bootstrap method was used for estimation of errors. If spectroscopy becomes available, simple error propagation will therefore immediately yield the absolute parameters together with appropriate errors.

The 25 systems analyzed in this part of the work were found to contain 13 detached, 4 semi-detached and 4 overcontact systems. Four “special cases” with unusual configurations or special properties like multiple solution regimes were also found. Several correlations between light curve parameters became evident during the analyses. One of the most intricate dependencies explains the varying determinateness of the derived parameters with binary configuration: when changing the mass ratio q from a small value to a higher one (i. e. $q = M_2/M_1 \rightarrow 1$) in a detached system, the center of mass of the system shifts towards the secondary component. This reduces the tidal distortion of the secondary component while at the same time increases it for the primary star. The associated change in relative luminosities must then be counteracted by a change in relative radii, a compensation mechanism clearly seen in most of the analyzed stars. This on the other hand modifies the depth of both light curve minima and has to be counteracted in turn by a change in orbital inclination. However, this mechanism does not work so well for semi-detached or overcontact binaries, as in these cases one or both surface potentials are fixed with the mass ratio. Therefore the freedom of the radii to change is severely limited, even more so because for these strongly distorted stars even small parameter changes have severe effects on the light curve shape. The range of photometrically possible mass ratios can be narrowed down significantly. This explains nicely why close, possibly Roche lobe-filling eclipsing binaries are preferable targets, especially if no spectroscopic observations are available.

The bulk of analyzed systems was found to be consistent with main sequence or only mildly evolved stars, while some of the more complicated cases can obviously only be explained by assuming significantly evolved stars and strong close-binary interactions. Several indications for mass transfer between binary components were found in the light

curves. For some of the “special cases” mentioned, two entirely different solution regimes were found in the parameter space, which both yield light curve fits of equal quality. No further conclusions about these systems can be drawn without a fair bit of speculation.

One of the most important advances of this work over earlier studies analyzing large samples of extragalactic binaries is its general admittance and systematic evaluation of a large range of physically reasonable values for the mass ratio. Despite best efforts, no photometric mass ratio can be uniquely established except for some very rare special cases featuring Roche lobe-filling components and total eclipses (see also Terrell & Wilson 2005). Nevertheless, other works simply used a statistical approach by setting the mass ratio generally to 1 (Wyithe & Wilson 2001, 2002; Michalska & Pigulski 2005), inducing severe errors especially in the relative radii and the orbital inclination with immediate consequences for the derived masses. Others attempted to constrain the mass ratio by using mass-luminosity-relations for Galactic main-sequence stars (Graczyk 2003), a more pragmatic but still very inaccurate approach. Additionally, the error estimation technique used here is state-of-the-art and far superior to the standard “formal” error estimates produced by the respective χ^2 minimization methods.

5.2 Results of the spectroscopic analysis

The second part of this thesis is thought to prove the feasibility and full power of the suggested analysis technique. For this purpose a sample of five early-type eclipsing binaries in the SMC was selected, for which high-quality OGLE *I* band and partly also MACHO *V* and *R* band light curves are available; in addition, also 2dF spectra obtained with the Australian AAT telescope existed in the AAO archive. These objects were subjected to the proposed MORO / FITSB2 analysis and yielded results of extraordinary accuracy and consistency between photometric and spectroscopic parameters.

Photometric *I* band observations were retrieved from the OGLE database; for 3 of the 5 binaries also MACHO *V* and *R* curves existed. Orbital periods and times of minima were improved to a high precision to ensure optimum accuracy of the phase-folded light curves. The reduction of the spectra recorded with the AAT / 2dF multi-object spectrograph of the AAO Observatory was completely redone in all steps from raw data stage to the extraction of the final object spectra by use of the 2dFDR software package provided by AAO. Depending on the coordinates of the program stars in the 2dF fields, between 18 and 36 individual spectra could be used for each of the objects. These were sufficiently well distributed in phase to yield a rather homogeneous phase coverage. Note that similar previous attempts to evaluate spectroscopic information for larger object samples with the aim of stellar parameter determination often derived mass ratios from only very few radial velocity measurements randomly distributed over the phase interval, sometimes actually only two spectra taken close to both quadratures, which of course yielded very uncertain mass ratios.

A specifically devised procedure was applied to interrelate the photometric (MORO) and spectroscopic (FITSB2) adjustment algorithms iteratively to ensure a maximum degree of consistency. The FITSB2 spectrum fitting software was used to find the best

possible representation of all spectra of an object simultaneously by interpolating in a grid of synthetic spectra. Using this method combined with the simplex χ^2 -minimizing scheme allows to extract the complete set of stellar parameters for both components without previous separation (“disentangling”) of the component spectra. A unique method for alleviating the complex problem of fitting up to eight absorption lines in each (of up to 36) superimposed spectra taken at different orbital phases at once is the “orbit” mode of FITSB2. This mode requires the user to specify orbital period and phase zero point of the binary as well as the Julian Dates of all fitted observations, thereby removing one degree of freedom of the problem for each spectrum used, because the phasing is enforced. As the relative radial velocity for each phase is determined by the user-supplied orbital parameters, only the absolute radial velocity amplitudes remain to be adjusted. At the same time, temperature, surface gravities and rotational velocities can be independently adjusted. Synthetic spectra for the appropriate ranges of effective temperatures, surface gravities and metallicities based on two different state-of-the-art NLTE model atmosphere codes by Lanz & Hubeny (2003, 2007) and Nieva & Przybilla (2007) were used. The resulting parameters were hardly different for both grids. Subsequently the bootstrap algorithm was applied to derive realistic estimations of the spectroscopic parameter errors.

Employing this method, absolute parameters could be unambiguously derived for the five analyzed case studies. All of them are hot OB-type stars similar to many of those analyzed in Chapter 3. Three are in a contact or semi-detached configuration. These states are most probably reached while both components are still on or near the main sequence in the present cases. Two systems were found to be in a detached configuration. As expected, a wide range of mass ratio values cannot be sufficiently constrained by photometry alone, even for the much better determined semi-detached systems.

As for the distances, typical values for distance moduli of 18.8 to 18.9 (corresponding to 57 – 60 kpc) have been found, with two exceptions of $m - M \approx 18.7$ (55 kpc) and $m - M \approx 19.1$ (66 kpc). These are believed to be real due to the linear depth extent of the SMC. The mean value of $m - V = 18.87$ (59.5 kpc) corresponds to the mean distance of the SMC and lies right in the middle between the so-called “short” and “long” distance scales established by different methods in the literature.

5.3 Outlook

The parameter determination technique used in this work is not based on subjective estimates and uncertain spectral classification (especially doubtful in the case of superimposed component spectra) for deriving stellar temperatures like applied by, e. g., Harries et al. (2003). The approach presented here relies on actual physical models instead. The parameters derived this way are not only more accurate, they also have a higher degree of self-consistency. This is clearly obvious in the final step of the analysis, the determination of the distances. The distances were independently derived for each component of each analyzed binary. The distances found for both components of each binary are always completely consistent, within the mutual error margins (mostly < 1 kpc). This is not the case in the analysis of Harries et al. (2003). Even though the errors quoted by them are

much larger than the ones found in this work, the binary component distances are not even consistent at that level, but differ by as much as 10 kpc. Therefore it can be safely concluded that the methods and techniques presented in this work are excellent tools for effective and consistent parameter determinations of close binary stars.

It is the firm belief and hope of the author that future applications will contribute to a better understanding of stellar and especially binary evolutionary processes. An especially important progress is also expected with regard to the ongoing debate about the calibration of the cosmological distance scale. Thanks to the availability of always larger telescopes and more powerful spectrographs and detectors, distances far beyond that of the Magellanic Clouds and our Local Group galaxies will become accessible by means of the binary star method. It is highly important to complement the conventional methods of distance determination by the use of binary stars as a new class of standard candles, even more so because the accuracy to be achieved will clearly be unrivaled.

Bibliography

- Alcock, C., Allsman, R. A., Alves, D., et al. 1997a, *AJ*, 114, 326
- Alcock, C., Allsman, R. A., Alves, D., et al. 1997b, *ApJ*, 479, 119
- Alcock, C., Allsman, R. A., Alves, D., et al. 1998, *ApJ*, 500, 522
- Alcock, C., Allsman, R. A., Alves, D. R., et al. 1999, *PASP*, 111, 1539
- Ansari, R., Cavalier, F., Couchot, F., et al. 1995, *A&A*, 299, L21+
- Axelrod, T., Freeman, K., Peterson, B., et al. 1994, *Bulletin of the American Astronomical Society*, 26, 1336
- Bauer, M. 2004, Diploma thesis, Friedrich-Alexander-Universität Erlangen-Nürnberg
- Becker, A. 2005, priv. comm.
- Bessell, M. S. 1990, *PASP*, 102, 1181
- Bessell, M. S., Castelli, F., & Plez, B. 1998, *A&A*, 333, 231
- Carroll, B. W. & Ostlie, D. A. 1996, *An Introduction to Modern Astrophysics* (Reading, MA: Addison-Wesley, [c1996])
- Caughlan, G. R. & Fowler, W. A. 1988, *Atomic Data and Nuclear Data Tables*, 40, 283
- Claret, A. 2005, *A&A*, 440, 647
- Clausen, J. V., Storm, J., Larsen, S. S., & Giménez, A. 2003, *A&A*, 402, 509
- Cox, A. N. 2000, *Allen's astrophysical quantities* (Allen's astrophysical quantities, 4th ed. Publisher: New York: AIP Press; Springer, 2000. Edited by Arthur N. Cox. ISBN: 0387987460)
- Crowl, H. H., Sarajedini, A., Piatti, A. E., et al. 2001, *AJ*, 122, 220
- Drechsel, H., Haas, S., Lorenz, R., & Gayler, S. 1995, *A&A*, 294, 723
- Efron, B. 1979, *Annals of Statistics*, 7, 1
- Efron, B. & Tibshirani, R. J. 1993, *An Introduction to the Bootstrap* (Chapman and Hall)
- Fitzpatrick, E. L., Ribas, I., Guinan, E. F., et al. 2002, *ApJ*, 564, 260

- Fitzpatrick, E. L., Ribas, I., Guinan, E. F., Maloney, F. P., & Claret, A. 2003, *ApJ*, 587, 685
- Graczyk, D. 2003, *MNRAS*, 342, 1334
- Grison, P., Beaulieu, J.-P., Pritchard, J. D., et al. 1995, *A&AS*, 109, 447
- Guinan, E. F., Fitzpatrick, E. L., Dewarf, L. E., et al. 1998, *ApJ*, 509, L21
- Haas, S. 1993, Diploma thesis, Friedrich-Alexander-Universität Erlangen-Nürnberg
- Hadrava, P. 1995, *A&AS*, 114, 393
- Hadrava, P. 1997, *A&AS*, 122, 581
- Halbwachs, J. L. 1986, *A&A*, 168, 161
- Harmanec, P. 1988, *Bulletin of the Astronomical Institutes of Czechoslovakia*, 39, 329
- Harries, T. J., Hilditch, R. W., & Howarth, I. D. 2003, *MNRAS*, 339, 157
- Hilditch, R. W. 2001, *An Introduction to Close Binary Stars (An Introduction to Close Binary Stars, by R. W. Hilditch, pp. 392. ISBN 0521241065. Cambridge, UK: Cambridge University Press, March 2001.)*
- Hilditch, R. W., Howarth, I. D., & Harries, T. J. 2005, *MNRAS*, 357, 304
- Hubeny, I. & Lanz, T. 1995, *ApJ*, 439, 875
- Iglesias, C. A. & Rogers, F. J. 1996, *ApJ*, 464, 943
- Kallrath, J. & Linnell, A. P. 1987, *ApJ*, 313, 346
- Kallrath, J. & Milone, E. F., eds. 1999, *Eclipsing binary stars : modeling and analysis*
- Karttunen, H., Kröger, P., Oja, H., Poutanen, M., & Donner, K. J. 1994, *Fundamental Astronomy (Fundamental Astronomy, XV, 511 pp. 399 figs. including 36 color plates. Springer-Verlag Berlin Heidelberg New York)*
- Konacki, M., Torres, G., Jha, S., & Sasselov, D. D. 2003, *Nature*, 421, 507
- Kopal, Z. 1959, *Close binary systems (The International Astrophysics Series, London: Chapman & Hall, 1959)*
- Lanz, T. & Hubeny, I. 2003, *ApJS*, 146, 417
- Lanz, T. & Hubeny, I. 2007, *ApJS*, 169, 83
- Lewis, I. J., Cannon, R. D., Taylor, K., et al. 2002, *MNRAS*, 333, 279
- Lorenz, R. 1988, Diploma thesis, Friedrich-Alexander-Universität Erlangen-Nürnberg

- Lucy, L. B. 1976, *ApJ*, 205, 208
- Martin, N., Maurice, E., & Lequeux, J. 1989, *A&A*, 215, 219
- Michalska, G. & Pigulski, A. 2004, *New Astronomy Review*, 48, 719
- Michalska, G. & Pigulski, A. 2005, *A&A*, 434, 89
- Napiwotzki, R., Christlieb, N., Drechsel, H., et al. 2001, *Astronomische Nachrichten*, 322, 411
- Napiwotzki, R., Christlieb, N., Drechsel, H., et al. 2003, *The Messenger*, 112, 25
- Napiwotzki, R., Yungelson, L., Nelemans, G., et al. 2004, in *Astronomical Society of the Pacific Conference Series*, Vol. 318, *Spectroscopically and Spatially Resolving the Components of the Close Binary Stars*, ed. R. W. Hilditch, H. Hensberge, & K. Pavlovski, 402–410
- Neßlinger, S. 2004, Diploma thesis, Friedrich-Alexander-Universität Erlangen-Nürnberg
- Nieuwenhuijzen, H. & de Jager, C. 1990, *A&A*, 231, 134
- Nieva, M. F. & Przybilla, N. 2007, *A&A*, 467, 295
- Oestreicher, M. O., Gochermann, J., & Schmidt-Kaler, T. 1995, *A&AS*, 112, 495
- Paczyński, B. 1986, *ApJ*, 304, 1
- Paczyński, B. 1997, in “The Extragalactic Distance Scale”, 273–280
- Przybilla, N. 2007, priv. comm.
- Repolust, T., Puls, J., & Herrero, A. 2004, *A&A*, 415, 349
- Ribas, I., Fitzpatrick, E. L., Maloney, F. P., Guinan, E. F., & Udalski, A. 2002, *ApJ*, 574, 771
- Ribas, I., Guinan, E. F., Fitzpatrick, E. L., et al. 2000, *ApJ*, 528, 692
- Roche, E. A. 1849, in “Mémoires de l’Acad. des Sciences de Montpellier”, Vol. 1, 243ff and 333ff
- Ruciński, S. M. 1969, *Acta Astronomica*, 19, 245
- Schwering, P. B. W. & Israel, F. P. 1991, *A&A*, 246, 231
- Simon, K. P. & Sturm, E. 1994, *A&A*, 281, 286
- Stellingwerf, R. F. 1978, *ApJ*, 224, 953
- Szymanski, M. K. 2005, *Acta Astronomica*, 55, 43

- Terrell, D. & Wilson, R. E. 2005, *Ap&SS*, 296, 221
- Udalski, A., Kubiak, M., & Szymanski, M. 1997, *Acta Astronomica*, 47, 319
- Udalski, A., Soszynski, I., Szymanski, M., et al. 1998, *Acta Astronomica*, 48, 563
- Udalski, A., Szymanski, M., Kaluzny, J., et al. 1993, *Acta Astronomica*, 43, 289
- Udalski, A., Szymanski, M., Kaluzny, J., Kubiak, M., & Mateo, M. 1992, *Acta Astronomica*, 42, 253
- Udalski, A., Szymanski, M., Kubiak, M., et al. 2002, *Acta Astronomica*, 52, 217
- Udalski, A., Zebrun, K., Szymanski, M., et al. 2000, *Acta Astronomica*, 50, 1
- van Hamme, W. 1993, *AJ*, 106, 2096
- Wilson, R. E. & Devinney, E. J. 1971, *ApJ*, 166, 605
- Worthey, G. & Lee, H. . 2006, *ArXiv Astrophysics e-prints*
- Wyithe, J. S. B. & Wilson, R. E. 2001, *ApJ*, 559, 260
- Wyithe, J. S. B. & Wilson, R. E. 2002, *ApJ*, 571, 293
- Wyrzykowski, L., Udalski, A., Kubiak, M., et al. 2003, *Acta Astronomica*, 53, 1

Acknowledgements

The successful preparation of this thesis was possible only with much help and continuous support from many friends and colleagues.

First of all, I would like to thank Prof. Dr. Horst Drechsel for the opportunity to prepare my PhD thesis under his supervision. The successful application for funding by the Deutsche Forschungsgemeinschaft, which was a tedious process, was largely undertaken by him. If not for his unfailing patience, with which he answered all my questions and supported me in every way imaginable, as well as his untiring efforts to solve every problem encountered on the way, I would never have been able to successfully complete this work.

I gratefully acknowledge the Deutsche Forschungsgemeinschaft (DFG), which funded my work for three years, including travel expenses for attending conferences in Syros, Greece and Prague, Czech Republic. Furthermore, I am indebted to the anonymous referee who reviewed our application for the DFG and gave us his approval. I would also like to express my gratitude to Prof. Dr. Stefan Dreizler who agreed to prepare the necessary second expertise for my work in spite of his many duties as the dean of his faculty at the University of Göttingen.

Special thanks go to Michael Bauer, Fernanda Nieva and especially Markus Firnstein, all three of which I had the privilege of sharing my office with. We had plenty of opportunities for talking and discussing many matters of various significance and hilarity, be it about astronomy or otherwise (mostly otherwise). Rarely resisting to join in a lively debate, Jasmin Löbl, Stephan Geier, Heiko Hirsch, Florian Schiller and Alfred Tillich contributed many interesting points of view and with their good-natured attitudes made for some of the funniest and most memorable moments at the office.

I would also like to specifically mention our system administrator Rainer Sterzer who was always at hand with most helpful advice and quickly found solutions to all computer-related problems I encountered, even if it meant a load of additional work to him.

Prof. Dr. Irmela Bues showed continuous interest in the progress of my work and contributed many interesting insights from her long career of astronomical research and teaching. I especially thank her for her good advice regarding the search for a chairman for my PhD exam which proved to be difficult due to the upcoming holiday season.

Of course, all other colleagues at the Dr. Remeis Observatory contributed their part to the extremely friendly and relaxed atmosphere which made every day at work a joy, even during the inevitable times when work itself was tedious and unnerving. In addition to the colleagues I already mentioned, I would like to specifically acknowledge the head of our institute, Uli Heber, as well as Edith Day, Heinz Edelmann, Manfred Hanke, Christian Karl, Simon O'Toole, Norbert Przybilla, Roland Richter, Christian Schmitt and Jörn Wilms.

Regarding more private matters, I would like to express my deep gratitude to Jasmin Löbl for her highly motivated (and motivating) efforts to teach my wife and me the intricate art of dancing during the weekends, and to Markus Firnstein for patiently sharing the challenging experience with us.

All my other friends, most notably Jürgen Ramspeck, Viola Baumgärtel, Stefanie Schetter, Michael Pruchnicki and Philipp Hilsdorf I would like to thank for their interest in my work, for many absorbing discussions and for keeping alive my interest in matters beyond my own nose. By showing me that not only astronomers live through many a motivational low, they helped me keep my faith in my project during difficult times.

My former physics teacher Wolfgang Dietz must also be mentioned here. It was him, who first fueled my enthusiasm for physics and especially astronomy, which ultimately led me to take up my studies of physics and subsequently enter my PhD studies. In all likelihood I will now follow in his footsteps and try my very best to offer to my students what he offered to me.

My enthusiasm alone would probably not have been sufficient, though, without the unfailing support (financial and otherwise) from my parents who offered me as much freedom in my decisions as I could ever hope for and still some more.

I would also like to explicitly thank all other people who in one way or another contributed to the success of this thesis, but were not mentioned here, be it due to lack of space or the imperfection of my memory.

Last but not least, I would like to thank my beloved wife Meike, who has been sharing my life for many years now. She is always there to listen to my problems and share my joys with me. Her infinite understanding for all my flaws and little quirks and her unselfish support under all circumstances conceivable are nothing short of amazing, as is the privilege of being able to enjoy them every single day. You are the best wife anyone on Earth (and beyond) could wish for.

This work utilizes public domain data obtained by the MACHO Project, jointly funded by the US Department of Energy through the University of California, Lawrence Livermore National Laboratory under contract No. W-7405-Eng-48, by the National Science Foundation through the Center for Particle Astrophysics of the University of California under cooperative agreement AST-8809616, and by the Mount Stromlo and Siding Spring Observatory, part of the Australian National University.

Lebenslauf

Name: Stefan Rainer Neßlinger
Geburtsdatum: 11. 06. 1978
Staatsangehörigkeit: Deutsch

Grundschule: 09/1984 – 07/1988 Christian-Maar-Grundschule Schwabach

Weiterführende Schule: 09/1988 – 06/1997 Wolfram-von-Eschenbach-Gymnasium Schwabach

Zivildienst: 07/1997 – 06/1998 Diakonisches Werk Schwabach e. V.

Studium: 10/1998 – 05/2004 Studium der Physik an der Friedrich-Alexander-Universität Erlangen-Nürnberg

07. 05. 2004 Abschluss: Dipl.-Phys. Univ. (1,33)

seit 08/2004 Promotionsstudent an der Dr. Remeis-Sternwarte Bamberg
Betreuer: Prof. Dr. Horst Drechsel

Berufliche Laufbahn: 08/2003 – 05/2004 Studentische Hilfskraft an der Dr. Remeis-Sternwarte Bamberg

seit 10/2004 Wissenschaftlicher Mitarbeiter an der Dr. Remeis-Sternwarte Bamberg

Curriculum Vitae

Name:	Stefan Rainer Neßlinger	
Date of birth:	11 Jun 1978	
Citizenship:	German	
University:	since Aug 2004	PhD student at the Dr. Remeis Observatory, Bamberg, Germany Supervisor: Prof. Dr. Horst Drechsel
	07 May 2004	Degree: Dipl.-Phys. Univ. (1,33)
	Oct 1998 – May 2004	Undergraduate studies at the Friedrich-Alexander University of Erlangen-Nuremberg, Germany
Secondary school:	Sep 1988 – Jun 1997	Wolfram-von-Eschenbach-Gymnasium Schwabach
Primary school:	Sep 1984 – Jul 1988	Christian-Maar-Grundschule Schwabach
Civilian service:	Jul 1997 – Jun 1998	Diakonisches Werk Schwabach e. V.
Employment history:	since Oct 2004	Scientific assistant at the Dr. Remeis Observatory, Bamberg, Germany
	Aug 2003 – May 2004	Student assistant at the Dr. Remeis Observatory, Bamberg, Germany